

**IMPLICIT MODELLING OF GEOMETALLURGICAL PARAMETERS FOR
APPLICATION IN MINE PLANNING**

By

TIYANI CHAUKE

submitted in accordance with the requirements for
the degree of

DOCTOR OF PHILOSOPHY

in the subject

MINING ENGINEERING

at the

UNIVERSITY OF SOUTH AFRICA

SUPERVISOR: Prof FRANCOIS MULENGA

March 2023

Declaration

Name: Tiyani Chauke

Student number: **66377056**

Degree: PhD

Exact wording of the title of the thesis as appearing on the electronic copy submitted for examination:

IMPLICIT MODELLING OF GEOMETALLURGICAL PARAMETERS FOR APPLICATION IN MINE PLANNING

I declare that the above thesis is my own work and that all the sources that I have used or quoted have been indicated and acknowledged by means of complete references.

I further declare that I submitted the thesis to originality checking software and that it falls within the accepted requirements for originality.

I further declare that I have not previously submitted this work, or part of it, for examination at Unisa for another qualification or at any other higher education institution.



17/03/2023

SIGNATURE

DATE

Dedication

My thesis is dedicated to my family, whose constant support and encouragement have been a great inspiration for me during my academic journey. Their unwavering belief in me has motivated me to put forth my best effort in my studies, and I am confident that they will take pride in the work that I have achieved.

Acknowledgements

First and foremost, I would like to thank my supervisor, Prof. Francois Mulenga, for his encouragement, patience, and meticulous supervision. The completion of this thesis would have been impossible without his suggestions and comments. His advice was extremely helpful in conducting my research and writing this thesis. I could not have asked for a better supervisor and mentor for my PhD research.

I am thankful for the Mighty God for protecting me and bestowing upon me the skills and knowledge needed to pursue research to this level.

I would also like to thank my family, Rose Ribisi, Musa Evans Shivambe, Ockkie Vincent Chauke, and Maringa Matimu, for all of their help from the start of this project to the end.

The University of South Africa Postgraduate funding bursary programme is acknowledged for its financial contribution to the success of this research.

Abstract

The objective of the thesis was two-fold: to investigate the potential of implicit modelling techniques for modelling geometallurgical parameters in mine planning and to generate synthetic geometallurgical data using Generative Adversarial Networks (GAN) models. Several geometallurgical parameters, including ore grade, Bond work index (BWI), rod mill index, rock quality designation (RQD), drop weight index (DWI), Axb, and Abrasion index (Ai), were modelled in this thesis using implicit and geostatistical methods, and their results were compared.

To generate synthetic geometallurgical data, GAN-based models were used, namely, Conditional Tabular Generative Adversarial Network (CTGAN), Copula Generative Adversarial Network (CopulaGAN), and Gaussian Copula. The process was conducted in Python® using a Synthetic Data Vault (SDV) library, based on original geometallurgical data obtained from previous research papers, theses, and online databases. Geometallurgical block models were produced using implicit (Radial Basis Function) and geostatistical (Ordinary Kriging) methods and compared. The following software packages were used in this study. Leapfrog® Geo, Microsoft® Excel®, and Microsoft® Paint®. The results of the Geometallurgical Block Model (GMBM) were compared using parameters of mine planning, such as the grade-tonnage curve and resource estimations.

In conclusion, the study found that the synthetic geometallurgical data generated in this research was of high quality and demonstrated that implicit modelling methods can improve the accuracy and efficiency of mine planning by modelling geometallurgical parameters. However, more research is recommended to explore other implicit-based methods, such as the potential field and the Hermite Radial Basis Function (HRBF).

Keywords: Implicit modelling, geostatistical modelling, synthetic data generation, geometallurgy.

Table of contents

Declaration	i
Dedication	ii
Acknowledgements	iii
Abstract	iv
Table of contents	v
List of appendices	x
List of figures.....	xi
List of tables.....	xviii
Acronyms and symbols.....	xx
Chapter 1 Introduction	1
1.1 Background of the research.....	1
1.2 Problem statement.....	3
1.3 Aim and objectives of the research	4
1.4 Scope and limitations of the research.....	5
1.5 Contribution to the body of knowledge.....	6
1.6 Organization of the thesis	7
Chapter 2 Literature review	9
2.1 Introduction	9
2.2 Synthetic data generation	10
2.2.1 Generative adversarial networks.....	11
2.2.2 Conditional tabular generative adversarial network.....	13
2.2.3 Copula generative adversarial network	14
2.2.4 Gaussian copula model.....	14
2.2.5 The synthetic data vault	15

2.2.6	Successful use of synthetic data generated for geometallurgical purposes.....	16
2.3	Geometallurgical block modelling	20
2.3.1	Basic principles of block modelling.....	20
2.3.2	Basic principle of kriging.....	21
2.3.3	Simple kriging.....	23
2.3.4	Ordinary kriging.....	24
2.3.5	A note on geometallurgical block models	25
2.4	Orebody modelling.....	26
2.4.1	Explicit orebody modelling.....	27
2.4.2	Implicit orebody modelling.....	29
2.4.3	Implicit over explicit orebody modelling	30
2.5	Implicit modelling methods.....	32
2.5.1	Radial basis function-based method	32
2.5.1.1	Simple radial basis function	33
2.5.1.2	Fast radial basis function	35
2.5.1.3	Leapfrog® methodology.....	36
2.5.1.4	Hermite radial basis function.....	37
2.5.1.5	Generalised radial basis function.	38
2.5.2	Applications of RBF-based methods in orebody modelling ..	39
2.6	Potential field-based implicit method	58
2.6.1	Applications of potential field implicit in ore modelling.....	60
2.7	Signed-distance interpolation method.....	66
2.8	Concluding remarks.....	69
Chapter 3	Research methodology and data collection	75
3.1	Introduction	75

3.2	Description of the original dataset.....	76
3.3	Pre-processing of the original data	82
3.4	Methods for generating the synthetic data	86
3.4.1	Computer-based generation of the synthetic data.....	87
3.4	Implicit modelling methodology.....	93
3.4.1	Software	93
3.4.2	Loading drillholes dataset.....	94
3.4.3	Validation of the original drillhole dataset	95
3.3.4	Numerical composite of drillholes dataset	97
3.3.5	Economic composition of the drillhole dataset	98
3.3.6	Orebody delineating using Indicator RBF.....	100
3.4	Variogram model for implicit and geostatistical modelling.....	101
3.5	Implicit modelling of geometallurgical data	103
3.6	Geostatistical modelling of geometallurgical data	105
3.6.1	Ordinary kriging of geometallurgical dataset	105
3.7	Block modelling of geometallurgical data.....	106
3.8	Challenges encountered.....	108
Chapter 4	Results of synthetic data generation.....	109
4.1	Comparison of similarity scores of synthetic data generated by CTGAN, CopulaGAN, and Gaussian Copula.....	109
4.2	Mean and standard deviation of original and synthetic data	114
4.3	Comparative visualization of synthetic and original data	121
4.4	Principal component analysis of synthetic and original data	135
4.5	Column correlations between synthetic and original data	145
4.6	Summarised conclusion.....	149

Chapter 5	Implicit Geometallurgical modelling with Radial Basis Functions	151
5.1	Introduction	151
5.2	Economic model of the original drillhole assay	152
5.3	Three-dimensional orebody modelling/domain	152
5.4	Validation of the 3D orebody model.....	154
5.4.1	Statistical comparison of 3D orebody and drillhole data assay economic model	154
5.4.2	Visual inspection of 3D orebody and economic model	155
5.5	Implicit geometallurgical modelling	157
5.5.1	Iso-surfaces of geometallurgical parameters created using implicit methods.....	158
5.5.2	3D geometallurgical model generated from iso-surfaces.....	161
5.5.3	Geometallurgical block models.....	165
5.6	Summary of the findings	171
Chapter 6	Geostatistical modelling of geometallurgical data	175
6.1	Introduction	175
6.2	Results of block modelling	175
6.3	Summary and conclusions.....	181
Chapter 7	Comparison of implicit modelling method with geostatistical method technique	183
7.1	Introduction	183
7.2	Comparison of block models of Bond work index generated through implicit and geostatistical methods	184
7.3	Comparison of block models of rod mill index generated through implicit and geostatistical methods	187

7.4	Comparison of block model for RQD index generated through implicit and geostatistical methods	190
7.5	Comparison of block model for drop weight index generated through implicit and geostatistical methods	194
7.6	Comparison of block model for Axb index generated through an implicit and geostatistical method	198
7.7	Comparison of block model for abrasion index generated through implicit and geostatistical methods	203
7.8	Application of geometallurgical block model on mine planning .	206
7.8.1	Grade-tonnage curve: implicit vs geostatistical	206
7.8.2	Geometallurgical orebody models combined	207
7.8.3	Resource estimation: implicit vs geostatistical	209
7.9	Summary and conclusion.....	211
Chapter 8	Conclusions and recommendations.....	213
8.1	Introduction	213
8.2	Summary of the thesis	213
8.3	Overall conclusion	215
8.4	Recommendations for further research.....	216
REFERENCES	218
APPENDICES	236

List of appendices

Appendix A: Python® code for collar synthetic data generation	236
Appendix B: Economic composite of drillhole datasets	237
Appendix C: Drillhole datasets combination.....	245
Appendix D: Geological modelling created through implicit modelling ...	246
Appendix E: Ethical clearance certificate	247

List of figures

Figure 2.1: Example of a generative adversarial network architecture (Little et al., 2021).....	12
Figure 2.2: Structure of the synthetic orebody model (Lishchuk, 2018) ...	17
Figure 2.3: Global methodology and tools for each stage (Garrido et al., 2020).....	18
Figure 2.4: Example of a block model (Poniewierski, 2019).	21
Figure 2.5: Grade estimation with exploratory boreholes Kriging method (view to the North) (Mousavi, 2022)	23
Figure 2.6: Process of creating an explicit orebody model (Abdollahi Sharif et al., 2020).....	28
Figure 2.7: Implicit modelling of orebody from drillholes (Zhong and Wang, 2020).....	30
Figure 2.8: RBF interpolation of scatter points (Hines, 2022)	34
Figure 2.9: Structural constraint types used for the implicit surface modelling in sparse data environments (Hillier et al., 2014).....	38
Figure 2.10: Inequality constraints in synthetic fold structure with cross-section comparison. A) Synthetic fold structure with data constraints, B) modelled surface using only on-contact and gradient constraints, C) using all constraints and D) cross section comparison (Hillier et al., 2017).	46
Figure 2.11: Comparison of the boundaries for categories 2, 3 and 4 modelled	49
Figure 2.12: Flow chart of the new algorithm (Guo et al., 2022)	56
Figure 2.13: Principle of the potential-field interpolation method in 2D: (a) A geological formation mapped by the position of its interfaces; (b) The geological formation modelled by the potential-field method (Calcagno et al., 2008).....	59
Figure 2.14: Simple two-dimensional example illustrating Signed-distance function modelling workflow (adapted from Silva, 2015; Rolo et al., 2017)	66
Figure 3.1: Libraries used in Python® for data pre-processing	83

Figure 3.2: Code used in Python® to convert categorical data to numerical data.....	85
Figure 3.3: Example of constraints set for original assay data	89
Figure 3.4: Code used for model training and data fitting for synthetic data generation.....	89
Figure 3.5: Code used o generating synthetic data.....	92
Figure 3.6: Code used to call up <code>table_evaluator</code> function.....	92
Figure 3.7: Importing drillhole data into Leapfrog® Geo	95
Figure 3.8: Original drillhole data with displayed in Leapfrog® Geo with their collar ID.....	95
Figure 3.9: Validating drillhole data in Leapfrog® Geo. Errors in the drillhole dataset are highlighted in the red circle	97
Figure 3.10: Settings used for the numerical composite of drillhole datasets in Leapfrog® Geo.....	98
Figure 3.11: Settings used for the economic composition of the drillhole dataset in Leapfrog® Geo.....	99
Figure 3.12: Settings for used for indicator RBF in Leapfrog® Geo	101
Figure 3.13: Settings used for variogram model for RQD data in Leapfrog® Geo	102
Figure 3.14: Variogram model of RQD data.....	103
Figure 3.15: Settings used for implicit model geometallurgical data for RQD data.....	104
Figure 3.16: Setting used for kriging interpolation of geometallurgical dataset.....	106
Figure 3.17: Settings used in Leapfrog® Geo for block modelling geometallurgical data.....	107
Figure 3.18: Evaluations selections for block modelling geometallurgical data in Leapfrog® Geo.....	107
Figure 4.1: The similarity score of synthetic collar data compared among CTGAN, CopulaGAN and Gaussian Copula.....	110
Figure 4.2: The similarity score of synthetic assay data compared among CTGAN, CopulaGAN and Gaussian Copula.....	111

Figure 4.3: The similarity score of synthetic geometallurgical data compared among CTGAN, CopulaGAN and Gaussian Copula	113
Figure 4.4: The similarity score of synthetic survey data compared among CTGAN, CopulaGAN and Gaussian Copula.....	114
Figure 4.5: Mean and standard deviation of real and fake collar data: a) CTGAN; b) CopulaGAN; and c) Gaussian Copula.....	116
Figure 4.6: Mean and standard deviation of real and fake for assay data: a) CTGAN; b) CopulaGAN; and c) GaussianCopula.....	117
Figure 4.7: Mean and standard deviation of real and fake geometallurgical data: a) CTGAN; b) CopulaGAN; and c) Gaussian Copula.....	119
Figure 4.8: Mean and standard deviation of real and fake survey data: a) CTGAN; b) CopulaGAN; and c) Gaussian Copula.....	120
Figure 4.9: Visual comparison of original and fake data for collar data generated by CTGAN	122
Figure 4.10: Visual comparison of original and fake data for collar data generated by CopulaGAN	123
Figure 4.11: Visual comparison of original and fake data for collar data generated by Gaussian Copula.....	124
Figure 4.12: Visual comparison of original and fake data for assay data generated by CTGAN	125
Figure 4.13: Visual comparison of original and fake data for assay data generated by CopulaGAN	126
Figure 4.14: Visual comparison of original and fake data for assay data generated by Gaussian Copula.....	127
Figure 4.15: Visual comparison of original and fake data for geometallurgical data generated by CTGAN	129
Figure 4.16: Visual comparison of original and fake data for geometallurgical data generated by CopulaGAN	130
Figure 4.17: Visual comparison of original and fake data for geometallurgical data generated by Gaussian Copula.....	131
Figure 4.18: Visual comparison of original and fake data for survey data generated by CTGAN	133

Figure 4.19: Visual comparison of original and fake data for survey data generated by CopulaGAN	134
Figure 4.20: Visual comparison of original and fake data for survey data generated by Gaussian Copula.....	135
Figure 4.21: Comparison of principal component analysis between original and fake data for collar data. a) CTGAN; b) CopulaGAN; and c) Gaussian Copula	138
Figure 4.22: Comparison of principal component analysis between original and fake data for assay data. a) CTGAN; b) CopulaGAN; and c) Gaussian Copula	140
Figure 4.23: Comparison of principal component analysis between original and fake data for geometallurgy data. a) CTGAN; b) CopulaGAN; and c) Gaussian Copula	142
Figure 4.24: Comparison of principal components analysis between original and fake data for survey data. a) CTGAN; b) CopulaGAN; and c) Gaussian Copula	144
Figure 4.25: Comparison of column correlations between original and synthetic collar data generated through CTGA, CopulaGAN and GaussianCopula	146
Figure 4.26: Comparison of column correlations between original and synthetic assay data generated through CTGA, CopulaGAN and Gaussian Copula	147
Figure 4.27: Comparison of column correlations between original and synthetic assay data generated through CTGA, CopulaGAN and Gaussian Copula	148
Figure 4.28: Comparison of column correlations between original and synthetic assay data generated through CTGA, CopulaGAN and Gaussian Copula	149
Figure 5.1: The economic model of original drillhole assay data	152
Figure 5.2: A 3D orebody model. Red is the ore and blue is the waste .	153
Figure 5.3: Cross-sectional view of the orebody model	153

Figure 5.4: Visual comparison of the 3D orebody model with the drillhole data. a) Cross sectional view of orebody, b) Full view of the orebody	156
Figure 5.5: Iso-surface of Bond work index generated in Leapfrog® Geo	158
Figure 5.6: Iso-surface of rod mill index generated in Leapfrog® Geo...	159
Figure 5.7: Iso-surface of RQD generated in Leapfrog® Geo	159
Figure 5.8: Iso-surface of drop weight index generated in Leapfrog® Geo	160
Figure 5.9: Iso-surface of Axb index generated in Leapfrog® Geo.	160
Figure 5.10: Iso-surface of abrasion index generated in Leapfrog® Geo.	161
Figure 5.11: A 3D model of the Bond work index generated using an implicit method.....	162
Figure 5.12: A 3D model of the rod mill index generated using an implicit method.....	163
Figure 5.13: A 3D model of RQD generated using an implicit method...	163
Figure 5.14: A 3D model of the drop weight index generated using an implicit method.....	164
Figure 5.15: A 3D model of the Axb index generated using an implicit method.....	164
Figure 5.16: A 3D model of the abrasion index generated using an implicit method.....	165
Figure 5.17: BWI-based block model generated using Leapfrog® Geo.	166
Figure 5.18: Block model of the rod mill index generated using Leapfrog® Geo	167
Figure 5.19: RQD-based block model generated using Leapfrog® Geo	168
Figure 5.20: DWI-based block model generated using Leapfrog® Geo.	169
Figure 5.21: Block model of Axb index generated using Leapfrog® Geo	170
Figure 5.22: Block model of abrasion index generated using Leapfrog® Geo	171

Figure 6.1: BWI-based block model generated through the geostatistical method.....	176
Figure 6.2: Block model of the rod mill index generated through the geostatistical method	177
Figure 6.3: RQD-based block model generated through the geostatistical method.....	178
Figure 6.5: Block model of the Axb index generated through the geostatistical method	180
Figure 6.6: Block model of the abrasion index generated through the geostatistical method	181
Figure 7.1: Comparison of swath plots between implicit and geostatistical methods for the BWI-based block models	185
Figure 7.2: Visual comparison between a) implicit method and b) geostatistical method for the BWI-based block models.....	186
Figure 7.3: Comparison of swath plots between the implicit and geostatistical method for the block models of the rod mill index	189
Figure 7.4: Visual comparison between a) implicit method and b) geostatistical method for the block models of the rod mill index	190
Figure 7.5: Comparison of swath plots between implicit and geostatistical methods for the RQD-based block models	193
Figure 7.6: Visual comparison between a) implicit method and b) geostatistical method for the RQD-based block models	194
Figure 7.7: Comparison of swath plots between implicit and geostatistical methods for the DWI-based block model	197
Figure 7.8: Visual comparison between a) implicit method and b) geostatistical method for the DWI-based block models	198
Figure 7.9: Comparison of swath plots between implicit and geostatistical methods for the block models of the Axb index.....	201
Figure 7.10: Visual comparison between a) implicit method and b) geostatistical method for the block models of the Axb index.....	202
Figure 7.11: Comparison of swath plots between implicit and geostatistical methods for the block models of the abrasion index	204

Figure 7.12: Visual comparison between a) implicit method and b) geostatistical method for the block model of the abrasion index.....	205
Figure 7.13: Comparison of grade tonnage curves generated using implicit and traditional methods.....	207
Figure 7.14: Combined geometallurgical block model generated using Implicit method.....	208

List of tables

Table 2.1. Explicit orebody modelling method compared with implicit orebody modelling (Birch, 2014)	31
Table 3.1. Representative of the original collar data	77
Table 3.2. Representative of the original assay data	78
Table 3.3. Representative of historical geometallurgical data for cobalt ..	80
Table 3.4. Representative of the original survey data	81
Table 3.5. Summary of statistics of the original collar data.	84
Table 5.1. Statistical comparison of the 3D orebody model with the economic drillhole model	155
Table 5.2. BWI data generated from the implicit block model	166
Table 5.3. Rod mill index data generated from the implicit block model	167
Table 5.4. RQD index data generated from the implicit block model	168
Table 5.5. DWI data generated from the implicit block model	169
Table 5.6. Axb index data generated from the implicit block model	170
Table 5.7. Abrasion index data generated from the implicit block model	171
Table 6.1. BWI data generated from the geostatistical block model	176
Table 6.2. Rod mill index data generated from the geostatistical block model	177
Table 6.3. RQD data generated from the geostatistical block model	178
Table 6.4. DWI data generated from the geostatistical block model	179
Table 6.5. Axb index data generated from the geostatistical block model	180
Table 6.6. Abrasion index data generated from the geostatistical block model	181
Table 7.1. Statistical comparison between implicit and geostatistical methods for the BWI-based block models	185
Table 7.2. Statistical comparison between implicit and geostatistical methods for the rod mill index block models	188
Table 7.3. Statistical comparison between implicit and geostatistical methods for the RQD-based block models	192

Table 7.4. Statistical comparison between implicit and geostatistical methods for the DWI-based block models	196
Table 7.5. Statistical comparison between the implicit and geostatistical method for the block models of the Axb index	200
Table 7.6. Statistical comparison between the implicit and geostatistical methods for the block models of the abrasion index	204
Table 7.7. Grade classes of drillhole data	208
Table 7.8. Resource estimation using implicit method	210
Table 7.9. Resource estimation using the geostatistical method	210

Acronyms and symbols

%	Percentage
$T^*(p_0)$	The estimated value of the property T at a reference location P_0 .
$T^*(p)$	The estimated value of the property T at location p .
a_j, e_t	Scalar coefficients
b_k	Vector coefficients with three components
$p_k(x)$	Basis functions for a polynomial of degree
p'_α	Corresponding location in a training image.
x_j	Parameter that specifies the location
β_j	Coefficients for a polynomial of degree
μ_α	Weight assigned to the difference between the property values at the location P_α and P'_α .
$\langle \cdot, \cdot \rangle$	Inner product operation of two vectors
∇'	Differential operator
\circ	Degree
2D	Two-dimension
3D	Three-dimension
Ai	Abrasion index
BWI	Bond work index
CDF	Cumulative distribution function
CNN	Convolutional neural network
CopulaGAN	Copula generative adversarial networks

CPU	Central processing unit
CSV	Comma-separated values
CTGAN	Conditional tabular generative adversarial networks
CV	Coefficient of variation
DD	Decimal degree
DEM	Digital elevation models
Depth_max	Maximum depth
DWT	Drop weight test
FastRBF	Fast radial basis function
g/cm ³	Gram per cubic centimetre
g/t	Gram per ton
GAN	Generative adversarial networks
GB	Gigabyte
GMBM	Geometallurgical block model
GPU	Graphics processing unit
GRBF	Generalised radial basis function.
HLW	High-level radioactive waste
Hole_ID	Hole identification
HRBF`	Hermite radial basis function
HTML	Hypertext markup language
km ²	Square kilometre
kWh/t	Kilowatt-hour per tonne
m	Metre

m ³	Cubic metre
MPS	Multiple-point geostatistics
OK	Ordinary Kriging
os	Operating system
PCA	Principal component analysis
RBF	Radial basis function
RQD	Rock quality index
SDF	Signed-distance function.
SDV	Synthetic data vault
SIS	Sequential indicator simulation method
SK	Simple Kriging
SKUA	Subsurface knowledge unified approach
Std	Standard deviation
t	Tonnes
TB	Terabyte
TC _o	Total cobalt
TGAN	Tabular generative adversarial network
TVAE	Triplet-based variable auto encoders
UVT	Uniform Value Table
WGAN	Wasserstein generative adversarial network
X	Longitude
Y	Latitude
Z	Elevation

ε	Fitting accuracy
M	The number of domain constraints
$\Phi(x, x_j)$	Radial basis function
$\Phi(x, x_{\mu+k})$	Radial basis function evaluated at the
Q	Number of data points
$f(x)$	Implicit potential field function $k - th$
$p(x)$	Low-degree polynomial.
$p = (x, y, z)$	Point in 2D/3D space.
$s(x)$	Implicit radial basis field function
σ	Number of gradient constraints
τ and $t_{\mu+\sigma+l}$	Number of tangent constraints

Chapter 1 Introduction

1.1 Background of the research

Geometallurgy is a field of study that combines geology, engineering, economics, and environmental factors to maximize the benefits of mining while minimizing negative impacts (Bye, 2011; Ehrig, 2013; Dominy et al., 2018). It is useful for improving mine planning and plant performance by gathering information on variations in metallurgical and mining characteristics (Garrido et al., 2018 & 2020). The incorporation of key metallurgical factors in orebody models helps to address processing difficulties and optimize mineral resources, leading to enhanced profitability (Philander and Rozendaal, 2013; Coward and Dowd, 2015; Ortiz et al., 2015; Garrido et al., 2018; Lishchuk, 2018).

Orebody models are computerized representations of geological data below the surface of the earth (Fallara et al., 2006; Birch, 2019). They provide valuable information for exploration and mining and are important for mine planning and other downstream mine practices (Cowan et al., 2003). Two types of methods are used to generate orebody models: explicit or traditional wireframe and implicit modelling (Jessell et al., 2014; Vollgger et al., 2015; Guo et al., 2018). Explicit models are created by manually drawing orebody outlines as individual cross-sections. In contrast, implicit models use mathematically derived surfaces in 3D space. Both methods have advantages and limitations.

While orebody models have traditionally been based on geological grade factors, incorporating processing-related factors can also be important in determining the cost of mining and mineral projects. Recent studies have demonstrated the potential of implicit modelling in mine planning. For example, Hillier et al. (2014) used implicit modelling to create 3D geological models by integrating scattered multivariate data. Additionally, Stoch et al. (2018) used an implicit modelling method to create a detailed 3D model of

the entire mining volume of the Sishen mine. The method allowed for the development of continuous geological surfaces.

Although the results of implicit modelling in mine planning are promising, more research is needed to fully explore their potential. Challenges still exist in selecting suitable interpolation functions and integrating complex data types such as geometallurgical data. This is because they are often under-sampled in comparison to standard geological grade variables. This presents a challenge in incorporating them into resource models using traditional approaches (Hunt et al., 2013). Overall, the use of implicit modelling methods and geometallurgical models has become increasingly important in mine planning. This is because they seek to maximize the economic value of mineral deposits. This thesis aims to contribute to the growing body of literature on geometallurgy and mine planning. It does so by exploring the use of implicit modelling as a tool for modelling and predicting geometallurgical data.

Generative Adversarial Networks (GANs) are a powerful tool for synthetic data generation (Salehi et al., 2020). GANs consist of a generator and a discriminator network that compete in a game-theoretic manner (Goodfellow et al., 2020). The generator aims to produce realistic synthetic data, while the discriminator distinguishes between real and generated data. Through iterative training, GANs learn to generate synthetic data that closely resembles real data. GANs have applications in data augmentation, privacy preservation, and addressing data scarcity (Hernandez et al., 2022). They open new avenues for creating high-quality synthetic data. They enhance training, testing, and exploration in machine learning application. Their adversarial training paradigm offers unprecedented potential for creating realistic synthetic data (Ganguly, 2017).

To address this challenge, synthetic geometallurgical parameters were generated using a Generative Adversarial Networks-based model. The geometallurgical parameters were subsequently modelled using an implicit method and compared with geostatistical methods. The results from both

methods were then utilized to calculate mine planning parameters such as tonnage and volume of materials. Additionally, they were used to produce an orebody model that incorporates geometallurgical parameters.

1.2 Problem statement

Although geometallurgical variables are critical in the evaluation of the final cost of mining and mineral projects, orebody models have traditionally been based on geological grade variables. While some researchers (e.g., Dunham and Vann, 2007; Wambeke and Benndorf, 2014; Deutsch, 2015; Deutsch et al., 2016; Musafir and Thompson, 2017; Lishchuk, 2018; Navarra et al., 2018; Vieira and Costa, 2018; Abildin et al., 2019; Addo Junior, 2019) have all incorporated geometallurgical parameters into their orebody models, the potential of using implicit modelling methods to model geometallurgical parameters have still not been explored.

Furthermore, researchers such as Garrido et al. (2018 & 2020) and Lishchuk (2018) have highlighted how access to real geometallurgical data is very limited in practice. This is due to confidentiality restrictions and/or budget limitations as undertaking geometallurgical analysis of samples is quite expensive. This has made it difficult for practitioners, researchers, and students to test models, conduct research and reproduce results in the field of geometallurgy (Garrido et al., 2018).

The use of synthetic data has become increasingly popular in geometallurgical practices. However, there are only a few research studies available in the literature that focus on the generation of synthetic geometallurgical data (Garrido et al., 2018, 2020; Lishchuk, 2018). Furthermore, there is a lack of research that specifically investigates the use of Generative Adversarial Networks (GAN) models for generating synthetic data for geometallurgy. As a result, there is a knowledge gap regarding the application of implicit modelling methods for modelling geometallurgical data and the use of GAN models for generating synthetic geometallurgical

data. Therefore, this thesis aims to fill this knowledge gap by exploring the application of implicit modelling methods for modelling geometallurgical data. Additionally, it aims to use GAN models to generate synthetic geometallurgical data.

1.3 Aim and objectives of the research

Implicit modelling methods offer numerous advantages over explicit modelling methods, including faster computation, automation, and the ability to update geological models with new data. Consequently, there is a growing interest in utilizing implicit algorithms to model geometallurgical data. Traditionally, orebody models focused primarily on geological grade variables, but the significance of geometallurgical parameters has been increasingly recognized in recent years in mine planning. These parameters have a substantial impact on the cost and value of extracted minerals, making them crucial for effective mine planning (Bye, 2011; Dominy et al., 2018; Lishchuk, 2018; Dehaine et al., 2021). However, the potential of employing implicit modelling methods to incorporate geometallurgical data into orebody models remains largely unexplored. Therefore, there is a pressing need for research and investigation into the capabilities of implicit modelling in integrating geometallurgical data effectively.

The objective of this doctoral study is to utilize Generative Adversarial Network (GAN) models to generate synthetic geometallurgical data. Additionally, the study aims to explore the potential of implicit modelling methods in the context of modelling geometallurgical parameters for mine planning. The ultimate goal is to improve the accuracy and efficiency of mine planning by incorporating geometallurgical parameters. The specific research objectives were set as follows.

- To generate synthetic geometallurgical data using GAN-based models for geometallurgical modelling.

- To model the geometallurgical data using an implicit method and compare the results with traditional geostatistical methods.
- To develop an orebody model that incorporates geometallurgical data using the results of the implicit modelling approach and evaluate its application in mine planning.

Based on the information presented above, the primary research question for this thesis is whether a modelled orebody generated using implicit modelling can be as complex and useful for mine planning as models generated using geostatistical modelling. To answer this question, geometallurgical parameters were modelled using both implicit and geostatistical methods, and the results were compared. A geometallurgical block model was generated from the results and used to calculate parameters for mine planning. This study further provides insights into the use of implicit modelling for geometallurgical modelling and to evaluate its potential for generating useful and complex orebody models.

1.4 Scope and limitations of the research

The scope of this thesis is to model geometallurgical parameters using the implicit method, specifically the radial basis function (RBF) method. The study focuses on seven parameters, namely ore grade, Bond work index (BWI), rod mill index, rock quality designation (RQD), drop weight index (DWI), Axb and abrasion index (Ai). These parameters are important in mine planning and are mostly available in literature. The study relies exclusively on historical geometallurgical data and data published in previous research work or shared by other researchers (Mboyo, 2018; Dehaine et al., 2021; Mambwe et al., 2022). This is due to the cost and time required for undertaking a real geometallurgical program.

However, the limitations of the thesis include the narrow focus on a limited set of geometallurgical parameters, which may not represent the entirety of variables relevant to mine planning. Moreover, the study exclusively relies

on the RBF method due to software constraints (Cowan et al., 2011; Birch, 2014; de la Varga et al., 2019; Grose et al., 2021). This may limit the generalizability of the findings to other implicit modelling methods. Finally, the use of synthetic data to validate the model may have limitations in accurately capturing the variability and complexity of real-world data.

1.5 Contribution to the body of knowledge

The contribution of the body of knowledge in this thesis is significant in several ways. Firstly, it fills the gap in knowledge regarding the use of implicit modelling methods for geometallurgical modelling. This is important because, as noted earlier, the potential of using implicit modelling methods to model geometallurgical parameters has not been explored, and this has limited the ability of practitioners, researchers, and students to test models, conduct research, and reproduce results in the field of geometallurgy.

Secondly, the thesis provides a methodology for generating synthetic geometallurgical data using GAN models. This is important because the limited access to real geometallurgical data due to confidentiality restrictions and budget limitations (Garrido et al., 2018) has made it difficult for researchers to test models and conduct research in this field. The use of synthetic data provides a means of overcoming this challenge, and the methodology presented in this thesis can be useful for future research in geometallurgy.

Thirdly, the thesis contributes to the understanding of the level of complexity and usefulness of models generated using implicit modelling methods compared to geostatistical modelling methods for mine planning. This is important because mine planning requires accurate and reliable models that can guide decision-making processes. The results of this study provide insights into the strengths and limitations of both modelling methods, and this can help practitioners to make informed decisions regarding the choice of modelling method for their specific needs.

Overall, the contribution of the body of knowledge in this thesis can improve the understanding and practice of geometallurgy and can help to enhance the accuracy and reliability of models used in mine planning.

1.6 Organization of the thesis

This section outlines the structure of the thesis as well as the material covered in each chapter.

This thesis is organized into eight chapters. Chapter 1 introduces the background and context of the study, presents the objectives and motivation for the study.

In Chapter 2, a thorough literature review was conducted on various synthetic data-generating methods and implicit and geostatistical modelling methods. The review identified a research gap which this study aimed to address. The chapter also presented an in-depth discussion of Generative Adversarial Networks (GAN), geometallurgical block modelling, and implicit orebody modelling. Additionally, the chapter discussed the successful applications of these models in generating synthetic data and orebody modelling.

Chapter 3 explains the methodology adopted for synthetic data generation and geometallurgical modelling using implicit and geostatistical methods. The methodology covered the type of GAN models used, and the steps followed in python to generate the data. The method also includes the steps followed when modelling geometallurgical data using implicit and geostatistical methods.

Chapter 4 presents the results of synthetic data generation, while Chapter 5 presents the results of implicit modelling of geometallurgical parameters.

Chapter 6 provides the results of the geostatistical modelling of geometallurgical data.

Chapter 7 presents a comparison of implicit and geostatistical methods and their application in mine planning.

Finally, Chapter 8 summarizes the main conclusions and provides recommendations for further research.

Chapter 2 Literature review

2.1 Introduction

Implicit modelling techniques have gained significant attention in the mining industry as a powerful tool to create three-dimensional (3D) geological models, particularly when dealing with complex orebodies. In recent years, there has been a growing interest in applying implicit modelling techniques to orebody modelling. This provides a more comprehensive understanding of the ore deposit and facilitates better decision-making in mine planning and mineral processing.

This chapter provides a review of Generative Adversarial Networks (GAN) as a synthetic data generator for geometallurgical data. The review covers the fundamentals of GAN, including its architecture and training process. It also covers different types of GAN methods used in generating tabular data.

Additionally, the basis of the implicit modelling method and its application orebody are reviewed. The literature review covers various aspects of implicit modelling. This includes the definition of implicit modelling, its advantages and disadvantages over other modelling methods, and the different methods used in implicit modelling. The review also explores the applications of implicit modelling in the mining industry, with particular emphasis on orebody modelling. The other modelling methods reviewed in this chapter are the explicit methods and the geostatistical methods. Past work is also reviewed to highlight the successful application of implicit modelling in the mining industry.

This literature review offers a thorough examination of the current advancements in synthetic data generation and implicit modelling. The main emphasis is on the utilization of GAN-based models and implicit methods for the purpose of generating synthetic and modelling geometallurgical data. The insights gained from this review serve as the foundation for the subsequent chapters of the thesis, where the focus shifts towards exploring

the practical application of these methods in the context of modelling geometallurgical data.

2.2 Synthetic data generation

Synthetic data is created using a mathematical model and algorithm that copies the characteristics of real data with the intention to solve data science problems (Assefa et al., 2020; Jordon and Weller, 2022). Wu et al. (2019) and Keylock (2019) show how synthetic data can be used to solve data science issues. Wu et al. (2019) used synthetic data to enhance the accuracy and robustness of fault segmentation by training an end-to-end convolutional neural network (CNN). Keylock (2019), on the other hand, proposed using synthetic data for hypothesis testing in geosciences. This approach addresses the limitations of traditional methods, such as limited data sample size and difficulty in obtaining independent data.

The creation of synthetic data can be achieved through three methods. These are through perturbing real data, combining attributes from real data, and generating data from a defined distribution (Brenninkmeijer, 2019). In recent years, a new method known as Generative Adversarial Network (GAN) was introduced by Goodfellow et al. (2014). GANs are a type of generative deep learning technique that utilizes artificial neural networks. One of the key features of GANs is that the generative component does not have direct access to the original data during training. This allows for the production of synthetic data without the risk of directly interacting with the original data, which could reduce the potential for disclosure (Little et al., 2021).

Since their introduction, GANs have been applied in a variety of fields including medicine (Norgaard et al., 2018; Hernandez et al., 2022), finance (Assefa et al., 2020), and machine learning (Sivakumar et al., 2022). However, the majority of these applications have been limited to the generation of synthetic image data.

Several branches of GANs based models have emerged over the years to generate table-based datasets rather than images. These models for tabular data generation include Conditional Generative Adversarial Networks (CTGAN) (Xu et al., 2019), Tabular Generative Adversarial Networks (TGAN) (Park et al., 2018; Xu and Veeramachaneni, 2018), Gaussian Copula Model (Patki et al., 2016a), and Copula Generative Adversarial Network Model (CopulaGAN) (Patki et al., 2016b). The aforementioned models for generating tabular data are discussed further in the subsequent sections.

2.2.1 Generative adversarial networks

Generative Adversarial Networks (GAN) are a powerful form of neural network that employs an innovative approach to unsupervised learning (Salehi et al., 2020). GANs can generate realistic samples by discovering underlying structures, learning patterns and rules from the real data distribution (Ganguly, 2017). Since their inception as a concept for semi-supervised and supervised learning, GANs have attracted considerable attention. They are now considered as one of the most interesting developments in data generation over the years (Goodfellow et al., 2014; Hernandez et al., 2022).

The framework of a GAN is made up of two parts: a model that creates data and another model that checks if the data is real (original) or fake (synthetic). The second model gets better at telling if the first model is made of real or fake data as it goes along. The two models keep improving until the fake data made by the first model is so good that the second model cannot tell if it is real or fake (Salehi et al., 2020). Figure 2.1 illustrates how GANs generate fake data using two components: a generator and a discriminator.

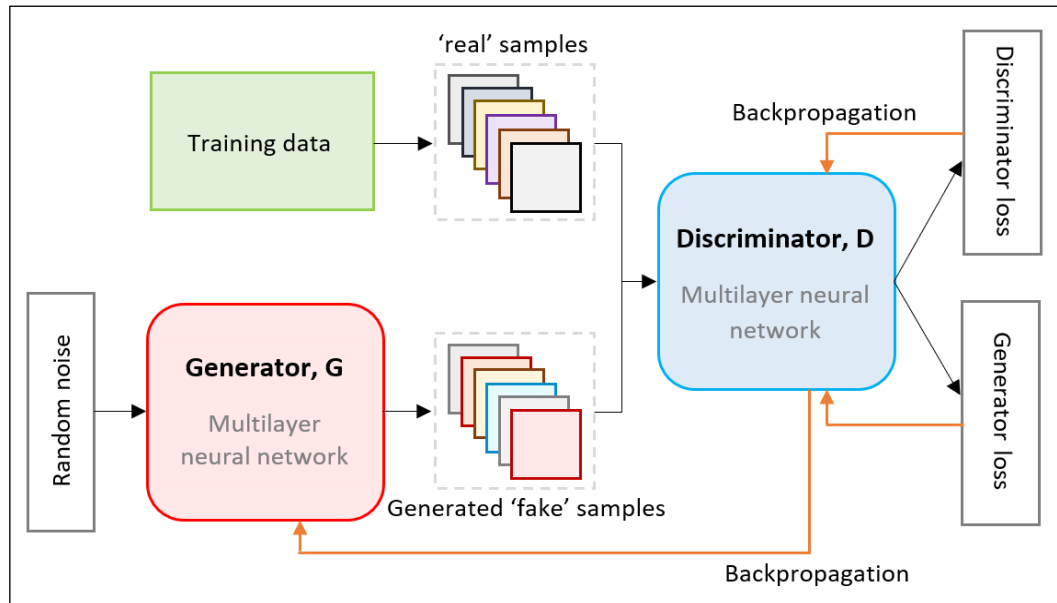


Figure 2.1: Example of a generative adversarial network architecture (Little et al., 2021)

Goodfellow et al. (2014) stated that the discriminative and generative models in GANs are typically implemented as multilayer neural networks. These networks are trained using algorithms such as backpropagation or dropout. The backpropagation and dropout algorithms are used to help the neural network learn from data and make accurate predictions on new data. In GAN frameworks, training is performed alternately with the discriminator being trained while the generator is kept constant and vice-versa. As such, the discriminator can be thought of as a supervised classification model. The discriminator in GANs (see Figure 2.1) takes in batches of labelled real and generated data samples, and produces a single output for each sample, representing the probability that it came from the real data distribution rather than being generated by the generator (Little et al., 2021).

The next three sub-sections discuss the CTGAN, CopulaGAN, and Gaussian Copula models respectively. These three models are all based on the GAN framework.

2.2.2 Conditional tabular generative adversarial network

Zhang et al. (2021) have shown that GAN models are effective in various machine-learning applications, including tabular data generation. The conditional tabular generative adversarial network (CTGAN) is a GAN-based method specifically designed to model tabular data distributions and sample rows from them. The CTGAN method was developed to improve how tabular data is modelled using a type of artificial intelligence called GANs (Xu et al., 2019). In order to make this process more effective, CTGAN includes several important improvements including mode-specific normalization. This process converts continuous values into a bounded vector, which is a more suitable format for neural networks. When a model is being trained, the data used to train it must be diverse and balanced. One way to achieve this is to ensure that all the categories in columns that contain categorical data (such as colours, types of products, etc.) are evenly represented in the training data (Bourou et al., 2021). This means that the model is exposed to an equal amount of each category, which can help it learn to make accurate predictions across all categories.

The CTGAN method uses a type of data representation called a one-hot encoded conditional vector. This enables the model to condition the value of a specific column during the generation process.

In terms of architecture, the CTGAN model also includes a generator as shown in Figure 2.1. This generator is designed to create new data based on random noise and the one-hot encoded conditional vector. The model uses this information to learn and generate synthetic data that matches the desired conditional value.

During the training process, CTGAN uses a loss function called Wasserstein GAN (WGAN) with a gradient penalty to improve the accuracy of the model (Xu et al., 2019). The GAN model includes a critic, which evaluates the generated data by measuring the distance between the learned (generated) distribution and the real distribution (Bourou et al., 2021). This is done to

ensure that the generated data is accurate and representative of the original dataset.

2.2.3 Copula generative adversarial network

Copula Generative Adversarial Network (CopulaGAN) refers to a variation of CTGAN where the cumulative distribution function transformation is applied via GaussianCopula while the network attempts to learn the correlations between columns in a table (Patki et al., 2016a; Cullen et al., 2022).

The CopulaGAN model utilizes a transformation based on the cumulative distribution function, using Gaussian Copula, to learn the data types and format of the training data. Copulas describe the intercorrelation between random variables. During the training procedure, non-numerical and null data are transformed using reversible data transformation (Patki et al., 2016b). This process creates a fully numerical representation from which the model can learn the probability distributions of each table column. This approach allows CopulaGAN to learn the data easily and accurately (Bourou et al., 2021). It should be noted that the CopulaGAN is implemented and included in the synthetic data vault (SDV) open-source library.

2.2.4 Gaussian copula model

The Gaussian Copula model is a statistical model used in synthetic data generation that describes the correlation between variables in a dataset (Patki et al., 2016a). It is particularly useful for modelling complex dependencies between variables, such as those found in financial data or other complex systems.

In the context of synthetic data generation, the Gaussian Copula model is often used as a component of a larger generative model such as CopulaGAN or CTGAN (Meyer et al., 2020; Benali et al., 2021). These

models use the Gaussian Copula to describe the correlation between variables. Once the correlation is modelled, other techniques are used to generate synthetic data that follow the same statistical patterns as the original dataset (Patki et al., 2016a; Bourou et al., 2021).

The basic idea behind the Gaussian Copula model is to transform the marginal distributions of each variable in the dataset into a standard normal distribution (Meyer et al., 2020). After the transformation, a copula function is used to describe the correlation between variables. The copula function takes as input the marginal distributions of each variable and produces a joint probability distribution that describes the correlation between the variables (Patki et al., 2016a).

The Gaussian Copula model has been used in a variety of applications, including risk management, finance, and insurance. Copula-based synthetic data generation is useful for preserving the privacy and confidentiality of the original data. It can also generate synthetic data that closely resembles the statistical patterns of the original dataset (Patki et al., 2016b).

2.2.5 The synthetic data vault

The Synthetic Data Vault (SDV) is an open-source library that was developed by Patki et al. (2016b). It can be accessed at <https://sdv.dev/SDV/index.html> (last accessed on June 11, 2022). The library uses a three-step process. First, the data navigator extracts relevant information from the dataset. Then, the modeller creates generative models of the input, and finally, the sampler generates synthetic rows of data (Hittmeir et al., 2019). The data is provided in comma-separated-value (CSV) files, while its structure and data types are specified in a Javascript-Object-Notation (JSON) file.

This section reviewed the fundamental principle of GAN-based models, which highlights their potential to generate high-quality geometallurgical data. These models can be utilized to generate synthetic geometallurgical

data that can be useful in mining. The subsequent section will discuss some of the methodologies used in generating synthetic geometallurgical data.

2.2.6 Successful use of synthetic data generated for geometallurgical purposes

There seems to be a scarcity of published research on the generation of synthetic data for geometallurgical purposes. The existing research on methodologies for simulating geometallurgical block models appears to be limited, with notable contributions found in the works of Lishchuk (2018) and Garrido et al. (2020). These studies report cases where synthetic data was generated for use in geometallurgical applications.

The first application is the thesis by Lishchuk (2018) in which he proposed a methodology, termed geometallurgical testing framework, for building a synthetic ore deposit model for data integration. This framework was done by using a synthetic deposit, mine production constrained by a mine plan, and a simulated beneficiation process. According to the thesis, the Synthetic Deposit Module utilizes a three-dimensional voxel model and database to describe its features. The primary function of the module is to define the boundaries of the deposit and assign geological, mining, processing, and economic characteristics to each voxel in the model.

As shown in Figure 2.2, the synthetic orebody model is comprised of two modules: the synthetic deposit module and the synthetic sampling module. Each of these modules consists of a spatial component that takes into account the location of every point in a physical space. Additionally, there is a database that stores non-spatial quantitative and qualitative data for each point. The spatial and non-spatial data are linked using a unique identification number allocated to each point in the physical space and a corresponding record in the database. Both the deposit module and the sampling module databases have identical metadata. They also contain the same kind of information including elemental composition, mineralogy,

recoveries, throughput, mining costs, value, and so on. For each block within the synthetic deposit and for each segment of a synthetic drill core.

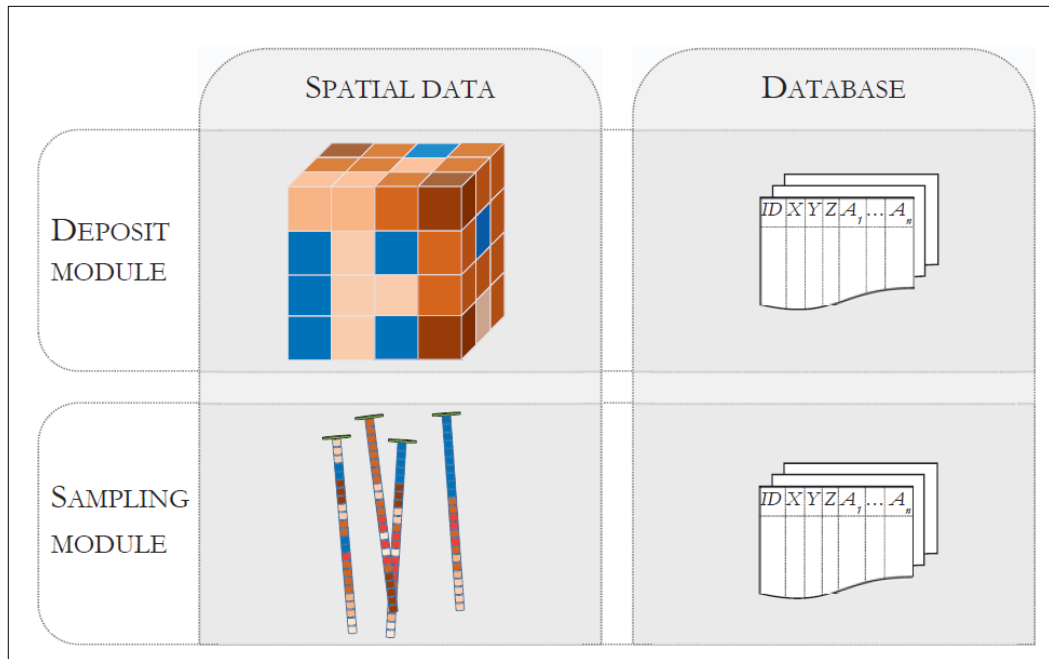


Figure 2.2: Structure of the synthetic orebody model (Lishchuk, 2018)

A mine production plan was created using the synthetic deposit model to generate a simulated process feed. The process feed contained information on modal mineralogy, the chemical composition of minerals, grain size, and specific gravity. This type of information is known to be necessary for a beneficiation process simulation. Using the synthetic system, the benefits of a geometallurgical program developed for actual cases were evaluated. This strategy offers a lot of flexibility compared to production analysis which is only optimized for the head grade. Other advantages include a dependable sampling strategy and confidence in the forecast of feed quality for economic assessment. Most importantly, Lishchuk (2018) found the synthetic deposit model to be a suitable tool for the evaluation of various geometallurgical scenarios.

The second case is a research paper by Garrido et al. (2020) who proposed a geostatistical methodology for simulating synthetic geometallurgical block

models. The steps involved in the approach are listed below while associated tools are summarised in Figure 2.3:

1. Identification of variable types.
2. Generation of a consolidated database.
3. Simulation of geological primary variables:
 - a. Definition of geometallurgical domains.
 - b. Simulation of domains.
 - c. Compositional geostatistical simulation of minerals.
 - d. Geochemical simulation.
4. Simulation of geometallurgical responses
 - a. Simulation of variables for comminution process
 - b. Simulation of variables for flotation process
5. Simulation of spatial drillholes
 - a. Topographic simulation
 - b. Simulation of density of drillholes
 - c. Survey and length simulation

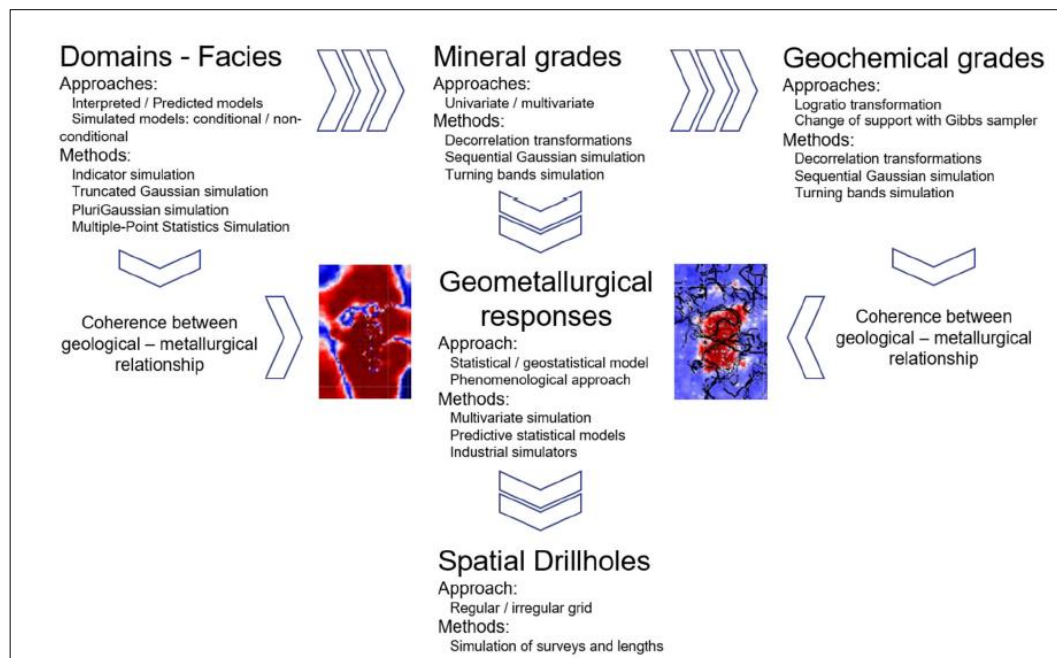


Figure 2.3: Global methodology and tools for each stage (Garrido et al., 2020)

Garrido et al. (2020) showed that the simulated geometallurgical drillholes that were generated through the methodology are realistic. The methodology exhibits consistency with respect to input statistics, geology, and mineralogy. It also generates authentic processing metallurgical performance responses. The generated data can be used to evaluate and compare different geometallurgical modelling methods and mine planning optimization solvers as well as perform risk assessments based on various blending schemes. Moreover, the datasets created are openly available in a public repository. The proposed methodology also provides a clear and understandable way of simulating synthetic geometallurgical data, and any algorithm that follows this methodology is likely to perform well. However, if other algorithms are used that are not aligned with this methodology, their performance may be poor. This is a limitation of any simulation method, as the accuracy and effectiveness of the simulations are closely tied to the underlying assumptions and algorithms used in the model.

As highlighted in this section, it is possible to generate synthetic geometallurgical datasets that are realistic and that can be used to test various mine planning scenarios. This can be done by voxel simulation using mathematical functions (Lishchuk, 2018) and by simulation using geostatistics (Garrido et al., 2020). One drawback of these simulation methods is that their accuracy and effectiveness are tied to the underlying assumptions and the algorithms themselves. This means that if the methodology is not followed correctly, the results may be poor. However, GAN-based models may solve this issue as they learn the structure of the dataset first before producing synthetic data. The generated geometallurgical data can be used to create block models. This is presented in the next section.

2.3 Geometallurgical block modelling

This section provides an overview of the fundamental principles of geometallurgical block modelling, the processes involved in generating a block model, and a summary of their applications in geometallurgical block modelling. A geometallurgical block model is typically a 2- or 3-dimensional block model enriched with geometallurgical parameters (Dunham and Vann, 2007; Deutsch et al., 2016; Garrido et al., 2018; Lishchuk, 2018).

2.3.1 Basic principles of block modelling

A block model represents a mineral deposit and its surroundings in a simplified manner, created using computer-generated "bricks" or cells that reflect small volumes of ore and waste rock (Poniewierski, 2019). It is a subdivision of an ore deposit into smaller blocks of dimensions determined according to required parameters (e.g., lithology, hydrogeology, dominant foliation/bedding orientation, shear strength) (Creus et al., 2019). These cells contain estimates of geological attributes such as elemental grade, density, and mineral composition. The block model is constructed by georeferencing the orebody model. It is then divided into fixed-size blocks using a model framework that describes the rectangular area in which the cells are located (Abzalov, 2006).

The position of each block can be determined by the coordinates of its centroid or the vertex closest to the framework origin. The dimensions of each block may remain constant or vary depending on the structure of the orebody. Figure 2.4 shows a model framework used in block modelling, which includes an origin distance and specific unit lengths and directions for each axis.

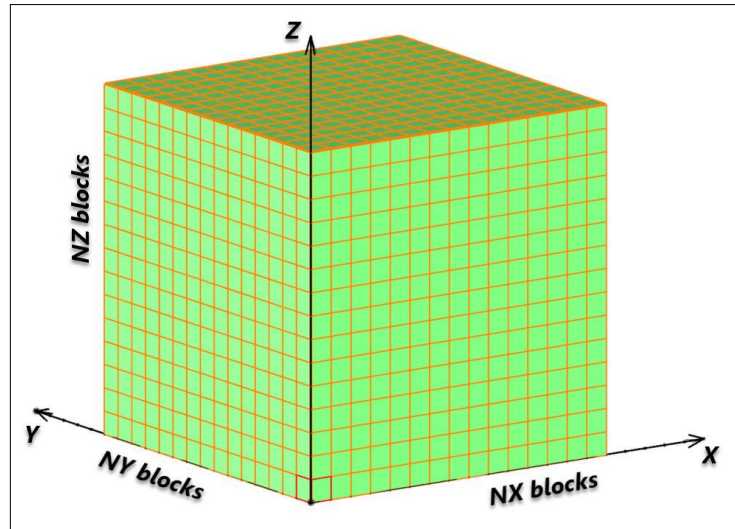


Figure 2.4: Example of a block model (Poniewierski, 2019).

To build the geological block model, the desired properties from drill core samples are transferred or interpolated into the blocks. This process is commonly known as Kriging, where local properties from the drill core samples are propagated throughout the orebody (Dominy et al., 2018; Poniewierski, 2019; Adeli et al., 2021). The basic principle of Kriging is reviewed in the next section.

2.3.2 Basic principle of kriging

Kriging, also known as Gaussian process regression, is a widely used spatial interpolation technique that considers each input as a random variable. The main objective is to minimize the covariance function in order to obtain the best linear unbiased predictor (Matheron, 1981; Cressie, 1990; de la Varga et al., 2019). Kriging generates weights from surrounding measured values to predict values at an unmeasured location. The technique was first introduced by Danie Krige, a South African mining engineer in the 1950s (Myers and Armstrong, 2000; Webster and Oliver, 2008). Since then, Kriging has been applied in various fields including mining, geology, geography, ecology, and environmental science (Zůvala et al., 2016).

Kriging is founded on the notion that the spatial autocorrelation of the data can be represented mathematically by a variogram (Myers and Armstrong, 2000; Chilès and Desassis, 2018). This variogram is used to calculate the spatial covariance between data points separated by varying distances and directions. These estimates are then used by the Kriging method to interpolate the data at unsampled locations and estimate the ambiguity of the interpolated data (Matheron, 1981; Myers, 1992).

Kriging differs from traditional interpolation methods in two ways. First, it predicts the value of a function at any unsampled location. Second, it provides an estimate of the predicted value's uncertainty at that unsampled location (the Kriging variance) (Cressie, 1990). Another appealing feature of Kriging is its ability to generate highly complex functional landscapes from a small number of sample locations (Myers, 1982; Chilès and Desassis, 2018). Kriging is extremely popular as a surrogate model due to this characteristic. The location of the samples determines the quality of a Kriging-based surrogate model, and deciding the sampling locations is an open question. Strategic sampling schemes are techniques that aim to answer this question.

Kriging is expressed as: (Cressie, 1990; Myers, 1992; Chilès and Desassis, 2018; Chung et al., 2019):

$$Z_k^* = \sum_{i=1}^n \lambda_i Z_i \quad (2.1)$$

Where Z_k^* is the estimated value of the variable at the location of interest (k).

λ_i is the weight assigned to the measured value Z_i at location i

$\sum \lambda_i = 1$ (The sum of weights equals 1).

Figure 2.5 provides an example of grade estimation for drillhole data, illustrating Kriging in action. In this example, drill core samples are characterized and recorded in a geological database that includes the spatial locations of each segment based on the collar and in-situ orientation

of the drill core. Equation (2.1) is then utilized to interpolate and estimate the grade of the mineral or ore where drillhole data is not available.

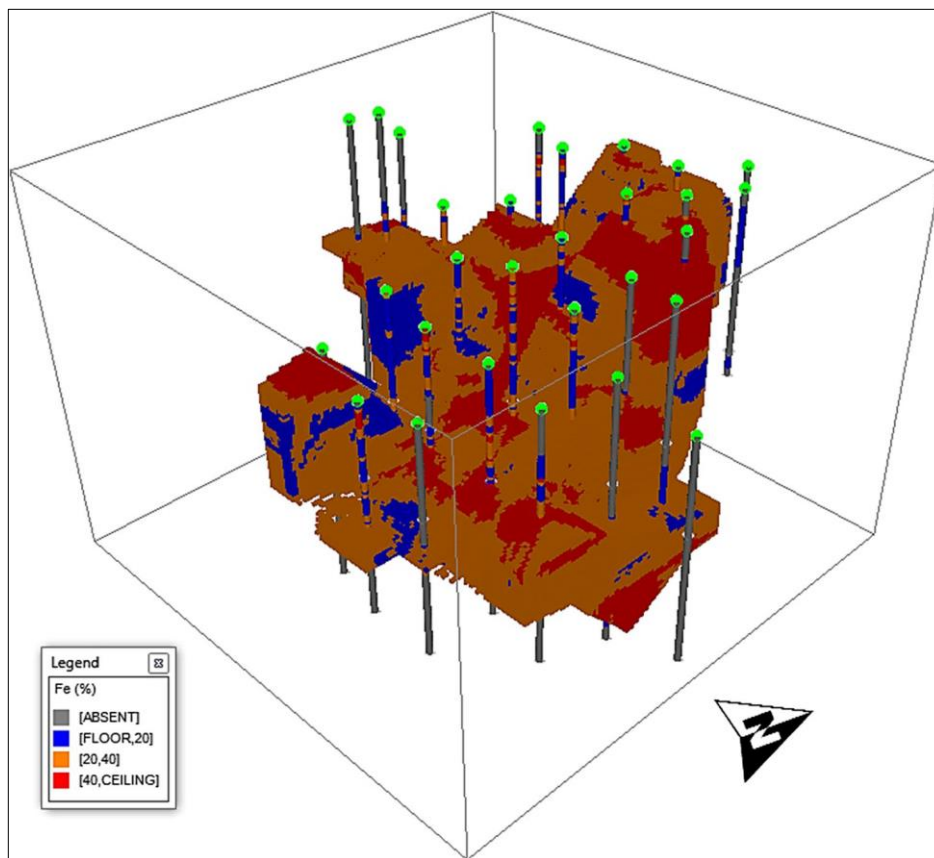


Figure 2.5: Grade estimation with exploratory boreholes Kriging method (view to the North) (Mousavi, 2022)

There are several types of Kriging methods: Ordinary Kriging, Simple Kriging, Universal Kriging, and Indicator Kriging available (Deutsch and Journel, 1998). Each method has its assumptions and limitations, and the choice of method depends on the nature of the data and the objectives of the analysis. The following sections highlight the principles of Simple Kriging (SK) and Ordinary Kriging (OK).

2.3.3 Simple kriging

The Simple Kriging (SK) is a fundamental but limited approach that can be utilized for constructing a geological block model. It is based on the

assumption that the average value m of the stationary random variable is unchanging and already known before the Kriging process (Deutsch and Journel, 1998).

The basic equation used in SK can be expressed as follows (Rojimol, 2013):

$$Z_{SK}^*(x) = m + \sum_{i=1}^n \lambda_i [Z(x_i) - m] \quad (2.2)$$

Where $Z(x_i)$ is the value of a random variable at i^{th} location.

n is the total number of data locations.

λ_i is the Kriging weight for the measured value to be determined.

m is the mean value of the stationary variable.

The SK method is used to estimate the deviations from a known reference value ω . Therefore, it is also known as "Kriging with known mean" in some contexts (Wackernagel, 2003). SK is an exact interpolator that assumes the Kriging weights λ_i are unbiased in the estimation of the residuals. It also uses the average of the entire dataset while the values of the weights do not sum to unity. This is why SK is less accurate than Ordinary Kriging but produces a smoother result (Rojimol, 2013).

2.3.4 Ordinary kriging

The Ordinary Kriging (OK) method is a type of non-stationary algorithm that estimates a constant mean value (Rojimol, 2013). In this technique, a location-dependent estimate of the mean is computed by moving search neighbourhoods. What sets OK apart from other Kriging methods is that it treats the trend component of the variable as an unknown local constant within the area being interpolated as noted by Lundqvist (2022). This distinguishes it from Universal Kriging which permits the mean to vary with location.

Mathematically, OK is defined as follows (Deutsch and Journel, 1998):

$$Z_{OK}^*(x) = \sum_{i=1}^n \lambda_i(x) \cdot [Z(x_i) - m(x)] \quad (2.3)$$

Where $m(x) = E\{Z(x)}$ is the location-dependent expected value of $Z(x)$ and $\lambda_i(x)$ is the estimated Kriging weight.

2.3.5 A note on geometallurgical block models

Traditional geostatistical methods such as SK and OK are mainly used to construct block models in terms of grade (Lotfolah Hamedani et al., 2012). In this case, the block models produced are spatial grade distribution models of mineral deposits also known as grade models. In contrast, geometallurgical block models are expected to display the distribution of key metallurgical and mining parameters including grade throughout the orebody.

These additional attributes are informed by the requirements underpinning the financial analysis and planning of mining projects. Incorporating geometallurgical modelling into 3D block models and mine planning yields a comprehensive approach for quantifying inherent geological variability, thereby enabling a better understanding of its impact on metallurgical performance and mine economics.

This method facilitates the quantification of geological variations and helps in evaluating their effects on the efficiency and profitability of the mine. It also serves as the foundation for several other benefits, such as enhancing energy efficiency, mitigating technical risk, optimizing the economics of mineral production, and maintaining sustainable mine development (Adeli et al., 2021).

Coward and Dowd (2015) explained that geometallurgical modelling is about identifying the variables required to understand critical process responses. And as stated by Dominy et al. (2018), geometallurgical modelling is also about sampling and measuring these variables, developing techniques to estimate and simulate them spatially at the correct scale, and incorporating their respective values into a block model.

From the above, it is evident that samples, drill cores, and block models constitute the three main units in geometallurgical modelling (Lishchuk, 2018). However, the modelling exercise itself is concerned with the variability of process parameters. In a highly heterogeneous orebody, this exercise is usually involving but can be simplified by what is known as domaining. This is the delineation of the continuous areas with homogeneous processing or geological properties (David, 2007; Sanchidrián et al., 2012).

The description of the variability of process parameters within an orebody or a domain is done by classifying the ore samples, drill core samples or blocks in a block model. The classification procedure assigns process properties to the block based on the geological properties of the block. These properties include elemental grade, mineral grade, grain size, lithological type, colour, and specific gravity amongst others.

In the preceding section, the importance of geometallurgical block models in mining was highlighted. Although geostatistical methods are commonly used to build block models, there are other methods available in orebody modelling, including explicit and implicit modelling methods. The next section will explore these methods in more detail.

2.4 Orebody modelling

An orebody model is a comprehensive representation of a mineral deposit, which provides a detailed understanding of its geometry, mineral content, and grade distribution (Roy et al., 2000). It is an essential tool used by mining engineers and geologists to make informed decisions on mine planning, design, and optimization. The model is created using data from various sources, including drilling, geophysics, and geology, and can be updated as new information becomes available.

The accuracy of the orebody model is critical, as it directly affects the overall economic viability of a mining project. The concept of orebody modelling

has been widely studied and discussed in the mining industry, with several peer-reviewed publications highlighting its importance (Lotfolah Hamedani et al., 2012; Powell, 2013; Wang et al., 2016). For example, an orebody model plays a crucial role in the estimation of ore reserves and the optimization of mining operations (Chanderman, 2017; Abuntori et al., 2021).

Two techniques are commonly used in the creation of the orebody model. These are explicit, also known as geometric modelling and implicit modelling (Cowan et al., 2002 & 2003; Birch, 2014; Jessell et al., 2014; Vollgger et al., 2015; Guo et al., 2020). The mining industry's current usage of the terms "implicit" and "explicit" originated from the paper by Cowan et al. (2003). This section provides an in-depth review of two techniques, their respective advantages and disadvantages as well as their applications in orebody modelling.

2.4.1 Explicit orebody modelling

An explicit/traditional orebody model is created by using a type of modelling method called a wireframe. Wireframes refer to Sectional polylines that are tied in three-dimensions and are an ambiguous representation of a solid volume (Cowan et al., 2011). This design is based on information gathered from the geological logging of boreholes (Birch, 2014).

Cowan et al. (2003) considered a wireframe model to be a straightforward method. The shape of the orebody is drawn by hand, piece by piece, based on the information gathered from the drilling holes. This creates a model of the orebody that shows the arrangement of different parts of the orebody (Figure 2.6). The orebody is then divided into sections and the sections are connected by strings to make the wireframe.

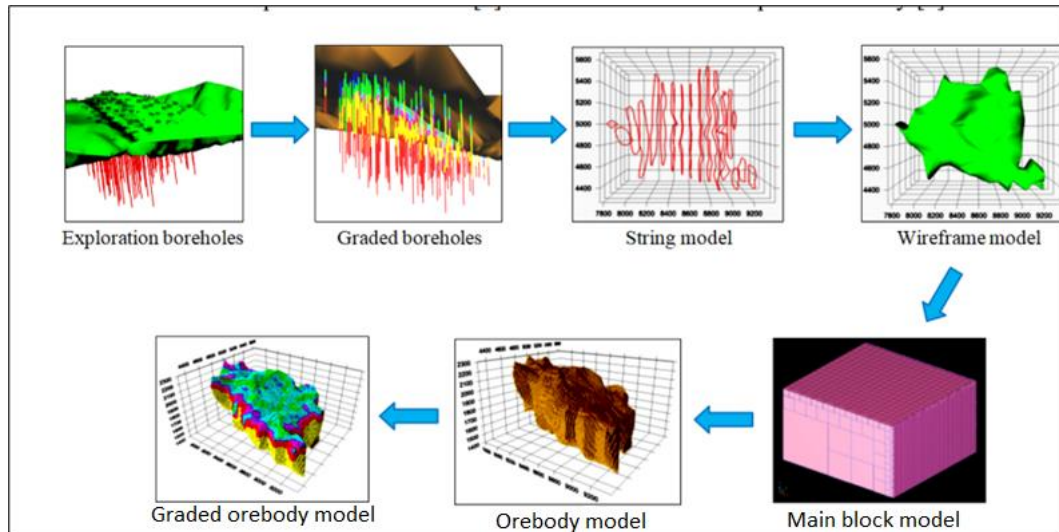


Figure 2.6: Process of creating an explicit orebody model (Abdollahi Sharif et al., 2020)

Despite its appeal, explicit modelling has a lot of drawbacks. Firstly, it is important to carefully check this method for any errors, such as cross-over lines or gaps (Kentwell, 2019). These errors can prevent the model creation software (such as Datamine®) from filling the wireframe with blocks for evaluation (Birch, 2014). The amount of data, the complexity of the geological features, the level of detail desired in the model, and the orientation of the model parts all significantly impact explicit modelling (Stoch et al., 2018). Creating the wireframe by hand and linking the cross-sections requires a lot of simplification of the design (Cowan et al., 2002 & 2003; Jessell et al., 2014), which may not accurately reflect the geological or structural complexities (Vollgger et al., 2015).

The manual digitization process is time-consuming and labour-intensive. Additionally, the final model is unique to each geologist's interpretation, making it nearly impossible to reproduce the same model by different geologists (Cowan et al., 2003). Making changes or adding to the model requires intricate and time-consuming manipulation, which results in models that are not frequently updated. As a result, orebody models cannot easily be modified when new or updated data becomes available. Birch (2014) acknowledged the drawbacks of the traditional modelling technique. To

address these limitations, a new method for orebody modelling was proposed called implicit modelling.

2.4.2 Implicit orebody modelling

The concept of implicit modelling was first introduced in computer graphics literature (Bloomenthal et al., 1997). It refers to the creation of mathematically derived surfaces in three-dimensional space (Caumon et al., 2013). Implicit modelling eliminates the problem of the segment-based method giving biased results. This results in smooth and more accurate cross-sections of any orientation within the modelled orebody, unlike explicit modelling. Implicit orebody modelling is a technique that creates and updates orebody models from borehole data, outcrop data, manually interpreted vertical or horizontal portions, and structural data using a special type of mathematical function (Cowan et al., 2011; Birch, 2014). It is a relatively simple and efficient method. The implicit orebody modelling method does not require the use of arbitrary rules when digitizing and putting together information about rock types. This leads to a more accurate picture of complex rock information (Stoch et al., 2018).

Cowan et al. (2003 & 2011) first investigated a technique called "direct-to-block" geological modelling. This method uses information from drillholes to fill in a block model using mathematical calculations. This approach can be considered a precursor to creating an orebody model without specific rules. Instead, mathematical techniques are used to create the model based on available data.

Implicit modelling creates a 3D orebody model through computer-generated reconstruction of the surface using an implicit function (Figure 2.7) (Zhong et al., 2019). This approach, due to its high degree of automation and ability to quickly update the model, is becoming increasingly popular. It has been researched and applied in various fields such as digital terrain modelling,

geological structure modelling, reservoir modelling, hydrogeological modelling, and orebody modelling (Wang et al., 2018).

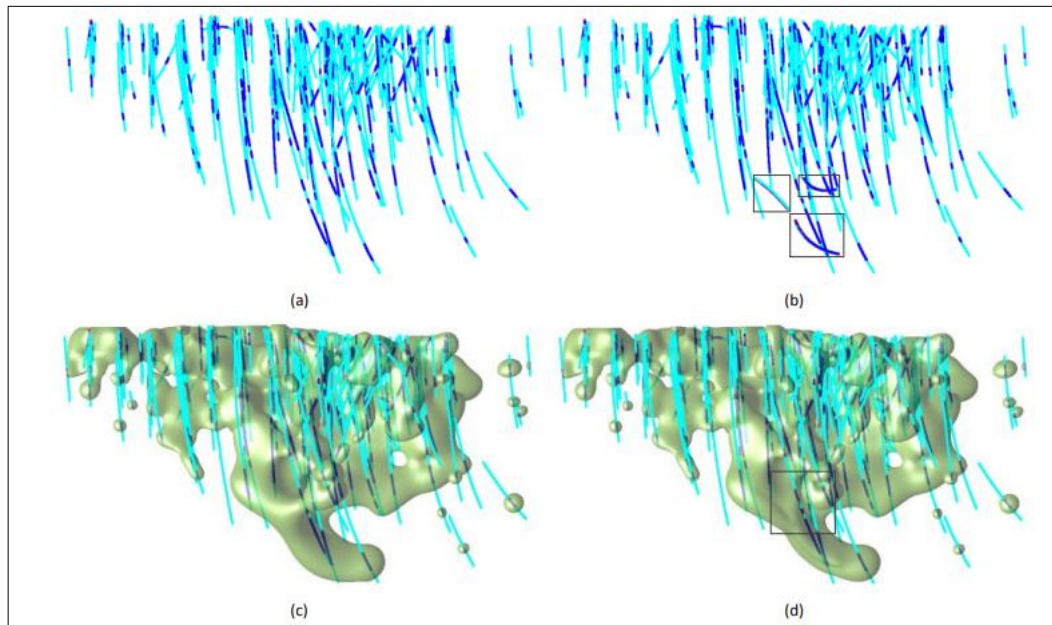


Figure 2.7: Implicit modelling of orebody from drillholes (Zhong and Wang, 2020)

As stated in this section, there are differences between explicit and implicit orebody models. The major difference is that explicit models utilize wireframes (as seen in Section 2.4.1) while implicit models use a mathematical function as highlighted above. Further discussion on the difference between the two methods is presented in the following section.

2.4.3 Implicit over explicit orebody modelling

Table 2.1 provides a comparison between explicit and implicit orebody modelling. According to Birch (2014), there is no evidence supporting the claim that explicit modelling is superior to implicit modelling in generating orebody models. Implicit geological modelling employs interpolation methods that do not rely on cross-sectional information, making it a more favourable choice for creating accurate 3D models such as ore bodies. In contrast, traditional modelling constructs the 3D model based on multiple

interpretations from cross-sectional data, which presents a limitation (Cowan et al., 2011).

Table 2.1. Explicit orebody modelling method compared with implicit orebody modelling (Birch, 2014)

Aspect	Explicit modelling	Implicit modelling
Drillhole contact honouring	Yes (manual)	Yes (automated)
Minimum curvature fit between points	No. Only straight lines. Curvatures are manually digitized	Yes
Modelling speed	Slow	Very fast
True 3D modelling, i.e., drillhole sectional fences are not needed	No. Limited to sectional digitization	Yes. Not limited to a sectional interpretation
Models can be replicated	No. manual digitization cannot be replicated	Yes. Given the same variables
Can multiple models be generated from the same data?	Yes. But not very practical as it is very time-consuming	Yes

Through the review highlighted in Section 2.4, it appears that implicit modelling offers more advantages than explicit modelling. Because of the advantages the implicit modelling method offers over the explicit modelling method, it is given more attention in the next section.

2.5 Implicit modelling methods

Implicit methods for orebody modelling are becoming increasingly popular in mining applications. This section focuses on reviewing three specific implicit modelling methods: the radial basis function-based method, the potential field-based method, and the signed-distance method.

2.5.1 Radial basis function-based method

The Radial Basis Function (RBF) is a mathematical method used to approximate multivariate functions based on sample data (Buhmann and Levesley, 2004; Hillier, 2020). It involves representing a function as a linear combination of radial basis functions centred at different locations in space (Guo et al., 2020). The RBF method is commonly used for the implicit modelling of orebodies due to its ability to accurately capture the non-linear relationship between input data and output data (Zhong et al., 2019). Over the years, several radial basis function methods have been developed for orebody. These include the simple radial basis function, the leapfrog methodology, the Fast Radial Basis Function (FastRBF), the Hermite Radial Basis Function (HRBF), and the Generalised Radial Basis Function (GRBF).

The simple radial basis function involves using a set of radial functions to approximate a given function. The FastRBF method is an optimization of the simple RBF method that reduces the computational time required for processing large amounts of data. It is particularly useful in geospatial modelling where vast amounts of data are commonly used (Guo et al., 2020). The Leapfrog® methodology is a form of the FastRBF method developed by Seequent as a proprietary method for their implicit modelling software called Leapfrog® Geo. The Hermite Radial Basis Function (HRBF) is an extension of the RBF method that includes first-order derivatives in the function approximation.

The Generalised Radial Basis Function (GRBF) is a type of RBF method that allows for the representation of functions with arbitrary smoothness properties. This method is commonly used for the implicit modelling of geological structures such as orebodies, as it can effectively capture the complex relationships between input data and output data (Zhong et al., 2019).

Each of these radial basis function-based methods has its strengths and weaknesses, and the choice of method for implicit modelling of orebodies depends on the specific requirements and characteristics of the orebody being modelled.

2.5.1.1 Simple radial basis function

Radial Basis Functions (RBFs) were initially introduced as a mathematical tool for interpolating scattered data in the field of surveying and mapping by Hardy (1971). They were later utilized for approximating solutions to partial differential equations in various disciplines including fluid mechanics and engineering (Piret et al., 2020). Biancolini (2018) stated that RBFs are a popular way to estimate values for scattered data (Figure 2.8). They can give very accurate estimates at any point, even if there is no data at that exact spot. This is because they use specific data points to make an overall estimate. The RBF interpolant can be expressed mathematically as follows (Jakobsson et al., 2009; Zhong et al., 2019 – 2021):

$$s(x) = \sum_{j=1}^{\mu} a_j \Phi(x, x_j) + p(x) \quad (2.4)$$

where μ is the number of domain constraints; a_j are polynomial coefficients to be determined; $\Phi(x, x_j)$ is a radial basis function and $p(x)$ is a low-degree polynomial.

RBFs have found extensive usage in mathematics, computer science, physics, and geospatial modelling, with a superior fitting effect on scattered data as exemplified in Figure 2.8 (Li et al., 2022). Most geological and mine

planning packages for implicit modelling, such as Leapfrog®, utilize radial basis functions as a basis for interpolation (Cowan et al., 2003; Choudhury, 2017; Hillier, 2020).

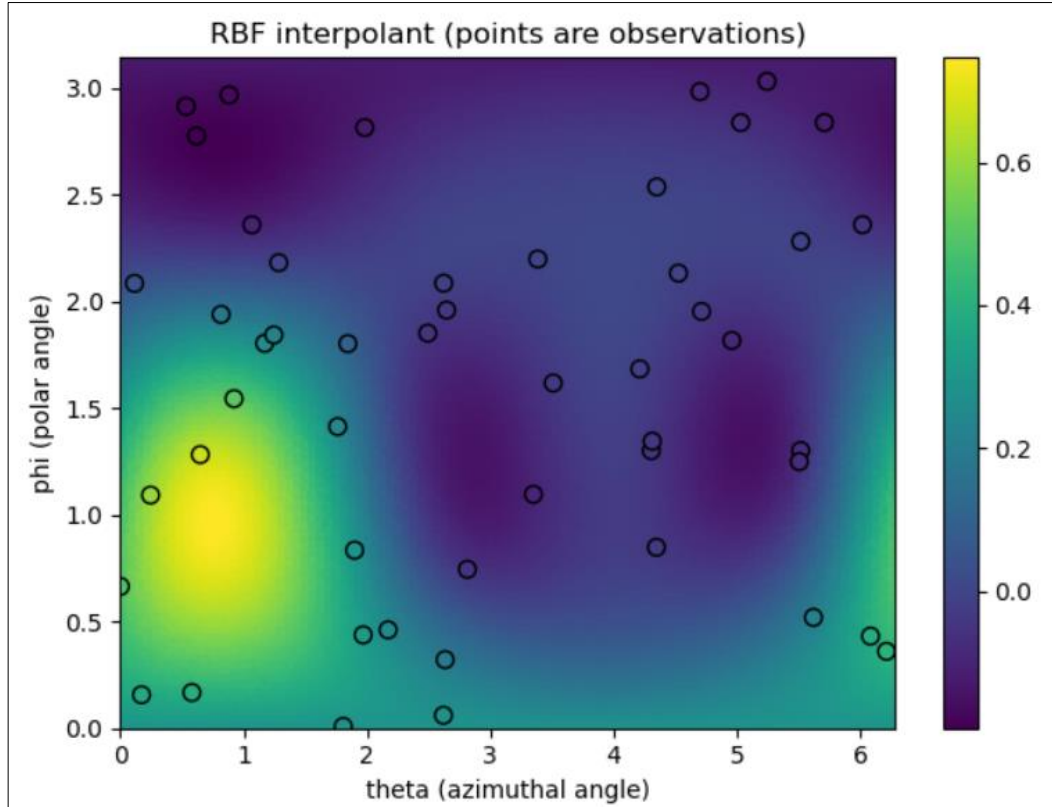


Figure 2.8: RBF interpolation of scatter points (Hines, 2022)

The simple radial basis function (RBF) method has the advantage of flexibility, allowing it to be applied to various applications such as interpolation, surface fitting, and data smoothing (Sharkawy, 2020). In addition, the method is relatively easy to implement and does not require complex programming (Yu et al., 2011).

However, the simple RBF method has some limitations. One of the major disadvantages is its scalability. The method can be computationally expensive for large datasets, which limits its scalability (Biancolini, 2018). Another issue is overfitting, which occurs when the number of radial basis functions is too large, leading to poor generalization performance (Sharkawy, 2020). Therefore, careful consideration of these limitations is necessary when applying the simple RBF method to a practical problem.

2.5.1.2 Fast radial basis function

In the previous section, a basic Radial Basis Function was introduced, but it has limitations when it comes to interpolating data sets with more than 10 000 interpolation constraints (Beatson et al., 2001; Biancolini, 2018; Zhong et al., 2019; Zhong and Wang, 2020). This is due to the resulting high computational costs and processing power. As a result, a new type of Radial Basis Function-based method was introduced.

The FastRBF method is a technique used to solve the equations for radial basis function interpolation (Equation 2.5). This method uses a domain decomposition approach to reduce the computational cost when dealing with large datasets that have over 10 000 interpolation constraints. To further enhance the performance of the FastRBF method, a better radial basis is chosen to replace the natural radial basis within the same subspace of the RBF interpolant. The resulting method is better conditioned and more efficient. The FastRBF interpolant has the following form (Beatson et al., 2001; Zhong et al., 2019; Zhong and Wang, 2020):

$$s(x) = \sum_{j=1}^Q \beta_j p_k(x) + \sum_{j=Q+1}^M a_j \Phi(x, x_j) \quad (2.5)$$

Where β_j and a_j are unknown coefficients and can be also determined by solving the corresponding linear system of interpolation conditions. Q is defined as the number of data points that are used for interpolation. β_j and $p_k(x)$ are the coefficients and basis functions for a polynomial of degree $Q - 1$, respectively. The other variables like $p(x)$ still have the same meaning as Equation (2.4).

One of the advantages of the FastRBF method is its ability to achieve high accuracy in approximating complex orebody models (Zhong and Wang, 2020). The FastRBF method is also computationally efficient and can process large datasets quickly, which can improve productivity and reduce costs. However, the FastRBF method has some limitations, including its sensitivity to kernel parameters, which can be difficult to determine (Biancolini, 2018).

2.5.1.3 Leapfrog® methodology

The Leapfrog® methodology utilizes a similar approach to the FastRBF method, which was discussed in the previous Section 2.5.1.2. Although the exact algorithm and mathematical formula of the Leapfrog method are not publicly available, and it is proprietary. Hence, only the fundamental concept of their method is discussed here.

Cowan et al. (2003) introduced the concept of volume functions in geology, which was based on the work of Savchenko et al. (1995) for modelling objects that interpolate volume functions. A volume function is defined as the distance to an interface that separates two different domains and can be either positive or negative depending on whether the location is inside or outside of the domain (Rolo et al., 2017). The interface of interest is usually the surface corresponding to a particular iso-value of the volume function, which is typically the iso-surface zero (McLennan, 2007). To define the boundary interface, the volume function must be interpolated using an RBF method, which is a fast-scattered interpolator. The RBF method represents the interpolator as a linear combination of basic functions, similar to dual Kriging (Journel, 1989).

Leapfrog® software has one of the earliest commercial implementations of implicit boundary modelling. The methodology for implicit boundary modelling involves five steps: data validation and compositing, interpolation and meshing, incorporation of geological morphology, interpolation of the geological morphology, and morphologically constrained interpolation (Rolo et al., 2017). However, RBF functions cannot incorporate anisotropy into the boundaries because they do not derive covariance functions from the data. As a result, anisotropy must be manually injected in the form of deterministic morphological constraints (McLennan and Deutsch, 2006). Additionally, dealing with multiple domains is not straightforward in this approach (McLennan, 2007).

2.5.1.4 Hermite radial basis function

The Hermite Radial Basis Functions (HRBF) were introduced by Macêdo (2009 & 2011). This technique combines Hermite-Birkhoff interpolation theory with the radial basis function (Wang et al., 2018). Hermite-Birkhoff interpolation theory is a mathematical technique used for approximating a function using a set of sample points first introduced by Georges Birkhoff in 1934 (Allasia et al., 2018; Kashpur, 2021).

Hermite Radial Basis Function (HRBF) is a technique that is used to create a function that can interpolate scattered data points (Wang et al., 2018; Zhong et al., 2019). It does this by building an implicit function which can approximate the position and normal direction of the scattered data points (Macêdo et al., 2009). HRBF makes use of the positions of the scattered data points to create the function, and this helps it to fully utilize the field effect of these positions (Guo et al., 2020). Additionally, the function value of HRBF is dependent only on the distance from the scattered data points' position, unlike other methods.

The HRBF interpolant can take the form below (Liu et al., 2016; Guo et al., 2018; Zhong et al., 2021):

$$s(x) = \sum_{j=1}^{\mu} a_j \Phi(x, x_j) + \sum_{k=1}^{\sigma} \langle b_k, \nabla' \Phi(x, x_{\mu+k}) \rangle + p(x) \quad (2.6)$$

where σ is the number of gradient constraints same as the number of domain constraints μ ; a_j are scalar coefficients; b_k are vector coefficients with three components; ∇' is the differential operator concerning the second variable, $\Phi(x, x_{\mu+k})$, which represents the radial basis function evaluated at the k -th gradient centre, where μ is the number of data points used as centres in the RBF interpolant, and k ranges from 1 to the number of gradient centres σ . and $\langle ., . \rangle$ is an inner product operation of two vectors. The other variables are still the same as Equations (2.4) and (2.5).

The advantages of HRBF are that it can provide a high degree of smoothness in the interpolant, which can be beneficial in applications where

the underlying function is expected to be smooth (Macêdo et al., 2011). The HRBF approach can handle functions with higher-order derivatives, which can be useful in applications where the function has complex behaviour or features (Kashpur, 2021). The limitations of HRBF are that it can be sensitive to the choice of parameters, such as the number and placement of centres and the shape parameter of the radial basis function. The HRBF approach can be prone to overfitting, especially when the number of centres is large, or the function has noise or outliers.

2.5.1.5 Generalised radial basis function.

Hillier et al. (2014) introduced a generalized interpolation framework that uses RBFs to model three-dimensional continuous geological surfaces from scattered multivariate structural data. The multivariate structural data include on-contact, gradient, tangent and inequality (off-contact) constraints (Figure 2.9). This method permits multiple independent geological constraints by deriving linearly independent functions for each constraint. The Generalized Radial Basis Function (GRBF) interpolant is also based on the generalized Hermite-Birkhoff interpolation theory with RBFs, similar to HRBF discussed in Section 2.5.1.4 (Hillier et al., 2017).

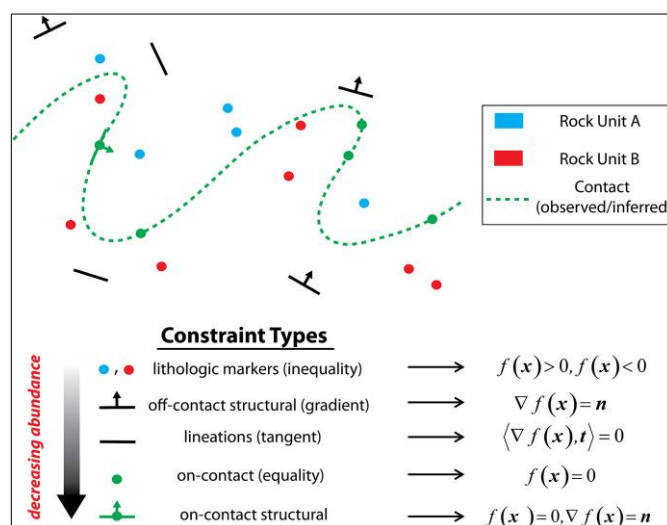


Figure 2.9: Structural constraint types used for the implicit surface modelling in sparse data environments (Hillier et al., 2014).

The GRBF interpolant can be expressed as follows (Hillier et al., 2014 & 2017; Zhong et al., 2019):

$$s(x) = \sum_{j=1}^{\mu} a_j \Phi(x, x_j) + \sum_{k=1}^{\sigma} \langle b_k, \nabla' \Phi(x, x_{\mu+k}) \rangle + \sum_{l=1}^{\tau} e_l \langle t_{\mu+\sigma+l}, \nabla' \Phi(x, x_{\mu+\sigma+l}) \rangle + p(x) \quad (2.7)$$

where τ and $t_{\mu+\sigma+l}$ are the number of tangent constraints which are used to capture second-order derivative information. a_j, e_t are scalar coefficients and b_k are vector coefficients with three components. The other variables are still the same as Equations (2.4), (2.5) and (2.6).

The advantage of the GRBF is that it can provide a high degree of accuracy in the interpolant, which can be beneficial in applications where the underlying function is complex or noisy. Furthermore, it can be flexible in the choice of basis functions, which can allow for better adaptation to the structure of the data. Its limitation is that it can be sensitive to the choice of parameters, such as the number and placement of centres and the shape parameter of the basis functions. It can also be prone to overfitting, especially when the number of centres is large or the function has noise or outliers (Zhong et al., 2019).

The preceding section discussed the fundamental principles of RBF-based methods and their pros and cons. The next section examines the effective implementation of these methods in orebody modelling.

2.5.2 Applications of RBF-based methods in orebody modelling

According to existing knowledge, the first documented work on the use of RBF-based methods for orebody modelling could be attributed to Cowan et al. (2002). In their paper, the authors had proposed and successfully implemented the RBF-based framework in geological modelling. The method had been encapsulated into specialized software for RBF-based data interpolation, which had been integrated into Leapfrog® software.

The method was used to model a variety of exploration and grade control data. Cowan et al. (2002) evaluated the pertinence of the RBF-based method over the explicit method as discussed in Section 2.5.1. The researchers reached a conclusion that the utilization of Radial Basis Functions (RBFs) led to a significant reduction in the time needed for geologic modelling.

Instead of taking weeks or months to generate an orebody model using explicit modelling methods, the model could be generated in just a matter of hours using RBFs. Furthermore, models built using RBFs could be updated and rebuilt as new data became available, while explicit orebody models could not be updated, as referred to in Section 2.4.3.

Cowan et al. (2003) highlighted several case studies on the possibility of applying an RBF-based method to model geological surfaces directly from drillhole databases without digitization. The RBF-based technique was applied to six distinct types of geological constraints. The first case study focused on the near-mine investigation and targeting of the Cosmo Howley gold deposit.

After Harmony Gold acquired the deposit, an internal review was conducted to identify drillhole targets and assess the resource within the existing 155 m deep pit (Cowan et al., 2002). The main data used for this review was a resource and grade control drillhole database. To identify the major trends in mineralization below the pit, 3D solids of grade cut-off mesh were constructed using the data.

Initially, the researchers attempted explicit modelling with manual digitization. However, due to the high nugget effect of the assay data, it was difficult to assess grade continuity, and the manual digitization was deemed inappropriate.

To overcome this issue, the researchers chose to model the grade data using an RBF method, which did not require time-consuming pre-processing steps. The RBF method was employed to interpolate 293,690 composite

grade values and generate seamless grade iso-surfaces. This process took 2 hours and 40 minutes and successfully identified approximately 4 million tons of resources below the present pit. The implicit modelling method not only saved time but also provided valuable insights into the grade trends, making it suitable for presentation purposes.

The second application of the RBF-based technique was the delineation of ore boundaries for resource estimation of the Saratoga gold deposit. The challenge was that the deposit lacked distinct lithological limits governing gold mineralization, which is generally the case in many deposits (Cowan et al., 2003). The team determined the ore-waste boundary of the gold deposit using both explicit and RBF-based implicit techniques.

The explicit technique took more than a month to model a single-grade cut-off and complete the geological validation. The cut-off grade was determined to be 0.25 g/t for the explicit modelling. In contrast, using the RBF-based implicit technique, the team achieved a faster result, taking only 2 days and 1.2 hours to validate the cut-off grade of 0.5 g/t.

The third case study focused on the geological modelling and delineation of the kimberlite pipe at the BHP Billiton Ekati Diamond Mine. The objective was to determine whether the kimberlite pipe model could be efficiently updated when new drillhole data became available. Explicit modelling, as known, is time-consuming as each iteration requires 1 to 2 days of hand digitization and editing. However, with implicit modelling, the entire process was completed in just 10 minutes, significantly faster than the explicit method which would typically take an hour.

In the fourth case study, the team explored contour modelling without tie-lines. The researchers demonstrated how the RBF method could be employed for 3D modelling of mineral deposits, with a particular focus on kimberlite pipes, using the drillhole database without the need for digitization. Unlike the explicit approach, which involves digitizing numerous polylines, the implicit modelling technique directly utilizes these polylines to construct the 3D surface models. This approach eliminates the time-

consuming and potentially challenging task of digitizing tie-lines, which can be particularly burdensome in large operations with hundreds of contours to process.

The process involved converting the polyline data into a suitable format, creating signed off-surface polylines, interpolating the data using RBFs, and evaluating the zero iso-surface wireframe mesh. This method eliminated the need for tie-lines and allowed for the modelling of surfaces that are overturned or bifurcating.

The implicit modelling technique can also be applied to interpolate other three-dimensional attributes and evaluate them on the surface. Additionally, the polyline node density on the implicit surface serves as a confidence map for the interpolation.

The fifth application involved the single-domain geological modelling of a granite-porphyry unit in an anonymous gold deposit located in the Western Australian goldfields. The study used this example to showcase the effectiveness of implicit modelling. The intrusion patterns of the granite-porphyry unit demonstrated a consistent anisotropic trend, which could be easily modelled by assuming continuity patterns.

By using this approach, multiple conditional models could be generated to test various 'what-if' scenarios. This capability allowed for the assessment of mining risks associated with each geological model, providing valuable insights for decision-making and resource management.

The study revealed that the implicit modelling method was remarkably straightforward and efficiently meshed the granite-porphyry data, which included 1 594 drillholes, within just 20 minutes. In comparison, manual digitization would have taken many days to achieve the same result. The ability to generate multiple conditional models with implicit modelling was also highlighted as a significant advantage. Trying to create multiple models using manual digitization would be impractical due to the substantial time and effort required for each iteration.

The results demonstrated that implicit modelling offered a practical and efficient approach to generating multiple conditional geological wireframe models. These models were valuable for testing various scenarios that could potentially impact grade estimations and subsequent mining procedures. Consequently, the use of implicit modelling enabled a more comprehensive assessment of mining risks associated with each geological model.

In conclusion, implicit modelling proved to be a viable solution to the challenges of digitizing geological boundaries from drillhole datasets. Its application facilitated more efficient and accurate orebody modelling, allowing for improved decision-making and resource management in mining operations.

The last case study focused on modelling the Wallaby gold deposit using a user-defined geological morphology. The unconstrained isotropic modelling of grade from composited grade control and resource drilling gold assays in the Wallaby gold deposit was shown to have disjointed high grades, which could be more realistically interpreted as being continuous along convex-up planes.

These planes were saved as a geological morphology data file that could be used to constrain the grade interpolation, resulting in grade boundary meshes that honoured the trends envisaged by the geologist.

The constrained interpolation technique saved time and bypassed the need for time-consuming manual digitizing. Various geological morphologies were defined and then used to generate contrasting conditional models that honoured the data. This approach allowed for the direct construction of multiple grade distribution or lithological models from sparse drillhole data without the necessity for gridding the data.

The user-dependent contouring method not only saved time in producing a geologically realistic model but also allowed multiple geological ideas to be used to generate 'what if?' scenarios for testing. This method enabled

geologists to incorporate their knowledge and expertise into the modelling process, leading to more accurate and reliable geological models. These models were valuable for mining risk assessment, grade estimation, and downstream mining procedures.

Now, let us discuss the construction of orebody models. Birch (2014) investigated if a geologist student might construct accurately a basic model from a borehole dataset using Leapfrog®, the RBF-based implicit modelling software of choice. From his observations, Birch (2014) noted that implicit techniques speed up the geological modelling process and produce reliable results irrespective of the level of competency of the geologist.

As such, Leapfrog® can be regarded as a good tool because it gives one more time to focus on the interpretation of the output model and its quick revision when required. Furthermore, the learning of the RBF-based implicit modelling software is faster than that of the explicit method. The skillset necessary for the creation of successful models is also decreased. In view of the above, Birch (2014) concluded that Leapfrog® as an implicit geological modelling software is superior to traditional methods and is one of the best practice tools for geological modelling.

Hillier et al. (2014) also utilized a GRBF (see Section 2.5.1) method to implicitly model continuous 3D geological surfaces from dispersed multivariate data. The authors implemented their implicit method using a generalized interpolation approach that was then tested in two scenarios. The first scenario involved studying the impact of adding local anisotropy to the modelling process, using a sparse data configuration.

This occurred when gradient constraints were not sufficient to create an accurate geologic surface with isotropic methods. RBF interpolation using an isotropic weighting scheme often resulted in radially symmetrical spherical surfaces, which were not always realistic. To obtain more realistic solutions that followed the fold geometry of the data, the method involved modelling local anisotropy through Eigen analysis of the gradient constraints.

The eigenvectors obtained from the analysis were interpolated and incorporated into the modelling process as tangent constraints. In the second scenario, the researchers employed inequality constraints to represent geological surfaces, as depicted in Figure 2.10A-D. Figure 2.10A depicts a synthetic fold structure with data constraints. Figure 2.10B illustrates the linear solution, which incorporates only on-contact and gradient constraints.

In contrast, the quadratic solution (Figure 2.10C) incorporates stratigraphic inequality constraints and exhibits superior geometric correspondence to the synthetic surface when compared to the solution that includes only on-contact and gradient constraints. Notably, the modelled surface in Figure 2.10C represents parasitic folds, whereas the regionally smooth surface in Figure 2.10D lacks these fold structures.

For a comparison from a down plunge view, Figure 2.10D displays cross sections of the synthetic fold structure (white), the solution using only on-contact and gradient constraints (green), and the solution incorporating all constraints (red).

The model was created using data from 24 on-contact points, 20 gradient planes, and 155 inequality constraints. The model was created using the conditionally positive definite function and a Lagrange polynomial basis. The weights for the model are obtained using a quadratic optimization algorithm. The resulting model shows parasitic folds, which are not present in a similar model created using only on-contact and gradient constraints.

The authors' work was special because it allowed for different kinds of limits to be added to the model using straight lines and inequality constraints, which was not possible in the previous RBF method presented in Section 2.5.1.1.

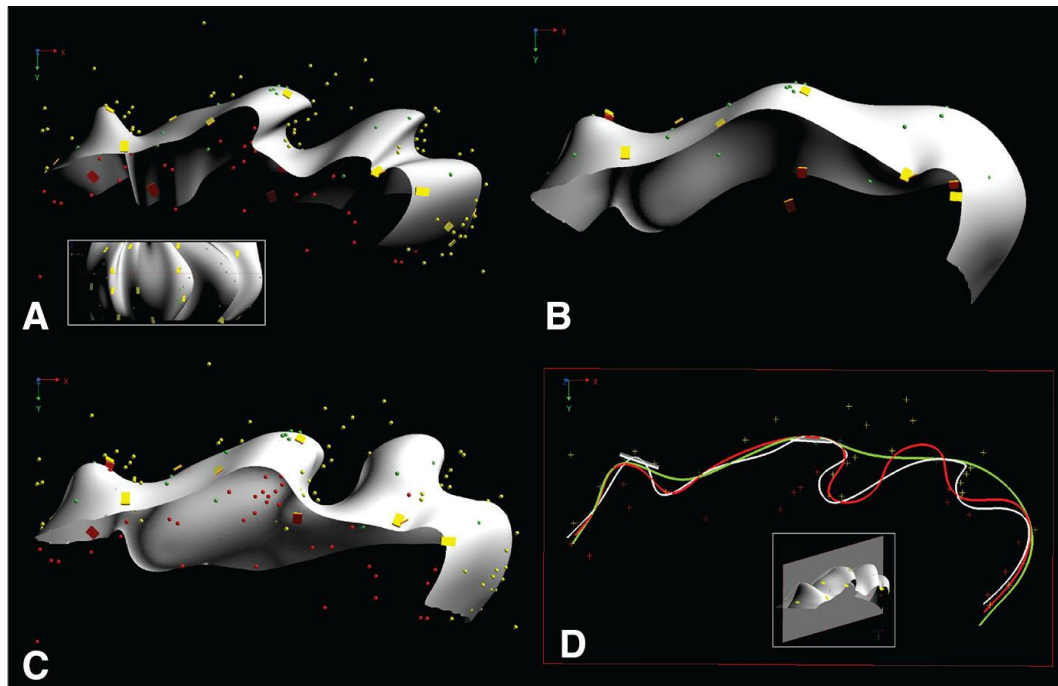


Figure 2.10: Inequality constraints in synthetic fold structure with cross-section comparison. A) Synthetic fold structure with data constraints, B) modelled surface using only on-contact and gradient constraints, C) using all constraints and D) cross section comparison (Hillier et al., 2017).

Vollgger et al. (2015) used the Leapfrog® methodology (see Section 2.5.1) to analyse and evaluate the structural framework of the Navachab gold deposit in Namibia. The objective of the study was to interpret the structural features of the Navachab gold deposit using a 3D geological model. The interpretation was based on drillhole data, as well as structural data obtained from geological maps and field surveys. The authors implemented a 3D implicit modelling workflow, focusing on areas with dense drillhole data.

The researchers successfully generated 3D models of the Navachab gold deposit without the need for manual digitization, distinguishing their approach from traditional explicit modelling methods. In explicit modelling (as discussed in Section 2.4.1), 3D models were constructed based on pre-assumed geological and structural frameworks derived from cross-sections. In contrast, the authors demonstrated that their 3D implicit models

accurately captured the geometries of ore bodies and their relationships with local and regional structural patterns.

The most important factors for economic mineralization were included in their 3D models for the Navachab gold deposit. To further support their structural interpretation, small-scale structures that couldn't be captured by their models were also taken into account. The authors utilized an isotropic spatial interpolation method to minimize modelling bias and enable the 3D implicit models to be used effectively for structural interpretation.

The results suggested that this workflow improved the identification and evaluation of structural controls on mineralization when combined with structural fieldwork. The proposed RBF-based implicit method was found to reduce user-based modelling bias. This was because the implicit method created a closed surface from geochemical, lithological, or structural data without human digitization or connection of sections or level plans. Instead, a mathematically defined spatial interpolation was employed to construct 3D models that revealed trends and patterns in huge drillhole datasets.

In a follow-up work, Hillier et al. (2017) described an interpolation algorithm that was developed to model 3D geological surfaces and its application in modelling regional stratigraphic horizons in the Purcell basin. The algorithm utilized a generalized interpolation framework that employed RBFs to implicitly model 3D continuous geological surfaces from scattered multivariate structural data.

This framework allowed for the inclusion of additional geologic information in the interpolation process, such as stratigraphic data from above and below targeted horizons, modelled anisotropy, and orientation constraints like planar and linear constraints.

The GRBF algorithm was applied in a project under the Targeted Geoscience Initiative (TGI) 4 program to construct a regional 3D structural model of the Purcell Anticlinorium in Southern British Columbia, Canada.

The algorithm was used to model individual fault surfaces separately using interpretative map traces of the fault and limited structural observation data at the surface. Key stratigraphic horizons were also modelled separately within each modelled fault domain using appropriate structural and stratigraphic data from its domain.

The complete set of modelled stratigraphic horizon patches and fault network were used in a Subsurface Knowledge Unified Approach (SKUA) workflow that employed a Uniform Value Table (UVT) transformation to generate a complete 3D structural model topologically consistent throughout the model space (even across faults).

The final model provided insights into the upper and Lower Aldridge Formation contact, which is a key stratigraphic target horizon and host of the Sullivan Zn-Pb-Ag deposit. The authors recommended that future work involves enhancing the algorithm to model multiple surfaces simultaneously and incorporating geological rules such as stratigraphic relationships.

developed an RBF-based method centred on domain decomposition. The proposed methodology was a non-stationary boundary interpolation technique that worked well when there was an abundance of data and local anisotropic properties could be directly inferred from the samples. This was often the case in mining, where there is a wealth of data available for model construction, and accurately representing complex orientations of continuity in 3D using advanced visualization is crucial.

The proposed methodology was demonstrated using a dataset of 8 527 samples from 316 drillholes, which sampled a large Cu-porphyry deposit. The resulting boundaries smoothly honoured the data locations within the partitioning framework while considering global anisotropy.

However, upon inspection of the model, it was found that the variogram model might need refinement, or sub-domaining may be required to separate zones with distinct local anisotropic properties. The highest continuity modelled from the variograms for categories 3 and 4 was found

to be steeply dipping and variably oriented in some areas, which could be exaggerated due to parameterization issues (Figure 2.11).

Similar conclusions were drawn for category 3, where the northwest portion of Figure 2.11 remained relatively isotropic, but anisotropy was inferred in the southeast based on the local geometry implied by the data. In areas where data density was sparser, the interpretation was more varied, relying on the local data and changing anisotropic properties.

The researchers concluded that the proposed methodology was a useful tool for modelling complex geological datasets with locally varying features, provided there was sufficient sample density. It allowed for the automatic inference of local anisotropy from the data, akin to a "bootstrap" workflow. By considering features extracted from previous models, a better model could be constructed. This methodology offered experts a better starting point for modelling geology and had the potential to improve the accuracy of geological models.

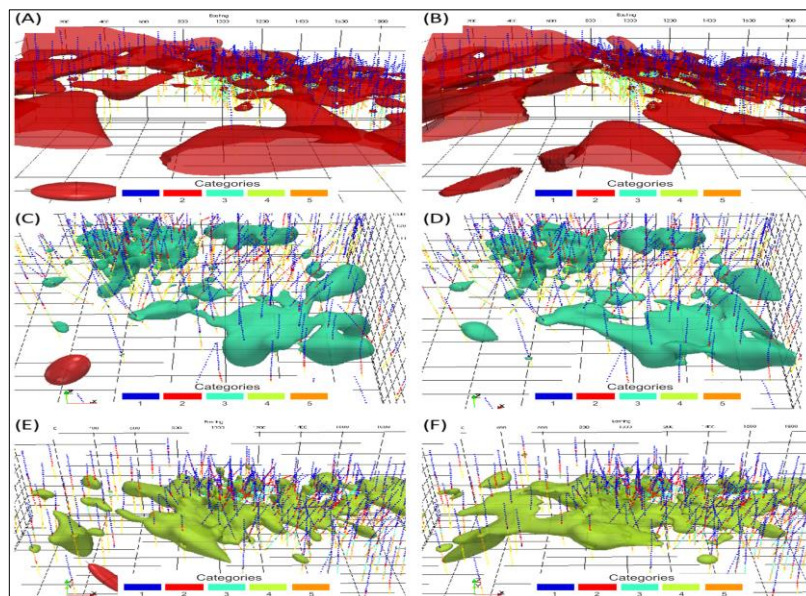


Figure 2.11: Comparison of the boundaries for categories 2, 3 and 4 modelled with A), C), and E) global anisotropy. The red ellipsoid shows the global anisotropy used in each interpolation in A), C) and E). Automatic local anisotropy refinements are shown in B), D) and F) (Martin and Boisvert, 2017)

Basson et al. (2017) also investigated the ore structural connections at the Sishen mine in South Africa using an RBF-based implicit 3D model within the Leapfrog® methodology. The authors presented a detailed analysis of the structural setting of mineralization at Sishen Mine using a newly developed, fully constrained, implicit 3D model of the entire mining volume. This approach provided a comprehensive understanding of the deposit and the surrounding rock mass, which was essential for the optimal extraction of the ore.

The contact points were used to create implicit radial base function surfaces in Leapfrog®. From these surfaces, solids were generated and exported for additional analysis. Their study revealed that the position, depth, and geometry of both laminated and conglomeratic ore were influenced by several overlapping controls at various scales. These controls were mostly structural and could be related to the kinematic history of the volume, major structures, and their intersections.

Stoch et al. (2018) proposed a detailed methodology for creating a fully constrained, 3D implicit model in Leapfrog® covering a vast volume of more than 70 km³ and incorporating more than 60 years of data. This comprehensive model provided a detailed understanding of the entire life-of-mine volume at Sishen, allowing for a reassessment of lithological, unconformity, and structurally related controls on the ore.

The model was built to the original, pre-mining surface, providing a unique opportunity to re-evaluate Sishen in the context of its regional geological setting and current research on large, high-grade iron deposits. The development of a 3D model construction workflow based on observed geological relationships and dense data sets resulted in a fully constrained 3D implicit geological model of ore solids, non-ore solids, and major structures at Sishen Mine.

Spatial analysis of several parameters derived from this model suggested that the majority of iron mineralization at Sishen was not contained in sinkholes or palaeosinkholes.

Guo et al. (2018) presented a modified HRBF interpolation, as discussed in Section 2.5.1, for creating 3D geological models using geological boundaries, attitudes, and sections. The method involved the use of interactive tools that enabled geologists to sketch constraint lines and transform their expert knowledge into models.

The geometric characteristics of section lines were abstracted to coordinates and normal vectors, and these, along with the transformed coordinates and vectors from boundaries and attitudes, were used to co-calculate the implicit geological surface function parameters of the HRBF equations. This process formed constrained geological interfaces from topographic and subsurface data.

The novelty of this method lay in the integration of manual interactive manipulation tools, allowing geologists to add their expert knowledge to the models. Additionally, the approach treated geological sections as auxiliary constraints, contributing to the construction of more reasonable 3D geological models.

The experimental results showed that the constrained models were consistent with expert explanations, and all boundary, attitude, and section data were well represented. The advantages of this method were that it allowed for the creation of more reasonable 3D geological models and provided a flexible and convenient way for geologists to transform and apply their expert knowledge.

Although the method allows for the construction of topologically consistent 3D models, the reasonability and accuracy of non-supervised subsurface modelling may be limited without further modifications generated through analyses performed by geology experts. Overall, the findings demonstrate the feasibility and effectiveness of the modified HRBF interpolation method for creating 3D geological models, and the interactive tools for adding expert knowledge provide a useful addition to the field.

Zhong et al. (2019) described a method for the implicit modelling of complex orebodies using an anisotropic Generalized Radial Basis Function (GRBF) interpolant. This method allowed for the conversion of geological constraints into interpolation constraints and constraint rules, which facilitated the creation of smooth, continuous, and closed geological surfaces.

The RBF-based method proved particularly useful for constraint-based modelling of sparse drillhole data, enabling the modelling of local continuity and extension trends in mineralization areas.

The anisotropic GRBF method was demonstrated to be effective in modelling complex orebodies in sparse data environments. By converting geological constraints into interpolation constraints and constraint rules, the resulting implicit models were smooth, continuous, and closed without any mistakes such as intersections. The method was also suitable for constraint-based modelling of sparse drillhole data and could be used to construct anisotropic orebody models by constraining the geological trends in different directions.

The performance of the method mainly depended on the number of constraints and the resolution size. The running time was primarily influenced by solving large-scale linear systems in the interpolation stage and evaluating sampling grids in the reconstruction stage. The improved algorithm demonstrated faster reconstruction efficiency compared to traditional Marching Cube and parallel Marching Cube extraction methods, especially when dealing with larger solution equations or lower reconstruction resolutions.

Based on their numerical findings, the processing technique could rapidly, accurately, and dynamically recreate the 3D orebody model. The rebuilt modules were guaranteed to be smooth, continuous, and closed geological surfaces, free of errors like junctions.

The main advantage of this method was its ability to model complex orebodies using sparse drillhole data and its suitability for constraint-based

modelling. Anisotropic constraints were utilized to construct geological trends in different directions based on the interpretation requirements of structural geologists. The resulting implicit models were smooth and continuous, allowing for easy representation of orebody models with complex topology and enabling Boolean operations to be performed effectively.

One of the limitations of the method is that it still requires input from a structural geologist to ensure that the reconstructed models are consistent with the actual geological conditions of the drillhole data and the trend of the mineralization domain. This dependency on expert input may introduce subjectivity and potential biases into the modelling process.

Another limitation is that the performance of the method depends on the number of constraints and the size of the resolution. The running time is dominated by the solution of large-scale linear systems in the interpolation stage and the evaluation of sampling grids in the reconstruction stage. This can be computationally demanding, particularly for large datasets or high-resolution models, and may lead to longer processing times.

Overall, the findings of this article suggest that the anisotropic GRBF method is an effective and efficient approach for the implicit modelling of complex geological orebodies, especially when compared to traditional radial basis functions without constraints. However, further research is needed to explore ways to reduce the reliance on input from structural geologists and improve the running time of the algorithm to make it more practical for large-scale applications.

Zhong and Wang (2020) discussed an approach to solve the large RBF interpolation problem for efficient reconstruction of complex orebody models. The authors focused on optimizing the RBF equation to improve the efficiency of a single iteration by simplifying the problem and utilizing a fast evaluation method.

The authors employed the FastRBF method with a two-level domain decomposition approach to iteratively solve the large RBF interpolation problem. To enhance conditioning and achieve an efficient solution, the authors introduced a new kernel and anisotropic RBF interpolant.

The optimized solution method, based on the FastRBF method, was successfully applied to two real orebody modelling case studies. In the first case study, the authors utilized their method to interpolate drillhole data from a tungsten deposit containing 72 drillholes with 2 778 constraints. The researchers employed a two-level domain decomposition approach, breaking the domain into subdomains, and further decomposed each subdomain into smaller domains.

The FastRBF method was used iteratively to interpolate the drillhole data. The researchers employed the centre reduction strategy to reduce the number of constraints to 1 195, while setting the fitting accuracy to $\epsilon = 2.5$.

In the second case study, the authors applied their method to interpolate the drillhole data in a copper deposit, which consisted of 59 drillholes with 14 105 constraints. Following a similar approach as in the first case study, the authors decomposed the domain into subdomains and iteratively applied the FastRBF method. Through the centre reduction strategy, the researchers reduced the number of constraints to 4,056, setting the fitting accuracy to $\epsilon = 5.0$.

In both case studies, the authors compared the reconstructed implicit models using the marching cubes method with the actual orebody models to assess the accuracy of their approach. The results demonstrated high accuracy, indicating that the optimized solution method based on the FastRBF method is an efficient and accurate approach for orebody modelling.

The authors also emphasized the potential for further improvements in the method, including studying the efficiency of matrix-vector product

calculation and implementing a multilevel domain decomposition method to increase the rate of convergence for larger drillhole data sets.

The experimental results from several drillhole data sets showed that the optimized solution method rapidly converged within a small number of iterations. Moreover, the implementation was kernel independent, making it easily extendable for other radial basis functions in various applications.

In the future, the method can be improved by further studying the efficiency of matrix-vector product calculation and avoiding overlapping interpolation centres. The paper also suggests implementing a multilevel domain decomposition method to increase the rate of convergence for larger drillhole data sets.

Zhong et al. (2021) proposed a novel implicit geological modelling method based on the combination of multiple constraints. The proposed method utilizes an RBF interpolation to build an implicit function that satisfies multiple geological constraints.

The method starts by defining the geological constraints, such as the orientation of geological layers, the position of ore bodies, and the trend of mineralization. Then, the RBF interpolation is used to interpolate the constraints and build the implicit function. The article proposes a combination of two different RBF functions, one for the position constraints and one for the orientation constraints. The combination of these RBF functions produces a unified implicit function that satisfies all the constraints.

The proposed method was tested on a complex geological model, and the results show that the method can successfully handle multiple constraints and produce accurate geological models. The method is also shown to be more efficient and accurate than traditional explicit modelling methods.

One advantage of this method is that it can handle multiple constraints and produce accurate geological models. Additionally, the method is shown to be more efficient and accurate than traditional explicit modelling methods.

However, the article does not provide a detailed comparison of the proposed method with other existing methods.

Overall, the article provides a promising method for implicit geological modelling that can handle multiple constraints and produce accurate geological models.

Using the HRBF implicit function in Equation (2.5), Guo et al. (2022) presented a three-dimensional geological modelling method using multiple point geostatistics (MPS) for borehole data. The method uses an MPS algorithm to simulate the geological facies based on a set of training images and then applies a geological boundary extraction algorithm to extract the geological interfaces from the simulated facies. A stochastic simulation algorithm is also used to estimate the uncertainty of the model (Figure 2.12).

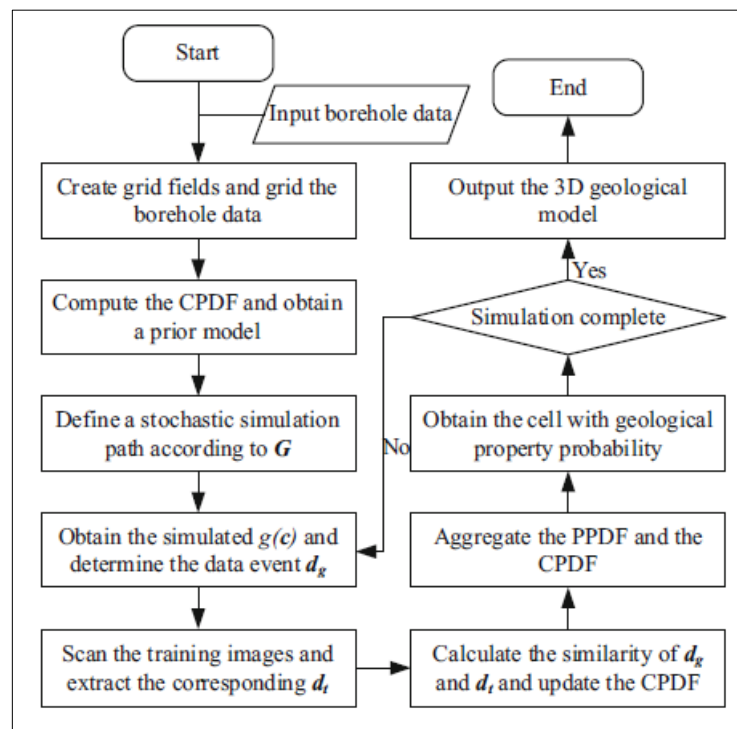


Figure 2.12: Flow chart of the new algorithm (Guo et al., 2022)

The proposed method is evaluated on a synthetic dataset, and the results show that the method can effectively capture the geological features and reproduce the facies distribution. The uncertainty analysis shows that the method can effectively estimate the uncertainty of the geological model. The

method is also compared with a traditional sequential indicator simulation (SIS) method, and the results show that the MPS-based method outperforms the SIS method in terms of accuracy and efficiency.

The proposed method has several advantages over traditional modelling methods. First, it can handle complex geological structures and reproduce facies distribution with high accuracy. Second, it can estimate the uncertainty of the geological model and provide a measure of the model's reliability. Third, it can automatically extract geological interfaces from the simulated facies, which saves time and effort. Finally, the method is computationally efficient and can be applied to large datasets.

One limitation of the proposed method is that it requires a set of training images, which may be difficult to obtain in some cases. Another limitation is that the method assumes stationarity, which may not hold in some geological environments. Overall, the proposed method provides a promising approach for automatic geological modelling and uncertainty analysis for borehole data.

Zhong et al. (2022) designed an autonomous modelling technique for narrow vein-type ore bodies based on Boolean combination restrictions. In contrast to the direct interpolation method, the researchers created implicit functions for the hanging wall and footwall surfaces. Using the Boolean combination constraints, the combined implicit function is then created to represent the entire orebody model. Finally, the orebody is produced by performing a Boolean operation on the hanging wall and footwall surfaces.

The approach is applicable to narrow vein-type ore bodies (for example, vein gold deposits and mineral sand deposits) that are big in two dimensions but narrow in three. Utilizing genuine geological sample data from mines, numerous experiments are conducted using the implicit function of radial basis functions interpolation. The experimental findings demonstrate that the approach is appropriate for modelling thin vein-type ore deposits.

RBF-based methods have proven to be efficient and accurate approaches for geological modelling. From the literature review conducted above, it is evidence that there is potential for further research and development in this area, particularly in the application of RBF-based methods for orebody modelling. There are still opportunities to improve and refine RBF-based methods to enhance their accuracy and efficiency in geological modelling applications.

2.6 Potential field-based implicit method

This section reviews the potential field-based implicit method, including its fundamental principles and its application in orebody modelling. The potential field method has been widely used in various geologic and geophysical tasks (Wang et al., 2015). The implicit potential field method can integrate multiple types of data, such as contact points and structural orientations, into the model by solving a co-kriging system (Lajaunie et al., 1997; Chiles et al., 2004; Calcagno et al., 2008; Gonçalves et al., 2017).

This method involves using various data types to construct a 3D model that represents the geological features of an area. Specifically, the potential field method is a co-kriging system that takes contact points and orientations as inputs (Lajaunie et al., 1997; Aug et al., 2005) and outputs an implicit function, called a potential field, to represent geological data (Chilès and Delfiner, 1999; Calcagno et al., 2008; Gonçalves et al., 2017; de la Varga et al., 2019). The implicit potential field function $f(x)$ is then used to represent the mineralisation domain of the orebody model (Zhong et al., 2022).

The potential field method was originally designed to construct 3D geological models from data available in geology and mineral exploration, such as geological maps, associated digital terrain models (DTMs), structural data, borehole data, and interpretations of geologists (Chiles et

al., 2007). Figure 2.13 in the source illustrates the principle of potential field interpolation in 2D.

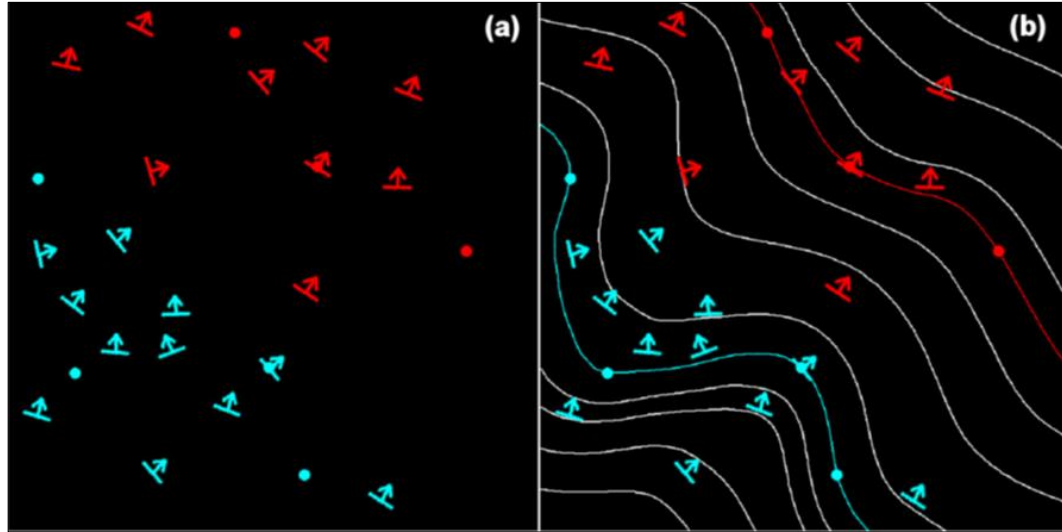


Figure 2.13: Principle of the potential-field interpolation method in 2D: (a) A geological formation mapped by the position of its interfaces; (b) The geological formation modelled by the potential-field method (Calcagno et al., 2008)

The primary purpose of the fundamental technique is to represent a single geological interface, or a series of sub-parallel interfaces denoted by l_k , $k = 1, 2 \dots$ (Lajaunie et al., 1997). The method involves summarizing the geology using a scalar function $T(p)$ of any point $p = (x, y, z)$ in 2D/3D space, known as the potential field (Figure 2.13). The interface l_k is defined as an iso-potential surface, where the set of points p that satisfies $T(p) = t_k$ represents the interface. Similarly, the geological formation between two successive interfaces, l_k and l'_k can be defined by all the points p whose potential-field value lies in the interval between t_k and t'_k (Calcagno et al., 2008).

To estimate the potential increment $T(p) - T(p_0)$ at any point p , an arbitrary origin p_0 is fixed, and a co-kriging estimator of the form is used (Feng et al., 2010). This is achieved using a co-kriging estimator of the form:

$$T^*(p) - T^*(p_0) = \sum_{\alpha=1}^M \mu_{\alpha} [T(p_{\alpha}) - T(p'_{\alpha})] + \sum_{\beta=1}^N v_{\beta} \frac{\partial T}{\partial \mu_{\beta}}(p_{\beta}) \quad (2.8)$$

where the weights μ_α and v_β determined by the co-kriging system, are functions of p (and p_0). Equation (2.8) is related to multiple-point geostatistics-based three-dimensional automatic geological modelling. Below is an explanation of the terms in Equation (2.8):

- $T^*(p)$: The estimated value of the property T at location p .
- $T^*(p_0)$: The estimated value of the property T at a reference location P_0 .
- μ_α : A weight assigned to the difference between the property values at the location P_α and P'_α , where p'_α is the corresponding location in a training image.
- $T(p_\alpha)$: The property value at the location p_α in the training image.
- v_β : A weight assigned to the derivative of the property T with respect to a conditioning variable μ_β at location P_β .
- $\partial T / (\partial \mu_\beta)(p_\beta)$: The partial derivative of the property T with respect to the conditioning variable μ_β at location p_β .
- M : The number of matched patterns between the simulation grid and the training image.
- N : The number of conditioning variables.

2.6.1 Applications of potential field implicit in ore modelling

In terms of applications in orebody modelling, Lajaunie et al. (1997) presented and evaluated a modelling method based on the principle of a potential field. Equation (2.8) was utilized by the researchers to develop their methodology. The proposed method incorporates both known locations on a geological interface and plane orientation data, such as stratification or foliation planes. The objective was to estimate the values of the scalar field for certain sites with unknown values. This was achieved by utilizing the known gradient of the scalar field or a perpendicular direction to it at other points.

The method is based on the interpolation of a scalar field defined in the space the gradient, which is orthogonal to the orientations, given that some points have the same but unknown scalar value (points of the same interface), and that scalar gradient is known on the other points (foliations). The modelled interfaces are represented as iso-values of the interpolated field.

The findings of the study demonstrate the validity of the method based on preliminary two-dimensional tests carried out with different covariance models. The method is easily transposable in three-dimensions. The method provides a way to model geological interfaces that take into account both known points and plane orientation data, improving the accuracy of geological models.

This approach has the benefit of incorporating several forms of independent geological information in the same interpolator. Known points on interfaces, orientation data at other sites, and gradient data are examples of such information.

Chiles et al. (2004) analysed the practical implementation and construction of 3D geological models using the potential field method. Subsequently, issues related to the method were identified by the researchers. These challenges encompassed managing faults, accurately representing borehole ends, accounting for interactions between multiple interfaces, and integrating gravimetric and magnetic data. The non-exhaustive list was compiled mostly from the application of the potential field method to a deposit in the Broken Hill area of Australia.

McInerney et al. (2007), on the other hand, used the potential field interpolation to model the Elk gas field of the Eastern Papuan Basin in Papua New Guinea. The validation of the model was then done by calculating the anticipated gravity signature and comparing it with the observed gravity data. This consequently led to the creation of an improved 3D geology model of the gas field.

The model honoured the available geology constraints from outcrop, drilling, and seismic data. This was achieved while also having a modelled gravity response that was more consistent with the observed gravity data. The research enhanced the understanding of the structure of the Elk field which has limited seismic control.

Calcagno et al. (2008) proposed a new method for creating three-dimensional (3D) geological models based on geological map data. The authors identified the limitations of traditional 2D mapping and the advantages of 3D modelling, including increased accuracy and improved visualisation. A method was proposed by the researchers, which involves combining geological map data with Digital Elevation Models (DEM) to generate a 3D geological model.

The method involves several steps, including the digitisation of geological maps and the creation of a DEM, which are combined to form a digital geological map. This digital map is then converted into a 3D geological model using a voxel-based approach. The authors also developed a new method for visualising the 3D geological models using colour-coded surfaces to represent different geological units.

The proposed method was tested in a study area in the Czech Republic, and the results showed that the method was effective in creating accurate and detailed 3D geological models. The authors also noted that the method is flexible and can be easily applied to other areas using different geological map data.

Overall, the article provides a valuable contribution to the field of geological modelling and highlights the importance of incorporating 3D models in geological studies. The proposed method has the potential to enhance the accuracy and efficiency of geological mapping and could be used in various applications such as mineral exploration, groundwater management, and environmental studies.

Renard et al. (2013) proposed a method for modelling geological interfaces that incorporates both known points on the interface and plane orientation data such as stratification or foliation planes. The aim is to determine surfaces that pass through the known points on the interfaces and are compatible with the orientation data, even if the orientations do not belong to one of the interfaces but rather sample the main anisotropy of the geological formation.

The principle of the method is to derive the geometry of the domain under study from a 3D interpolation of a scalar field, known as the potential field. This is achieved by co-kriging from information on contacts from drillholes and on structural data linked with the gradient of the potential field.

The potential field method efficiently adds soft information to the hard contact data using control points processed with the Gibbs sampler algorithm. By-products of the potential field approach include the co-kriging variance and the gradient of the estimated potential field, which can be turned into an uncertainty measure on the location of the domain boundary or used to map the probability to be within the given domain.

In a case study of a gold porphyry deposit in the Central Cordillera of Colombia, hardness measurements related to lithology and alteration were collected on exploration drill cores using the Equip hardness tester. After the simple pre-processing of this data, one domain was modelled, and a probability map was calculated.

A potential field method is a valuable tool for mineral deposit modelling, particularly when there is a large amount of drillhole data available but limited structural data. The method allows for the efficient incorporation of soft information and provides useful by-products such as uncertainty measures and probability maps. Further testing and validation of the method in other mineral exploration scenarios would be beneficial to fully assess its capabilities and limitations.

de la Varga et al. (2019) proposed an open-source geomodelling method based on an implicit potential-field interpolation approach. This method can construct complex full 3-D geological models, including fault networks, fault-surface interactions, unconformities, and dome structures. The algorithm is implemented in Python®, making use of a highly efficient underlying library for efficient code generation that enables a direct execution on a Graphical Processing Unit (GPU).

The authors also provide additional assets for advanced scientific investigations, such as machine learning and Bayesian inference frameworks, which enable stochastic geological modelling and inversions. Additionally, the authors provide methods to analyse model topology and compute gravity fields on the basis of the geological models and assigned density values. Overall, the authors aim to provide a basis for open scientific research using geological models, with the aim to foster reproducible research in the field of geomodelling.

In another paper, Li et al. (2021) proposed an optimized potential field interpolation modelling method based on co-kriging for geological modelling of the Beishan preselected High-Level Radioactive-Waste (HLW) geological disposal repository. This method combines geological knowledge of fault networks with sequence identification to construct a 2D boundary/3D surface and a complex geological model.

The co-kriging method is used to integrate multiple related variables obtained through site observations and to determine weight coefficients through its semi-deviation function. The proposed method is suitable for geological modelling when only a small volume of outcrop data is available.

A robustness verification is performed, which confirms the significance of the proposed method for repository site selection and roadway design optimization in deep geological environments with low data density. An optimized potential field co-kriging modelling algorithm was proposed to establish a complex geological model for the Beishan HLW disposal repository.

Due to the lack of deep underground data, the algorithm was used to construct a regional model based on limited available outcrop and constraint data. The results show that the model is capable of demonstrating the geological structural characteristics and stratigraphic fault relationships of the study area, as well as the overlying and intrusive contact relationship between rock layers and the degree of influence between the fault network and the stratigraphic sequence.

However, the potential field interpolation effect depends on the quality and distribution of the data, and the algorithm tends to be spatially smooth, leading to weaknesses in dealing with problems of spatial disproportion. These issues can be further solved using the uncertainty method or by manual adjustment.

The established model can be verified and optimized with future detailed survey data, and a series of works can be carried out based on the model, providing strong reference points for the site selection, design, and construction of a repository. Overall, the proposed modelling algorithm is a valuable tool for predicting and approximating complex geological bodies with limited data density.

Finally, Yang et al. (2021) presented a unique framework based on the divide-and-conquer approach. The basic concept of the framework was to generate intermediate 3D geological models that fit subsets of data. From there, the subsets were merged into a single large 3D geological model while keeping data and geological rule restrictions in mind.

A large-scale banded iron ore formation in Western Australia was modelled using the framework. The outcome was the generation of a single geologically accurate 3D structural model that suited all of the data. The addition of stochastic orientations and the splitting of dense contact spots improved the model. This consolidated the robustness of the divide-and-conquer approach to orebody modelling.

2.7 Signed-distance interpolation method.

The signed-distance interpolation approach for multiple categories is a deterministic implicit modelling technique that constructs the implicit function by interpolating a distance measure based on conditioning data (Silva, 2015; Rolo et al., 2017). As the implicit function, the signed-distance function (SDF) represents the shortest distance between any two sample locations of a distinct category (Deutsch and Wilde, 2013).

The distance between a sample and the nearest sample from the opposite domain is determined and allocated to each sample (Figure 2.14). This means that the SDF calculates the separation of domains from one another (Silva, 2015). And for samples within the domain, negative values denote the distance to the boundary.

In other words, the sign of the calculated signed-distance values determines the interface that divides the areas in space (Rolo et al., 2017). The distance function is calculated at every data location to generate the new distance function variable (Osher and Fedkiw, 2002). To construct the new distance function variable, the distance function is computed at each data point. Each data location must be labelled as a sample or a non-sample.

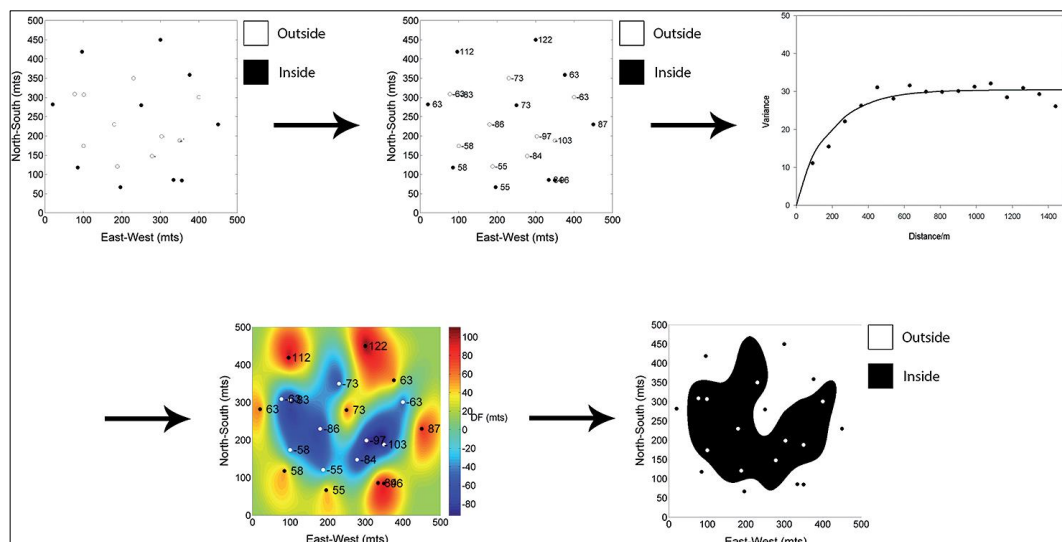


Figure 2.14: Simple two-dimensional example illustrating signed-distance function modelling workflow (adapted from Silva, 2015; Rolo et al., 2017)

The existence of the sample is indicated by a binary flag, $i(u)$, (Deutsch and Wilde, 2013):

$$i_k(u_\alpha) = \begin{cases} 1, & \text{if } Z(u_\alpha) \text{ is inside} \\ 0, & \text{if } Z(u_\alpha) \text{ is outside} \end{cases} \quad (2.9)$$

Equation (2.9) represents the indicator function for a spatial location u_α . If the variable Z at the location u_α is inside a defined domain, then the function $i_k(u_\alpha)$ equals 1 (Figure 2.14). Otherwise, if Z at u_α is outside the domain, then the function $i_k(u_\alpha)$ equals 0 (Figure 2.14) (Mallet, 2003; Silva, 2015). At each data location u , the nearest data location u' is determined such that $\text{Min}\{u - u'\}$, $i(u) \neq i(u')$.

For each data location, the algorithm finds the nearest neighbouring data location that is not from the same data set. This is done using the Euclidean distance between the two locations. The purpose of this is to avoid any bias in the estimation of the potential caused by having multiple data points in the same location. By using neighbouring data points that are not from the same location, the estimation is more robust and less likely to be affected by any noise or errors in the data.

Let us now review two pertinent applications of SDF-based methods in orebody modelling.

In the first selected application, Deutsch and Wilde (2013) proposed a methodology for modelling multiple coal seams using signed-distance functions and global Kriging is presented. The first step of the methodology involves data preparation, where two variables are calculated at each drillhole: coal accumulation and distance function.

Coal accumulation is the total amount of coal present at a location, while the distance function estimates the distance between the location and the coal/non-coal interface. The distance can be positive or negative, depending on whether the data is inside or outside the coal using Equation (2.8).

The second step is to interpolate coal accumulation using a global interpolation algorithm such as global Kriging. This algorithm assigns a weight to each data and calculates an estimate without searching for data since all of the data are used to estimate at every location.

The third step is to interpolate the distance function at every cell in the 3D grid. This is done by identifying the appropriate data and applying the global Kriging weight assigned to a given drillhole to each of the data from that drillhole that fall within the vertical search window.

The fourth step involves determining the locations of the coal seams by considering individual columns of distance function estimates from the 3D grid. This is done by applying a distance function threshold, which identifies the neighbourhoods where the distance function should be estimated on a finer grid. The distance function threshold is adjusted until the thicknesses match.

Finally, the methodology is extended to multiple coal seams, where the same procedure for interpolating coal thickness and distance function is followed. Applying a distance function threshold to a column of distance function estimates can identify any number of seams in the column.

The resulting numerical model of the coal seams can be gridded for various post-processing steps such as flow simulation or mine planning. Examples in the paper demonstrate the efficiency and precision of the methodology in locating numerous thin coal seams.

The final paper with selected applications is by Rolo et al. (2017). In this case, the researchers investigated the use of the signed-distance function methodology for implicit geologic modelling. The study aimed to determine the applicability of this methodology in providing accurate estimates of the grade and location of mineral deposits in the subsurface.

The implicit orebody modelling methodology was introduced in the field of geology by Cowan et al. (2003) and is based on the concept of a volume function attached to the distance to an interface, which separates two

distinct domains. The bounding interface of interest is usually the iso-surface zero of the volume function. To define the boundary interface, the volume function was interpolated using an RBF, which is a fast-scattered interpolator method. The study found that the SDF methodology is a simple and fast way to model multiple coal seams. A categorical scatterplot was constructed to compare the results of the algorithm with those of a trained professional.

The scatterplot showed a high linear correlation coefficient of 0.93, indicating that 95% of the estimated blocks were consistent in both models. However, the study also identified some limitations of the method, including the non-stationarity of the distances, which can make variogram modelling arbitrary and questionable. Additionally, the method is based on Kriging, so only linear relationships between domains are modelled, unless a large amount of data is available.

Overall, the study concludes that while the SDF methodology cannot replace a trained professional, its simplicity and speed justify its usage, especially in the early stages of modelling. Future research could focus on combining boundary simulation with the deterministic method to overcome some of the limitations of the method.

2.8 Concluding remarks

This section summarizes the review work conducted in Chapter 2, which focused on identifying limitations and gaps in the methods and models used for synthetic geometallurgical data generation and implicit orebody modelling. The section provides a brief overview of the gaps identified and offers a way forward to address them.

In Section 2.2, the reviewed literature suggests that the use of techniques for synthetic data generation in geometallurgy is still not widely adopted. Out of the limited number of scientific articles dealing with synthetic data in geometallurgy, only two methods were identified: synthetic orebody

modelling using a mathematical function through a three-dimensional voxel model (Lishchuk, 2018) and geostatistical simulation (Garrido et al., 2018). The limitation of the work by Lishchuk (2018) is that it assumes the ore response uncertainty during the process is only influenced by factors such as extraction sequence, processing techniques, operator team, and blending of the extracted block. Other factors that may influence the uncertainty are not considered.

Furthermore, in real-world applications, there may be other factors that could influence the ore response uncertainty, and these factors are not accounted for in the model. Additionally, the model assumes that the database for each point in the physical space is identical, which may not always be the case in real-world applications, where there may be variations in the quality and quantity of data available.

The limitation of the work by Garrido et al. (2018) is that their proposed methodology requires a consolidated database to generate synthetic geometallurgical block models. This means that if there are gaps or inaccuracies in the data, the resulting models may not be representative of the actual deposit.

Additionally, the methodology relies on certain assumptions about the underlying geology and mineralogy, and if these assumptions are incorrect, the simulated data may not accurately reflect the true characteristics of the deposit. Another potential limitation is that the methodology may not be suitable for deposits with complex geometries or mineralogy, as the simulation may oversimplify these features.

The two scientific studies mentioned above suggest that more work is needed in the field of generating synthetic geometallurgical data. Additionally, the literature review conducted in Section 2.4 indicates that no studies have yet utilized GAN-based models to generate synthetic geometallurgical data, despite the well-established methodology and principles of using GANs for this purpose. Therefore, the researcher of this

thesis believes that there is still an opportunity to explore the use of GAN-based models for generating synthetic geometallurgical data.

The utilization of implicit modelling algorithms for creating geospatial surface models has been in practice since the late 1990s. The pioneering work in using implicit methods for orebody modelling was conducted by Lajaunie et al. (1997) as discussed in Section 2.6. A 3D geological model was developed by the researchers using the potential field approach.

Cowan et al. (2003) later presented an RBF framework upon which the widely accepted 3D geological modelling software package Leapfrog® is based. Over the years, the RBF and potential field techniques have established themselves as the preferred methods for implicit geological modelling. However, in recent times, the signed-distance function (SDF) has emerged as another type of implicit method that can also be utilized in orebody modelling (Rolo et al., 2017).

Over the last few decades, research in implicit geological modelling has mostly concentrated on method development and application (Feng et al., 2010; Choudhury, 2017; Zhong et al., 2019; Zhong and Wang, 2020; Zhong et al., 2021). And as a relatively new thematic area when compared to explicit orebody modelling, implicit modelling has received a lot of interest and consistent improvements of underlying algorithms (Wellmann and Caumon, 2018).

However, this has resulted in numerous problem-specific solutions. In simple terms, the researchers concluded that the proposed implicit solutions can only be effectively utilized for the specific issues they were designed for until modifications are made. The research conducted on implicit methods has resulted in the development of several software packages, including Leapfrog®, 3D GeoModeller®, and Gocad-SKUA®, which are commonly used (Birch, 2014).

However, these products often have black-box algorithms that are tied to commercial software, limiting researchers' ability to scrutinize or modify the

underlying algorithms or adjust key parameters. Fortunately, recent years have seen an increase in the development of open-access software, with examples such as Gempy® and Loopstructural® (de la Varga et al., 2019; Grose et al., 2021).

The implicit framework is particularly useful for creating geometries of mineral deposits that are too complex to be manually digitised. Moreover, the implicit modelling algorithms enable a significant reduction in the ratio of time spent building models to time spent considering the geological implications of the models.

This is because the algorithms automate the process of creating complex geometries. Additionally, implicit modelling algorithms have been shown to produce solutions that were not previously considered due to operator bias and experience (Cowan et al., 2003; Grose et al., 2017; Zhong, et al., 2019).

Despite the advantages of implicit modelling approaches, there are also limitations to consider. Firstly, there are costs associated with geological model automation. Converting geological data and concepts into a matching 3D model using automated methods can be challenging.

Secondly, seemingly basic tasks such as maintaining a smooth and uniform stratigraphic thickness within a stack of conformable surfaces can yield unsatisfactory results. Laurent et al. (2016) reported inconsistencies caused by upright or inverted cones when horizons were force-fitted around good markers. Additionally, there is a risk that implicit models, which can be quickly constructed and appear polished, may be incorrect.

Significant work has been done on the implicit modelling of orebodies (e.g., Newell, 2018; Wang et al., 2018; Zhong et al., 2019 & 2021; Zhong and Wang, 2020; Guo et al., 2022). Based on the review of the papers in this section, several gaps in the literature were identified.

One significant research gap is the consistent lack of the use of real-world data in the evaluation of available implicit algorithms. Instead, most

proposed implicit algorithms are tested using computer-generated data, which is more predictable than real-world data.

The other research gap is related to the role of uncertainties in primary data on geospatial models. Zhong et al. (2019) attempted to establish an implicit modelling framework and explore the concept of data uncertainty. The conclusion of the study suggests that constraints, unknown geological data, and geospatial models are subject to uncertainties and limitations originating from the collection and processing of primary data. Further research is needed to gain a better understanding of the extent of this problem.

Another topical theme is scenario testing. Indeed, one benefit of implicit modelling resides in its ability to evaluate alternative orebody situation models without wasting time or money. These various models may be used to simulate 'what-if' scenarios that could affect grade prediction and downstream mining operations.

Consequently, the tested scenarios would allow for an assessment of mining hazards associated with each geological model (Cowan et al., 2003). Future studies should concentrate on scenario testing to enhance not just the algorithms but also the models. The problem is that much of the work done to date is centred on orebody modelling for grade distribution. Extension to other geometallurgical parameters is the next logical move that may benefit the mining industry at large.

The last note is that lithology, structural information, grade, and assay are the parameters most employed in orebody modelling (Steward, 2014; Laurent et al., 2016; Grose et al., 2017; Stoch et al., 2018; Zhong et al., 2022). Emerging trends are now exploring the incorporation of geometallurgical data such as the Bond work index. However, there has not been much research on how implicit modelling algorithms can deal with geometallurgical data.

It is conjectured for this doctoral research that implicit methods can effectively and accurately model geometallurgical parameters for use in mine planning, leading to improved decision-making and potentially increased profitability for mining operations. This is important because, as noted earlier, the potential of using implicit modelling methods to model geometallurgical parameters has not been explored.

The objective of this doctoral research is to develop a novel methodology to model geometallurgical parameters using implicit methods, thus contributing to the body of knowledge and bridging the gap in the application of implicit methods in geometallurgy. By doing so, a better understanding of the potential and limitations of implicit methods in geometallurgy can be achieved.

Chapter 3 Research methodology and data collection

3.1 Introduction

This chapter details the computer modelling methodology followed in the collection of data for subsequent analysis. The chapter is divided into three sections. The first is the generation of synthetic data using Generative Adversarial Networks (GANs). The second is the implicit Radial Basis Function and geostatistical (Ordinary Kriging) modelling of geometallurgical parameters. The third section highlights the challenges and limitations encountered in this chapter.

As stated in Section 1.4, the geometallurgical parameters which will be modelled in this thesis are, Bond work index, rod mill index, rock quality designation, drop weight index, Axb, and abrasion index. These parameters were selected due to their availability in literature.

The Bond work index (BWI) is a measure of how much energy is required to break down a certain material from a starting size to a smaller, final size (Napier-Munn et al., 1999; Chakrabarti, 2000). The BWI is specifically the amount of energy needed to reduce the size of the material until 80% of it can pass through a sieve with very small holes (100 μm in size).

The abrasion index (A_i) is used as a measure of the relative abrasivity of different rock materials on metal (Clout and Manuel, 2022). It is important to understand process plant design and operation in crushing, screening, and especially grinding.

The rod mill work index is measured using Bond's standard rod mill grindability test, which is conducted in locked-cycle mode to emulate the continuous closed-circuit operation (Ahmadi et al., 2013).

The JK Drop Weight Test (DWT) is a laboratory test to measure the breakage parameters of a rock sample (Öfner and Zaurith, 2016). The

DWT comprises a simple mechanism that makes use of a drop weight of known mass falling under the influence of gravity from a known height.

Rock quality designation (RQD) is a standard technique in the mining industry for the qualitative and quantitative assessment of rock quality and degree of jointing, fracturing, and shearing in a rock mass. RQD is defined as the percentage of intact drill core pieces longer than 10 cm recovered during a single core run (Abzalov, 2006).

The Axb parameter is a measure of the abrasiveness of a rock sample, commonly used in the mining industry due to the wear and tear that a material can cause to grinding equipment (Danish, 2017). Axb describes the hardness of the ore. A higher value of Axb represents soft material and vice versa. The Axb parameter is determined through laboratory tests that involve crushing a sample of the material and measuring the energy required to produce a specific particle size distribution.

BWI, Ai, DWI, and Axb are all important parameters used in mining to optimize ore processing and mine planning. These parameters help to develop efficient process flowsheets that are tailored to the specific characteristics of the deposit. In block modelling, they can be used to estimate energy costs and wear rates, optimize mine planning, and select appropriate equipment for ore processing.

All experiments in this chapter were run on a Windows® 11 operating system, utilizing a computer with an Intel i5 CPU featuring 10 cores, 8 GB of memory, and 1 TB of storage space.

3.2 Description of the original dataset

This section provides a detailed account of the original data used in the generation of synthetic data. The data utilized in the study was drillhole data that was obtained from a previous study conducted by Mboyo (2018). The drillhole data were acquired during a cobalt exploration drilling campaign in the Democratic Republic of Congo by Iverland Mining. Due to the high cost

of collecting geometallurgical data on-site or in the laboratory, this data was obtained from previous research papers by Dehaine et al. (2021) and Mambwe et al. (2022).

The data for drillholes are recorded in collar data, which contains both categorical and numerical information. The numerical data is organized in 65 rows/columns, while the categorical data includes column headers like 'Hole_ID', 'X', 'Y', 'Z', and 'Depth_max', as listed in Table 3.1. The 'Hole_ID' header serves to identify each drillhole with its unique coordinates (latitude, longitude, and elevation) indicated by 'X', 'Y' in decimal degrees (DD), and 'Z' in meters (m) respectively.

The 'Depth_max' in meters (m) column indicates the maximum depth for each drillhole. The mean X (DD) coordinate is estimated to be around 530,120.5, accompanied by a standard deviation of 131.9. Y (DD) remains constant at 8,710,000.0 for all observations. The mean Z (m) value is found to be 1,330.6 m, with a standard deviation of 0.9 m.

The range of Depth_max (m) spans from 77.0 to 287.0 m, while the mean depth recorded is 148.3 m, with a standard deviation of 45.4 m. These statistics provide valuable insights into the distribution and characteristics of the dataset, facilitating an understanding of the variability and central tendencies of the variables.

Table 3.1. Representative of the original collar data

	X (DD)	Y (DD)	Z (m)	Depth_max (m)
count	66.0	66.0	66.0	66.0
mean	530 120.5	8 710 000.0	1 330.6	148.3
Std	131.9	139.0	0.9	45.4
Min	529 863.8	8 710 000.0	1 328.9	77.0
25%	530 027.7	8 710 000.0	1 329.9	116.6
50%	530 123.0	8 710 000.0	1 330.6	144.8
75%	530 218.6	8 710 000.0	1 331.3	170.0
Max	530 397.3	8 710 000.0	1 332.6	287.0

The assay data for the original drillholes is structured in 4 717 rows and is categorized into four headers: 'Hole_ID', 'Depth_From', 'Depth_To', and 'TCo'. The "depth from" and "depth to" in meters refer to the starting and ending depths of a specific interval in the drillhole. The "depth from" is the depth at which the interval starts, while the "depth to" is the depth at which the interval ends.

These measurements are used to define the location and boundaries of geological features, mineralization zones, and other geological data in the drillhole. The 'TCo' header represents the total cobalt concentration analyzed in the ore of the drillhole. The values for 'TCo' are expressed as grades in percentages (%), indicating the amount of total cobalt in the ore. Table 3.2 provides a summary of the structure of the assay data.

The descriptive statistics reveal that the mean depth from the surface is approximately 80.9 m, with a standard deviation of 36.8 m. The minimum and maximum depths recorded are 2.0 m and 197.5 m, respectively. The median depth (50th percentile) is 79.5 m, indicating that half of the observations fall below this value.

The TCo values range from 0.0% to 25.4%, with a mean of 0.8% and a standard deviation of 1.8%. The dataset provides a comprehensive overview of the distribution and characteristics of the measurements, enabling a better understanding of the variables' variability and central tendency.

Table 3.2. Representative of the original assay data

	Depth_From (m)	Depth_To (m)	TCo (%)
count	4 717	4 717	4 717
mean	80.9	81.6	0.8
std	36.8	36.8	1.8
min	2.0	2.4	0.0
25%	52.2	52.8	0.1
50%	79.5	80.4	0.2
75%	107.2	107.9	0.8
max	197.5	198.5	25.4

The geometallurgical data is comprised of 1 122 rows and 9 columns, with headers including 'Hole_ID', 'Depth_From', 'Depth_To', 'Bond work index', 'Rod mill index', 'RQD', 'Drop weight index', 'Abrasion index', and 'Axb'. See Section 3.1 for an explanation of these geometallurgical parameters.

These columns contain various parameters related to the geometallurgical properties of the drillhole data. Table 3.3 presents an example of the metallurgical data for a single drillhole, ranging from the horizon to a depth of 27.0 m. As stated in Section 3.1, the geometallurgical data were obtained from historical papers and online databases.

Descriptive statistics reveal that the mean values for Depth_From, Depth_To, Bond_Work, Abression, Rodmill_In, Drop_Weigh, RQD, AxB, X, Y, Z, and Depth_max are approximately 76.61, 85.32, 11.12, 0.29, 13.48, 8.56, 49.58, 21.55, 530 120.57, 8 714 420.00, 1 330.58, and 150.07, respectively.

The standard deviations provide information about the spread of the data, with values of 51.80, 51.77, 4.48, 0.45, 5.22, 6.58, 20.34, 17.67, 123.72, 127.70, 0.82, and 43.79 for each respective variable. The minimum, maximum, and quartile values further characterize the range and distribution of the data.

Table 3.3. Representative of historical geometallurgical data for cobalt

	Depth_From (m)	Depth_To (m)	Bond_Work (kWh/t)	Abression (kWh/t)	Rodmill_In (kWh/t)	Drop_Weigh (kWh/t)	RQD (%)	AxB (kWh/t)
count	1 122.00	1 122.00	1 122.00	1 122.00	1 122.00	1 122.00	1 122.00	1 122.00
mean	76.61	85.32	11.12	0.29	13.48	8.56	49.58	21.55
std	51.80	51.77	4.48	0.45	5.22	6.58	20.34	17.67
min	0.00	4.80	0.00	0.00	0.00	0.00	0.00	0.00
25%	33.83	44.63	7.00	0.00	12.00	0.02	36.33	0.32
50%	70.5	77.60	12.00	0.02	13.80	11.30	54.74	29.10
75%	112.15	122.38	14.30	0.78	18.90	12.43	70.00	41.10
max	281.80	287.50	19.60	6.70	18.90	21.00	72.00	41.10

	Depth_From (m)	Depth_To (m)	X (DD)	Y (DD)	Z (m)	Depth_max (m)
count	1 122.00	1 122.00	1 122.00	1 122.00	1 122.00	1 122.00
mean	76.61	85.32	530 120.57	8 714 420.00	1 330.58	150.07
std	51.80	51.77	123.72	127.70	0.82	43.79
min	0.00	4.80	529 863.84	8 714 125.00	1 328.93	77.00
25%	33.83	44.63	530 029.72	8 714 331.00	1 329.94	118.50
50%	70.95	77.60	530 119.97	8 714 418.00	1 330.59	154.50
75%	112.15	122.38	530 218.65	8 714 516.00	1 331.13	171.50
max	281.80	287.50	530 397.28	8 714 717.00	1 332.65	287.00

The final dataset in this study is the survey data, which provides information on the dip and azimuth of the drillhole data. This dataset is comprised of 1 122 rows and 4 columns, including 'Hole_ID', 'Depth', 'Azimuth', and 'Dip'. The 'Azimuth' column represents the horizontal angle measured in degrees between a line in a horizontal plane and a line in the direction of the drillhole. The 'Dip' column measured in degrees (°) represents the angle between a line in a vertical plane and the drillhole.

Together, these measurements provide important information on the orientation and structure of the geological features present in the drillhole data, which can be used to guide further exploration and resource estimation efforts. 'Depth' refers to the vertical depth of the survey data point in meters. Each survey data point corresponds to a specific depth in the drillhole. The 'Depth' column in the survey data provides information on the location of the survey data point along the vertical axis of the drillhole. Table 3.4 provides a summary of the structure of the survey data.

The summary of descriptive statistics reveals that the average depth is approximately 80.73 m, with a standard deviation of 64.57 m. The depth measurements range from 0.00 to 287.00 m. The azimuth values range from 80.40 to 140.40°, with an average of 113.96° and a standard deviation of 19.72°. The dip measurements range from -65.10 to -45.80°, with an average of -55.65° and a standard deviation of 3.40°.

Table 3.4. Representative of the original survey data

	Depth (m)	Azimuth (Degree)	Dip (Degree)
count	278.00	278.00	278.00
mean	80.73	113.96	-55.65
std	64.57	19.72	3.40
min	0.00	80.40	-65.10
25%	50.00	91.90	-57.40
50%	81.50	126.05	-55.75
75%	125.00	130.10	-54.43
max	287.00	140.40	-45.80

Tables 3.1 – 3.4 displays the original datasets that will be utilized in this study to create synthetic data. The objective of the study is to predict whether synthetic survey data can be created from the original data without any loss of quality. This is an important task as synthetic data has a variety of useful applications, such as preserving privacy when original data cannot be shared.

However, the value of the synthetic data is highly dependent on the quality of the original data. Therefore, the study aims to investigate whether the original data is of sufficient quality to generate synthetic data that can be used for various purposes without any loss of important information. By evaluating the original data and its ability to generate high-quality synthetic data, the study provides insights into the suitability of using synthetic data for a range of applications.

3.3 Pre-processing of the original data

Before any experiment or modelling could be undertaken, the original data was pre-processed. This consisted in cleaning up and transforming the original raw data coming from different sources like historical data, stream data, and application data so that it is structured for the intended purpose (Pandey et al., 2020). In this doctoral study, Python® libraries were used to pre-process the original data following the steps below:

Step 1. Importing relevant libraries

The pre-processing of raw data involved several steps. The datasets were pre-processed using Python® version 3.10.10. The first step was to import all the necessary libraries relevant to the pre-processing. Figure 3.1 shows the commands used for this purpose. The libraries used to pre-process data were Pandas, NumPy, os, matplotlib, and seaborn. Pandas are used to import, export datasets and create data structures. NumPy is used for

mathematical calculations. The `os` module is used to manage files and directories and Retrieve information about the file system. Matplotlib and seaborn are used for data visualization.

After importing the necessary libraries, the original data was cleaned up and transformed into a structured format suitable for synthetic data generation.

```
In [1]: import os
import numpy as np
import pandas as pd
from matplotlib import pyplot as plt
%matplotlib inline
import seaborn as sns
import warnings
warnings.filterwarnings("ignore")
```

Figure 3.1: Libraries used in Python® for data pre-processing.

Step 2. Loading the datasets

The next step after importing the libraries is loading the datasets. Using Python®, one can read data files of different formats like image files, comma-separated value files (or CSV files), Excel® files, text files, HTML, hierarchical data formats, audio files, video files and many more.

The following Pandas instruction illustrates how the original datasets in Excel® CSV formats were loaded and read in Python®:

```
Variable_name = pd.read_FileFormat("file_location/path  
of the file")
```

where `Variable_name` is the name of the variable in which the data will get stored; `pd` means Pandas® libraries were used to read the datasets; and `FileFormat` is the format that the datasets were saved under; `file_location` is the location where the file was saved; and `path of the file` was the location where the file originated in the computer.

The datasets were loaded using the following code:

```
collar=pd.read_csv("C:/Users/TIYANI/Videos/Final/Collar
.csv").
```

with `collar` representing the name of the collar dataset. The other datasets were loaded the same way while replacing the `collar`, with either `assay`, `survey` or `geometallurgical` data.

Step 3. Checking data

This step entailed checking the first 5 rows of the data, the data type, the data columns, missing values, and the statistic of the data.

The `head()` function was made use of to display a few rows of data. Alternatively, the `print()` function could be invoked to display the loaded datasets.

The following codes were also used during this process: `collar.head()`, `collar.columns`, `collar.isna().any()`, `collar.describe()`.

These steps were repeated for the other datasets, with the only change being the replacement of the term "`collar`" with either "`assay`", "`survey`", or "`geomet`". Table 3.5 shows statistics of collar data based on the following code. `collar.describe ...` was entered.

Table 3.5. Summary of statistics of the original collar data.

	X (DD)	Y (DD)	Z (m)	Depth_max (m)	Target
count	66	66	66	66	66
mean	530 120.5	8.71E+06	1330.575	148.2652	1.121212
Std	131.8543	1.39E+02	0.914364	45.39292	0.328875
Min	529 863.8	8.71E+06	1328.925	77	1
25%	530 027.7	8.71E+06	1329.912	116.625	1
50%	530 123	8.71E+06	1330.555	144.75	1
75%	530 218.6	8.71E+06	1331.29	170	1
Max	530 397.3	8.71E+06	1332.649	287	2

Step 4. Handling the null values

The next and most crucial step in data pre-processing is to handle the missing values or null values rendered in Python® as NaN.

The simplest way of handling null values is to drop the entire row containing the null values. This sometimes tends to produce unpredictable results and therefore may not be the best way of handling missing values. Other options include the use of specialised Python® libraries or implementing strategies involving computing the mean, median or mode depending upon the problem and the data at hand. However, the most common strategies are to assess “mean” or “std” or “Zero” or to drop the column with missing data.

In the case of this doctoral study, geometallurgical data was noted to have a lot of missing values. The following instruction was used to check for missing values: `geomet.isnull().sum()`. Then, the columns with missing values were dropped to keep the analysis as simple as possible.

Step 5. Converting categorical data to numerical data.

To facilitate synthetic data generation and ensure proper handling in the process, the categorical data in the 'Hole_ID' column needed to be converted into numerical data. The Figure 3.2 presents the code that was used. In this step, the scikit-learn library in Python® was used to perform label encoding on a column named 'Hole_ID'.

```
In [5]: ► from sklearn.preprocessing import LabelEncoder
        label_encoder = LabelEncoder()

        # Fit and transform the labels to integer values
        survey['Hole_ID'] = label_encoder.fit_transform(survey['Hole_ID'])
```

Figure 3.2: Code used in Python® to convert categorical data to numerical data

Label encoding is a preprocessing technique used to convert categorical (textual) data into numerical values. It is often necessary because many machine learning algorithms work with numerical data and cannot directly handle categorical features.

After running this step, the 'Hole_ID' column in the 'survey' DataFrame will contain integer values instead of the original text labels. These integer values will represent the different categories present in the 'Hole_ID' column, allowing the data to be used in machine learning models that require numerical input. Each unique label will be mapped to a unique integer value.

3.4 Methods for generating the synthetic data

This section outlines a study that focused on data augmentation using GANs. The research involved the use of CTGAN, CopulaGAN, and Gaussian Copula to generate synthetic data that could accurately replicate the distribution and relationships present in the original data. It should be noted that Section 2.2 of this thesis provides detailed information regarding the GANs employed in this section. The section discusses the particulars of CTGAN, CopulaGAN, and GaussianCopula, which were the GANs employed to generate synthetic data for data augmentation.

To generate synthetic data, it is crucial to have access to the original datasets to enable the GANs to learn from the data. The original data used in this study, are four diverse datasets that included the collar, assay, geometallurgical and survey datasets. The datasets used in the study contained both categorical and numerical attributes. The categorical attribute was 'Hole_ID,' while the numerical attributes were 'X (DD),' 'Y (DD),' 'Z (m),' and 'Depth_max (m).' For more information about the original datasets used in this study, refer to Section 3.2 of the thesis.

In this section, a summary of the steps used in generating synthetic data is provided, while the detailed code used for each step can be found in Appendix A, which contains Jupyter® notebooks.

3.4.1 Computer-based generation of the synthetic data

To create synthetic data for the study, various methods were employed, including CTGAN, Gaussian Copula, and CopulaGAN models, which were discussed in Section 2.2. Additionally, the SDV libraries version 0.18.0 (see Section 2.2.4), which consist of multiple modules for synthetic data generation, were utilized. The following steps were employed during the synthetic data generation process.

Step 1: The initial data was generated in such a way that it met the requirements of the original data presented in Section 3.2.1. This step involves pre-processing and preparing the data for modelling, which was carried out using the steps outlined in Section 3.2.2.

Step 2: The SDV library was loaded in python® using the following code: `import SDV`. If the SDV library is not available in python® it can be installed using the following code: `pip install SDV`. From the SDV library, the models used to generate synthetic data were loaded. These are CTGAN, CopulaGAN and Gaussian Copula. The code that was used for loading the model was, `from sdv.tabular import CTGAN`. The rest of the models were loaded the same way by replacing CTGAN from the code with either CopulaGAN or GaussianCopula.

Step 3: Constraints were set for data. Constraints refer to the specific conditions and limitations that are applied to the process of generating synthetic data. In order for synthetic data to inherit the qualities and data structure of the original data constraints need to be set. The SDV library has

predefined constraints that are commonly found in the datasets. The constraints include `FixedCombination` constraints, inequality, scalar inequality as well as positive and negative constraints among others. More information can be obtained at

https://sdv.dev/SDV/user_guides/single_table/handling_constraints.html#predefined-constraints.

For this study, the `FixedCombination` and negative constraints were used (Figure 3.3).

The `FixedCombinations` constraint enforces that the combinations between a set of columns are fixed, that is, no other permutations or shuffling is allowed other than what is already observed in the real data. The data utilized in this study contains a `FixedCombinations` constraint. Specifically, for collar data (as shown in Figure 3.3), the variables X (DD), Y (DD), Z (m), and `max_depth` (m) is subject to this constraint. Similarly, for assay data, the variables `Depth_From` (m) and `Depth_To` (m) are constrained.

For survey data, the variables `Depth` (m), `Azimuth` (degree), and `Dip` (degree) are subject to the constraint. Finally, for Geometallurgy data, the parameters were `Depth_From` (m), `Depth_To` (m), `BWI` (kWh/t), `rod mill index` (kWh/t), `RQD` (%), `DWI` (kWh/t), `Ai` (KWh/t), and `Axb` (kWh/t) are constrained. It is important to note that these variables should not be shuffled or mixed up in the synthetic data, as they must remain in their original form to ensure the quality and accuracy of the data.

In the data, the negative constraint was defined. All the `Dip` values must be negative from the synthetic data. The code for negative constrains was as follows: `from sdv.constraints import Negative`

```
dip= Negative(column_name='Dip').
```

```
In [7]: from sdv.constraints import FixedCombinations

In [8]: Location = FixedCombinations(column_names=['Depth (m)', 'Azimuth (Degree)', 'Dip (Degree)'])

In [9]: from sdv.constraints import Negative
        dip = Negative(column_name='Dip (Degree)')

In [10]: constraints = [Location, dip]
```

Figure 3.3: Example of constraints set for original assay data

Step 4: The model was fitted to the data. Once the constraints were set and the data prepared, this data was set for fitting on the model. Figure 3.4 illustrates the code that was used to fit and set the model. Model fitting and training are important steps in the process of creating a machine-learning model.

In general, model fitting involves selecting a model architecture and defining the parameters to be used to generate the model. This is typically done using a training dataset, which is a set of data that the model will be trained on to learn the relationship between the input data and the target variable.

During model training, the model is adjusted to optimize its performance on the training data, which involves adjusting the model parameters to minimize the difference between the predicted values and the actual values in the training data.

```
batch_size = 1000
epochs = 100

model = CTGAN(constraints=constraints, generator_dim=(256, 256, 256),
              discriminator_dim=(256, 256, 256), batch_size=batch_size, epochs=epochs, verbose=True)
model.fit(geo)
```

Figure 3.4: Code used for model training and data fitting for synthetic data generation

Step 5: Hyperparameters were set. This step involved setting hyperparameters, which are user-defined parameters used to control the learning process of the synthetic data generation models. By optimizing the hyperparameters, the models can perform better. The hyperparameters

used in this study for synthetic data generation are: The `primary key`, `epochs`, `batch size`, `generator_dim` and `discrimination_dim`, `verbose`, `field_distribution`, and `disct`. The `primary key` is a column in a table that serves as the index or unique identifier for each row of data in the table. It helps to identify and locate specific data within the table.

The `primary key` hyperparameter was used for all the models during synthetic data generation. However, for datasets that did not have a unique Hole ID, like assay data, the `primary key` was not used. The hyperparameters, `epochs` and `batch size`, shown in Figure 3.4, determine how many times the model will update its parameters and how many samples are used in each update during the optimization process. These parameters were used for CTGAN and CopulaGAN models.

The `generator_dim` and `discrimination_dim` hyperparameters are used to control the size of the output of the generator and discriminator networks, respectively. This helps to ensure that the generated synthetic data is of an appropriate size. The default values for these two parameters were 256, 256, and 256.

These values were used as they performed better during model training. The `verbose` hyperparameter, on the other hand, is used to control whether the fit progress is printed on the screen. By default, this setting is false, but it can be changed if necessary. These hyperparameters were used for all the models.

The Gaussian Copula algorithm uses the `field_distribution` hyperparameter to specify the distribution that can be used for a particular column in the dataset. The `disct` argument can be set to one of the following possible values:

- "gaussian": This value indicates the use of a Gaussian distribution for the column.

- "gamma": This value indicates the use of a Gamma distribution for the column.
- "beta": This value indicates the use of a Beta distribution for the column.
- "student_t": This value indicates the use of a Student t-distribution for the column.
- "gaussian_kde": This value indicates the use of a non-parametric GaussianKDE distribution for the column. However, if this value is used, the `get_parameters` function cannot be used.
- "truncated_gaussian": This value indicates the use of a Truncated Gaussian distribution for the column.

For more information on the hyperparameters of the two modules can be accessed here

https://sdv.dev/SDV/user_guides/single_table/ctgan.html#advanced-usage.

In this research, the beta was used as it showed better performance in generating synthetic data during the training process.

Step 6: Generation of the synthetic data. In this step, synthetic data was generated through the trained model. Model training is the process of feeding a machine learning algorithm with a set of input data and their corresponding output labels to enable the algorithm to learn patterns and relationships between the data. The trained model can then be used to make predictions on new, unseen data.

Once the model is trained with the appropriate hyperparameters, it can be used to generate synthetic data. The process of generating synthetic data involves feeding random noise into the generator of the model, which produces new data points that are similar to the real data in the training set as explained in Section 2.2. To generate synthetic data with the trained model, the `sample` method of the SDV library was used.

The `sample` method takes as input the name of the Table is used to generate data for, and the number of rows used want to generate. In this case, the name of the Table was `new_assay` and the number of rows was 4 717. The code in Figure 3.5 was used to generate the data.

The resulting synthetic data variable contained a Pandas data frame with 4 717 rows of synthetic data for the `new_assay` Table. This step was repeated for all the datasets presented in Section 3.2.1 using the different models in Section 2.4.

```
In [13]: n_generated_data = 4717
         new_assay = model.sample(n_generated_data)

         Sampling rows: 100%|██████████| 4717/4717 [00:01<00:00, 3635.72it/s]
```

Figure 3.5: Code used o generating synthetic data

Step 7: Evaluate the quality of the data using a `table_evaluator`. `Table_evaluator` is a library that is commonly used to evaluate the quality of synthetic datasets generated using GANs. The library evaluates how similar the synthesized dataset is to the real data. To use the library, the code in Figure 3.6 was used, and the 'target' column was specified as the target for evaluation. To visualize the results, the following code was utilized `table_evaluator.visual_evaluation()`.

This step was crucial to obtain a visual comparison between the synthetic and original data, as well as to analyse the mean, standard deviation, and principal component analysis of the data. To enhance the figures obtained, Matplotlib® library was employed.

```
from table_evaluator import load_data, TableEvaluator
table_evaluator = TableEvaluator(survey, new_data2)
table_evaluator.evaluate(target_col='target')
```

Figure 3.6: Code used to call up `table_evaluator` function

Step 8: Compute the correlation matrix and calculate the percentage of correlation coefficient. The Pandas® library was employed to calculate the correlation matrix and percentage between the original data and the synthetic data. To obtain the correlation matrix, the code `corr = survey.corr()` was utilized. For calculating the percentage, the code `percentage_corr = r * 100` was used to derive the percentage score representing the correlation between the original data and the synthetic data.

3.4 Implicit modelling methodology

This section of the thesis provides a detailed discussion of the software and methodology used for implicit modelling of the geometallurgical parameters. It outlines the step-by-step process followed during modelling and presents the methodology used for modelling geometallurgical parameters.

3.4.1 Software

Leapfrog® Geo is a popular software used for geological modelling and resource estimation. In this study, Leapfrog® Geo version 5.2.1 was used for implicit modelling and geostatistical modelling of drillhole data. The software was selected because it offers the FastRBF implicit method, as discussed in Section 2.5.1, which is a powerful and efficient method for building geological models from drillhole data.

One of the key advantages of Leapfrog® Geo is that it offers a range of geostatistical methods, including Kriging, which allows for the accurate estimation of values at unsampled locations. The software also enables the inclusion of different estimates and parameters into its block model, which allows for the comparison of multiple estimates in a single block model.

Overall, Leapfrog® Geo is a powerful and versatile software that offers a range of tools for geological modelling and resource estimation. Its user-

friendly interface and geostatistical methods make it a popular choice for researchers and professionals in the field marking it more popular to use than any other software packages.

3.4.2 Loading drillholes dataset

The original drillhole dataset and the historical geometallurgical datasets generated were utilized for implicit modelling. The drillhole data can be seen in Figure 3.8. The first step in utilizing these datasets for implicit modelling involved importing them into Leapfrog® Geo, which was done using the "import drillhole data" menu (refer to Figure 3.7). The data was uploaded in the following files: the collar data under "collar" and the survey data under "survey". The geology, assay, and geometallurgy data were uploaded under the "interval" menu.

Once the files were imported, the next step involved verifying the data. This step is essential to check all the columns and to decide whether all the columns should be uploaded or not. It also enables the user to specify which column represents what, using the Leapfrog® menu. For instance, in the collar data, X and Y denote the coordinates, while in Leapfrog® Geo, the coordinates are represented by East and North.

Therefore, this needs to be specified before proceeding. In this study, X and Y were specified as East and North, respectively, while Z representing elevation and Depth_max in the drillhole data was specified as Elev and Max_depth in Leapfrog®. In the case of survey data, the column names were the same in Leapfrog® and the data uploaded. Dip, Azimuth, and Depth were represented the same in Leapfrog®.

The assay and geometallurgical data contained numerical data that required specification before uploading. Hence, the TCo and geometallurgical parameters were specified as numerical data to enable Leapfrog® to process them. After specifying all these details, the data was uploaded into Leapfrog® Geo.

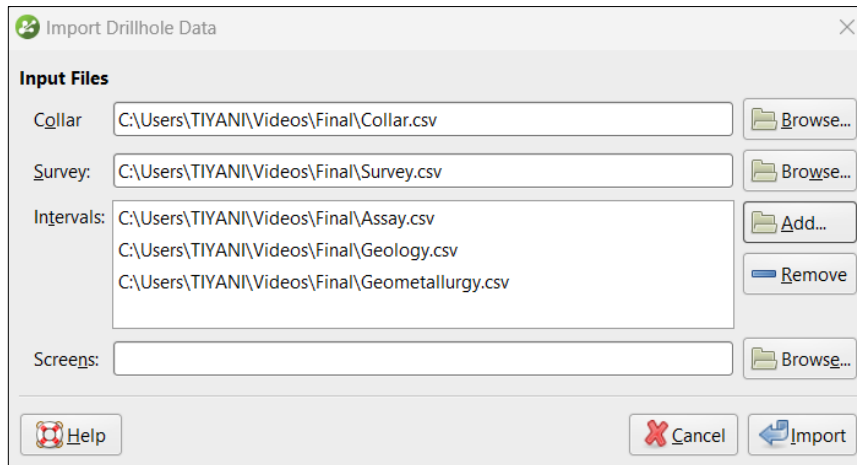


Figure 3.7: Importing drillhole data into Leapfrog® Geo

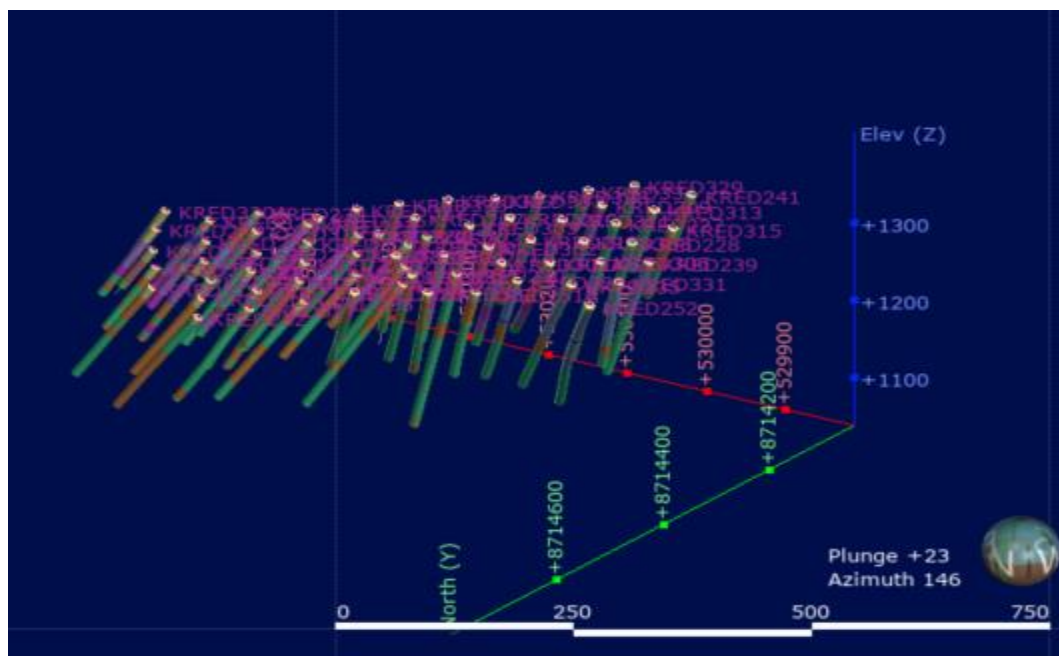


Figure 3.8: Original drillhole data with displayed in Leapfrog® Geo with their collar ID

3.4.3 Validation of the original drillhole dataset

Before beginning orebody modelling/estimation of a resource, it is important to assess the reliability of the exploration data through data validation. While this step may seem small in comparison to the overall project, it has the

potential to uncover database errors that could negatively impact the reporting of resource tonnage, grade, and classification.

Data validation helps identify and remove database errors that could potentially affect the accuracy of resource estimation. Regardless of the experience of the modelling geologist, inaccurate input data will result in inaccurate estimates. This highlights the importance of data validation as a critical stage in resource modelling to ensure the reliability of the resource model produced.

To prevent unpleasant surprises during the geostatistical estimation phase, a database audit was conducted to identify any inconsistencies such as duplicated collar data, and incorrect entries of drillhole depth and assay values.

Upon importing the drillhole data into Leapfrog® Geo software, several errors were identified and flagged on the screen (as shown in Figure 3.9). These errors included collar max-depth exceeded, invalid value handling, missing values, missing intervals, and hole-id not in the collar table. Leapfrog® Geo software provides users with the option to fix errors within the software or to download the data and fix it outside the software.

For this study, the errors were fixed within the software. The collar max-depth exceeded error was resolved by using the "fix max depth input" option in the software, which corrected drillhole data that exceeded the maximum depth. Invalid value handling, missing values, and missing intervals were fixed by omitting them, which ensured that Leapfrog® Geo software would not process this data during modelling. The same approach was applied to the Hole_ID, not in collar table error, which was resolved by omitting it from the data.

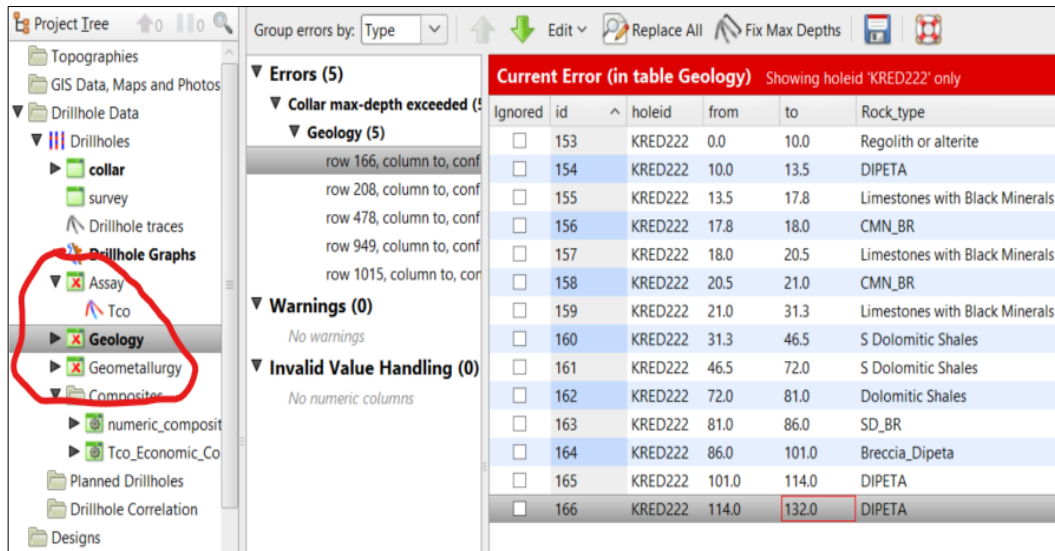


Figure 3.9: Validating drillhole data in Leapfrog® Geo. Errors in the drillhole dataset are highlighted in the red circle

3.3.4 Numerical composite of drillholes dataset

The process of compositing numeric data involves converting unevenly spaced drillhole data into regularly spaced data, which can then be interpolated (Seequent®, 2022). In the current study, compositing was performed on the entire assay drillhole data using a composite length or interval of 2 m, which was close to the original average intervals of the drillholes.

Additionally, the residual length was set to 0, meaning that any drillhole length that was less than zero would be discarded from the dataset. The data between 0 and 2 m in length is typically combined or averaged to create a single data point. This consolidation helps to simplify and condense the information, reducing the overall dataset size and providing a representative value for the composite interval. Figure 3.10 provides a visual representation of the various settings that were applied during the numeric compositing process.

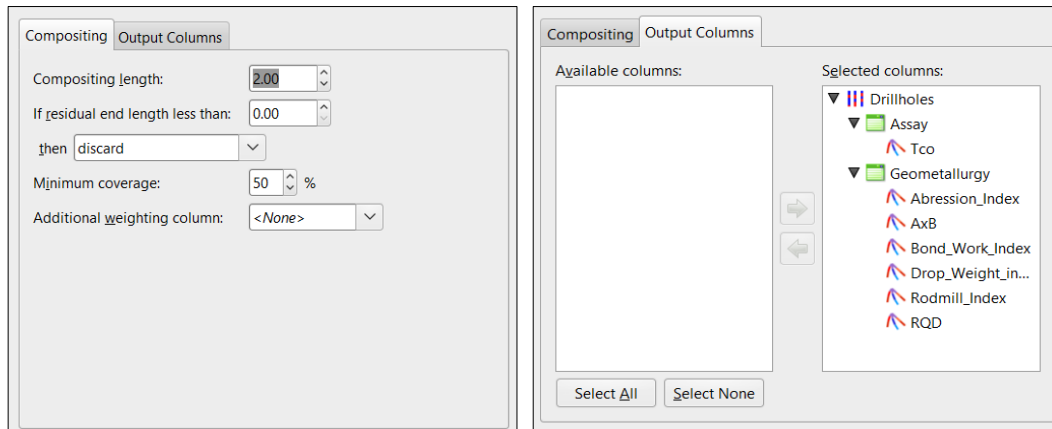


Figure 3.10: Settings used for the numerical composite of drillhole datasets in Leapfrog® Geo

The minimum coverage parameter is used to handle the impact of missing intervals in the drillhole data during processing, and in this study, it was set to 50%. However, since the drillhole data had no missing intervals, this parameter had no effect. This is because the missing intervals were removed during drillhole validation in Section 3.3.3. The additional weighting column can also be used to adjust the influence of each interval or sample on the final estimate based on its perceived reliability or accuracy. However, no additional weighting column was set for this study.

Once the compositing parameters were set, the “Output Columns” tab was selected to choose the numerical data columns. In this case, both the assay and geometallurgical data were selected since they both contained numerical data. Clicking “OK” created a table of the numerical composite of the drillhole data.

3.3.5 Economic composition of the drillhole dataset

Assay data is categorized into “ore” and “waste” by economic compositing, which considers grade thresholds, mining dimensions, and allowable internal dilution, according to Seequent® (2022). As a result, an interval table is produced that includes a column for ore/waste category data and a column for composited interval values.

In addition, the table contains extra columns that indicate the length, linear grade, included dilution length, included dilution grade, and the proportion of the composite that is made up of missing (and subsequently filled) interval data (Appendix B).

Economic compositions were created using the TCo numerical values for the assay data. A cut-off grade of 0.5% was used to delineate the drillholes from ore and waste. This cut-off grade was selected based on the study by Mboyo (2018) who used the same drillhole data for their research. Figure 3.11 shows how settings were entered for the economic composting of the drillhole data.

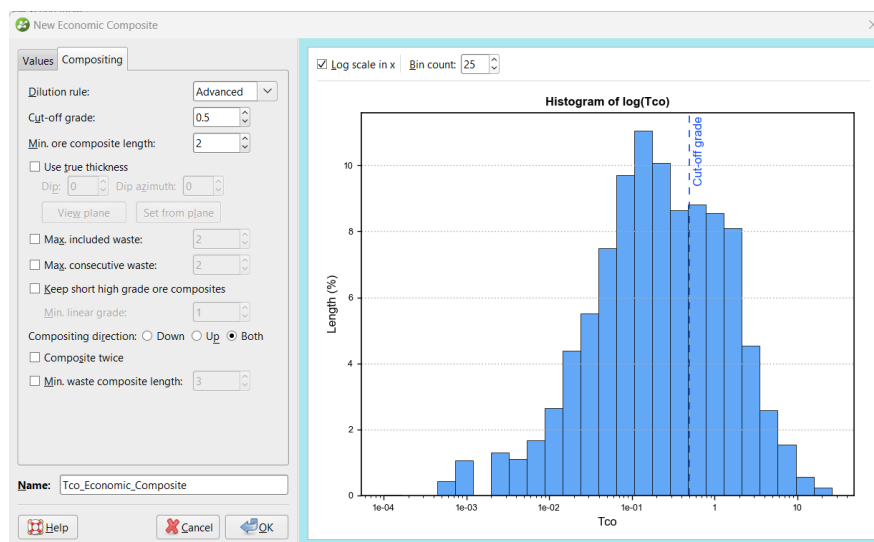


Figure 3.11: Settings used for the economic composition of the drillhole dataset in Leapfrog® Geo

A “Log scale in x” and a “Bin count” of 25 were used to control the distribution of data in the histogram. This resulted in a normal distribution of the data. The x-axis scale can be changed between a linear and logarithmic scale.

The Dilution rule affects how ore composites are created. There are three options: Basic, Advanced, and Advanced+. Basic simply averages the composite and waste-ore section, but it may create longer waste and ore composites. Advanced and Advanced+ are more cautious and create more

precise ore composites, with Advanced+ having an additional rule that checks if adding a waste-ore section will create a segment below the cut-off grade made up of waste-ore-waste.

For this study, the advanced dilution rule was chosen for creating ore composites. The minimum length for an ore composite was set to 2 m, based on the length of the numeric composite used in Section 3.3.4. The compositing direction was set to both down and up, which means that the entire length of the drillhole will be used to create the composites. Other optional settings, such as the true thickness, were left blank as they have minimal impact on the results needed for this study.

3.3.6 Orebody delineating using Indicator RBF

In this study, RBF-based interpolation was used to create a 3D model of the orebody using assay-grade data. To do this, a spheroidal variogram was used to set a geological threshold grade for the interpolation. The spheroidal interpolant function in Leapfrog® was selected to create the grade envelope based on the fixed-range spherical variogram used in geostatistical modelling.

The settings shown in Figure 3.12 for spheroidal models were used to improve the performance of the module. The indicator RBF Interpolant numeric modelling tool was used to create the orebody model in this study. This tool assigns a value of 1 to all data above a certain indicator grade value and a value of 0 to all data below it.

A shell is generated at a defined iso-value between 0 and 1 to avoid issues caused by high-grade data "blow-outs" and unrealistic volume estimates that result from them. Blow-outs can occur when using standard-grade shell modelling with highly skewed data populations.

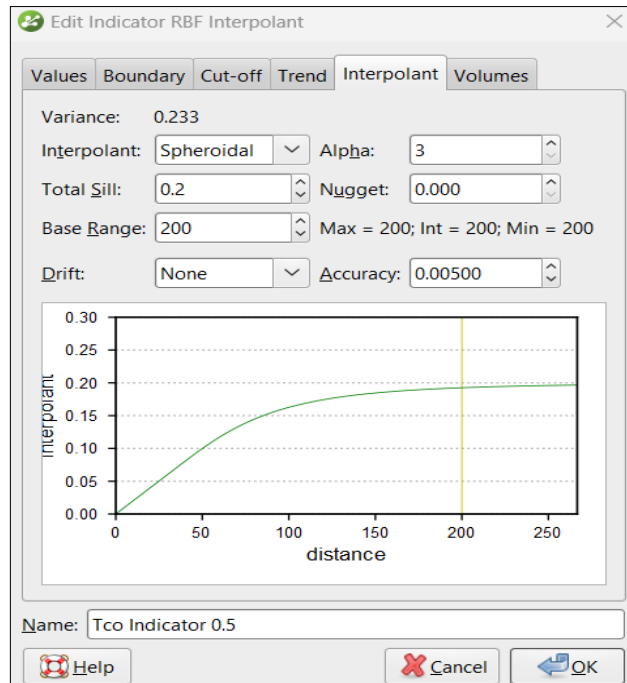


Figure 3.12: Settings for used for indicator RBF in Leapfrog® Geo

In Figure 3.12, the total cobalt grade assay data was used to create an orebody model. The boundary of the interpolation extent was set to be the drillhole data boundary. A cut-off grade of 0.5% was used to determine the ore and waste. The trend line was automatically set based on the orientation of the drillhole data.

The spheroidal interpolant was used, with a total sill of 0.2, a nugget of 0.00, a base range of 200 and an accuracy of 0.00500. The non-drift was used, which means the interpolant pulls down to zero away from the data. The spheroidal interpolant is used for metallic ores when there is a limited range beyond which the data has no significant influence on the model. The values used were set based on the drillhole data.

3.4 Variogram model for implicit and geostatistical modelling

A variogram is a tool used to display the spatial variability of grades within a region, and it plays a crucial role in mineral resource estimation (Seequent®, 2022). It is used to select appropriate sample weighting in

Kriging and RBF estimators and calculate the diagnostic statistics and associated quality of the estimators. The Spatial Models folder in Leapfrog® Geo-domains estimations is used to create and modify variograms.

Using a linear variogram for grade interpolation is not recommended, as it assumes that two samples, regardless of their distance apart, have a direct linear relationship, which is never true in reality. Understanding the relationship between samples is essential for accurate grade interpolation.

Two samples side by side will show some difference due to the nugget effect, and as the distance between samples increases, they lose their relationship, eventually bearing no relationship to each other. When two samples side by side bears no relationship at all, a pure nugget effect occurs, making it difficult to estimate a pure nugget deposit.

While Leapfrog® is known for its ability to rapidly assess a deposit, generating complex variograms is not necessary. A basic understanding of how a variogram should behave for various deposit types will allow for the approximation of the variogram for a specific dataset.

Direction		Variogram Model							
Dip:	0.00	<input type="radio"/> Sill	<input checked="" type="radio"/> Norm. sill	Type	Alpha	Major	Semi-major	Minor	
Dip Azimuth:	0.00	Nugget:	42.8600	0.1781					
Pitch:	90.00	Structure 1:	217.3000	0.9028995	Spheroidal	3	176.4	130.0	45.0
<input type="button" value="Set From Plane"/>		Structure 2:			None				
<input type="button" value="View Ellipsoid"/>		Total sill:	260.16	1.081					
		Variance:	240.657						

Figure 3.13: Settings used for variogram model for RQD data in Leapfrog® Geo

In Leapfrog® Geo domains estimations, variograms are created and modified using the Spatial Models folder. The variogram model is automatically calculated but the user can adjust it to fit the data properly. Figure 3.13 indicate the settings used to create the variogram model in Figure 3.14. The direction in Figure 3.13 referred to the direction of the data with the greatest continuity. This was set from a plane using the same settings as in Section 3.3.3. for the variogram model, a normal sill was used.

The nugget was calculated to be 0.1781 and the total sill to be 1.081. The variance is calculated automatically, and it was found to be 240.657. A spherical variogram was used same as Figure 3.12.

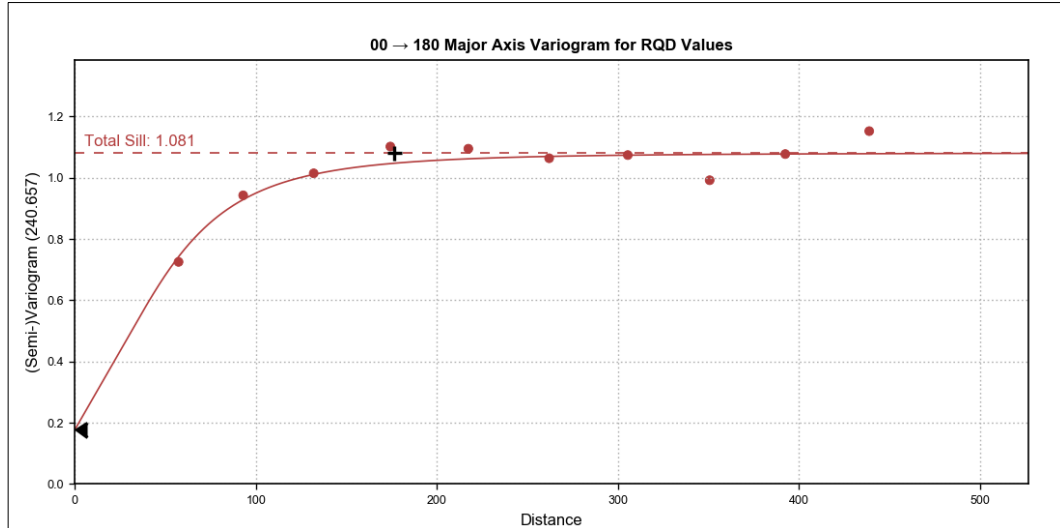


Figure 3.14: Variogram model of RQD data

3.5 Implicit modelling of geometallurgical data

An RBF-based implicit method was used to interpolate the geometallurgical data within the boundary of the orebody. The Leapfrog® Geo methodology discussed in Section 2.5.1 was used in this study. As mentioned in Section 2.5.1, Leapfrog® Geo uses the FastRBF method to implicitly model numerical and orebody models.

There are two ways to implicitly model data in Leapfrog® using the RBF method. The first is to use the estimator folder and the second is to use the numerical model folder. For this study, the estimator folder was used so that it can easily be compared to a geostatistical method which is also located in the estimator folder. The settings in Figure 3.15 were used to prepare the interpolation method. Leapfrog® Geo was used to model geometallurgical data using the implicit method.

In Figure 3.15, the variogram model created in Section 3.4 was used to interpolate geometallurgical data. The fitting parameters were as follows:

the drift explained in the section was specified so that the mean values of the data can be used. The mean of RQD data was 52.50. Leapfrog® Geo estimates the accuracy of the data values by taking a fraction of the smallest difference between measured data values (Seequent®, 2022).

The values were clipped between the lower and upper bound of the data so that the interpolator does not under or overestimate the data. The outputs were automatically generated by Leapfrog® Geo, which generates the iso-surfaces of the RQD after interpolating the data.

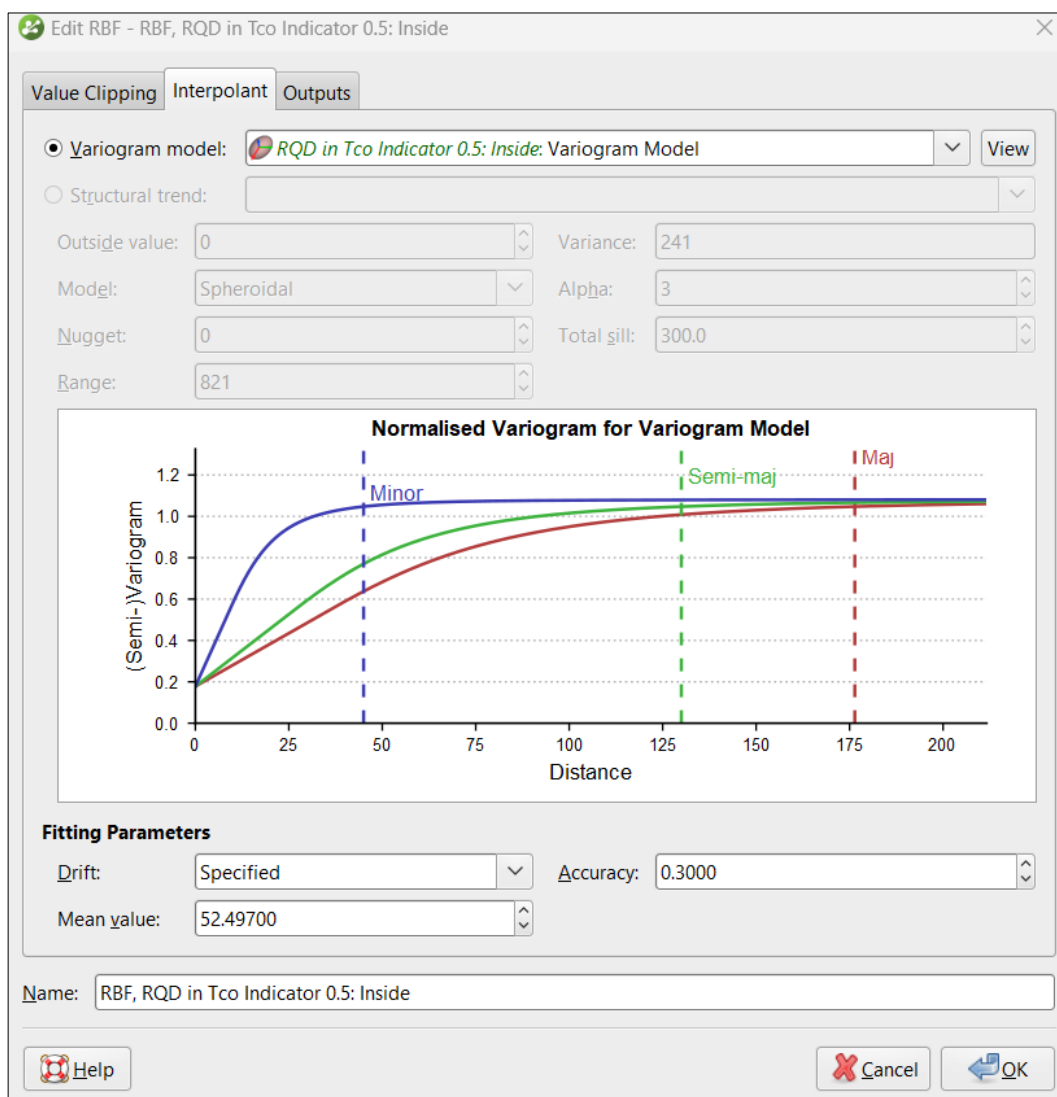


Figure 3.15: Settings used for implicit model geometallurgical data for RQD data

3.6 Geostatistical modelling of geometallurgical data

A geostatistical method was also used to model geometallurgical data. The reason for doing so was to compare the results of the geostatistical method with the implicit method. To evaluate which method performs better, the study selected the Ordinal Kriging (OK) geostatistical method discussed in Section 2.3. This is because OK is one of the most used geostatistical estimators in modelling (Abzalov, 2006).

3.6.1 Ordinary kriging of geometallurgical dataset

Kriging is a widely recognized and accepted technique used to estimate values for points that have not been directly measured or observed, by using measured data from neighbouring points. In other words, it is a method of interpolation that provides estimates for locations where data is missing or incomplete. Kriging relies on statistical models to analyse the spatial relationships between measured data points and the point being estimated, in order to generate a prediction with the lowest possible error.

Leapfrog® Geo was used for Kriging interpolation with relevant settings shown in Figure 3.16. The same variogram model created in Section 3.4 and used in Section 3.5 was also used in this section. For the Kriging option, Ordinary Kriging was used and does not require the mean values of the data. All values that were less than zero were set to be zero. Discretisation was automatically set by Leapfrog® to be X-5, Y-5, and Z-2.

Discretisation sets the number of discretisation points in the X, Y and Z directions for block Kriging (Seequent®, 2022). Block Kriging provides a means of estimating the best value for a block instead of only at the centre of the block. Just like in implicit modelling (Section 3.3), the values were clipped between the min and max boundaries. The ellipsoid was also the same as the implicit model. The outputs were set to be the values and statuses that will be generated after interpolating.

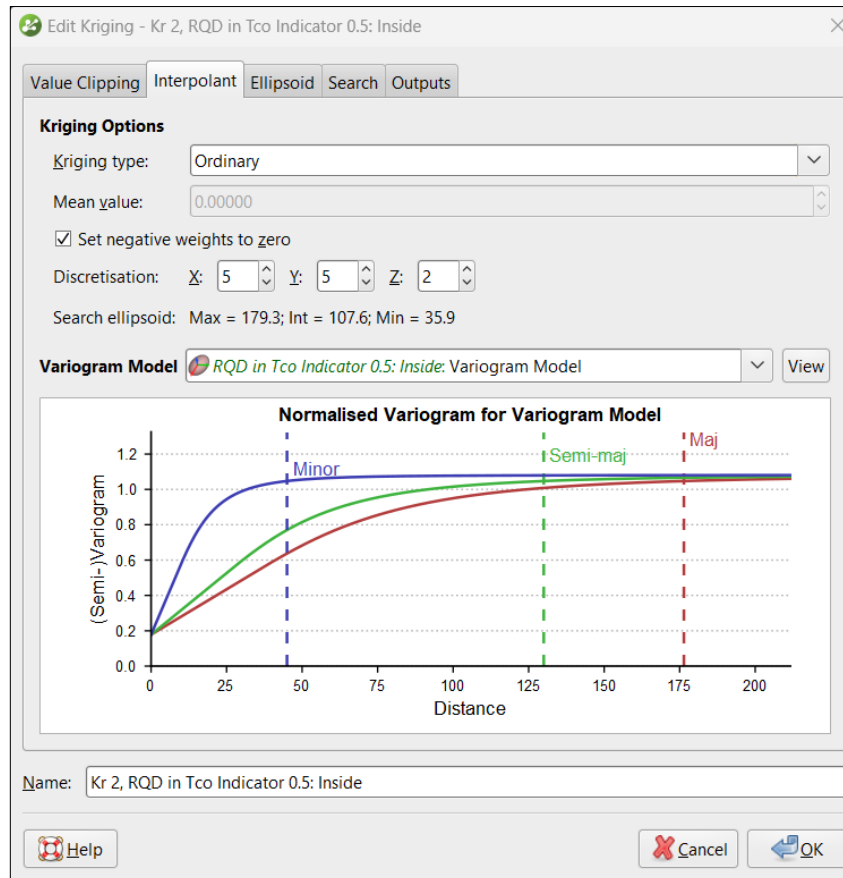


Figure 3.16: Setting used for kriging interpolation of geometallurgical dataset

3.7 Block modelling of geometallurgical data

A block size of 10 m (X) × 10 m (Y) × 10 m (Z) was used. This block size was used taking into consideration the processing time of the model and the size of the data. For larger data, it is advisable to use a larger block size to reduce processing time, as smaller block sizes can increase processing time. Figures 3.17 and 3.18 show the parameters of the setting required when creating a block model. Extents refer to the extent to which the block model should cover. This was set to enclose the orebody created in Section 3.3.6. The process depicted in Figures 3.17 and 3.18 refer to the method used to analyse and model the data into a block model. The evaluation method used in Sections 3.5 and 3.6 were selected (Figure 3.18). Thus, the

radial basis function and Ordinary Kriging were used as evaluating methods. After setting the parameter, “OK” was clicked and the block model was created.

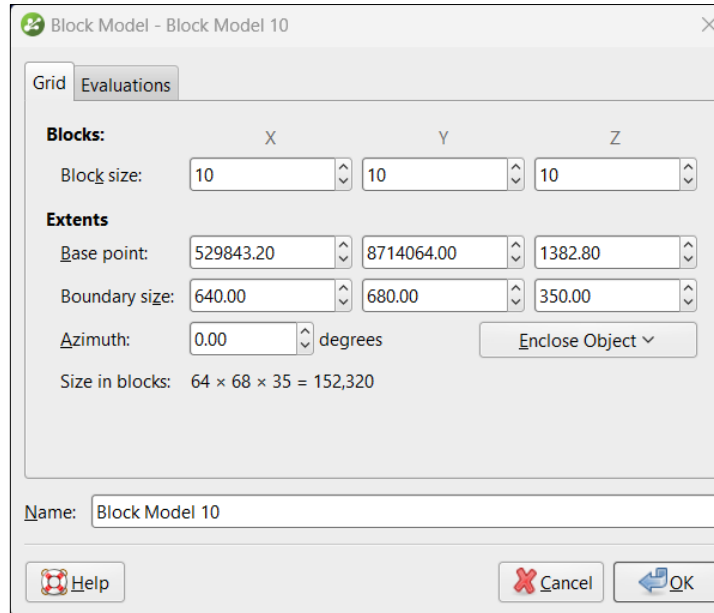


Figure 3.17: Settings used in Leapfrog® Geo for block modelling geometallurgical data

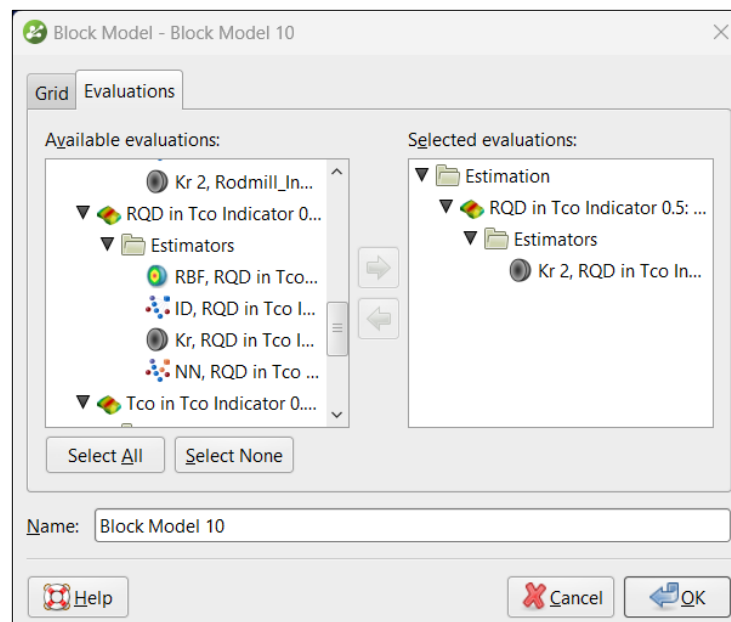


Figure 3.18: Evaluations selections for block modelling geometallurgical data in Leapfrog® Geo

3.8 Challenges encountered

This section addresses the challenges faced throughout the thesis journey, specifically focusing on the difficulties encountered during data collection, data analysis, and the thesis write-up.

The initial challenge happened during the process of data generation using the CTGAN model. When attempting to generate a large bulk of synthetic data through the CTGAN approach, a notable issue surfaced regarding the model's slow performance. Substantial efforts were made to optimize the CTGAN model specifically, focusing on enhancing its speed.

The second challenge encountered was when using `table_evaluator` to evaluate the quality of the synthetic data generated. The `table_evaluator` is a tool used to compare the statistics of the synthetic data with the original data. However, when the `table_evaluator` encounters columns with multiple values, it becomes difficult to evaluate the quality of the data.

To overcome this, a target column was added with only two distinct values. This target column was used to evaluate the quality of the synthetic data by comparing the statistics of the original and synthetic data for each value in the target column. This allowed for a more accurate evaluation of the synthetic data quality.

The last issue was that the geometallurgical data could not be measured directly due to budget constraints. Instead, historical data and synthetic data generated through a data generator were used, as obtaining this data requires expensive equipment that was not feasible within the allocated budget for the study.

Chapter 4 Results of synthetic data generation

The synthetic data generated in Section 3.2 is appraised in this chapter. The aim is to evaluate the quality of the generated synthetic geometallurgical data using GAN models. The study utilized three types of GAN-based models: namely, CTGAN, CopulaGAN, and Gaussian Copula.

To evaluate the quality of the generated synthetic data, the Python®-based `table_evaluator` module was used. The module uses various evaluating matrices to check the quality of the synthetic data against the original data. These evaluating matrices included the similarity score, absolute mean and standard deviation comparison, visual evaluation, and principal component analysis (PCA).

The similarity score measured how close the synthetic dataset was to the real dataset, while PCA was a statistical method used to reduce dimensionality without losing information. The visual evaluation employed various tools such as column-wise mean and standard deviation, cumulative sums, and column correlations to assess the generated data. The comprehensive report presented in Chapter 4 highlighted the benefits and drawbacks of each synthetic data generation technique used in the study.

The findings and analysis presented in this chapter are important for researchers and practitioners who utilize synthetic data generation techniques for various applications, especially in cases where data privacy and scarcity are issues. The results obtained based on the similarity score, visual evaluation and PCA, are presented and discussed in detail below.

4.1 Comparison of similarity scores of synthetic data generated by CTGAN, CopulaGAN, and Gaussian Copula

Figures 4.1 to 4.4 depict the similarity scores for synthetic data generated for collar, assay, geometallurgy, and survey data. The data was generated

using CTGAN, CopulaGAN and Gaussian Copula models. These Figures were plotted using Matplotlib® in Python® environment. The data itself was generated using a program called `table_evaluator` (as discussed in Section 3.2.3) in Python®.

The results of the synthetic collar data show that all three models generated synthetic data with a good degree of similarity to the real data (Figure 4.1). The CTGAN, CopulaGAN and Gaussian Copula models achieved perfect score for basic statistics, which is 1.00 respectively. For correlation column, CTGAN and CopulaGAN models achieved a low score of 0.31 and 0.45 respectively. This suggests that the two models had a hard time capturing the column correlations more accurately.

Compared to these two models, GaussianCopula had the highest score of 0.51, indicating that it captured the column correlations more accurately than the other two models. For the mean correlation between fake and real columns, all models achieved a correlation above 0.90.

For similarity score the GaussianCopula model achieved the highest similarity score of 0.76, indicating its superior performance in generating synthetic data that closely resembled the real data. In comparison, CTGAN and CopulaGAN achieved similarity scores of 0.71 respectively.

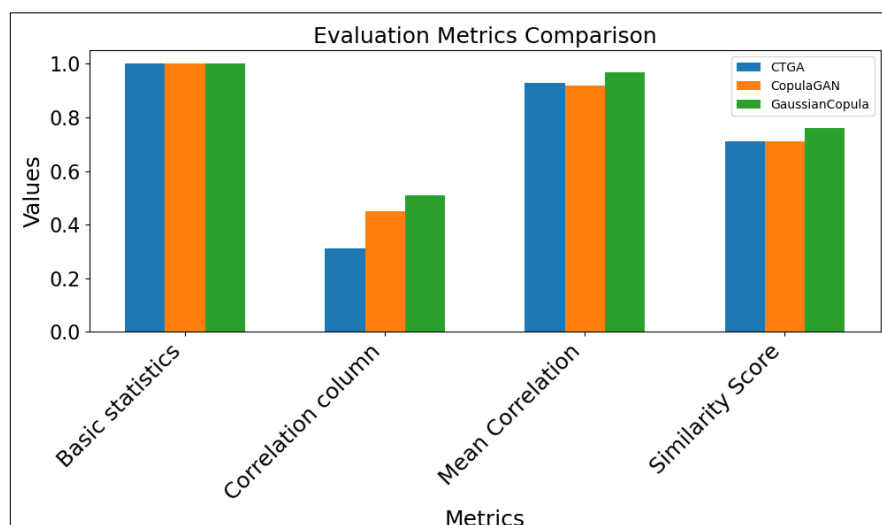


Figure 4.1: The similarity score of synthetic collar data compared among CTGAN, CopulaGAN and Gaussian Copula

The evaluation of synthetic data for the assay dataset indicates that CTGA, CopulaGAN, and GaussianCopula models performed well in generating data similar to the real data (Figure 4.2). For basic statistics, all models achieved a perfect score of 1.00, demonstrating their ability to capture essential data characteristics accurately.

Regarding correlation column correlations, the models exhibited strong performance. CTGA achieved a correlation of 0.92, CopulaGAN achieved 0.93, and GaussianCopula achieved the highest correlation of 0.98. This indicates that GaussianCopula excels in preserving the column-to-column relationships of the original data.

For mean correlation, CTGA achieved a score of 0.89, CopulaGAN achieved 0.92, and GaussianCopula achieved 0.96. These results demonstrate that all models effectively captured the overall correlation patterns in the synthetic data.

CTGA and CopulaGAN achieved a similarity score of 0.92 and 0.94 respectively. GaussianCopula achieved the highest score among the 3 models, which was 0.97. This indicates that all models produced synthetic data that closely resembled the real data. However, GaussianCopula achieved the highest similarity score.

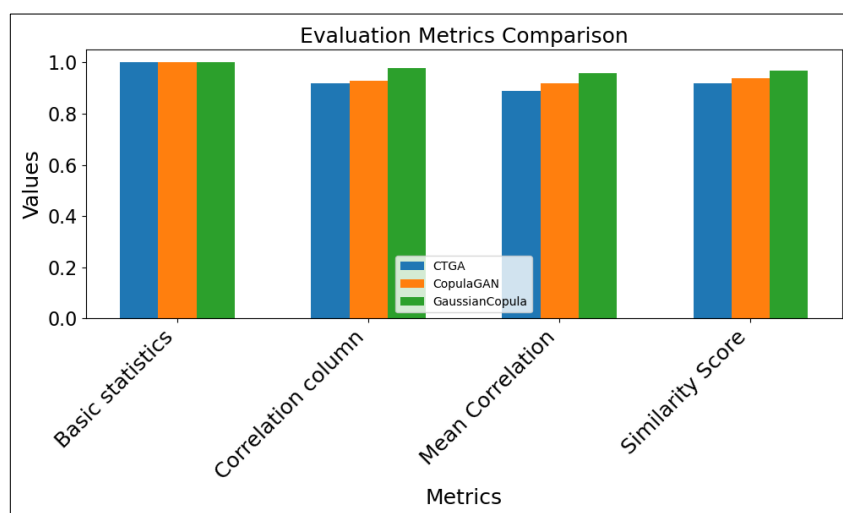


Figure 4.2: The similarity score of synthetic assay data compared among CTGAN, CopulaGAN and Gaussian Copula

The CTGA, CopulaGAN, and GaussianCopula models were evaluated on their ability to generate synthetic geometallurgical (Figure 4.3). In terms of basic statistics, all models achieved high scores: CTGA scored 0.99, CopulaGAN 0.98, and GaussianCopula scored 0.99.

When examining the correlation column relationships, all models performed well. CTGA and CopulaGAN achieved a correlation of 0.81 and 0.86 respectively. GaussianCopula reached the highest correlation of 0.91, showcasing its strength in preserving the column-to-column relationships of the original data.

In the context of the mean correlation between fake and real columns, all models displayed good performance. CTGA and CopulaGAN scored 0.89 and 0.93 respectively while GaussianCopula obtained the highest score of 0.98, highlighting their capability to effectively capture overall correlation patterns in the synthetic data.

Regarding similarity scores, CTGA and CopulaGAN achieved scores of 0.84 and 0.82 respectively. GaussianCopula obtained an impressive score of 0.94. These similarity scores indicate that all models generated synthetic geometallurgical data closely resembling the real data. Notably, GaussianCopula outperformed the other models, indicating its superiority in generating synthetic data that closely aligns with the real data.

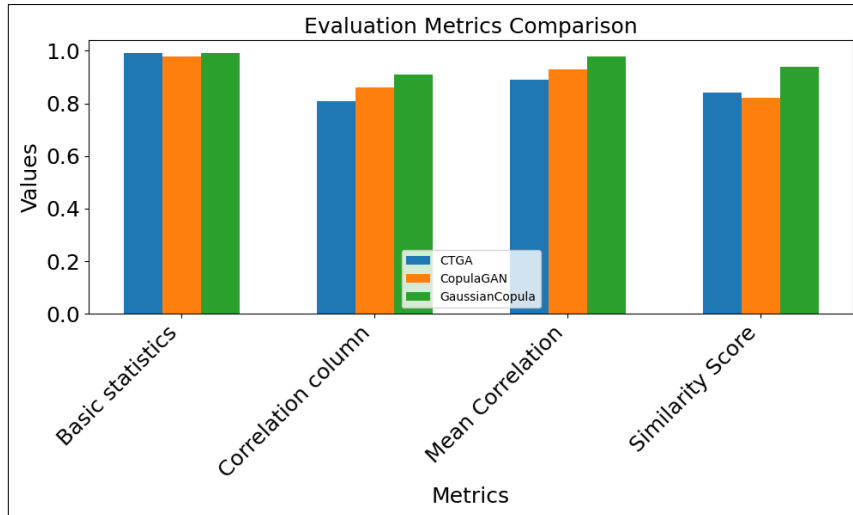


Figure 4.3: The similarity score of synthetic geometallurgical data compared among CTGAN, CopulaGAN and Gaussian Copula

For synthetic survey data (Figure 4.4), all three models achieved a perfect score of 1.00 for basic statistics. This indicates their excellent performance in capturing essential data characteristics. For correlation column CTGA demonstrated a correlation score of 0.07, CopulaGAN scored 0.24, while GaussianCopula obtained the highest score of 0.81.

The low score of CTGAN and CopulaGAN indicate that the two models struggled to preserve the relationships between columns in the original data. CTGA achieved a mean correlation score of 0.96, CopulaGAN scored 0.94, and GaussianCopula obtained the highest score of 0.97. This highlights their capability to effectively capture the overall correlation patterns between fake and real columns in the synthetic data.

Gaussian Copula models generated synthetic data with a high degree of similarity to the real data, with a similarity score of 0.91, respectively. The CTGAN and CopulaGAN model produced a similarity score of 0.64 and 0.72, respectively. These scores indicate how closely the generated synthetic data of each model resembled the real data, with GaussianCopula showing the highest similarity.

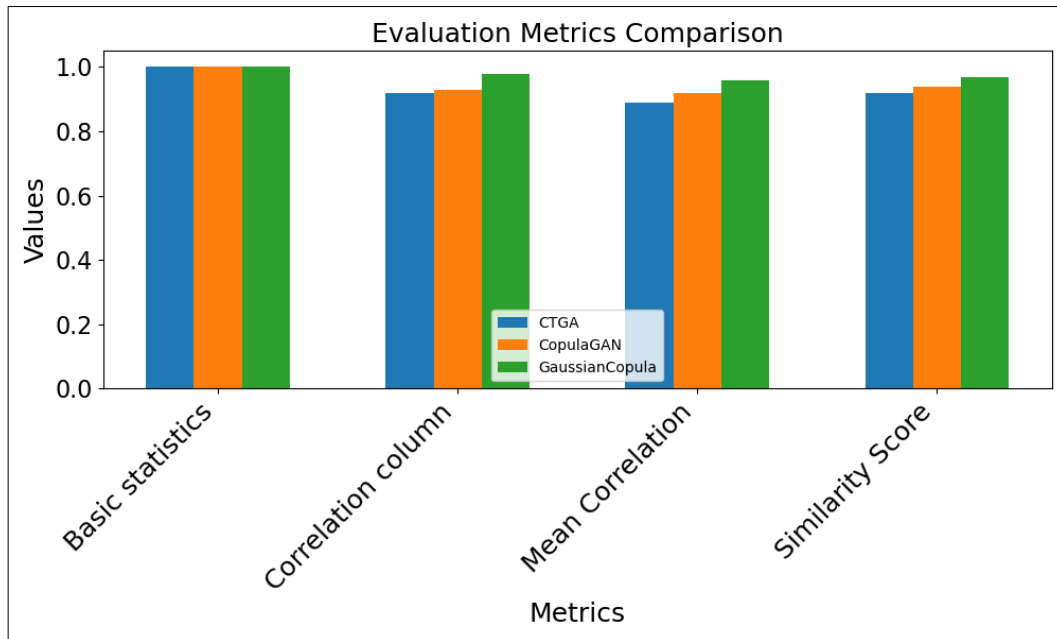


Figure 4.4: The similarity score of synthetic survey data compared among CTGAN, CopulaGAN and Gaussian Copula

4.2 Mean and standard deviation of original and synthetic data

Figures 4.5 to 4.8 display a comparison of the mean and standard deviation for original and synthetic datasets generated by CTGAN, CopulaGAN, and Gaussian Copula. The red circle drawn in Microsoft® Paint® represent the mean and standard deviation not captured by the models. The evaluation was performed on collar, assay, geometallurgical, and survey data, with the results, plotted on the log-transformed values of all numeric columns.

Computing the mean and standard deviation of the numeric columns in the synthetic data can help assess how well the synthetic data matches the statistical properties of the original data. If the mean and standard deviation of the synthetic data is close to those of the original data, it suggests that the synthetic data is a good representation of the original data. The assumption is that failure to capture these basic statistical properties could result in the inability to capture more complex features (Brenninkmeijer,

2019). The Figures were generated using the `table_evaluator` program in Python® and then edited using Microsoft® Paint®.

Based on the findings presented in Figure 4.5 for synthetic collar data, the models CTGAN and Gaussian Copula achieved a close match to almost all the log mean values of the original data, with the exception of one mean value, specifically the target. As for CopulaGAN, it managed to match 4 out of 6 of the means, with the mean of Depth_max (m) coming closer to the original data (Figure 4.5b). However, CopulaGAN failed to accurately match the Depth_max (m) mean, though it was relatively close.

In terms of log standard deviations, all models, except for CopulaGAN, successfully matched the properties of the original data. CopulaGAN showed a slight deviation in replicating the Depth_max (m) standard deviation (Figure 4.5b).

Overall, Gaussian Copula demonstrated the best performance among all the models, as it better matched both the mean and standard deviation properties of the original data.

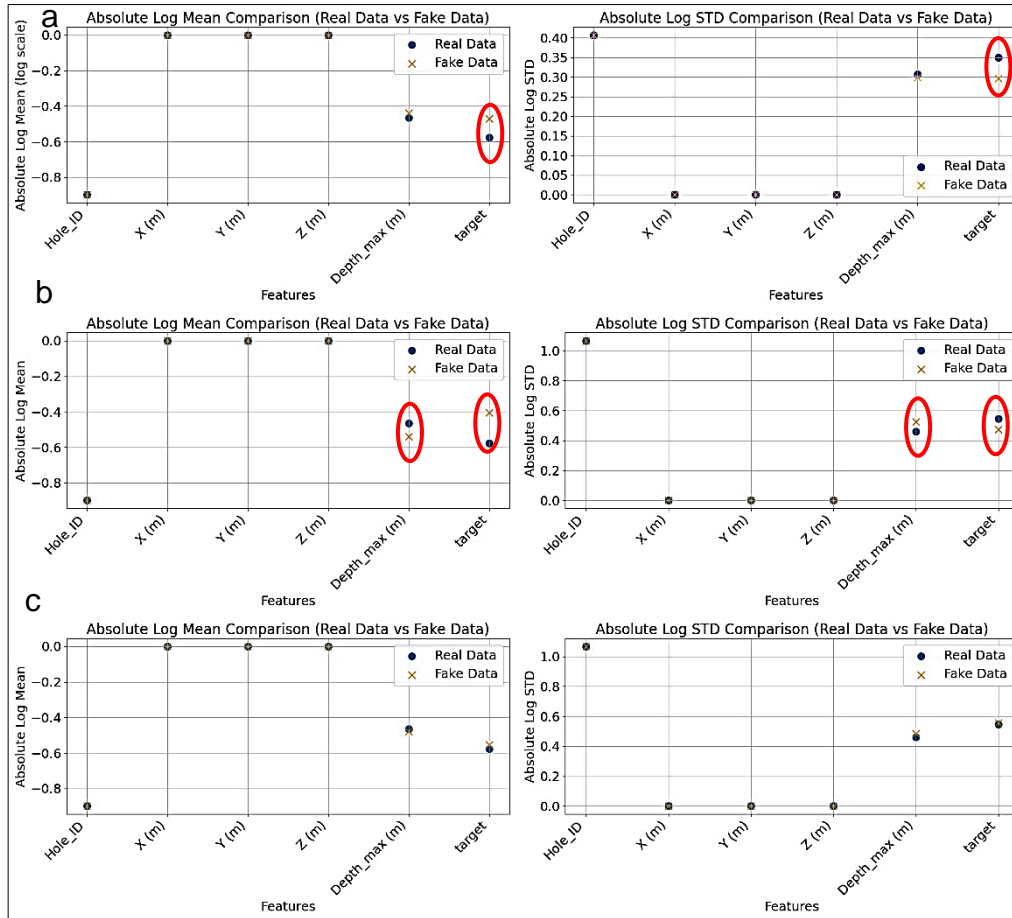


Figure 4.5: Mean and standard deviation of real and fake collar data: a) CTGAN; b) CopulaGAN; and c) Gaussian Copula

Based on the comparison of the synthetic assay data using the three models, as illustrated in Figure 4.6, it is evident that Gaussian Copula and CopulaGAN outperformed CTGAN in matching the log mean of the original data. Specifically, CTGAN only managed to match one out of the five means, indicating poor performance in this aspect. On the other hand, Gaussian Copula and CopulaGAN demonstrated better accuracy in reproducing the log mean values.

Regarding the standard deviation, all three models fell short in matching one of the five standard deviations of the original data. CTGAN and Gaussian Copula were unable to match the target, while CopulaGAN failed to match the Hole_ID. These discrepancies are depicted with red circles in Figure

4.6, highlighting the areas where the models struggled to replicate the log mean and standard deviation accurately.

In summary, Gaussian Copula and CopulaGAN showed superior performance in matching the log mean values of the original data, while all three models faced challenges in reproducing the standard deviations precisely. The visual representations in Figure 4.6 provide clear insights into the areas of success and limitations for each model in their synthetic assay data generation.



Figure 4.6: Mean and standard deviation of real and fake for assay data:
a) CTGAN; b) CopulaGAN; and c) GaussianCopula

In Figure 4.7, the comparison of geometallurgical data using the three models revealed their performance in matching the log mean and log standard deviation values of the original data.

CTGAN struggled to match five out of the ten log mean and log standard deviation values, indicating limitations in accurately capturing the central tendencies and variability of the original data.

CopulaGAN showed relatively better performance, failing to match only three out of the ten mean and two out of ten for standard deviation values. This suggests that CopulaGAN achieved a higher level of fidelity in representing the characteristics of the original data compared to CTGAN.

Same goes for Gaussian Copula method that demonstrated remarkable proficiency by accurately capturing seven out of the ten mean and standard deviations of the original data. However, for log standard deviation it didn't perform better than CopulaGAN as it only failed to match three of the ten log standard deviations.

This superior ability to represent the variability of the original data establishes Gaussian Copula as the most effective model in generating synthetic geometallurgical data that closely resembles the statistical properties of the real data.

The insights from Figure 4.7 indicate that Gaussian Copula stands out as the preferred choice for generating synthetic geometallurgical data due to its ability to preserve essential data characteristics, making it a valuable tool for simulations and analyses in the field of geometallurgy.

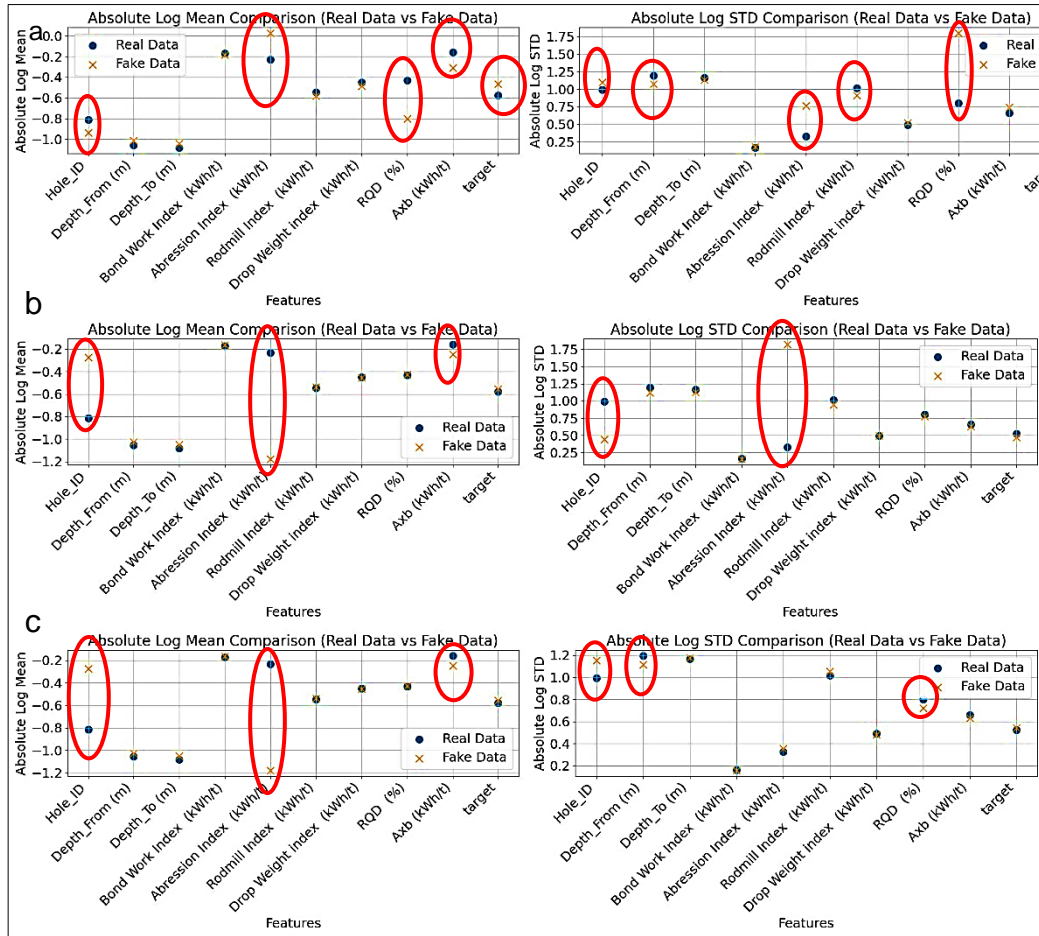


Figure 4.7: Mean and standard deviation of real and fake geometallurgical data: a) CTGAN; b) CopulaGAN; and c) Gaussian Copula

In Figure 4.8, the evaluation of the models on synthetic survey data showed consistent performance across all three models.

For CTGAN and Gaussian Copula, the log mean matching was generally successful, with only the Hole_ID log mean failing to be matched accurately. On the other hand, CopulaGAN performed slightly better, as it managed to match three out of the five log means, with two log means not being accurately captured.

Regarding the log standard deviation, both CTGAN and CopulaGAN closely matched the mean of the original data, indicating good performance in preserving the variability of the synthetic survey data. However, Gaussian Copula, while generally successful in matching log standard deviations,

failed to match one log standard deviation, specifically for the Hole_ID variable.

Overall, the models performed similarly across log mean matching, with CopulaGAN showing a slight advantage. However, Gaussian Copula demonstrated effective preservation of log standard deviations, with only one deviation not being accurately captured. The consistent performance of the models suggests that they can be relied upon for generating synthetic survey data with satisfactory statistical properties, providing valuable insights for survey-related analyses and simulations.

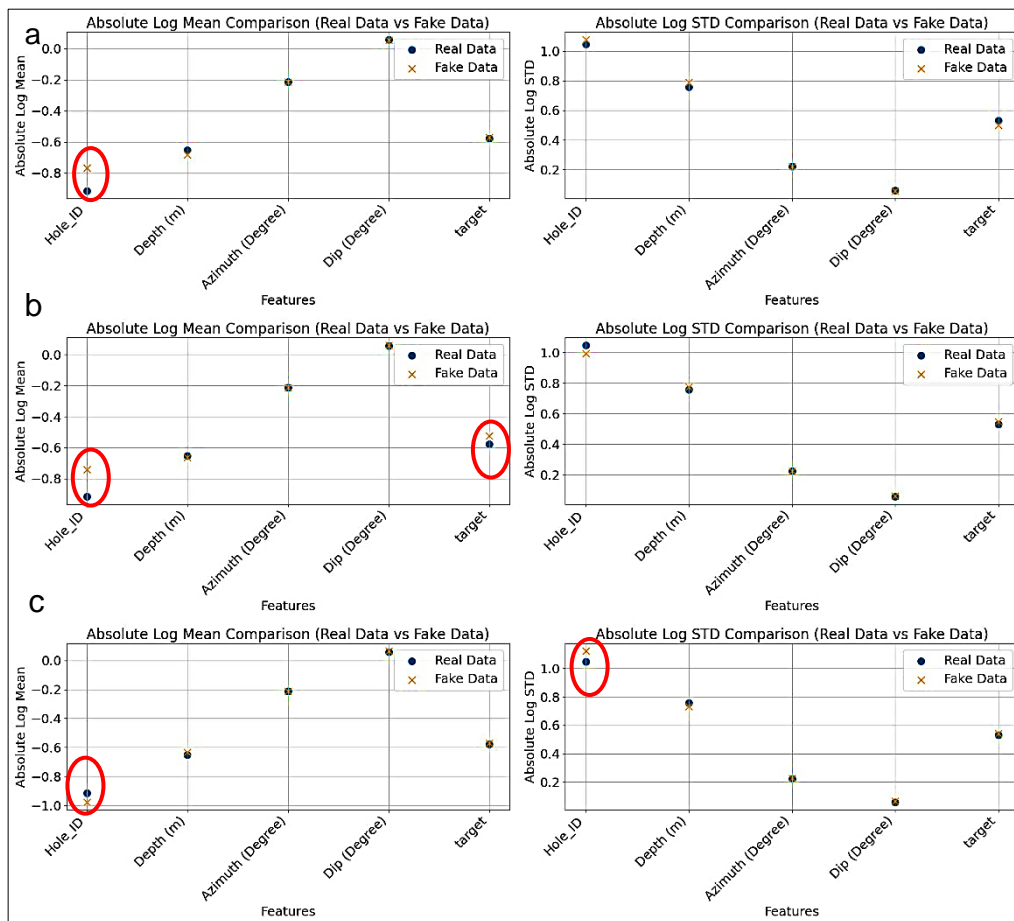


Figure 4.8: Mean and standard deviation of real and fake survey data: a) CTGAN; b) CopulaGAN; and c) Gaussian Copula

4.3 Comparative visualization of synthetic and original data

The comparison between synthetic and original data was evaluated through visualizations generated using the `table_evaluator` program in Python®. Figures 4.9 to 4.20 show the results of the analysis, where blue represents the original data and yellow represents the synthetic data.

To identify the areas of overlap between real and fake data, a red circle was added manually using Microsoft® Paint®. The graphs in Figures 4.9 – 4.20 depict the cumulative sums per feature, where features are represented by the data columns headings such as `Hole_ID` and `Depth_max`.

The comparison of synthetic collar data generated using CTGAN, CopulaGAN, and Gaussian Copula models (Figures 4.9 – 4.11) reveals that there is some overlapping between the real and synthetic data. In most cases, the features in the synthetic data closely resemble the actual data. However, the distribution per feature and difference plots of the models highlights instances where the generator struggles to replicate the actual data.

All three models successfully match the original data for the "`Hole_ID`," achieving a near-perfect match. CTGAN (Figure 4.9) encounters challenges in matching the original data for "`X (m)`," "`Y (m)`," and "`Z (m)`," resulting in noticeable differences. Despite these difficulties, CTGAN manages to match "`Depth_max (m)`" and the "target" feature quite well, with only minor differences.

CopulaGAN (Figure 4.10) faces difficulties in matching "`X (m)`," "`Y (m)`," "`Depth_max (m)`," and the "target" feature, showing noticeable discrepancies. However, it performs well in matching "`Z (m)`."

Gaussian Copula (Figure 4.11) struggles only with matching the "target" feature, while all other features match quite well, exhibiting only minor differences.

Overall, the similarity between the original and generated data is relatively high. Though the synthetic data does not precisely match the real data, its

quality is still considered good, as the generated data falls within the range of the actual data. This indicates that the models have been reasonably successful in replicating the key characteristics of the real data.

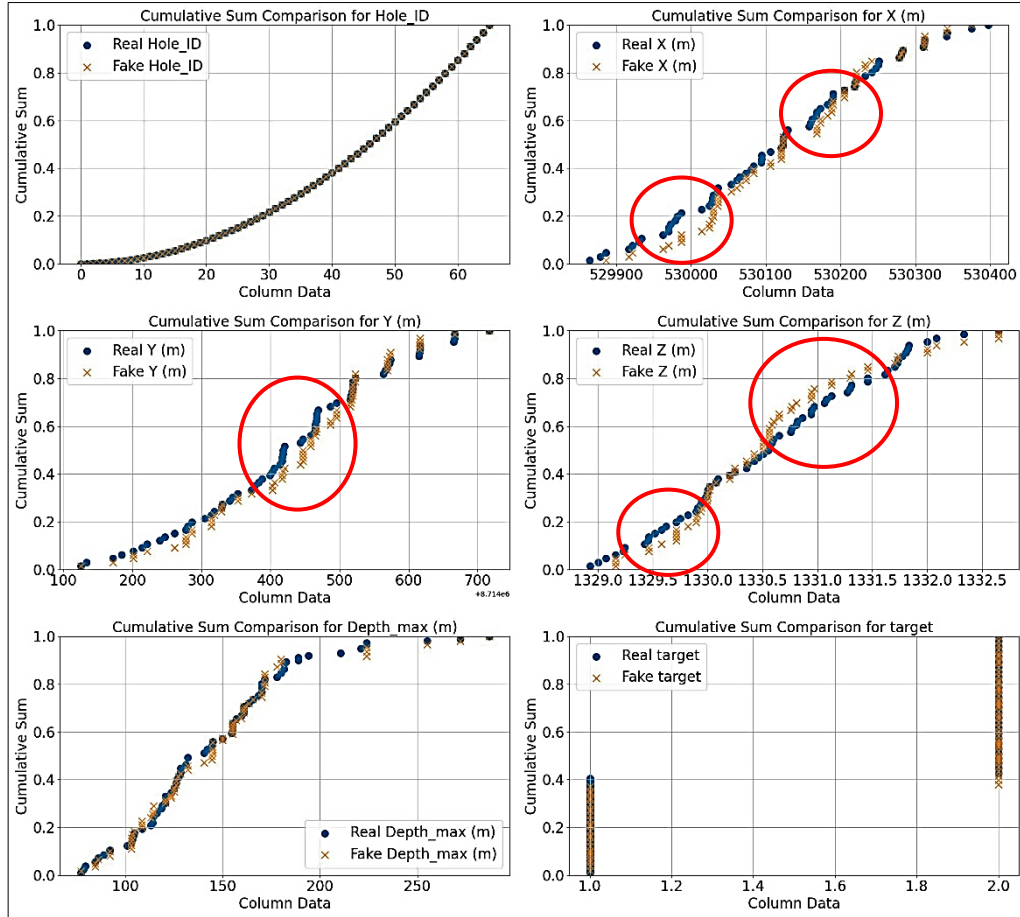


Figure 4.9: Visual comparison of original and fake data for collar data generated by CTGAN

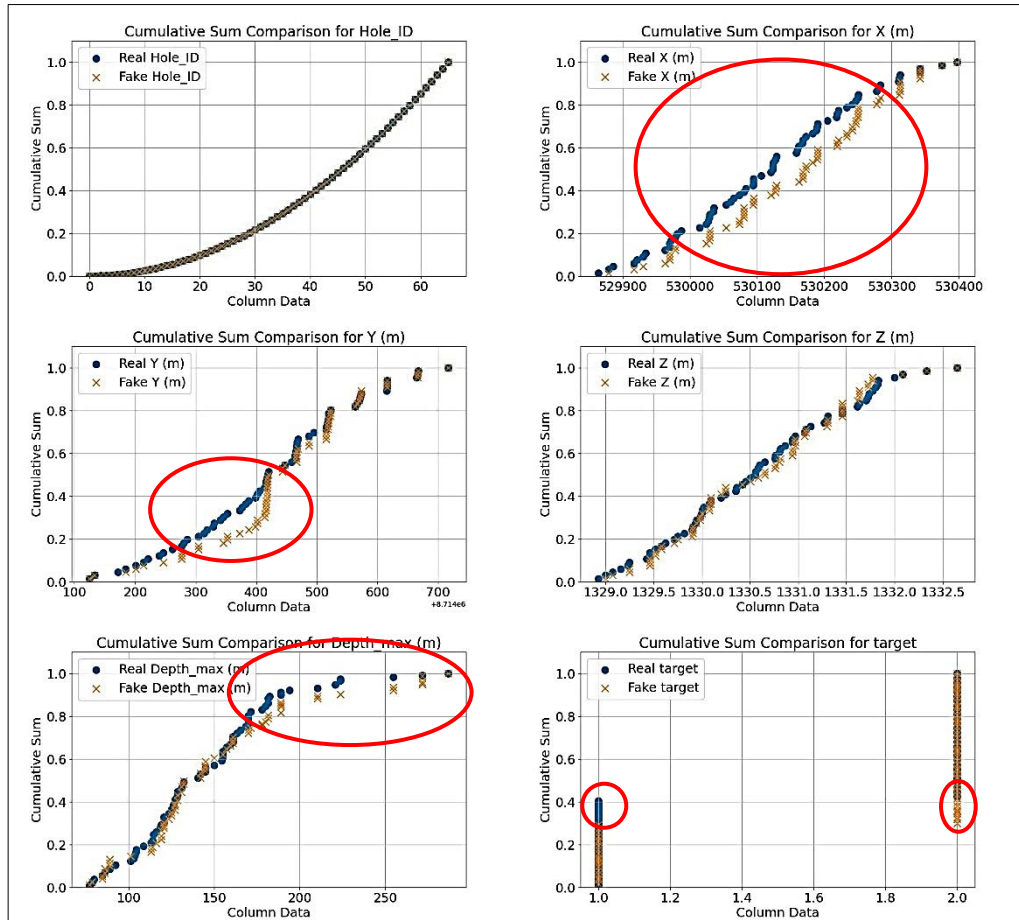


Figure 4.10: Visual comparison of original and fake data for collar data generated by CopulaGAN

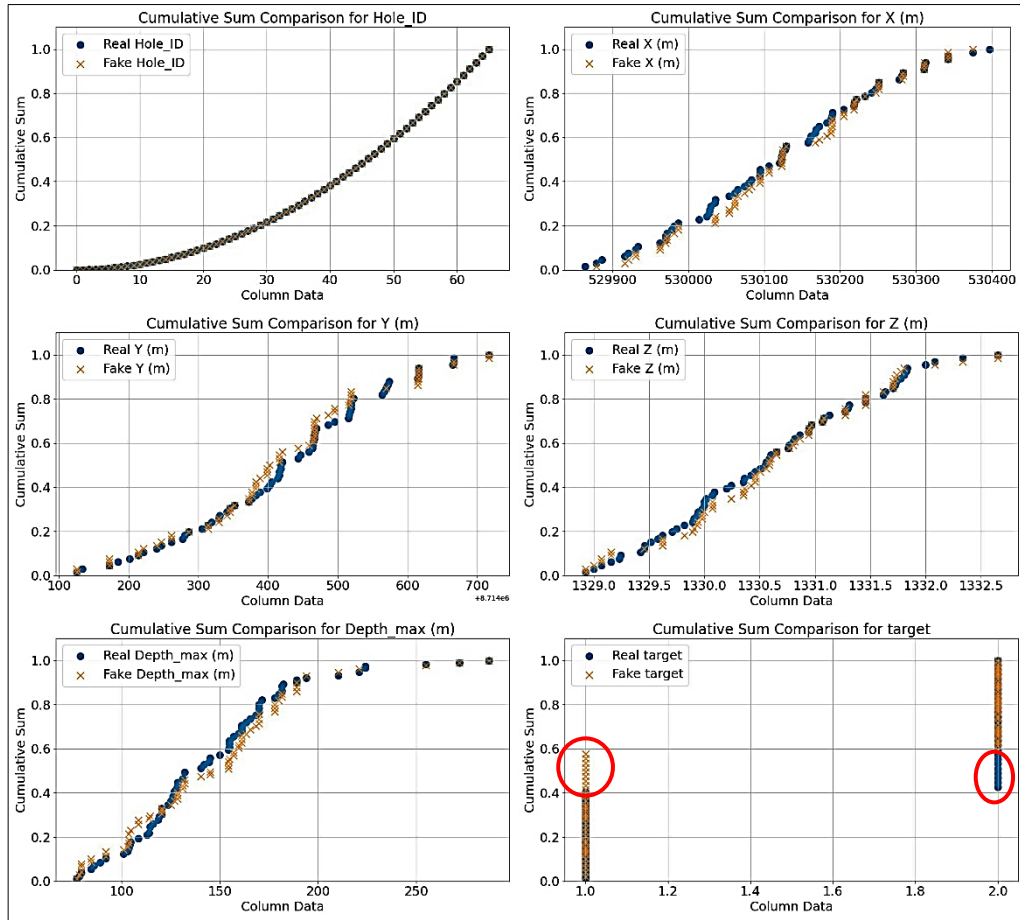


Figure 4.11: Visual comparison of original and fake data for collar data generated by Gaussian Copula

The visual comparison of synthetic assay data using CTGAN, CopulaGAN, and Gaussian Copula models (Figures 4.12 – 4.14) revealed that the generator faced challenges in accurately replicating the original data for the "Hole_ID" feature. The difficulty arose because the original "Hole_ID" values in the assay data were not unique. Consequently, the generated data for this particular feature did not match the original data closely.

However, the models demonstrated success in generating data that closely resembled the original data for the other features. There were only minor differences observed in the generated data for these features, indicating that the models were able to capture the essence of the data distribution quite well.

Both CTGAN (Figure 4.12) and CopulaGAN (Figure 4.13) encountered some minor difficulties in replicating the "target" feature of the data. While the generated data for this feature was close to the original, there were some discrepancies.

In contrast, Gaussian Copula performed comparatively better than the other models. It exhibited fewer minor differences from the original data, as depicted in Figure 4.14.

Overall, all the models performed well in generating synthetic assay data. The minor differences observed between the generated and original data were not significant and could be considered acceptable. Despite the challenges with the "Hole_ID" feature and some minor discrepancies with the "target" feature, the models were successful in generating synthetic data that closely approximated the original data distribution.

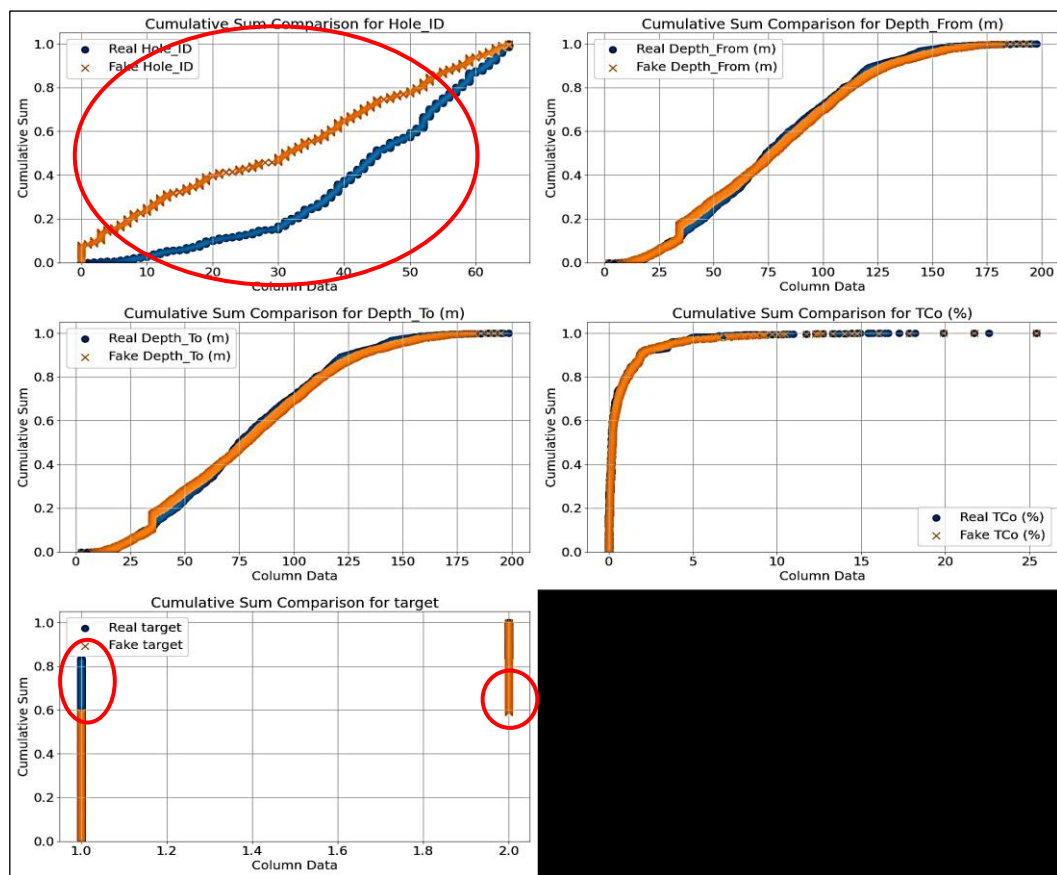


Figure 4.12: Visual comparison of original and fake data for assay data generated by CTGAN

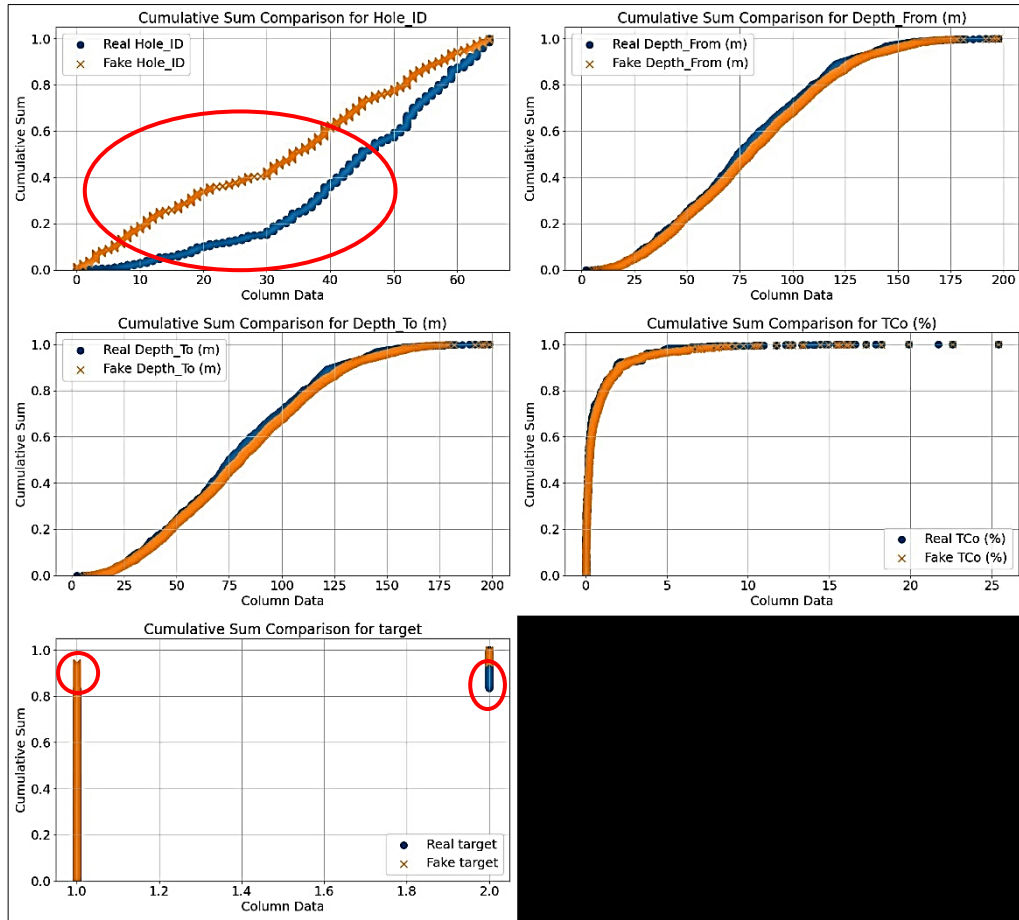


Figure 4.13: Visual comparison of original and fake data for assay data generated by CopulaGAN

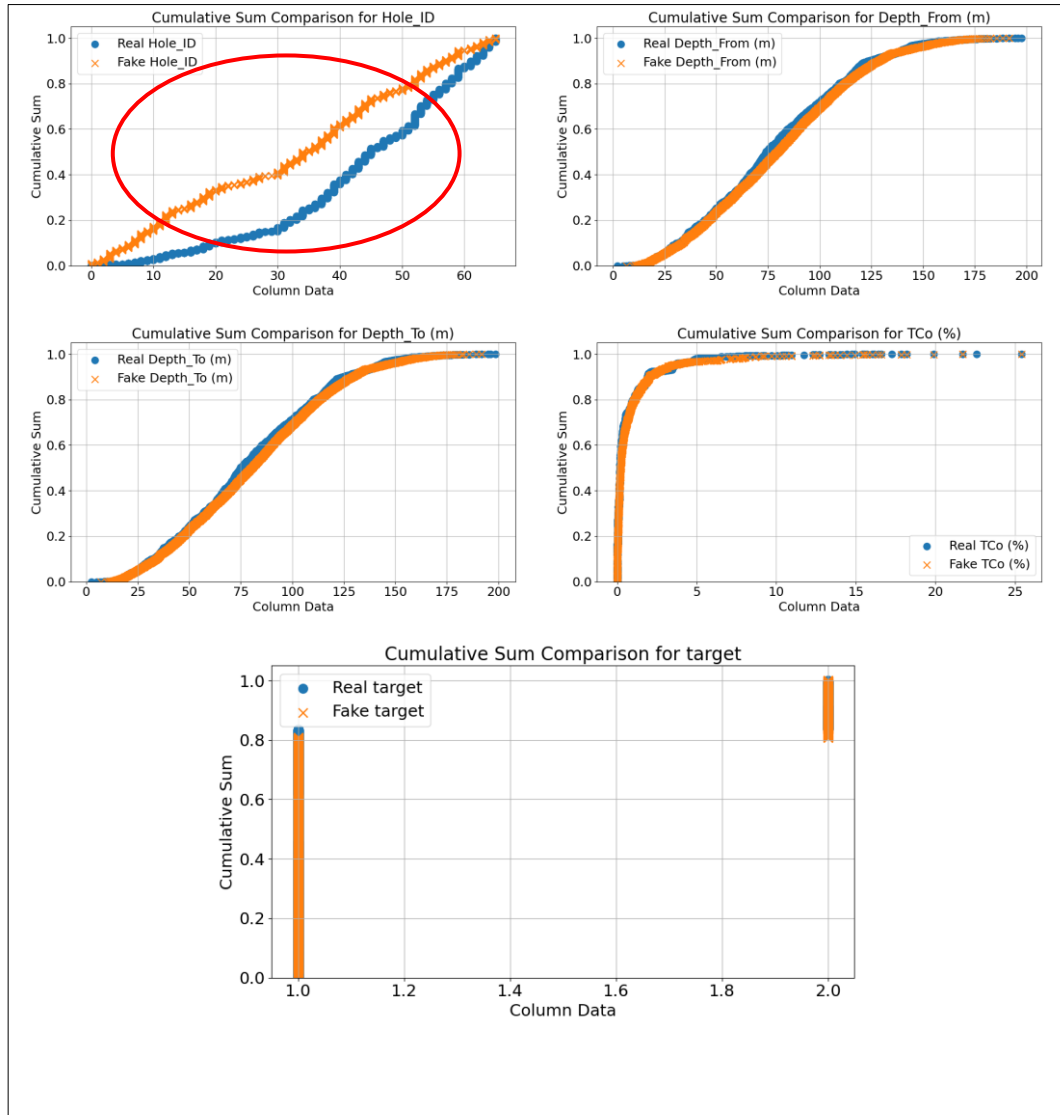


Figure 4.14: Visual comparison of original and fake data for assay data generated by Gaussian Copula

Figures 4.15 to 4.17 present the visual comparison of geometallurgical data, showcasing the differences between the original data and synthetic data generated by CTGAN, CopulaGAN, and Gaussian Copula models.

Similar to the observations made for synthetic assay data (Figures 4.12 – 4.14), all three models encountered difficulties in accurately replicating the "Hole_ID" feature. However, CTGAN (Figure 4.15) performed relatively better compared to the other models, displaying some differences but achieving closer matching.

This is followed by Gaussian Copula, with CopulaGAN performing the worst for "Hole_ID" feature. CTGAN demonstrated good performance in matching "Depth_From (m)" and "Depth_To (m)," achieving a perfect match. However, for other features, some minor differences, represented by red circles, were observed where CTGAN struggled.

Similarly, CopulaGAN faced challenges in replicating the exact original data, as evident in Figure 4.16. Like CTGAN, it encountered difficulties in matching "Depth_From (m)" and "Depth_To (m)" as well, not performing as well as CTGAN in these aspects.

On the other hand, Gaussian Copula (Figure 4.17) exhibited superior performance compared to the other models. Only minor differences were observed in "Depth_From (m)," "Depth_To (m)," and the "target" feature. For the rest of the features, it performed well, displaying relatively fewer discrepancies.

Overall, while all three models struggled with accurately replicating the "Hole_ID" feature, CTGAN showed better results compared to CopulaGAN. Gaussian Copula emerged as the most successful model, with fewer differences observed in the matched features, particularly for "Depth_From (m)," "Depth_To (m)," and the "target" variable. The models' performance on the remaining features was generally good, with only minor differences observed.

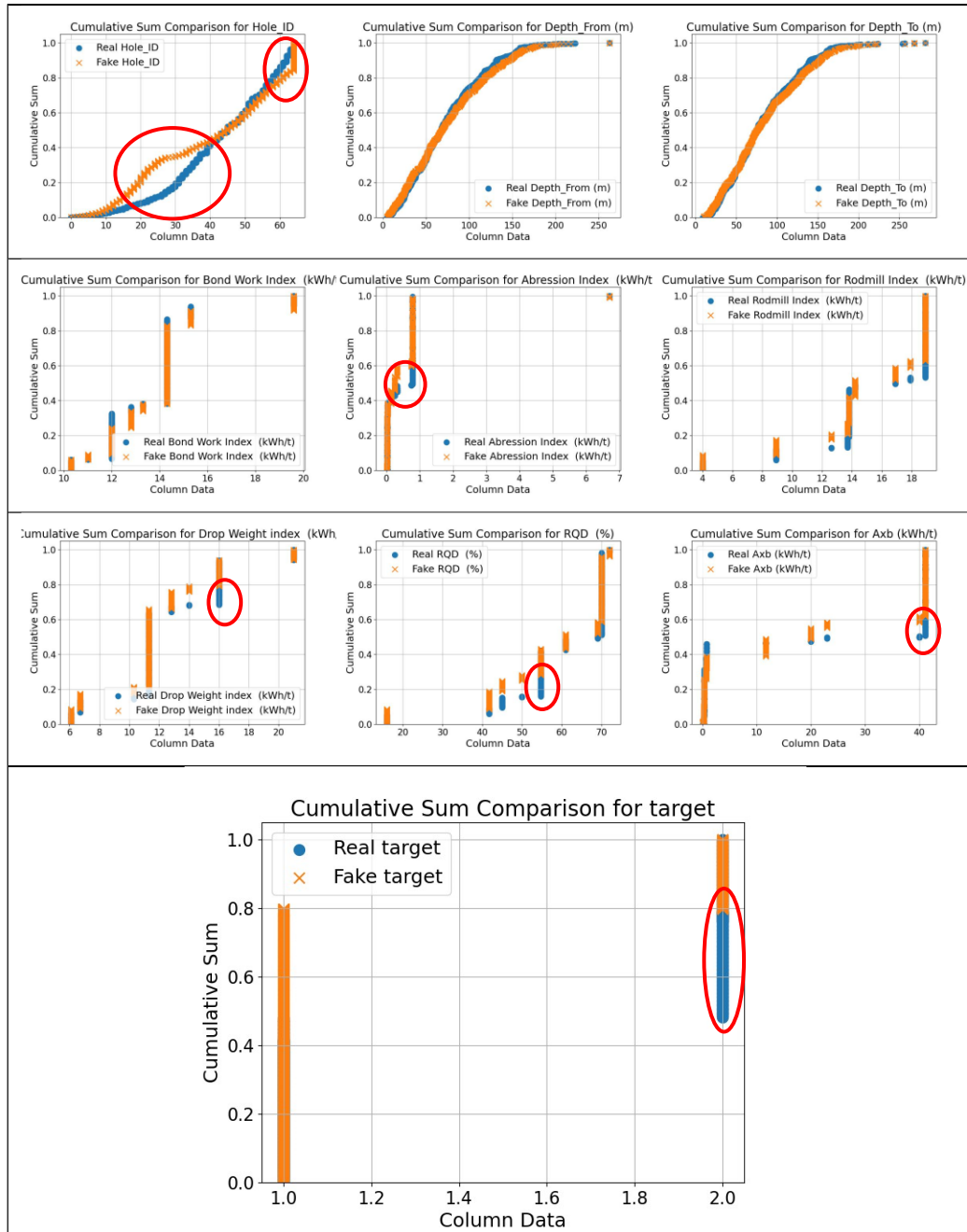


Figure 4.15: Visual comparison of original and fake data for geometallurgical data generated by CTGAN

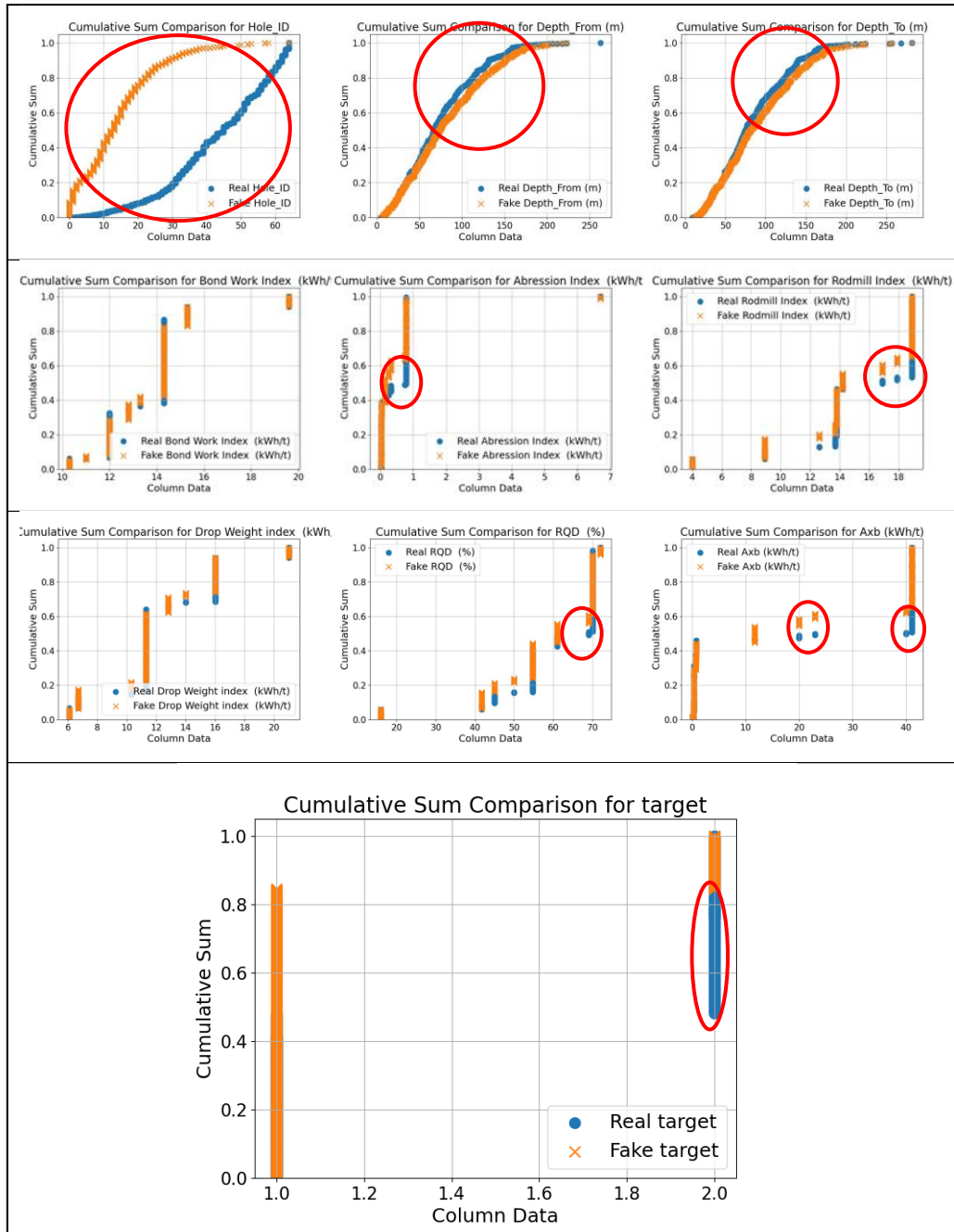


Figure 4.16: Visual comparison of original and fake data for geometallurgical data generated by CopulaGAN

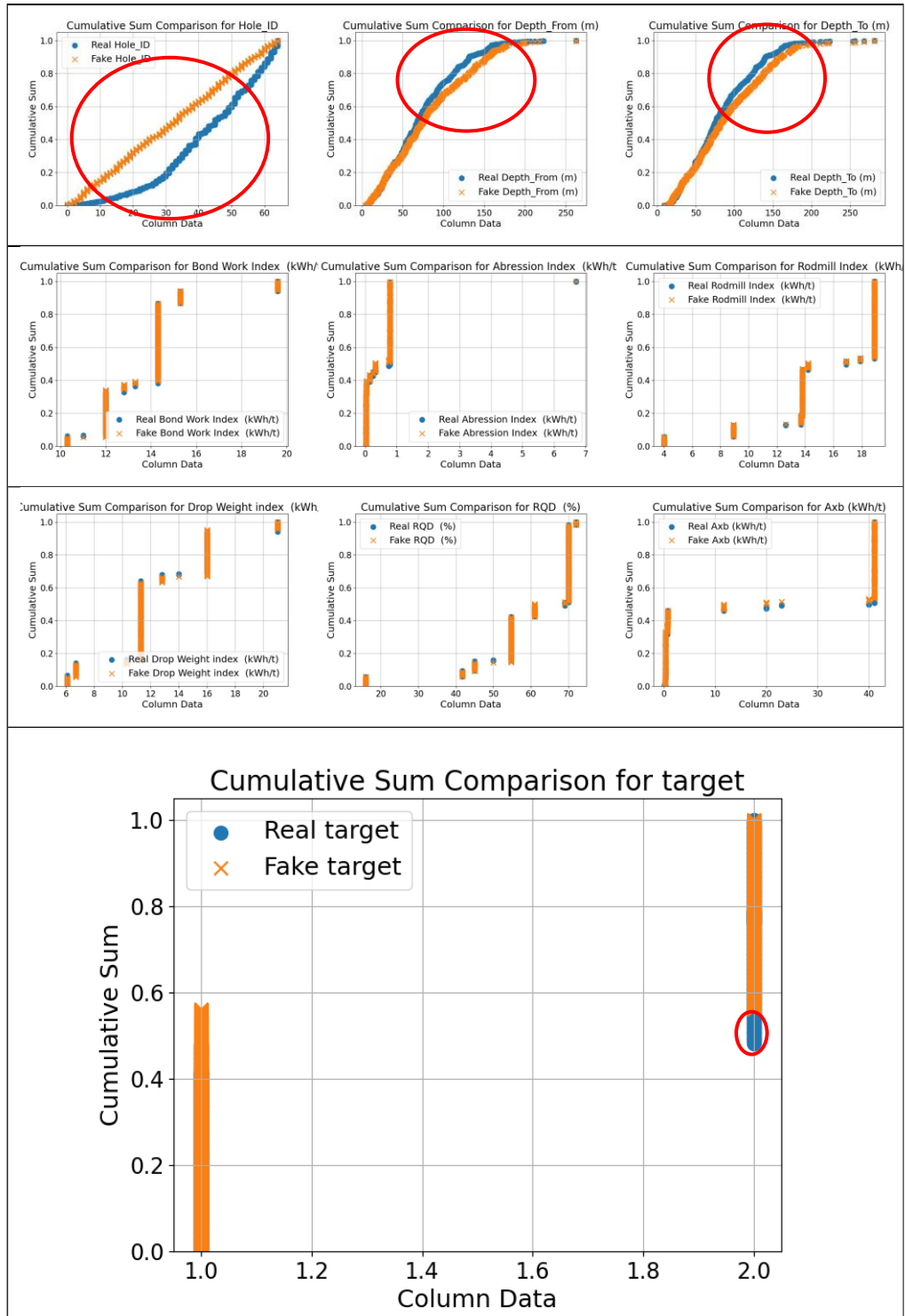


Figure 4.17: Visual comparison of original and fake data for geometallurgical data generated by Gaussian Copula

The visual comparison results for survey data are presented in Figures 4.18 to 4.20. As seen with previous datasets, the models faced challenges in

accurately replicating the "Hole_ID" feature of the original data. CTGAN (Figure 4.18) came relatively closer than the other models in matching this feature, with differences highlighted in red circles. CTGAN also performed better when it comes to the "Azimuth (Degree)" feature.

Minor differences were observed between the original and synthetic data for the other features across all models. For CopulaGAN (Figure 4.19), it struggled slightly in replicating the "Dip (Degree)" and "target" features. Similarly, Gaussian Copula (Figure 4.20) displayed minor differences in the "Depth (m)" and "Dip (Degree)" features.

Overall, all the models performed well in replicating the original assay data. CTGAN demonstrated better performance than the other models, particularly in matching the "Hole_ID" feature. Despite the challenges with this feature, the models generally achieved good results with minor differences observed in the matched features.

It is important to note that while the models struggled with the "Hole_ID" feature, they were still able to produce synthetic data that closely resembled the original data for the majority of the other features. This indicates that the models were successful in capturing the underlying patterns and characteristics of the survey data, despite some discrepancies in specific features.

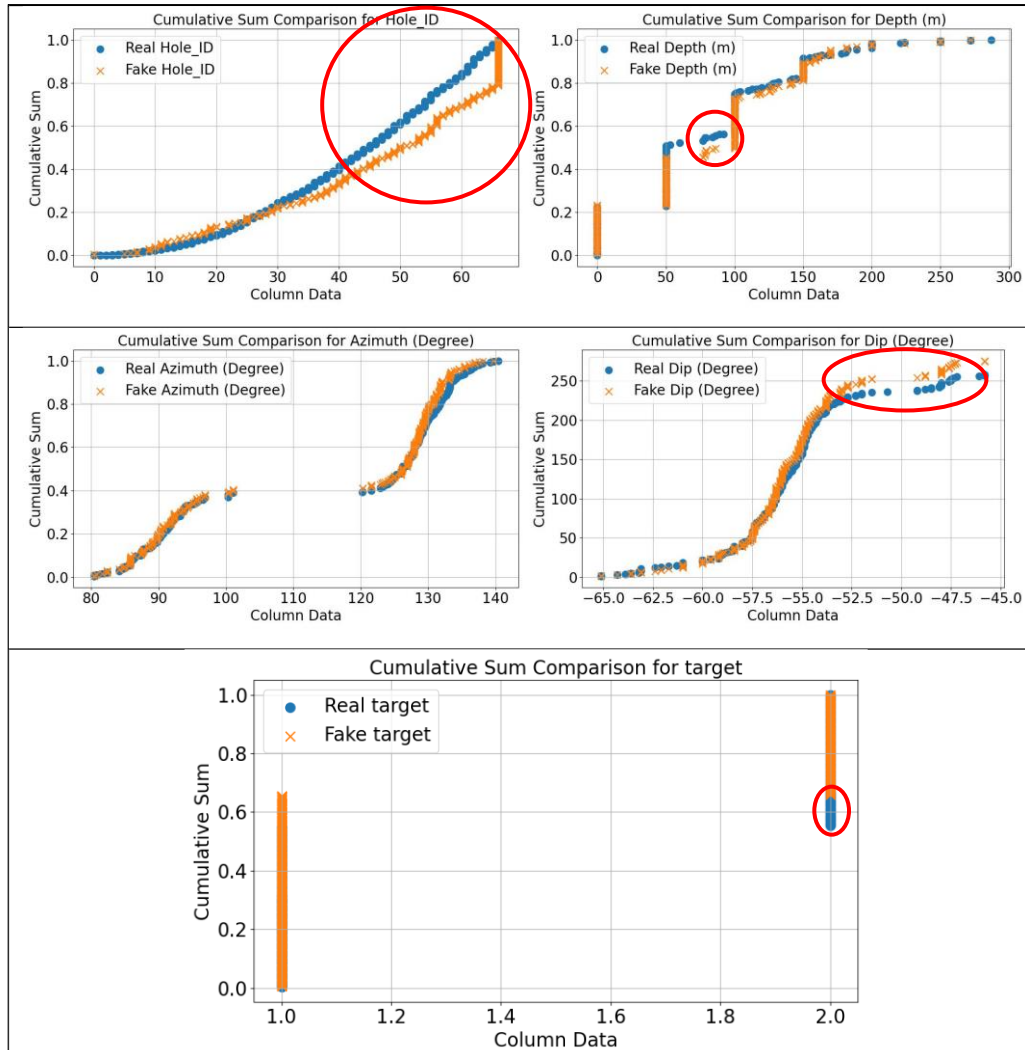


Figure 4.18: Visual comparison of original and fake data for survey data generated by CTGAN

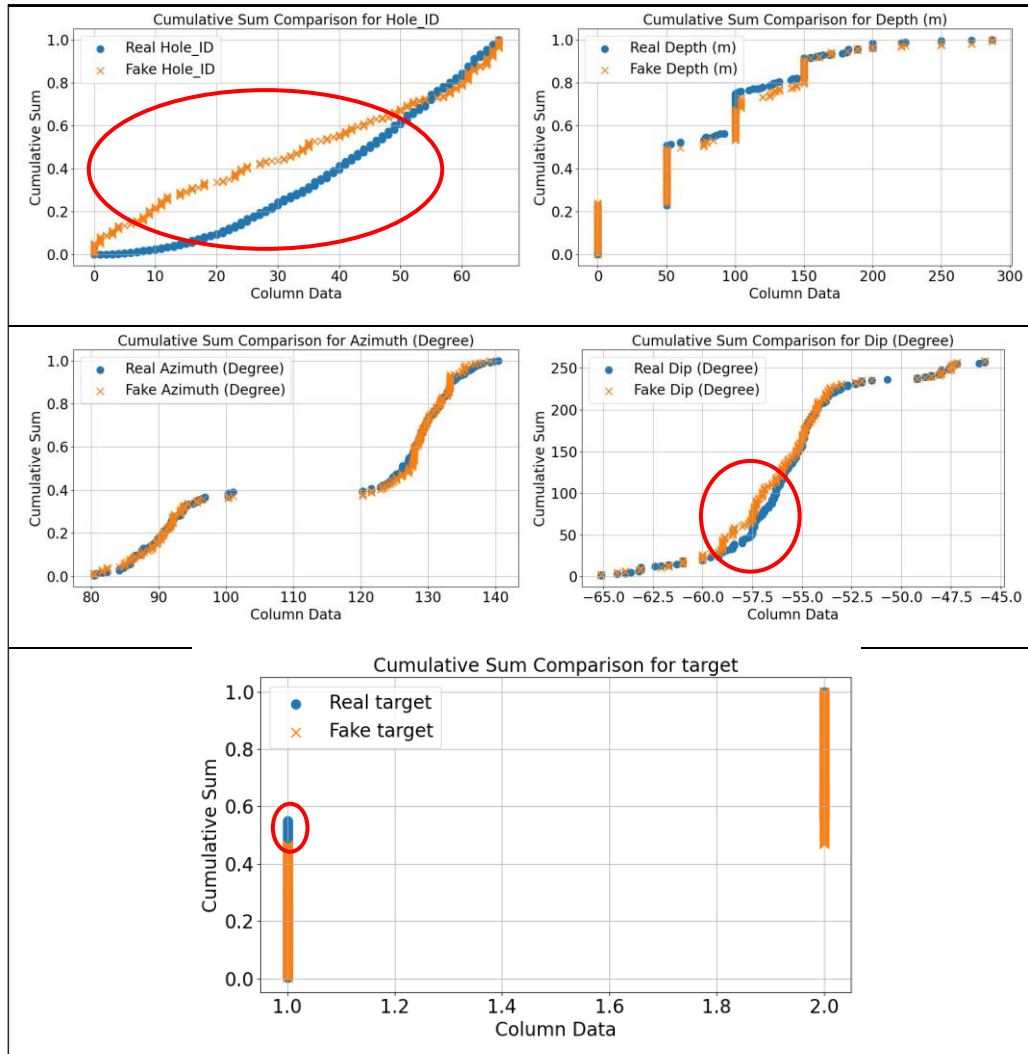


Figure 4.19: Visual comparison of original and fake data for survey data generated by CopulaGAN

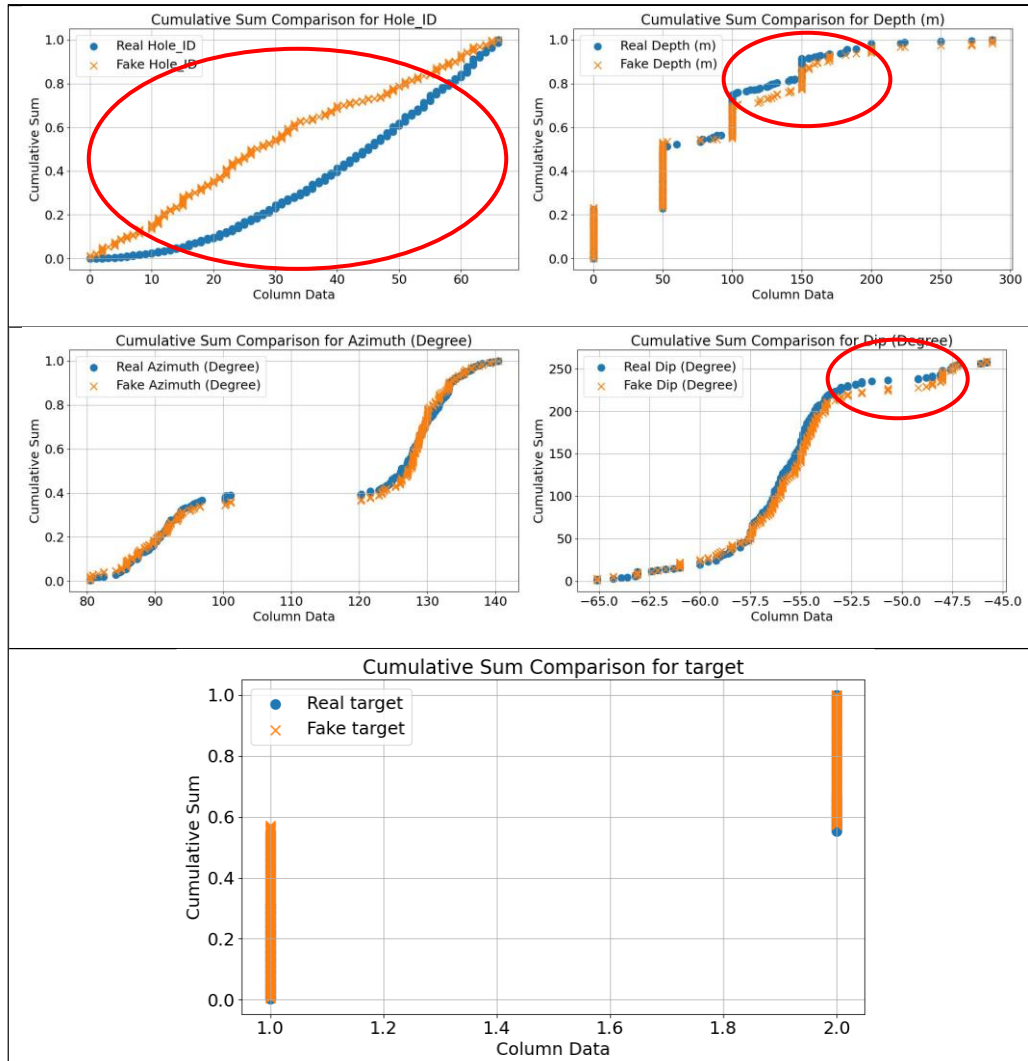


Figure 4.20: Visual comparison of original and fake data for survey data generated by Gaussian Copula

4.4 Principal component analysis of synthetic and original data

In this section, principal component analysis (PCA) metrics were used to evaluate the synthetic data generated by CTGAN, CopulaGAN, and Gaussian Copula models for collar, assay, geometallurgical and survey data. The first two principal components in PCA represent the two dimensions that capture the most variance in the dataset. In synthetic data evaluation, the first two principal components are used to visually compare the original and synthetic data using a scatter plot. If the scatter plot of the

first two principal components shows a clear separation between the original and synthetic data, then it indicates that the synthetic data is significantly different from the original data. On the other hand, if the scatter plot of the first two principal components shows a significant overlap between the original and synthetic data, then it indicates that the synthetic data is similar to the original data.

Figures 4.21 to 4.24 indicate the first two components of synthetic data generated using CTGAN, CTGAN, CopulaGAN, and Gaussian Copula models for collar, assay, geometallurgical and survey data. The graphs were generated using the `matplotlib` programme in Python® as indicated in Section 3.2.3.

The evaluation results for collar data demonstrate that the models successfully replicated the PCA of the real data. A visual comparison of the collar data generated by CTGAN and CopulaGAN (Figure 4.21) with the original data reveals similarities between the two datasets. This indicates that the models were able to capture all essential aspects of the underlying distribution and reproduce them in the synthetic collar data.

Similarly, Gaussian Copula also displayed more similarities with the original data, indicating its effectiveness in capturing the underlying distribution patterns.

However, there were some minor differences observed between the real and synthetic collar data in the PCA plot for Gaussian Copula. This indicates that while the model was able to capture the overall structure and trends of the original collar data, there might be some slight variations in the synthetic collar data compared to the real collar data.

Overall, the results suggest that the models performed well in replicating the PCA of the collar data and capturing the major distribution characteristics. The similarities between the real and synthetic data in the PCA plots indicate the ability of models to generate high-quality synthetic data that closely resembles the original data. The minor differences observed,

particularly in the case of Gaussian Copula, could be attributed to the inherent complexity of the real-world data and the challenges in perfectly reproducing all aspects of the original distribution.

Despite these minor differences, the success of the models in capturing the underlying distribution of the collar data is a positive indication of their effectiveness in generating reliable synthetic data for various applications in data analysis and modelling.

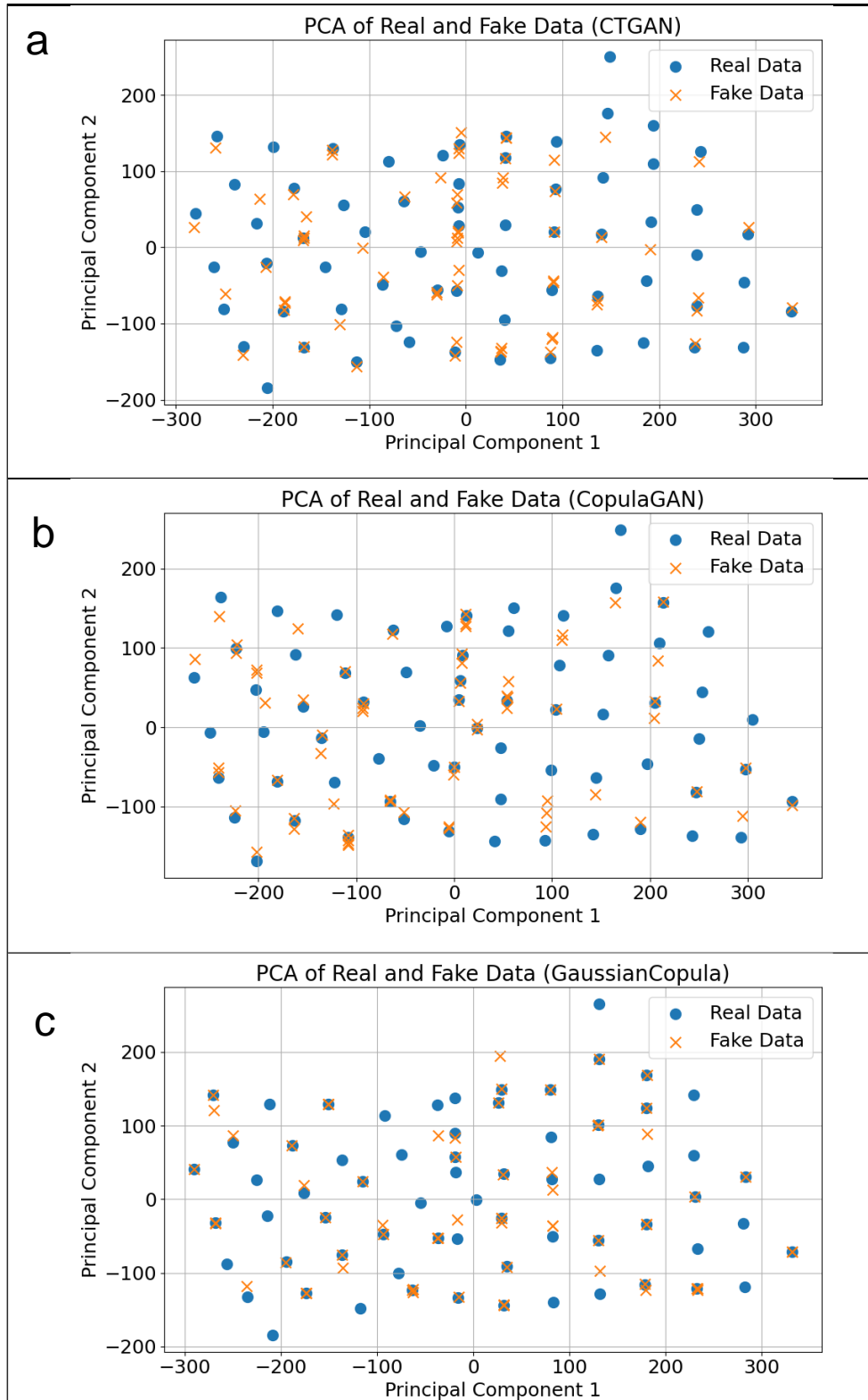


Figure 4.21: Comparison of principal component analysis between original and fake data for collar data. a) CTGAN; b) CopulaGAN; and c) Gaussian Copula

This outcome suggests that the synthetic data generated by all three models closely resembles the original assay data, and the models have been successful in capturing the essential patterns and variations present in the original assay dataset. The fact that the first two components of the PCA match perfectly indicates that the models have effectively replicated the major sources of variability in the data.

Having a perfect fit between the real and synthetic assay data in the PCA scatter plots is a positive sign and demonstrates the high quality and accuracy of the generated synthetic data. It indicates that the synthetic data is significantly similar to the original data, making it suitable for various data analysis and simulation purposes.

The successful performance of the models in replicating the PCA components further confirms the utility of generative models like CTGAN, CopulaGAN, and Gaussian Copula in generating synthetic data that is both statistically similar and structurally representative of the original data. These results provide confidence in the use of synthetic data for various applications, including data privacy protection, model training, and other scenarios where access to real data may be restricted or limited.

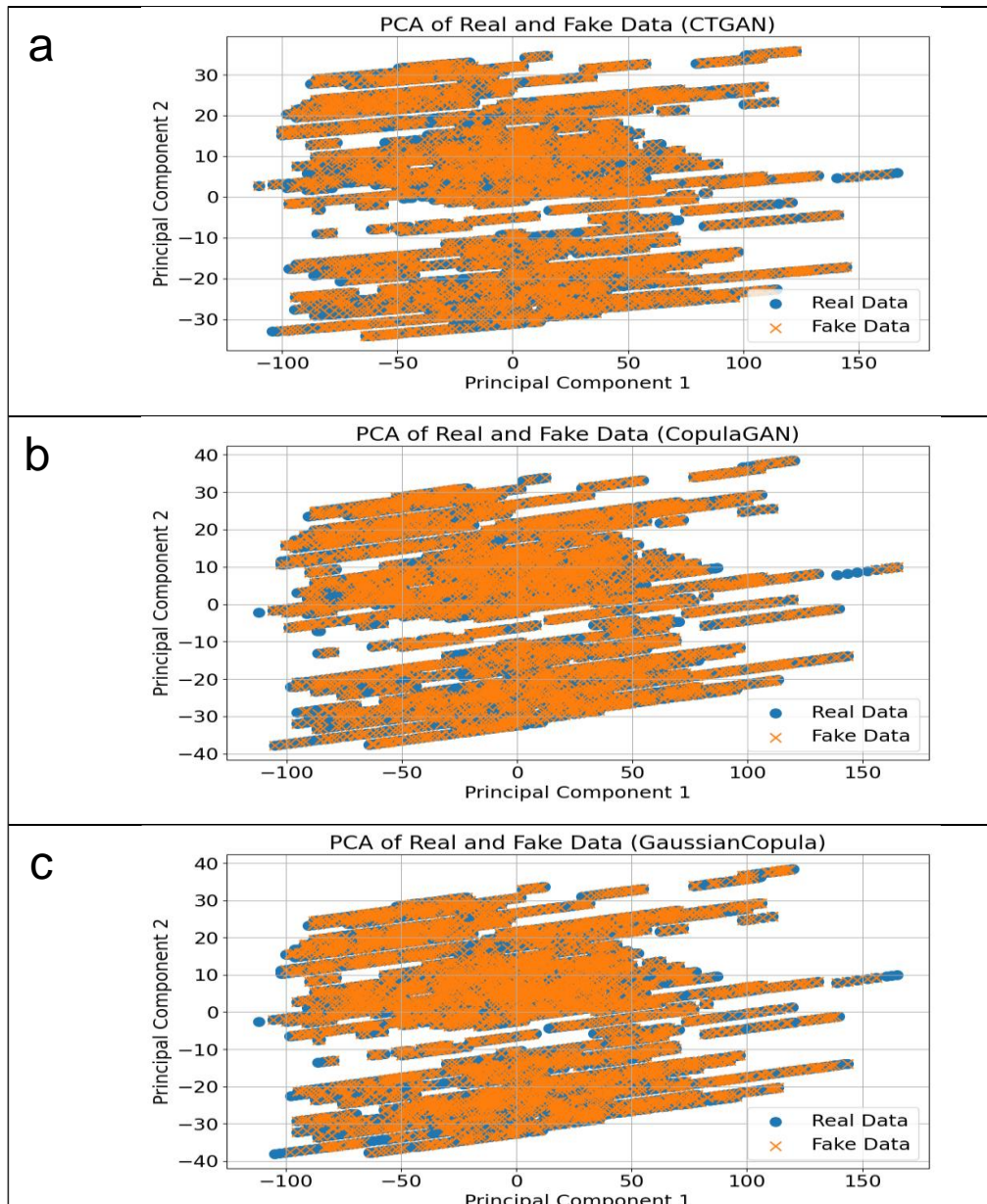


Figure 4.22: Comparison of principal component analysis between original and fake data for assay data. a) CTGAN; b) CopulaGAN; and c) Gaussian Copula

The visual comparison of the first two components of PCA for all the models (Figure 4.23) indicates that there is a clear and almost perfect match between the real geometallurgical data and the synthetic geometallurgical data. However, some minor differences can still be observed in all the plots.

Among the models, CTGAN shows slightly more differences compared to CopulaGAN and Gaussian Copula. CopulaGAN and Gaussian Copula seem to produce similar results, with fewer variations when compared to CTGAN.

These findings suggest that the synthetic geometallurgical data closely resembles the original geometallurgical data, and the models were able to capture the underlying patterns and structure of the original data quite effectively. Despite the minor differences observed, the overall similarity between the real and synthetic data in the first two PCA components indicates that the models have successfully generated synthetic data that preserves the essential characteristics and relationships present in the original data.

The results provide confidence in the quality and accuracy of the synthetic data, as the models have been able to replicate the key patterns and structures of the original data, which is essential for various analytical and modelling purposes. It is important to note that the minor differences observed in the plots are not unexpected and are considered acceptable, given the complexities of real-world data and the generative modelling process. Overall, the success of the models in producing synthetic data that closely aligns with the PCA components of the original data is a positive outcome for their utility and application in various data analysis and simulation scenarios.

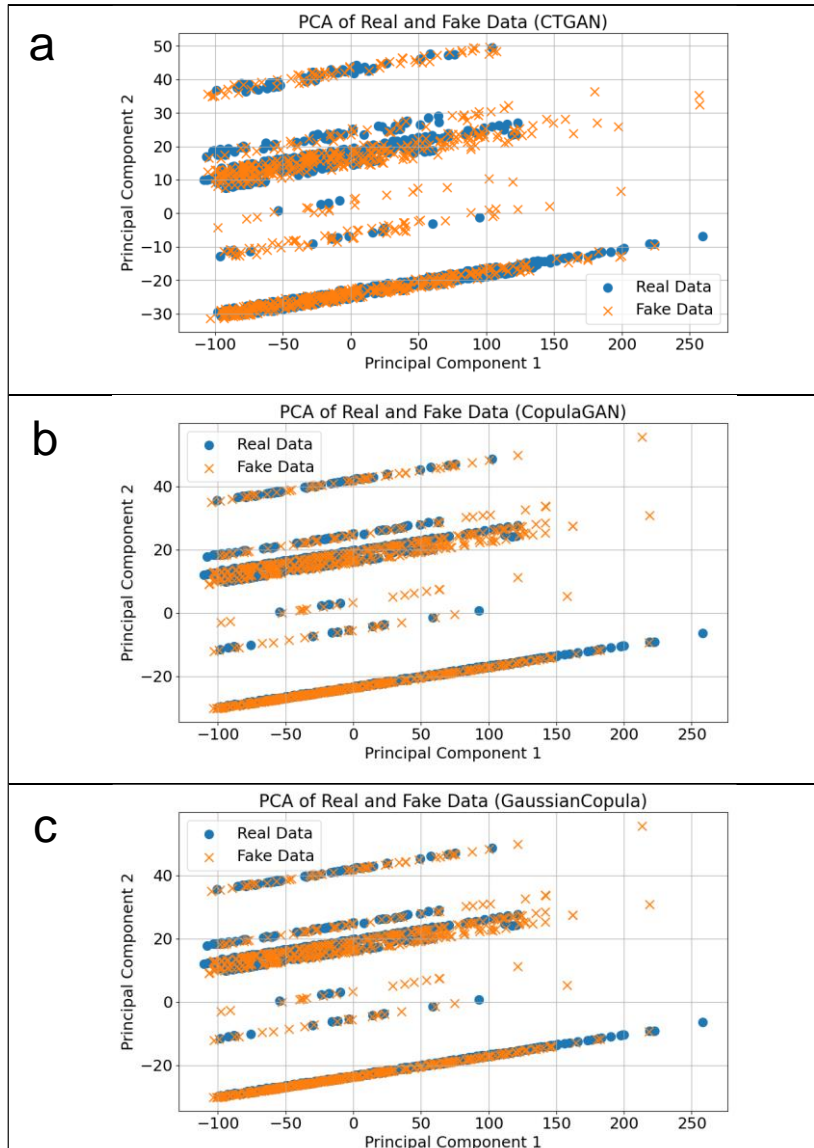


Figure 4.23: Comparison of principal component analysis between original and fake data for geometallurgy data. a) CTGAN; b) CopulaGAN; and c) Gaussian Copula

The PCA (Figure 4.24) results for the survey data demonstrate that the synthetic survey data generated by all models (CTGAN, CopulaGAN, and Gaussian Copula) closely match the original survey data. The scatter plots for the first two PCA components reveal a significant overlap between the original and synthetic survey data, indicating a high level of similarity between the two datasets.

This strong overlap in the PCA scatter plots suggests that the generated synthetic data is of good quality and effectively captures the major patterns and variations present in the original survey data. The models have successfully preserved the underlying structure of the data, leading to synthetic data points that align closely with the real data in the PCA space.

The ability of all three models to produce synthetic data that closely resembles the original data is a positive outcome. It means that the generated data can be used as a representative substitute for the real data in various applications, including data analysis, modelling, and simulations.

The results provide confidence in the use of synthetic data generated by CTGAN, CopulaGAN, and Gaussian Copula models for the survey data, as it reflects the essential characteristics and relationships present in the original dataset. This suggests that the synthetic data can be employed in scenarios where access to the real data is limited, or to protect sensitive information while still retaining the utility of the data for various analytical and modelling purposes.

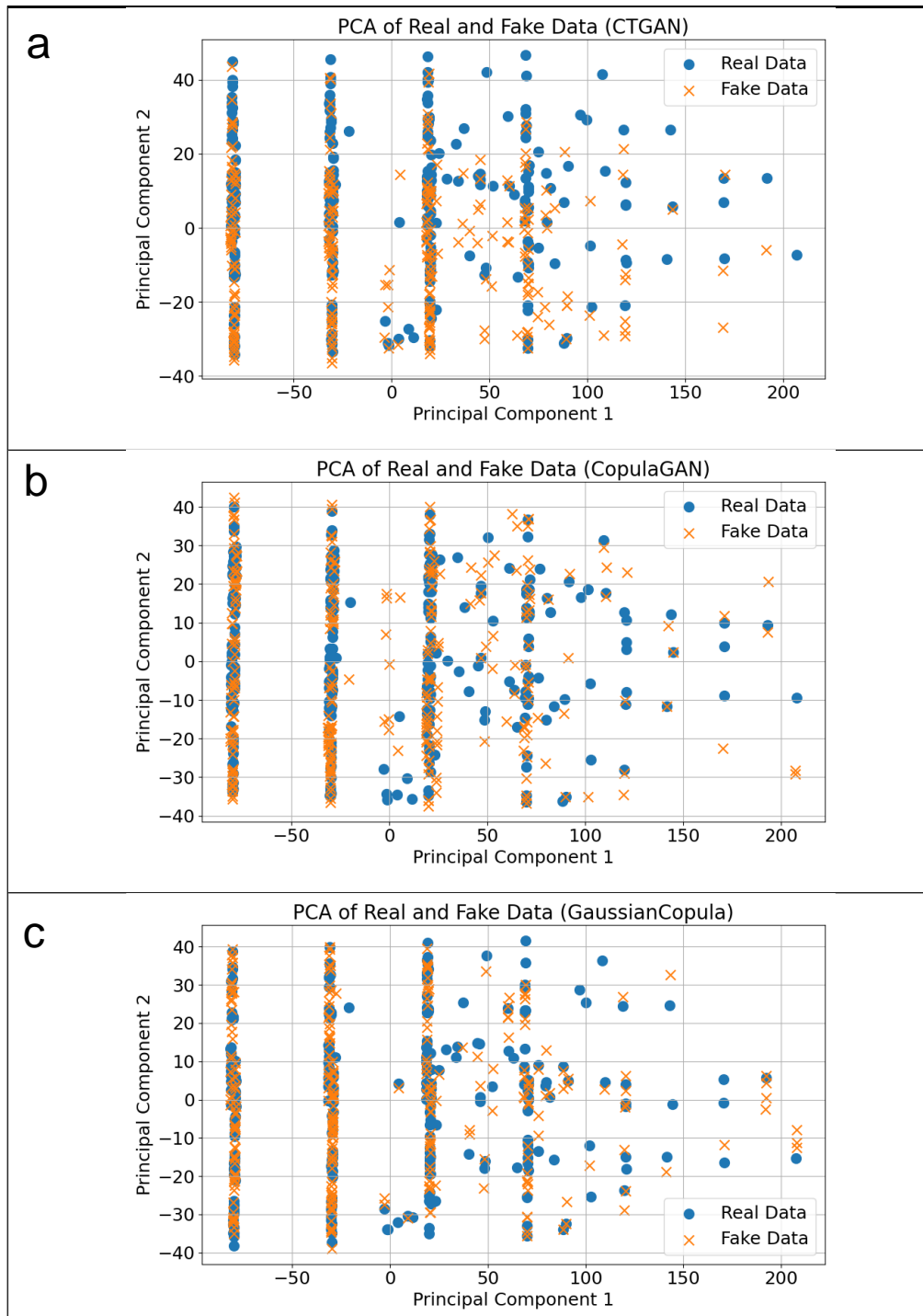


Figure 4.24: Comparison of principal components analysis between original and fake data for survey data. a) CTGAN; b) CopulaGAN; and c) Gaussian Copula

4.5 Column correlations between synthetic and original data

Figures 4.25 – 4.28 show the correlation matrix for four datasets: collar, assay, geometallurgical and survey. The correlation matrix displays the pairwise correlations between the original data and the synthetic data generated by the CTGAN, CopulaGAN and Gaussian Copula. The correlation matrix was calculated using `table_evaluator` and Pandas® `cor` function. Matplotlib® was used to plot the data. For more see section 3.4.1 and Appendix A.

When comparing the correlation matrices of the synthetic datasets to the collar dataset (Figure 4.25), it is observed that the sign of the correlations is consistent in most cases. The comparison of synthetic data models applied to collar data revealed interesting insights into their performance.

CTGAN, although capable of generating synthetic data, exhibited a correlation of 72.82% with the original data, indicating that it only captured around 72.82% of the patterns and relationships present in the original collar data.

CopulaGAN fared better, achieving a correlation of 76.47% with the original data, implying a closer resemblance to about 76.47% of the patterns and relationships. However, the standout performer was GaussianCopula, which achieved the highest correlation of 77.73% with the original data.

GaussianCopula demonstrated superior performance, producing synthetic data that closely matched approximately 77.73% of the patterns and relationships in the original collar data. These results indicate that GaussianCopula is the most effective model for generating synthetic data that closely replicates the statistical characteristics of the original data, making it the preferred choice for collar data synthesis.

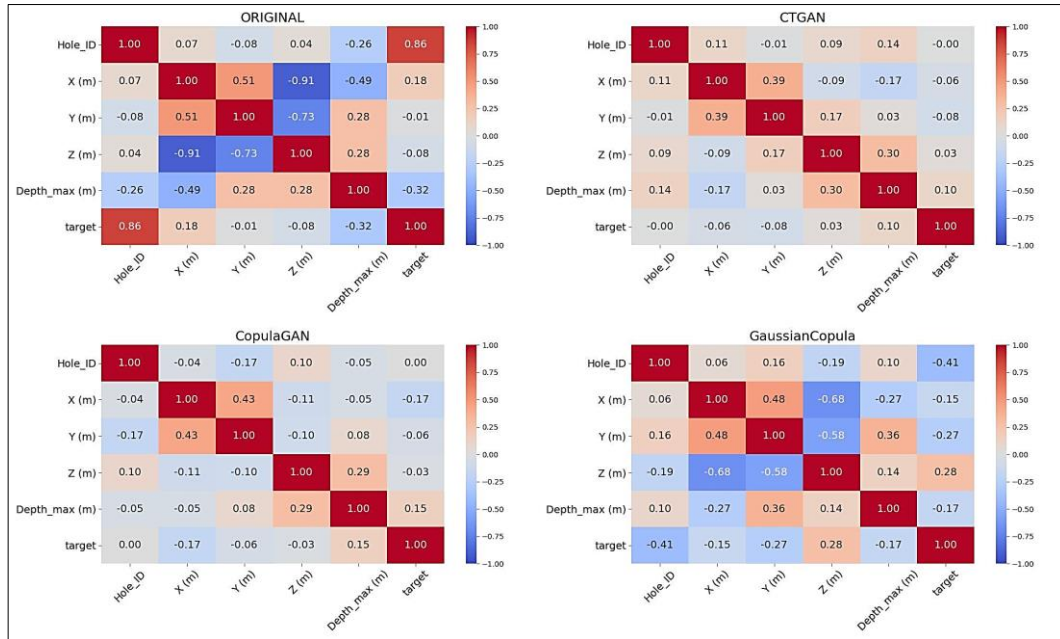


Figure 4.25: Comparison of column correlations between original and synthetic collar data generated through CTGA, CopulaGAN and GaussianCopula

In Figure 4.26, the results illustrate the correlations between features in the original assay dataset and synthetic assay datasets generated using different models, including CTGAN, CopulaGAN, and Gaussian Copula. The correlation values show that all three models perform well in generating synthetic data that resembles the original Assay data.

GaussianCopula demonstrates the highest correlation of 99.24%, indicating that the synthetic data generated by this model captures approximately 99.24% of the patterns and relationships present in the original Assay data. CopulaGAN also performs excellently with a correlation of 97.19%. CTGAN shows good performance with a correlation of 96.81%, but it has a slightly lower correlation compared to the other two models.

In summary, all three models, CTGAN, CopulaGAN, and GaussianCopula show promising results in generating synthetic data that closely resembles the original Assay data. GaussianCopula stands out with the highest correlation, suggesting that it is the most effective model for generating

synthetic data that accurately replicates the statistical characteristics of the original Assay data.

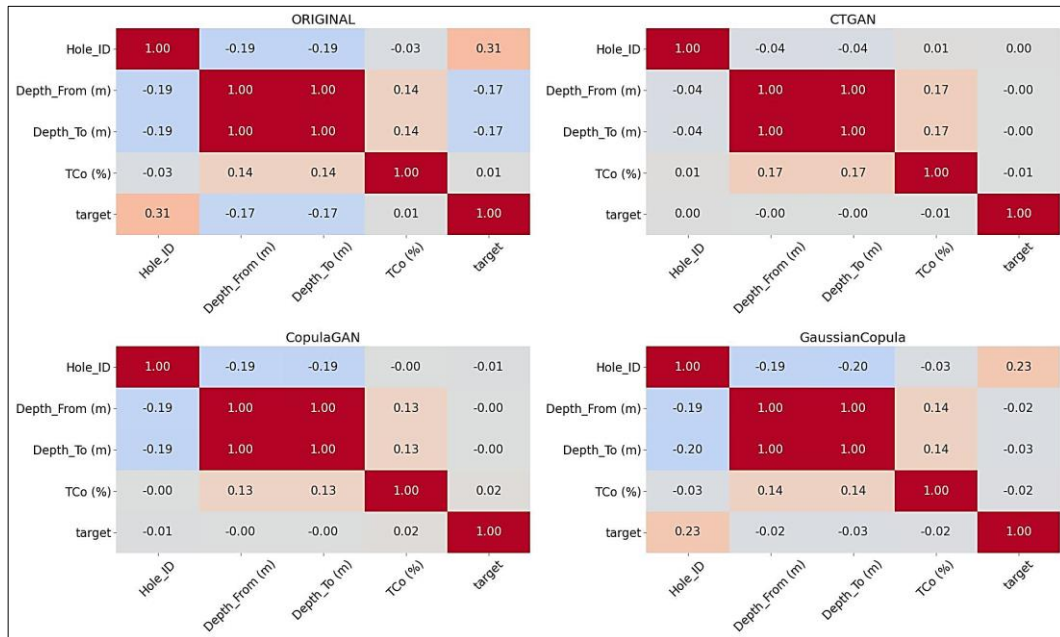


Figure 4.26: Comparison of column correlations between original and synthetic assay data generated through CTGAN, CopulaGAN and Gaussian Copula

The correlation results of the geometallurgical data (Figure 4.27) indicated that the CTGAN, CopulaGAN, and Gaussian Copula methods exhibited similar levels of correlation. There was not much difference between the three methods. Further examination of the correlation percentages revealed that the correlation between the original data and CTGAN was 88.37%. Similarly, the correlation between the original data and Gaussian Copula was 90.47%.

Finally, the correlation between the original geometallurgical data and Gaussian Copula was 94.47%. These findings suggest that all three methods performed reasonably well in generating synthetic data that closely resembled the patterns and statistical properties of the original geometallurgical data. However, Gaussian Copula demonstrated the highest correlation, indicating that it was the most effective method in replicating the statistical characteristics of the original data.

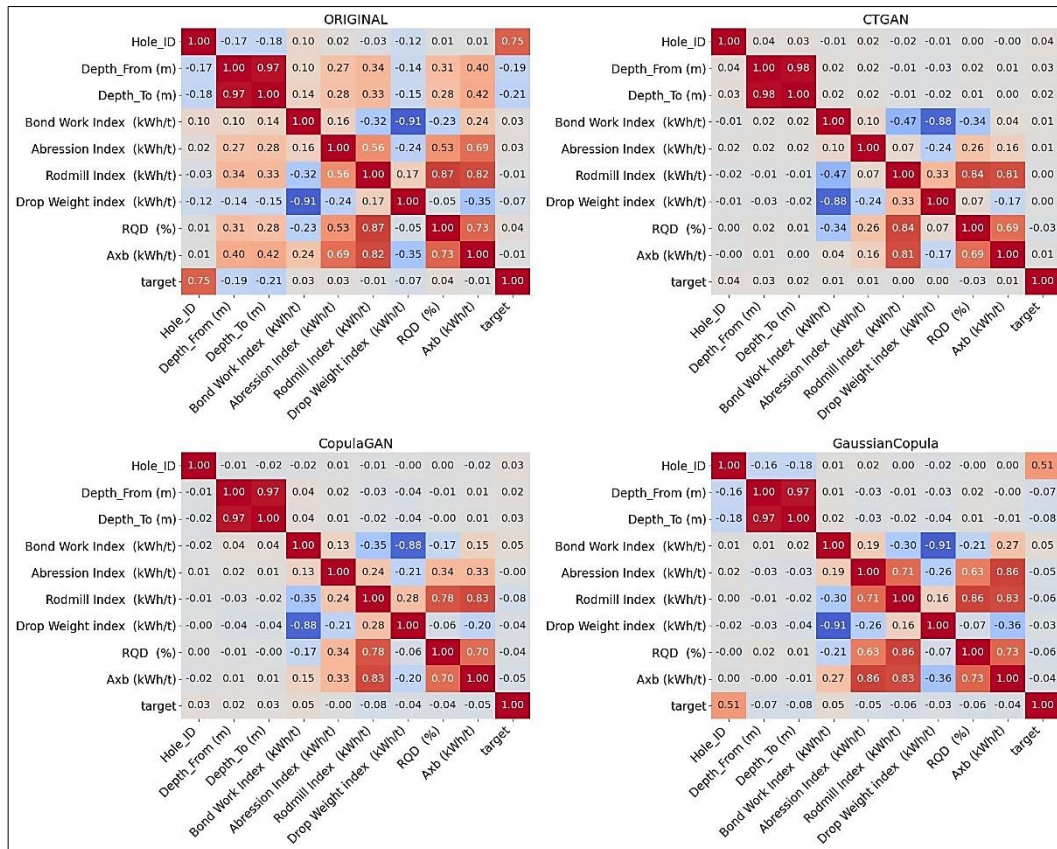


Figure 4.27: Comparison of column correlations between original and synthetic assay data generated through CTGA, CopulaGAN and Gaussian Copula

The results show the correlation matrices for the original survey data (Figure 4.28) and the synthetic data generated by four different methods: CTGAN, CopulaGAN, and Gaussian Copula.

The analysis of the correlation between the original Survey data and synthetic data generated by various models provided valuable insights. Among these models, GaussianCopula showed the highest correlation of 95.33%, indicating a successful capture of around 95.33% of the patterns and relationships present in the original Survey data.

CopulaGAN also performed well, achieving a correlation of 88.07%, which closely matched about 88.07% of the patterns and relationships. CTGAN had a slightly lower performance with a correlation of 86.25%.

Overall, both CopulaGAN and GaussianCopula were effective in generating synthetic Survey data that closely resembled the statistical properties of the original data. However, GaussianCopula demonstrated the highest performance, making it the preferred choice for synthesizing Survey data due to its superior ability to replicate the complex patterns present in the original dataset.

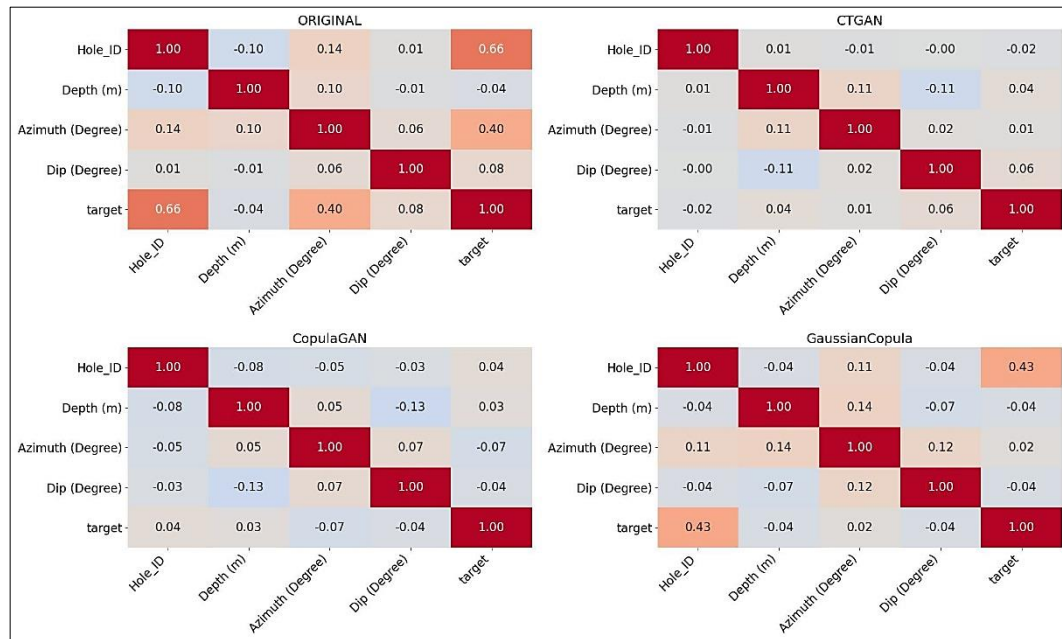


Figure 4.28: Comparison of column correlations between original and synthetic assay data generated through CTGA, CopulaGAN and Gaussian Copula

4.6 Summarised conclusion

Chapter 4 of the thesis focuses on the analysis and evaluation of the results obtained from synthetic data generation techniques used in Chapter 3. The study uses three synthetic data generation techniques: CTGAN, CopulaGAN, and Gaussian Copula. The chapter presents the benefits and drawbacks of each technique, as well as the findings and analysis of the study.

The evaluation of the generated synthetic data is based on the table evaluator, which employs various parameters to evaluate the data, including the similarity score, principal component analysis, and visual evaluation. The results indicate that CopulaGAN and Gaussian Copula are better at preserving the correlation structure of the original data than CTGAN. The synthetic datasets generated by these algorithms are useful for modelling and analysis purposes, but caution should be exercised when interpreting the results.

The results show that the percentage of pairs with the same correlation sign is highest for the Gaussian Copula method, followed by CopulaGAN and CTGAN. Gaussian Copula produced the highest similarity score, indicating that it was the most successful in generating synthetic data that closely matched the real data. For the mean correlation between fake and real columns, all models achieved a correlation above 0.93.

Overall, the findings and analysis presented in this chapter are important for researchers and practitioners who utilize synthetic data generation techniques for various applications, especially in cases where data privacy and scarcity are issues.

The results and discussion of the chapter have shown that GAN-based modules can be used to produce synthetic data for geometallurgical data. It produces high-quality data realistic data. The data can also be modelled after the original but be unique and anonymise the original data.

The geometallurgical data generated in this chapter can be used for any application in mine planning. The following chapter presents some of the applications where geometallurgical data can be used.

Chapter 5 Implicit Geometallurgical modelling with Radial Basis Functions

5.1 Introduction

This chapter focuses on the application of implicit modelling to geometallurgical data. The geometallurgical data analysed in this study include the Bond Work Index (kWh/t), rod mill index (kWh/t), RQD (%), drop weight index (kWh/t), Axb (kWh/t) and abrasion index (kWh/t) as described in Section 3.1.1.

The objective of this chapter is to investigate the application of implicit modelling in geometallurgical modelling and to provide insights into the spatial distribution and variability of mineral resources and their metallurgical characteristics.

Implicit modelling is a powerful tool that integrates multiple sources of data, such as geology, geochemistry, geophysics, and mineralogy, to create three-dimensional geological models. The study employs Leapfrog® Geo, a software application that utilizes implicit modelling to develop geological models, as explained in Section 3.1.

Leapfrog® Geo offers numerous benefits, such as incorporating multiple data sets and providing a user-friendly interface for model visualization. The software also enables statistical analysis tests, and model visualisation which assists in validating and refining models.

The outcomes of this study will provide useful information on the use of the implicit modelling method in modelling geometallurgical data. This data can be utilized to optimize mining activities and improve the efficiency of mineral processing. Furthermore, the study highlights the potential of implicit modelling as a powerful tool for geometallurgical modelling, which can enhance our understanding of complex ore deposits.

5.2 Economic model of the original drillhole assay data

Figure 5.1 represents the economic model of the original drillhole assay data. It was generated using an economic model in Leapfrog® Geo software. The figure also indicates the delineation of an economic model using an assay cut-off grade of 0.5% TCo to separate the ore and waste zones within the drillholes.

The grey zone represents the waste with TCo grades below 0.5%, while the red zone represents the ore with TCo grades of 0.5% and above. The Figure shows the orebody boundary within the drillhole, enabling better visualization and understanding of the location and size of the orebody. Furthermore, Figure 5.1 highlights the drillholes that contain ore and those that contain waste, providing valuable information for economic modelling and decision-making processes.

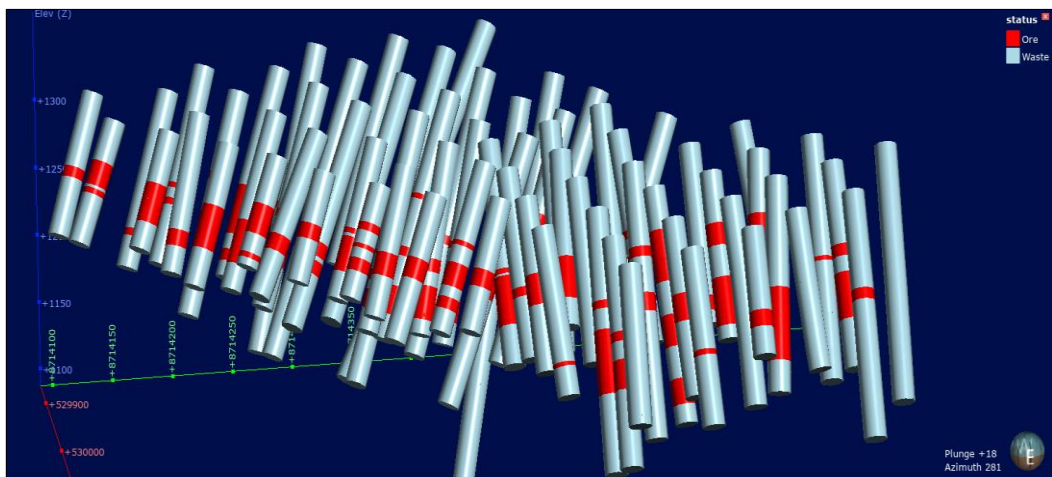


Figure 5.1: The economic model of original drillhole assay data

5.3 Three-dimensional orebody modelling/domain

Figures 5.2 and 5.3 present the 3D and 2D orebody domains, respectively, generated using the Leapfrog® Geo software. The domain boundaries were determined based on the grade data of TCo, with more information available in Section 3.3.6. An indicator radial base function was employed to create the orebody domain, and a cut-off grade of 0.5% TCo, as with the drillhole

domain (Section 5.2), was used to delineate the orebody. The two Figures illustrate two zones in different colours, with red representing values inside the 0.5% TCo, which is the ore, and blue representing values outside 0.5%, which is waste. The red colour clearly shows the boundary of the orebody within the waste.

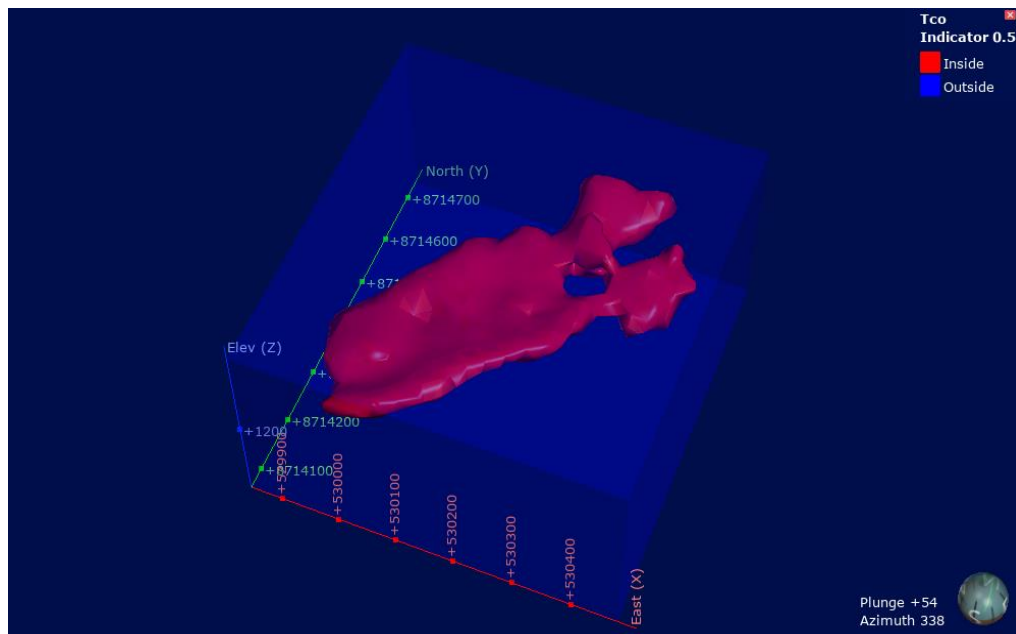


Figure 5.2: A 3D orebody model. Red is the ore and blue is the waste

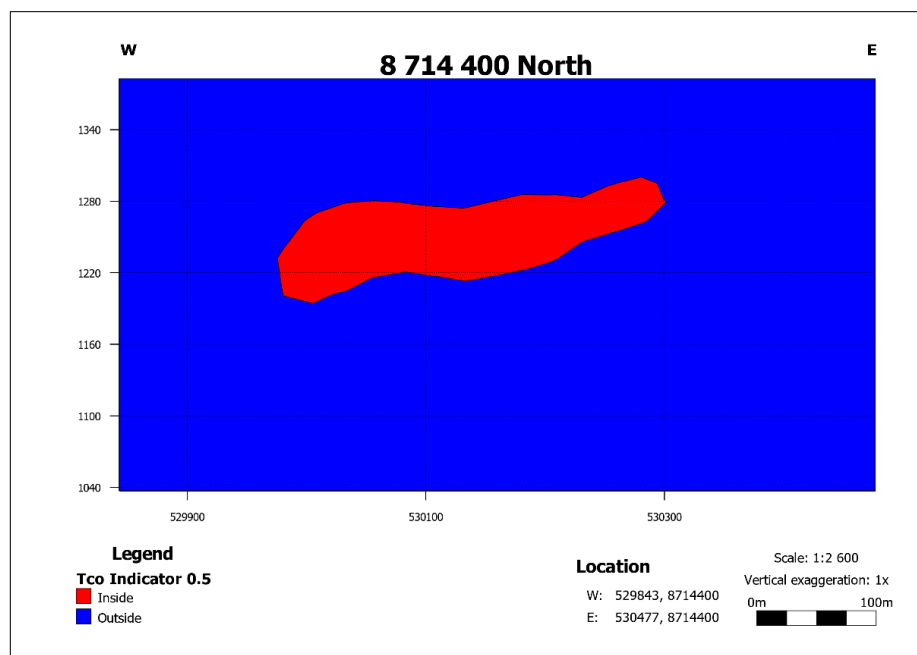


Figure 5.3: Cross-sectional view of the orebody model

5.4 Validation of the 3D orebody model

The purpose of validation is to assess the accuracy and reliability of the created model by comparing it with independent data or known results. In this case, the 3D model of the orebody was validated by comparing it with the original drillhole assay economic model. The validation involved both statistical analysis and visual analysis to ensure that the model accurately represented the grade and distribution of the orebody. By validating the model, it can be used with greater confidence to make predictions as a boundary for geometallurgical modelling. The following sections present the process used for validation.

5.4.1 Statistical comparison of 3D orebody and drillhole data assay economic model

Table 5.1 compares the statistical results of the ore and waste in the 3D model with the drillhole assay data. The purpose of this validation is to check the accuracy of the 3D model by comparing it with the known drillhole assay data.

In both the 3D model and the drillhole data, the number of points for ore and waste is consistent. Specifically, there are 91 points for ore and 157 points for waste. The mean value of the ore in the 3D model is slightly lower than that of the drillhole data, with values of 1.62% and 1.78%, respectively. This difference in mean values may be due to variations in the sample sizes and locations.

The minimum and maximum values of the ore in the 3D model and drillhole data are almost the same, with values ranging from 0.55% to 8.79%. The standard deviation and variance of the ore in the 3D model are slightly higher than those of the drillhole data, indicating that the data in the 3D model is more scattered than that of the drillhole data.

In terms of waste, the mean, minimum, and maximum values of the 3D model and drillhole data are very close to each other. However, the standard

deviation and variance of the waste in the 3D model are slightly higher than those of the waste drillhole data. This may be due to the smaller number of waste points in the drillhole data compared to the 3D model.

Overall, the statistical analysis of the ore and waste in the 3D model and the drillhole data show that the 3D model accurately represents the orebody and waste, as the differences in the mean, minimum, and maximum values are within an acceptable range. However, the higher standard deviation and variance of the ore and waste in the 3D model compared to the drillhole data indicates some level of uncertainty and variability in the 3D model.

Table 5.1. Statistical comparison of the 3D orebody model with the economic drillhole model

	Ore (%) (3D Model)	Ore (%) (Drillhole)	Waste (%) (3D Model)	Waste (%) (Drillhole)
Number of points	91	91	157	157
Mean value	1.62	1.78	0.08	0.05
Minimum value	0.55	0.55	0	0.00
Maximum value	8.79	8.79	0.41	0.41
Standard deviation	1.19	1.10	0.09	0.06
Coefficient of variance	0.73	0.62	1.13	1.18
Variance	1.4	1.21	0.01	0.00

5.4.2 Visual inspection of 3D orebody and economic model

Visual inspection of the 3D orebody model against the drillhole model is a crucial step in validating the accuracy of the model. This involves comparing the boundaries and distribution of the orebody as modelled in 3D to the actual drillhole data in order to identify any discrepancies that need to be addressed.

Figure 5.4 presents the comparison of the 3D orebody model and the economic model of the drillhole. The figure was generated in Leapfrog®

Geo. From Figure 5.4a and b, it can be observed that the ore is only located in areas where there is a grade above 0.5% TCo. The waste, on the other hand, is only in areas where the grade is below 0.5%. The Figure further indicates that there is a good intersection between the 3D model and the orebody, as the boundaries are clearly defined and match the drillhole model.

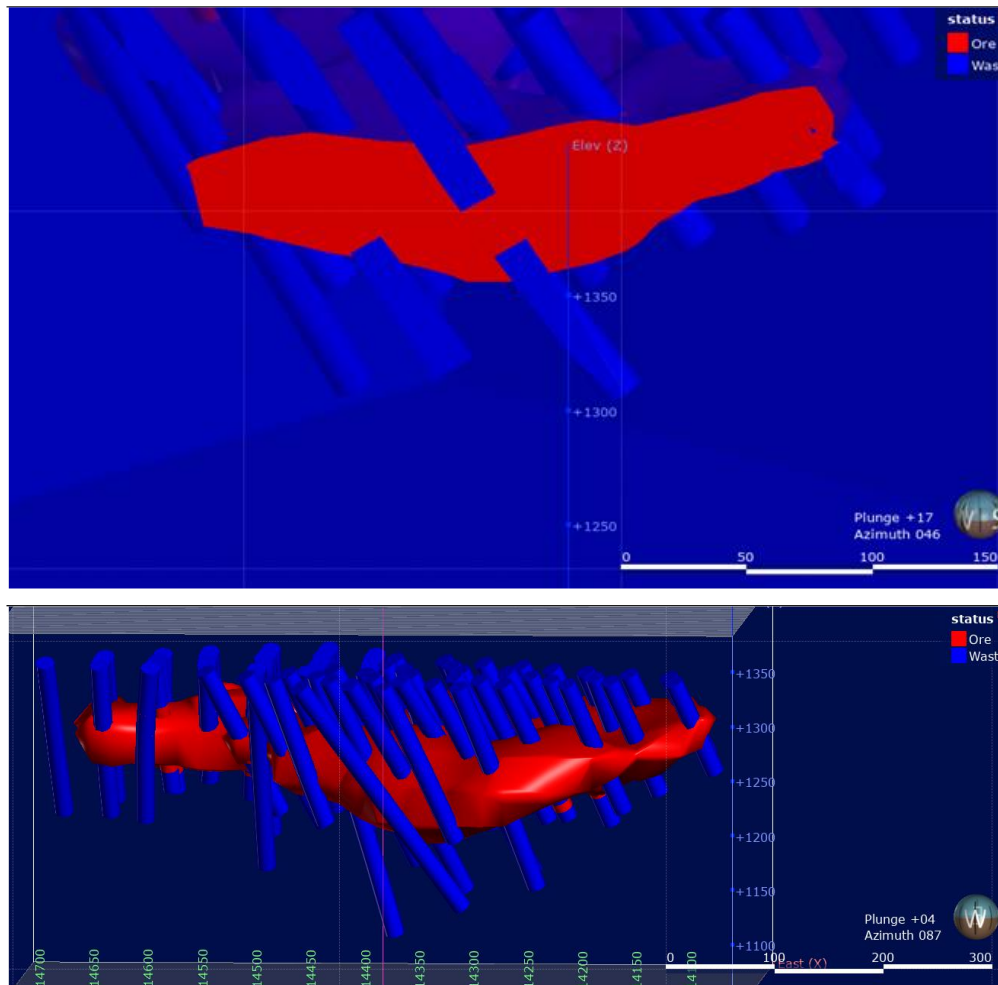


Figure 5.4: Visual comparison of the 3D orebody model with the drillhole data. a) Cross sectional view of orebody, b) Full view of the orebody

Overall, the validation of the data presented in this study is crucial for ensuring the accuracy and reliability of the 3D orebody model. The statistical and visual analyses performed against the drillhole data help to verify that the model accurately represents the deposit and identify any discrepancies that need to be addressed. The results of the validation process

demonstrate that the 3D orebody model produced using Leapfrog® Geo software accurately represents the deposit. The results of the validation indicate a good agreement between the 3D model and the economic drillhole model, and thus the orebody can be used as a reliable boundary during geometallurgical modelling using implicit and geostatistical methods. the orebody was used as a boundary from the following section up until the end of this thesis.

5.5 Implicit geometallurgical modelling

This section presents the results of implicit geometallurgical modelling. The methodology for this analysis is explained in Section 3.5. As stated in this chapter, the geometallurgical parameters modelled in this study include the BWI, rod mill index, RQD, DWI, Axb and Ai. The data were modelled using an implicit method called radial basis function, which is discussed in Section 2.5. The RBF method is a part of the Leapfrog® Geo software. In this section, the results of implicit geometallurgical modelling are presented in terms of iso-surfaces, 3D models and block models.

The iso-surface is a three-dimensional surface that represents a specific value of the parameter, with areas above the surface having higher values and areas below the surface having lower values. Three-dimensional models provide a comprehensive representation of the geometallurgical orebody. A block model represents a mineral deposit and its surroundings in a simplified manner, created using computer-generated "bricks" or cells that reflect small volumes of ore and waste rock (Poniewierski, 2019)

The iso-surfaces, 3D models and block models provide a comprehensive understanding of the geometallurgical parameters within the orebody and are a valuable tool for mine planning and optimization. In the following sections, modelling results and their implications for mining operations are discussed.

5.5.1 Iso-surfaces of geometallurgical parameters created using implicit methods

Figures 5.5 to 5.10 display the resulting iso-surfaces of the geometallurgical parameters created using the implicit method. The iso-surfaces are divided into three intervals. The software automatically selected these intervals by analysing the data.

The BWI iso-surfaces are shown in Figure 5.5, and three iso-surfaces were generated: 12 kWh/t (red), 13.2 kWh/t (blue), and 14.3 kWh/t (yellow). The iso-surface at 12 kWh/t represents values below this threshold while the iso-surface at 13.2 kWh/t represents values between 12 kWh/t and 13.2 kWh/t. Finally, the iso-surface at 14.3 kWh/t represents values above 13.2 kWh/t.

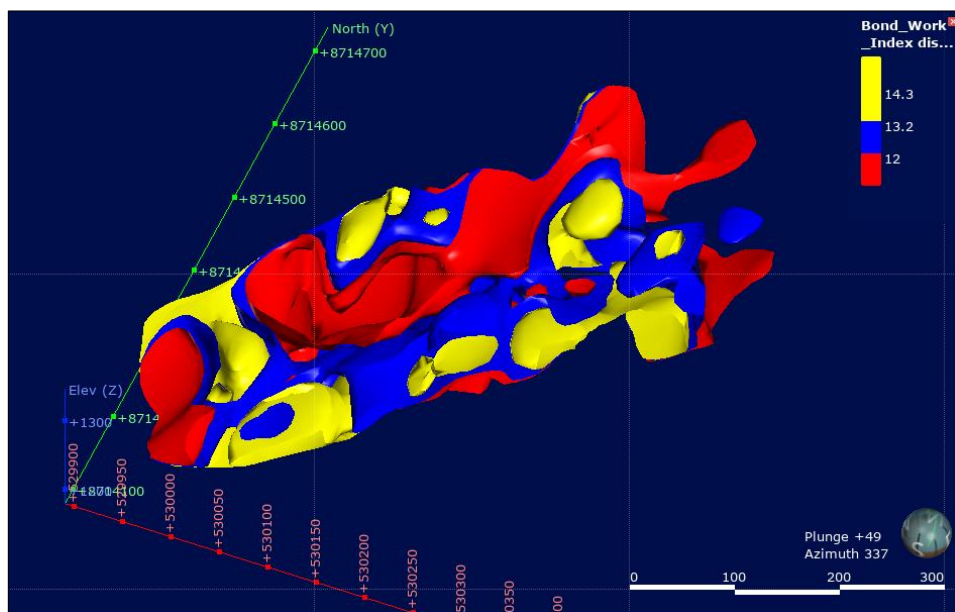


Figure 5.5: Iso-surface of Bond work index generated in Leapfrog® Geo

The implicit modelling of the rod mill index produced three iso-surfaces with values of 13.7 kWh/t, 15.2 kWh/t, and 18.9 kWh/t (Figure 5.6). The iso-surface at 13.7 kWh/t represents values below that threshold, while the 15.2 kWh/t iso-surface represents values between 13.7 kWh/t and 15.2 kWh/t. The 18.9 kWh/t iso-surface represents values above 15.2 kWh/t threshold.

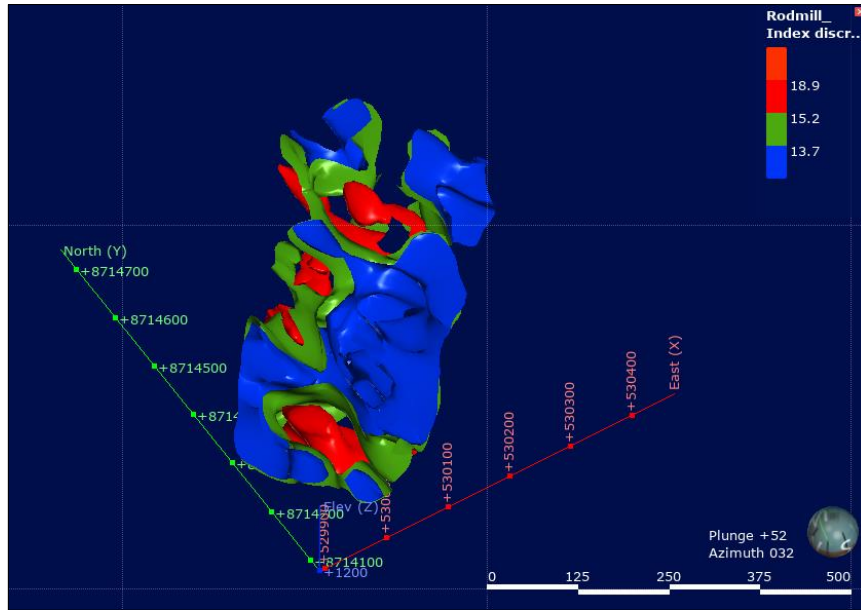


Figure 5.6: Iso-surface of rod mill index generated in Leapfrog® Geo

The RQD parameter resulted in three iso-surfaces of 50%, 61%, and 70% (Figure 5.7). The iso-surface at 50% represents values below this threshold, while the 61% iso-surface represents values between 50% to 61%. The 70.0% iso-surface represents values above 61%.

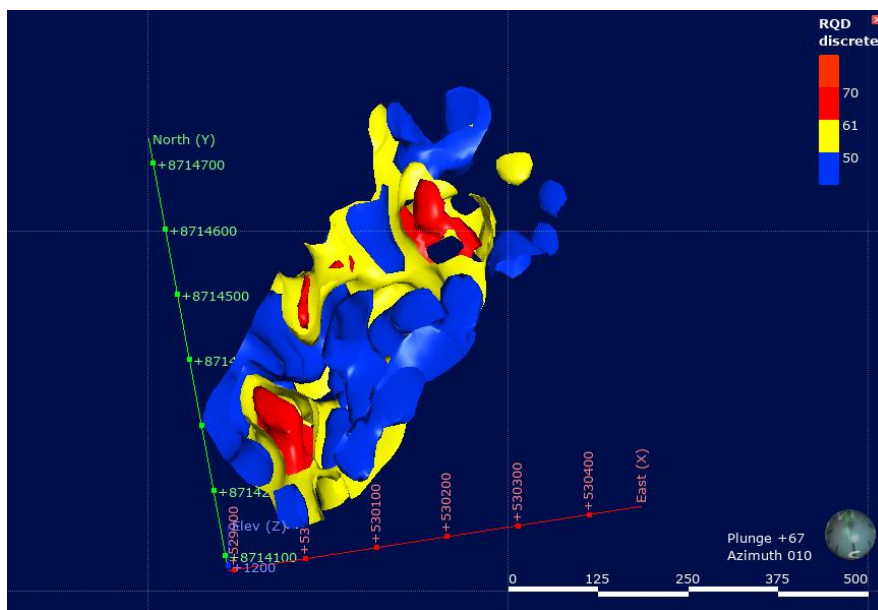


Figure 5.7: Iso-surface of RQD generated in Leapfrog® Geo

For the drop weight index, three iso-surfaces were created: 11.3 kWh/t, 13.7 kWh/t, and 16 kWh/t (Figure 5.8). The iso-surface at 11.3 kWh/t represents

values below this iso-surface. The 13.7 kWh/t represents values between 11.3 kWh/t and 13.7 kWh/t. The 16 kWh/t iso-surface represents values above 13.7 kWh/t.

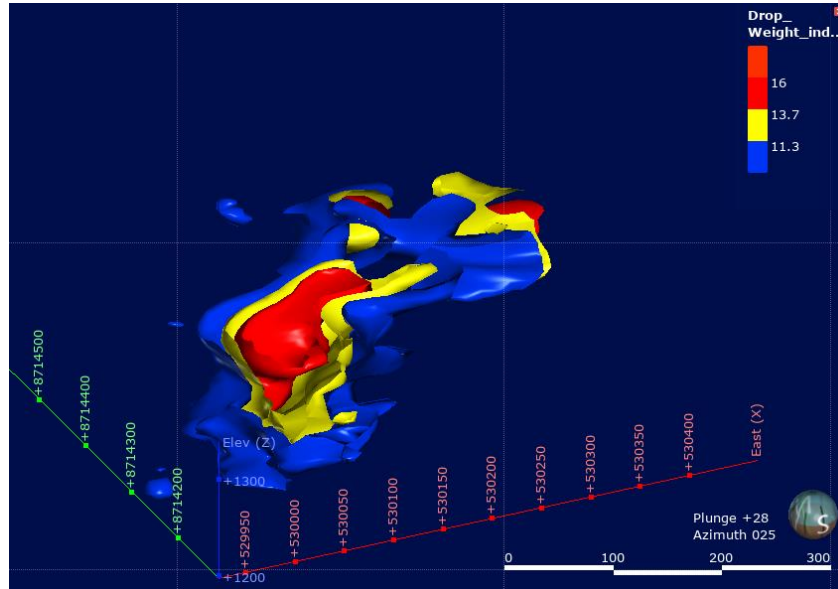


Figure 5.8: Iso-surface of drop weight index generated in Leapfrog® Geo

The results of the implicit modelling of the Axb index are presented in Figure 5.9, which shows three iso-surfaces of 1 kWh/t, 29 kWh/t, and 41.1 kWh/t. The iso-surface at 1 kWh/t represents values below this threshold, while the 29 kWh/t iso-surface represents values between 1 kWh/t to 29 kWh/t. The 41.0 kWh/t iso-surface represents values above 29 kWh/t.

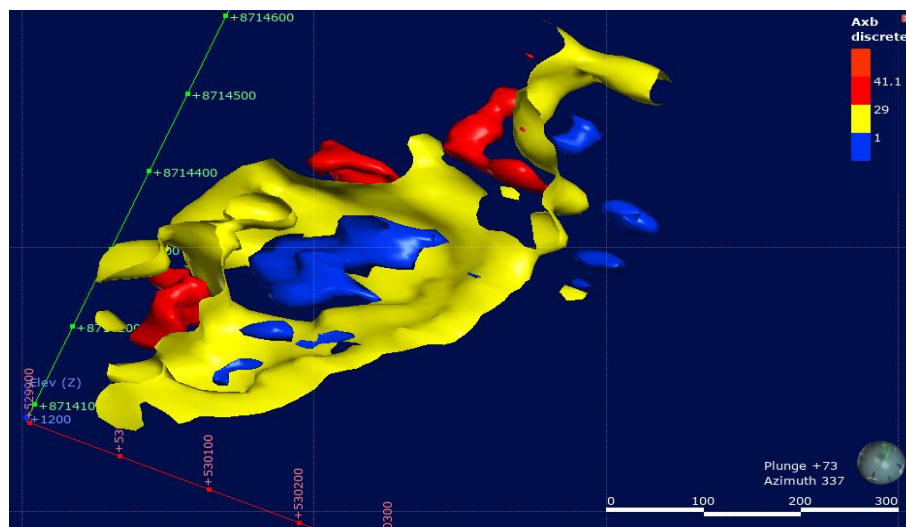


Figure 5.9: Iso-surface of Axb index generated in Leapfrog® Geo.

Finally, for the abrasion index, three iso-surfaces were created (Figure 5.10), with values of 0.02 kWh/t, 0.4 kWh/t, and 0.78 kWh/t. The iso-surface at 0.02 kWh/t represents values below this threshold, while the 0.4 kWh/t iso-surface represents values between 0.02 kWh/t to 0.4 kWh/t. The 0.78 kWh/t iso-surface represents values above 0.4 kWh/t.

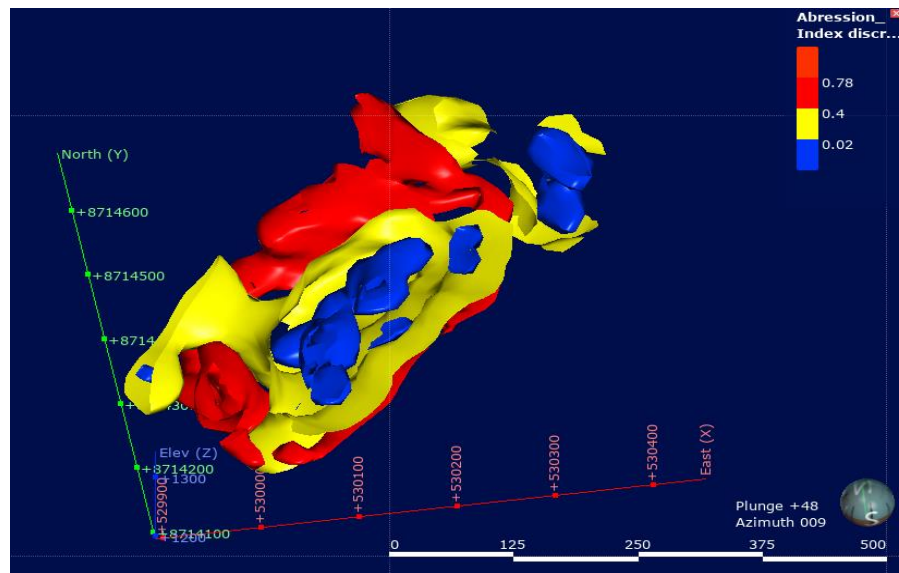


Figure 5.10: Iso-surface of abrasion index generated in Leapfrog® Geo.

The iso-surfaces created in this section are crucial for modelling. This is because they are used as a basis for creating a 3D model. The iso-surfaces created in this section were used in the following section to generate geometallurgical 3D models.

5.5.2 3D geometallurgical model generated from iso-surfaces

The iso-surfaces that were previously generated in Section 5.5.1 using Leapfrog® Geo software are used here as the basis for creating a 3D model, as described in Section 5.5.1. Now in this section, the iso-surfaces were interpolated using the RBF method reviewed in Section 2.5.1 about the Leapfrog® methodology, to generate 3D models. The methodology for modelling is highlighted in Section 3.5.

The 3D orebody domain created in Section 5.3 was used as a boundary during the interpolation of iso-surfaces. The software automatically created intervals during interpolation, based on the intervals of the iso-surfaces. In the Figures, the intervals are represented by different colours. The resulting 3D models provide a visual representation of the distribution of the geometallurgical parameters within the orebody.

Intervals for various parameters were generated and represented by 3D models. For BWI, the intervals were represented by 12 kWh/t, 13.2 kWh/t, and 14.3 kWh/t. The rod mill index had intervals represented 13.7 kWh/t, 15.2 kWh/t, and 18.9 kWh/t. For the RQD parameter, the intervals were represented by 50%, 61%, and 70%.

The DWI parameter had intervals represented by 11.3 kWh/t, 13.7 kWh/t and 16 kWh/t. The Axb index had intervals represented by 1 kWh/t, 29 and 41.1 kWh/t. Lastly, the Ai had intervals represented by 0.02 kWh/t, 0.4 kWh/t, and >0.78 kWh/t. Figures 5.11 to 5.16 represent the 3D models of the BWI, rod mill index, RQD, DWI, Axb and Ai, respectively.

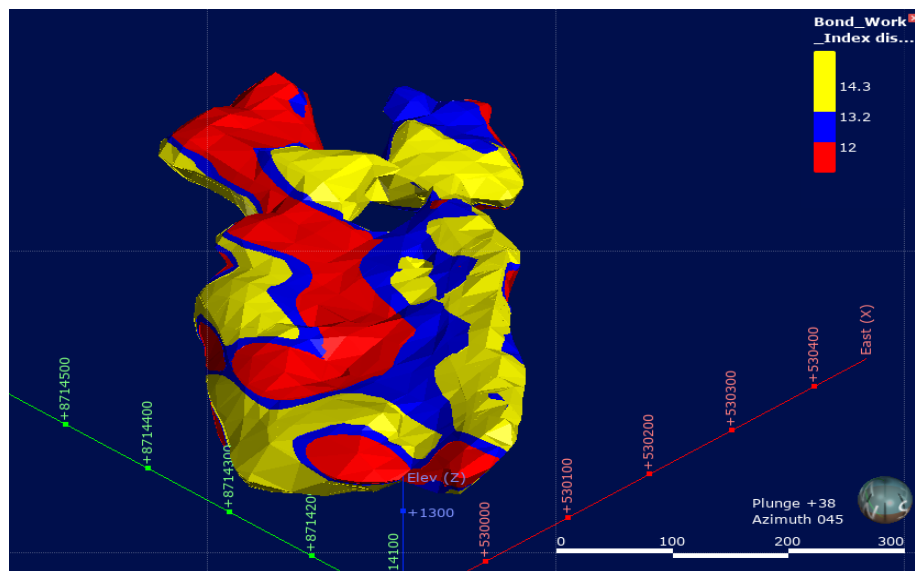


Figure 5.11: A 3D model of the Bond work index generated using an implicit method

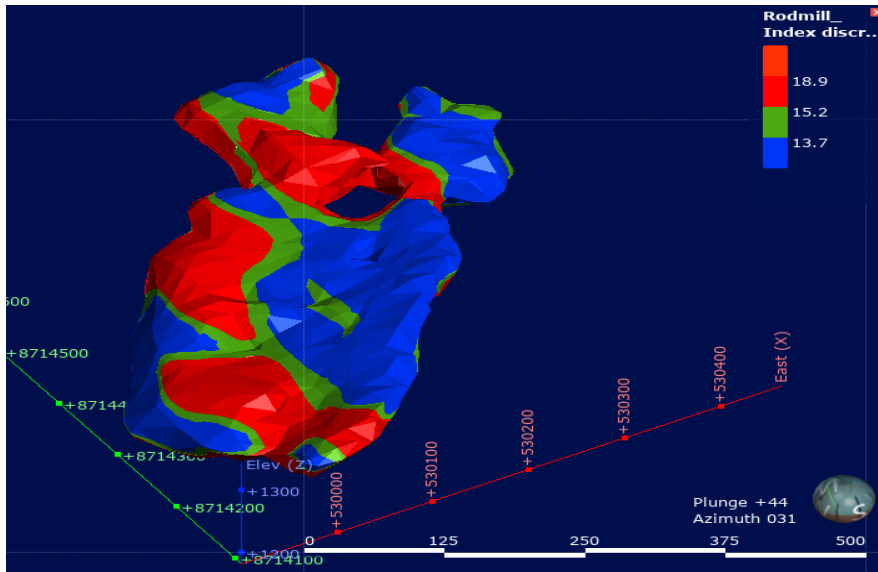


Figure 5.12: A 3D model of the rod mill index generated using an implicit method

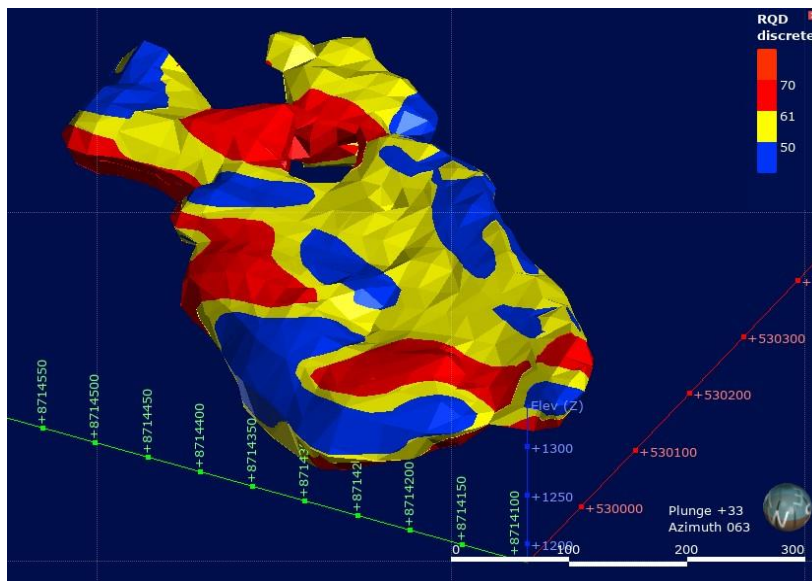


Figure 5.13: A 3D model of RQD generated using an implicit method

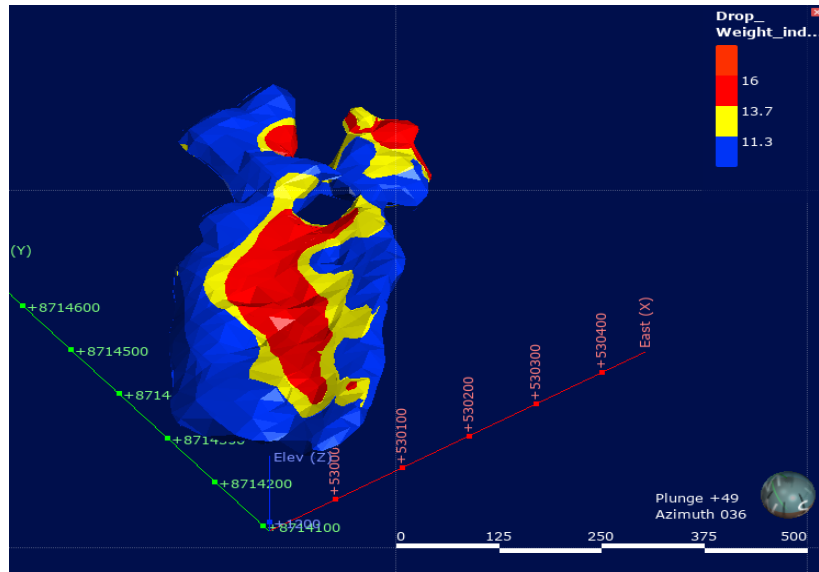


Figure 5.14: A 3D model of the drop weight index generated using an implicit method

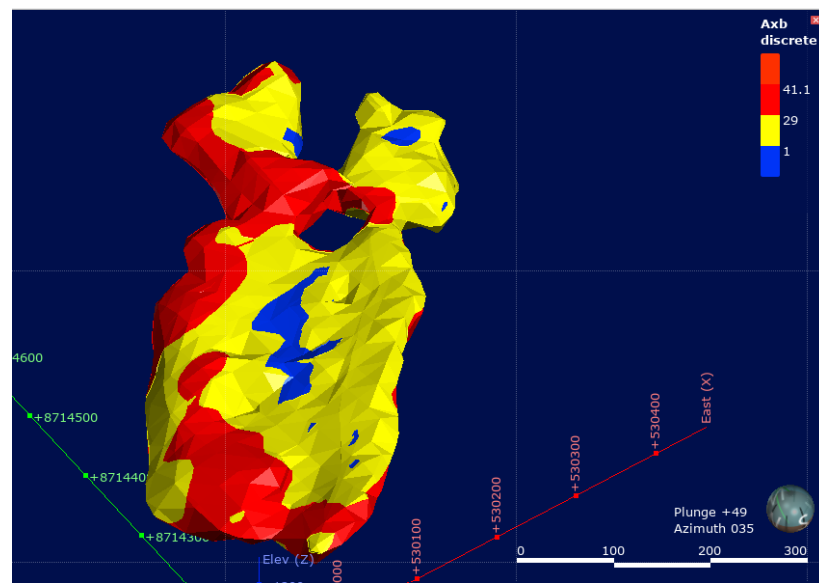


Figure 5.15: A 3D model of the Axb index generated using an implicit method

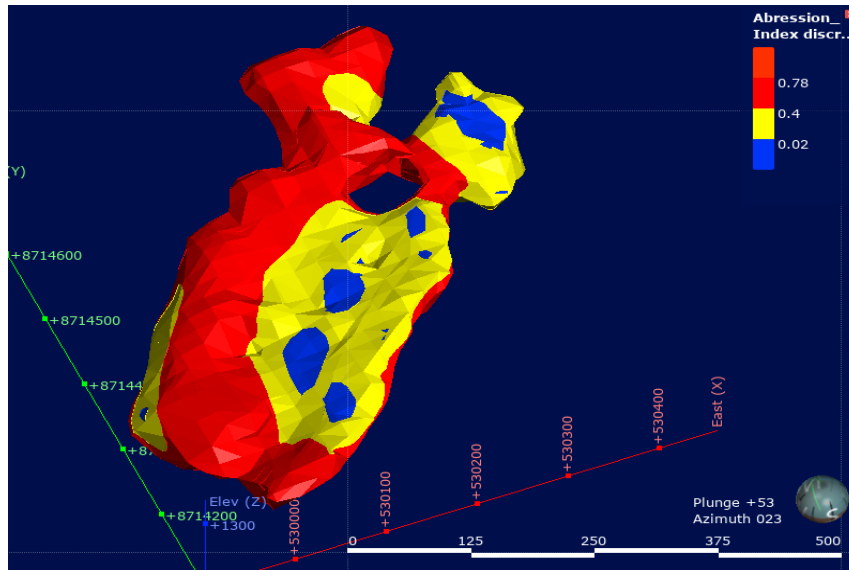


Figure 5.16: A 3D model of the abrasion index generated using an implicit method

Figures 5.11 to 5.16 indicate the geometallurgical 3D models that were interpolated from the iso-surfaces created in Section 5.5.1. The purpose of creating 3D models is to use them for block modelling. Block models are important in mine planning as they are used to calculate the parameters of mine planning. The following section presents the results of the block model based on the 3D model generated in this section.

5.5.3 Geometallurgical block models

This section presents the block modelling results obtained from 3D models generated using the implicit method as outlined in Section 3.7. The block models were created using Leapfrog® Geo software and are presented in Figures 5.17 to 5.22. Tables 5.2 to 5.7 provide the data for each block model. Each block model is composed of 6 416.00 blocks, with a total volume of 6 416 000.00 cubic metres (m³). The data for the tables were obtained from Leapfrog® Geo and plotted into a table format using Microsoft® Excel®.

The BWI block model results are shown in Figure 5.17 and Table 5.2. The blocks in the model are classified into three zones: those with values less than 12 kWh/t are shown in red, those between 12 kWh/t and 13.2 kWh/t are shown in blue, and those above 13.2 kWh/t are shown in yellow. The minimum and maximum values of the BWI among the blocks are 6.49 kWh/t and 19.97 kWh/t, respectively.

Table 5.2. BWI data generated from the implicit block model.

Name	Bond Work Index (kWh/t)
Block Count	6 416.00
Volume	6 416 000.00 m ³
Minimum	6.49 (kWh/t)
Maximum	19.97 (kWh/t)

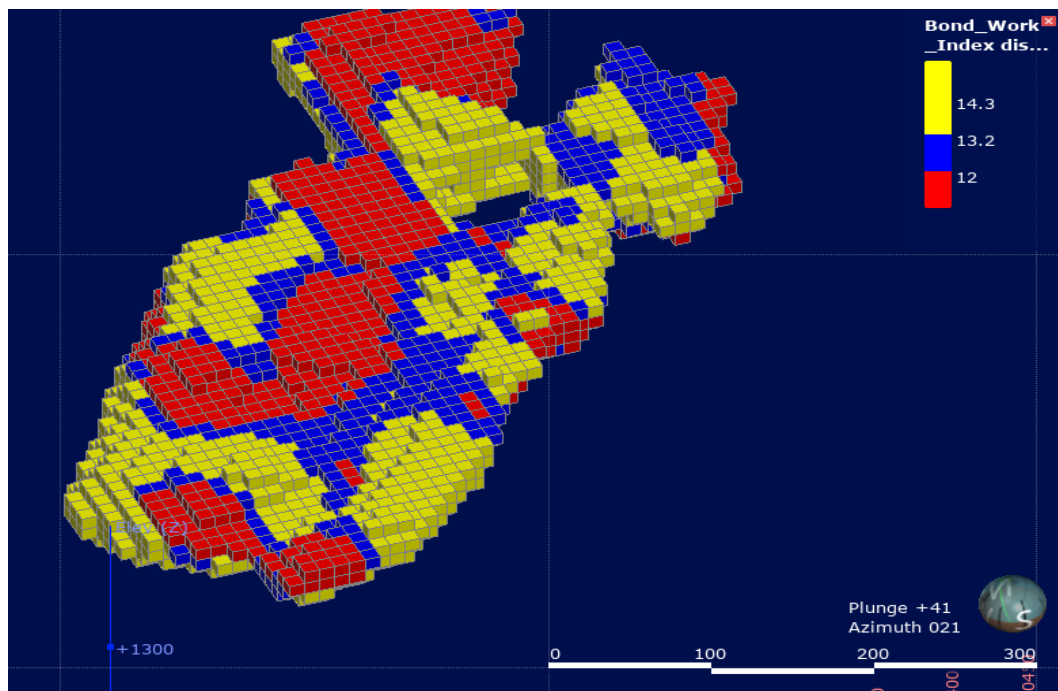


Figure 5.17: BWI-based block model generated using Leapfrog® Geo

The rod mill index block model results are shown in Figure 5.18 and Table 5.3. The blocks are separated into those less than 13.7 kWh/t in blue, those between 13.7 kWh/t and 15.2 kWh/t in green, and those above 15.2 kWh/t

in red. The minimum and maximum values of the rod mill index among the blocks are 3.75 kWh/t and 19.89 kWh/t, respectively.

Table 5.3. Rod mill index data generated from the implicit block model

Name	Rod mill index (kWh/t)
Block Count	6 416
Volume	6 416 000 m ³
Minimum	3.75 (kWh/t)
Maximum	19.89 (kWh/t)

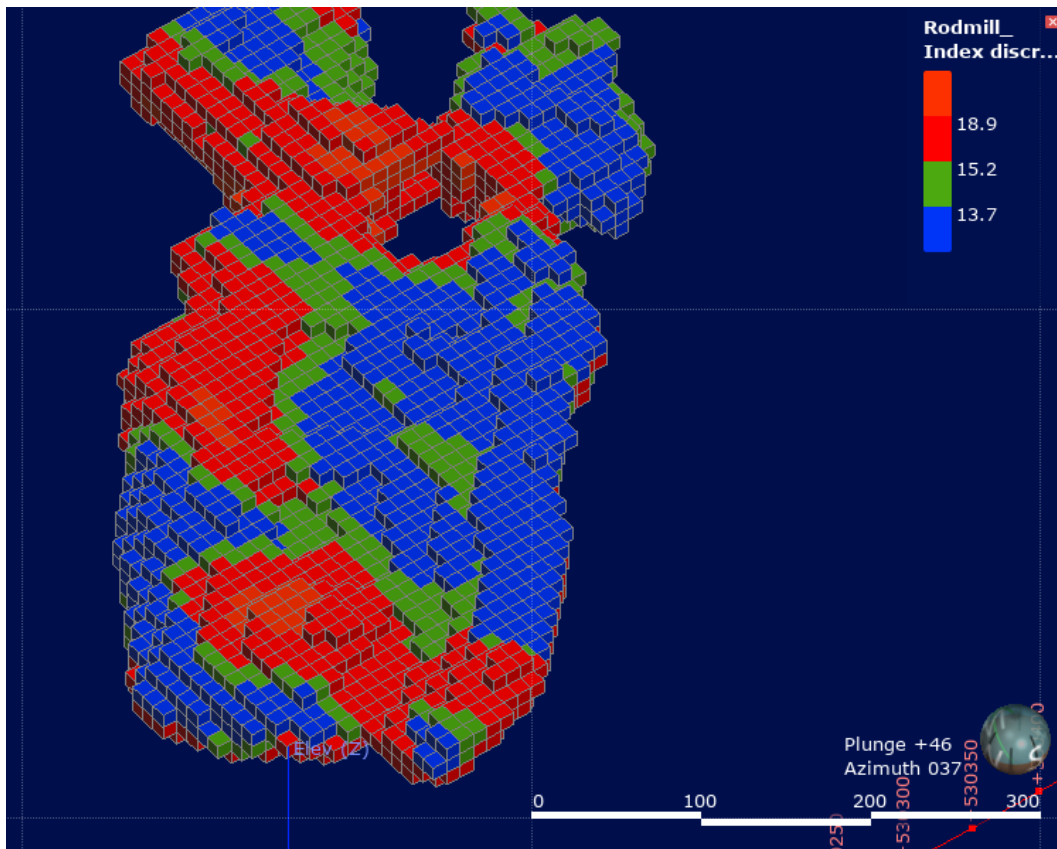


Figure 5.18: Block model of the rod mill index generated using Leapfrog® Geo

The RQD block model results are displayed in Figure 5.19 and Table 5.4. The blocks are separated into those lower than 50% in blue, those between 50% and 61% in yellow, and those above 61% in the red. The minimum and

maximum values of the RQD among the blocks are 15.03% and 75.85%, respectively.

Table 5.4. RQD index data generated from the implicit block model

Name	RQD (%)
Block Count	6 416
Volume	6 416 000 m ³
Minimum	15.03 %
Maximum	75.85 %

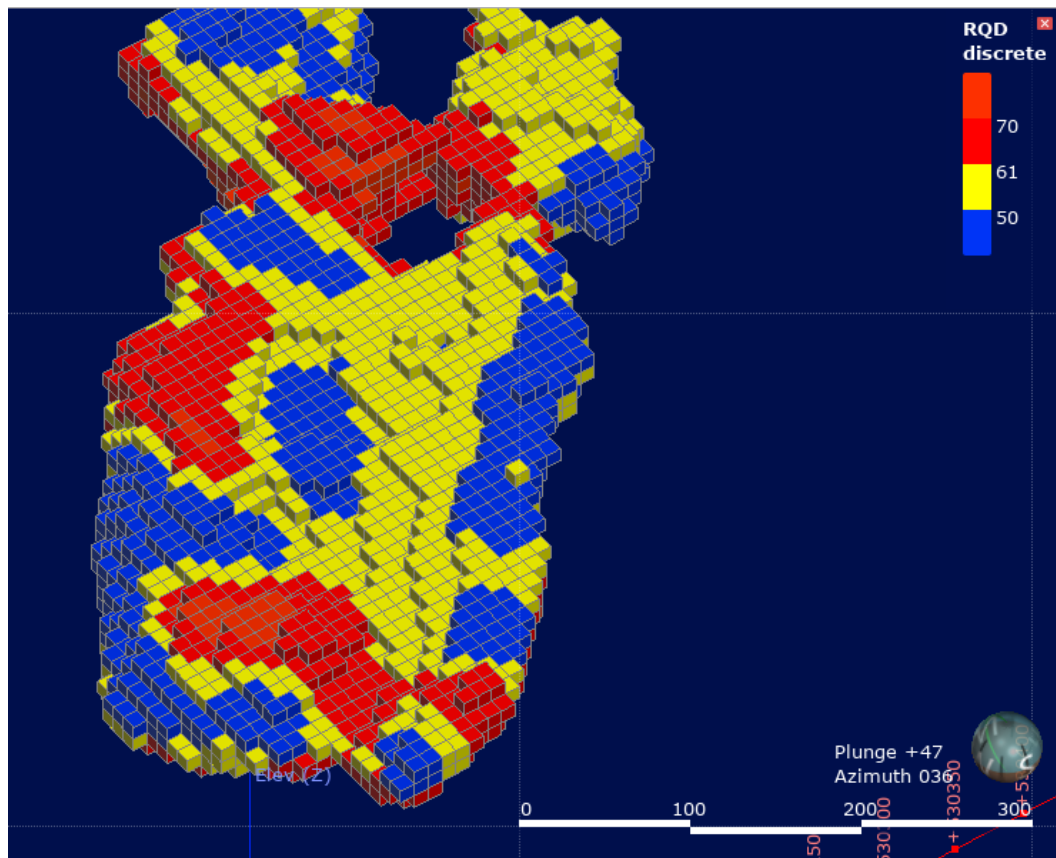


Figure 5.19: RQD-based block model generated using Leapfrog® Geo

The DWI block model results are shown in Figure 5.20 and Table 5.5. The blocks are separated into those less than 11.3 kWh/h in blue, those between 11.3 kWh/h and 13.7 kWh/t in yellow, and those above 13.7 kWh/t in red.

The minimum and maximum values of the drop weight index among the blocks are 0.00 kWh/t and 21.58 kWh/t, respectively.

Table 5.5. DWI data generated from the implicit block model

Name	Drop_Weight_index (kWh/t)
Block Count	6 416.00
Volume	6 416 000.00 m ³
Minimum	0.00 (kWh/t)
Maximum	21.58 (kWh/t)

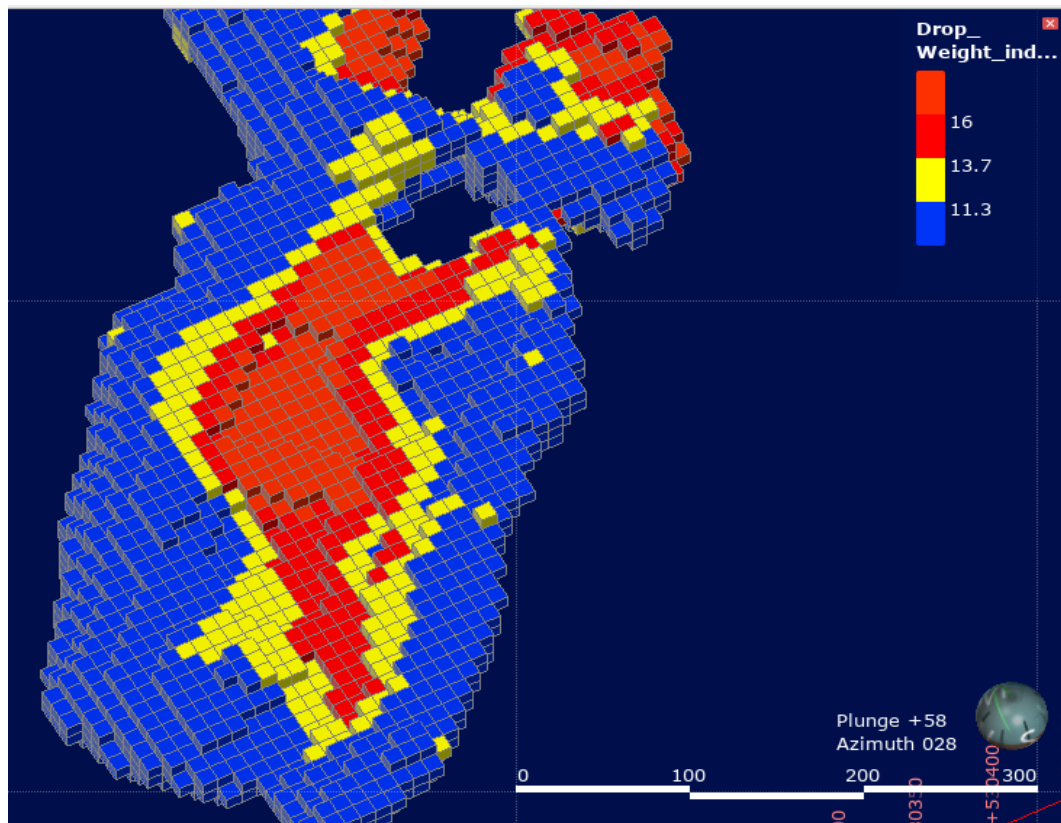


Figure 5.20: DWI-based block model generated using Leapfrog® Geo

The Axb index block model results are presented in Figure 5.21 and Table 5.6. The blocks are separated into those less than 1 kWh/h in blue, those between 1 kWh/h and 29 kWh/t in yellow, and those above 29 kWh/t in red. The minimum and maximum values of the Axb index among the blocks are 0.00 kWh/t and 45.49 kWh/t, respectively.

Table 5.6. Axb index data generated from the implicit block model

Name	Axb (kWh/t)
Block Count	6 416
Volume	6 416 000 m ³
Minimum	0.00 (kWh/t)
Maximum	45.49 (kWh/t)

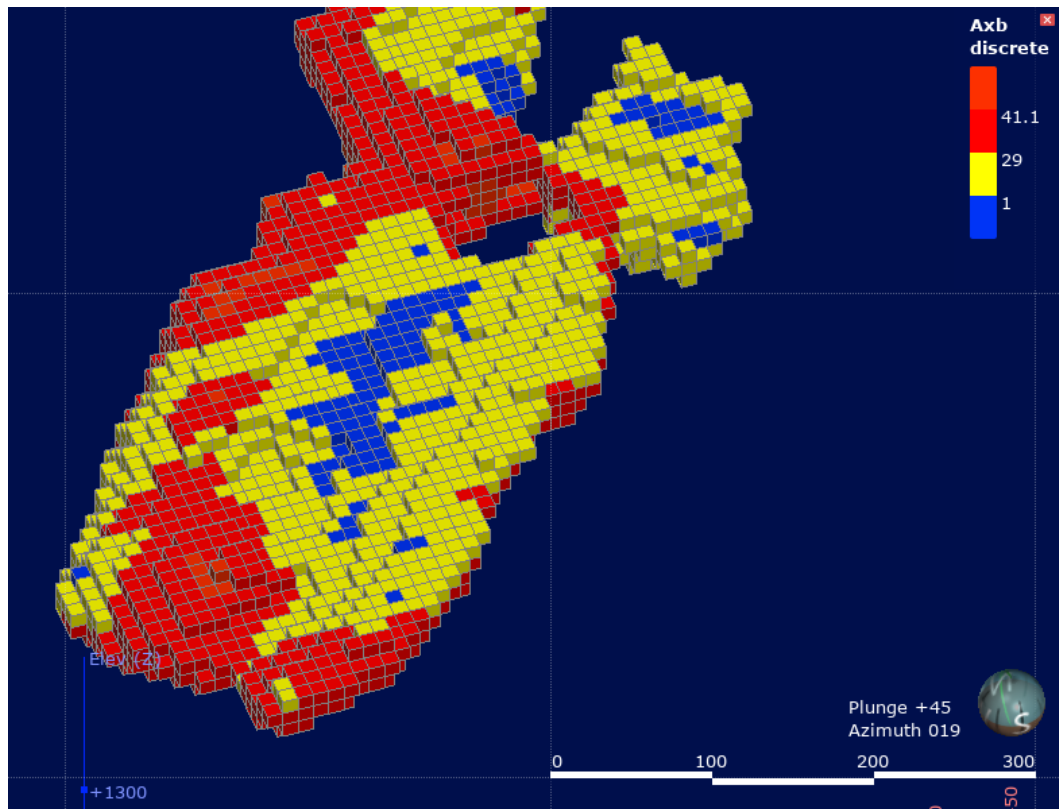


Figure 5.21: Block model of Axb index generated using Leapfrog® Geo

Lastly, the abrasion index block model results are shown in Figure 5.22 and Table 5.7. The blocks are separated into those less than 0.02 kWh/h in blue, those between 0.02 kWh/h and 0.4 kWh/t in yellow, and those above 0.4 kWh/t in red. The minimum and maximum values of the abression66 index among the blocks are 0 kWh/t and 0.93 kWh/t, respectively.

Table 5.7. Abrasion index data generated from the implicit block model

Name	Abrasion_Index (kWh/t)
Block Count	6 416
Volume	6 416 000 m ³
Minimum	0.00 (kWh/t)
Maximum	0.97 (kWh/t)

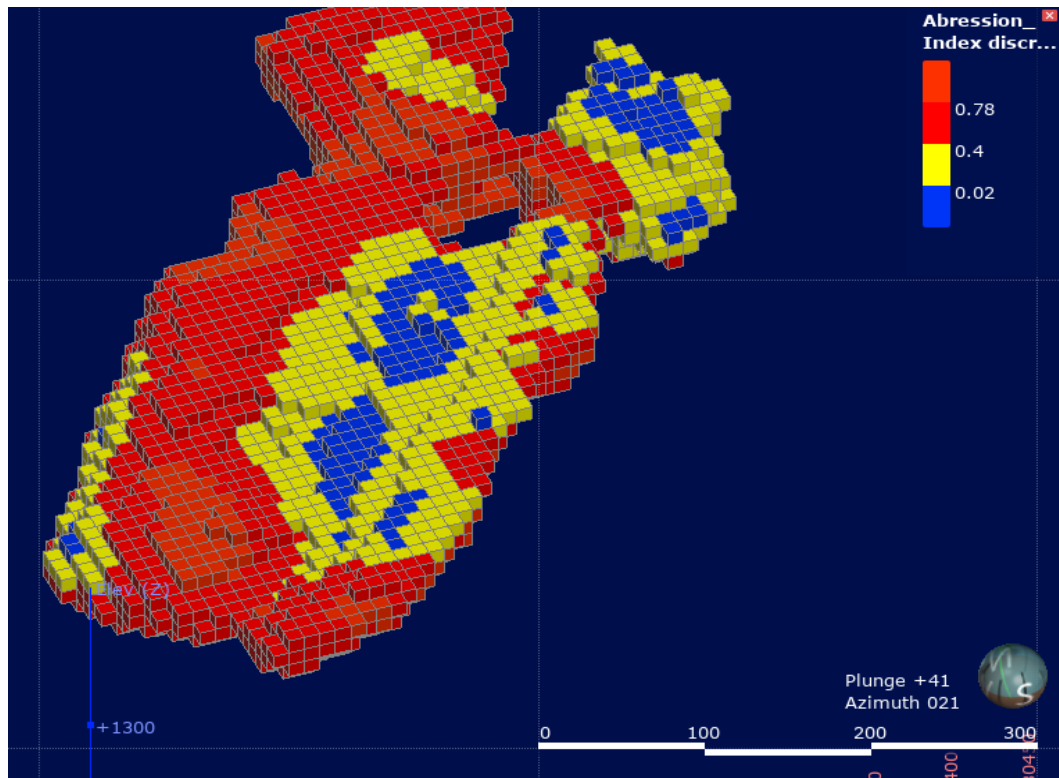


Figure 5.22: Block model of abrasion index generated using Leapfrog® Geo

5.6 Summary of the findings

The main objective of the chapter was to model geometallurgical data using the implicit method. The geometallurgical data modelled in this chapter included the Bond work index, rod mill index, RQD, drop weight index, Axb, and abrasion index. The radial basis function (RBF) was used to interpolate

the data. The workflow that was used to model the geometallurgical data was as follows. Firstly, the orebody model was delineated, and the iso-surfaces of the geometallurgical data were created. The iso-surfaces are created automatically during interpolation with RBF.

The study used Leapfrog® Geo software, which incorporates multiple sources of data to create three-dimensional geological models. The economic model of the original drillhole domain was delineated based on an assay cut-off grade of 0.5% TCo, separating the ore and waste zones. The 3D and 2D orebody domains were generated based on grade data of TCo, using an indicator radial base function and a cut-off grade of 0.5% TCo.

Validation of the 3D model was done by comparing it with the drillhole economic model. The statistical analysis of the ore and waste in the 3D model and the drillhole data show that the 3D model accurately represents the orebody and waste, as the differences in the mean, minimum, and maximum values are within an acceptable range.

The results of implicit geometallurgical modelling were presented. The modelling was conducted using the radial basis function method, which was discussed in Chapter 2. The results were presented in the form of iso-surfaces, 3D models, and block models. Iso surfaces are three-dimensional surfaces that represent a specific value of a parameter, with areas above the surface having higher values and areas below the surface having lower values. The iso-surfaces were divided into three intervals. The software automatically selected these intervals by analysing the data.

The iso-surfaces created for each parameter in this section were used as the basis for creating 3D models in the following section. For the Bond work index, rod mill index, RQD, drop weight index, Axb index, and abrasion index, three iso-surfaces were generated for each parameter. The iso-surface values for each parameter are presented in detail in Figures 5.5 to 5.10.

The 3D models provide a comprehensive representation of the geometallurgical orebody, and the block models represent the mineral deposit and its surroundings in a simplified manner. The results of the implicit modelling of the parameters were crucial for generating the iso-surfaces used in the 3D models.

In Figures 5.11 to 5.16, the 3D models for each parameter are presented. The models provide a detailed understanding of the geometallurgical parameters within the orebody and are valuable tools for mine planning and optimization. The 3D models were generated using Leapfrog® Geo software, and each block model was composed of 6 416 blocks with a total volume of 6 416 000 m³. The minimum and maximum values for each index among the blocks were obtained and presented in Tables 5.2 to 5.7.

Results of the BWI-based block model showed that the blocks were classified into three zones, with the minimum and maximum values among the blocks being 6.49 kWh/t and 19.97 kWh/t, respectively. The rod mill index block model results were separated into three zones, with the minimum and maximum values among the blocks being 4.86 kWh/t and 20.96 kWh/t, respectively. The RQD block model results were separated into three zones, with the minimum and maximum values among the blocks being 15.03% and 75.85%, respectively.

The results of the DWI-based block model were separated into three zones, with the minimum and maximum values among the blocks being 3.73 kWh/t and 20.57 kWh/t, respectively. The Axb index block model results were separated into three zones, with the minimum and maximum values among the blocks being 0 kWh/t and 44.67 kWh/t, respectively. Lastly, the abrasion index block model results were separated into three zones, with the minimum and maximum values among the blocks being 0 kWh/t and 0.93 kWh/t, respectively.

The results of this chapter show that implicit geometallurgical modelling using the radial basis function method is an effective approach for modelling the geometallurgical parameters of an orebody. These models could be

useful for orebody characterization, resource estimation, mine planning, and decision-making in the mining industry.

Chapter 6 Geostatistical modelling of geometallurgical data

6.1 Introduction

The aim of this chapter is to present the results of geostatistical block modelling of geometallurgical data using the Ordinary Kriging method. The primary objective of this study was to model the geometallurgical parameters for subsequent comparison with implicit geometallurgical modelling results (Section 5.5) in Chapter 7. The methodology used in generating the geometallurgical block models is discussed in Section 3.6.

The parameters modelled include BWI, rod mill index, RQD, DWI, Axb and Ai. The Leapfrog® Geo software was employed for the estimation and generation of the geometallurgical block models. Ordinary Kriging was selected as the geostatistical method for estimating the block models due to its common use in geostatistical modelling, as referenced. Section 3.6.1 outlines the methodology used for Ordinary Kriging. Results are presented in the form of tables and Figures, with data generated in Leapfrog® geo and plotted using Microsoft® Word®.

The generated block model (Figure 6.1) is made up of 6 416 blocks. The volume of the block model is 6 416 000 m³.

6.2 Results of block modelling

Table 6.1 and Figure 6.1 summarise the results of the BWI-based block model, with blocks classified into three zones based on their values. The blocks with values less than 12 kWh/t are shown in red, those between 12 kWh/t and 13.2 kWh/t are shown in blue, and those above 13.2 kWh/t are shown in yellow. The minimum and maximum values of the Bond Work Index among the blocks are 7 kWh/t and 19.43 kWh/t, respectively.

Table 6.1. BWI data generated from the geostatistical block model.

Name	Bond_Work_Index (kWh/t)
Block Count	6 416
Volume	6 416 000 m ³
Minimum	7.00 (kWh/t)
Maximum	19.43 (kWh/t)

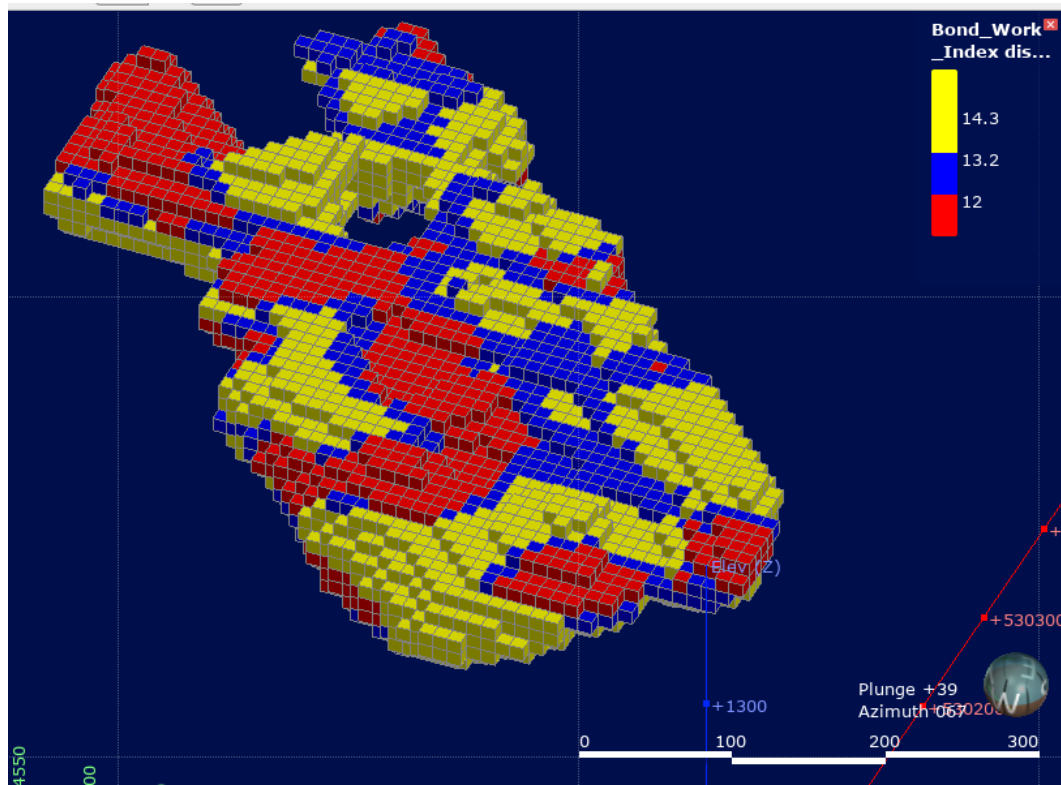


Figure 6.1: BWI-based block model generated through the geostatistical method

Similarly, the results of the block models representing the distributions of the rod mill index, RQD Index, drop weight index, Axb index, and Ai respectively are shown in Figures 6.2 – 6.5 and Tables 6.2 – 6.5, with blocks classified into three zones based on their values. The rod mill index blocks with values less than 13.7 kWh/t are shown in blue, those between 13.7 kWh/t and 15.2 kWh/t are shown in green, and those above 15.2 kWh/t are shown in red (Figure 6.2). The minimum and maximum values of the rod

mill index among the blocks are 4.25 kWh/t and 18.90 kWh/t, respectively (Table 6.2).

Table 6.2. Rod mill index data generated from the geostatistical block model

Name	Rod mill index (kWh/t)
Block Count	6 416
Volume	6 416 000 m ³
Minimum	4.25 kWh/t
Maximum	18.90 kWh/t

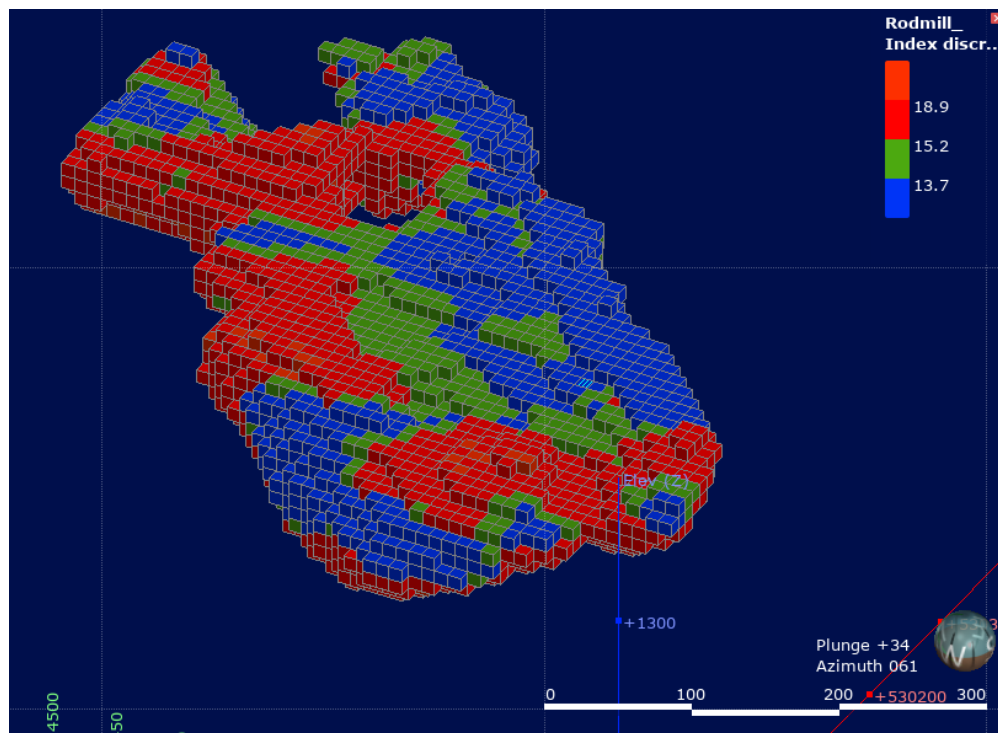


Figure 6.2: Block model of the rod mill index generated through the geostatistical method

For the RQD-based block model, blocks with values less than 50% are shown in blue, those between 50% and 61% are shown in yellow, and those above 61% are shown in red (Figure 6.3). The minimum and maximum values of the RQD index among the blocks are 16.99% and 71.31% respectively (Table 6.3).

Table 6.3. RQD data generated from the geostatistical block model

Name	RQD (%t)
Block Count	6 416
Volume	6 416 000 m ³
Minimum	16.99 %
Maximum	71.31 %

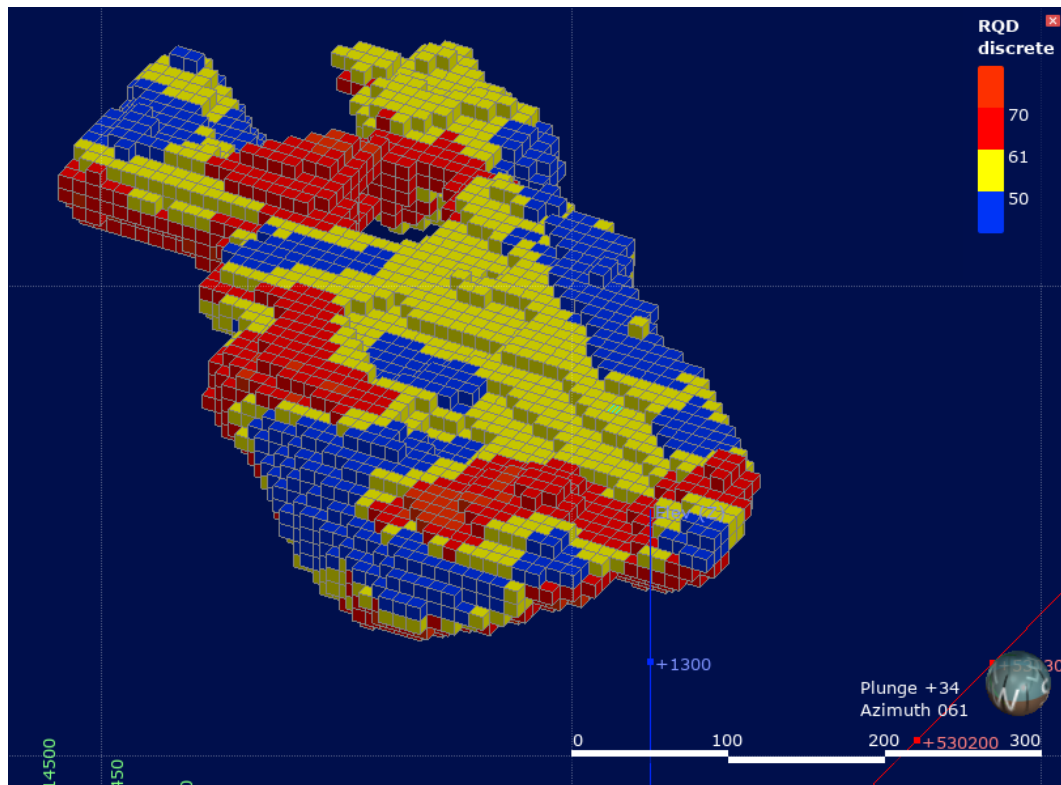


Figure 6.3: RQD-based block model generated through the geostatistical method

The DWI-based block model shows blocks with values less than 11.3 kWh/t in blue, those between 11.3 kWh/t and 13.7 kWh/t in yellow, and those above 13.7 kWh/t in red (Figure 6.4). The minimum and maximum values of the Drop Weight Index among the blocks are 0.06 kWh/t and 20.97 kWh/t, respectively (Table 6.4).

Table 6.4. DWI data generated from the geostatistical block model

Name	DWI (kWh/t)
Block Count	6 416
Volume	6 416 000 m ³
Minimum	0.06 kWh/t
Maximum	20.97 kWh/t

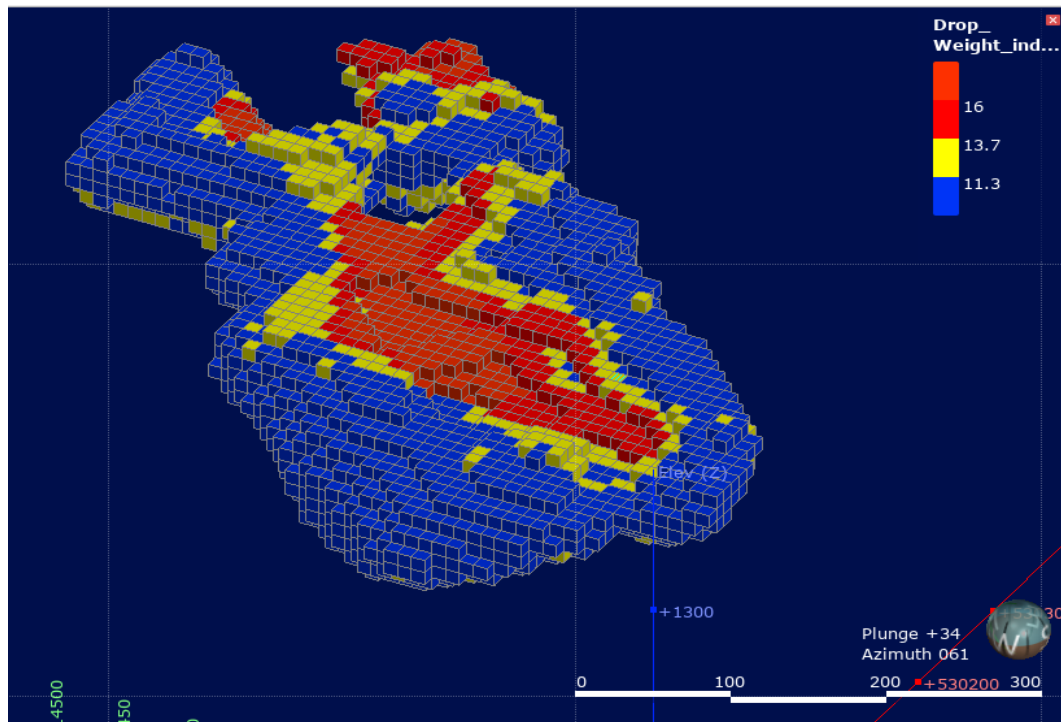


Figure 6.4. DWI-based block model generated through the geostatistical method

The block model of the Axb index displays blocks with values less than 1 kWh/t in blue, those between 1 kWh/t and 29 kWh/t in yellow, and those above 29 kWh/t in red (Figure 6.5). The minimum and maximum values of the Axb Index among the blocks are 0.31 kWh/t and 41.10 kWh/t, respectively (Table 6.5).

Table 6.5. Axb index data generated from the geostatistical block model

Name	Axb (kWh/t)
Block Count	6 416
Volume	6 416 000 m ³
Minimum	0.31 kWh/t
Maximum	41.10 kWh/t

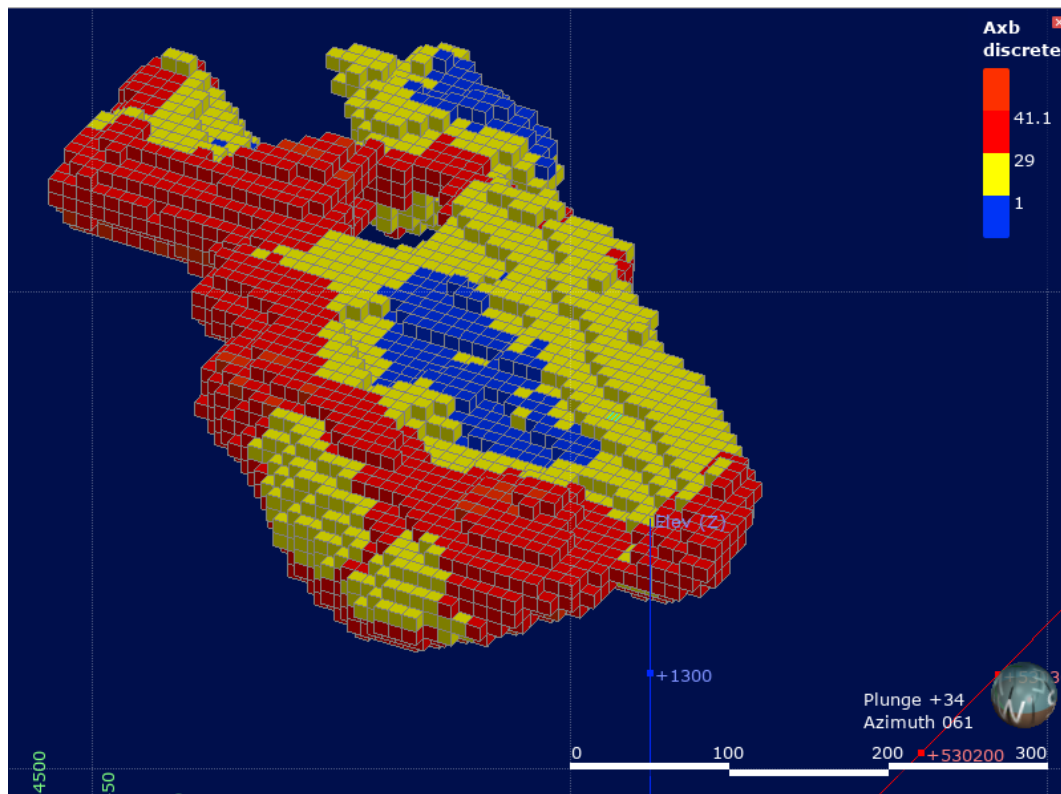


Figure 6.5: Block model of the Axb index generated through the geostatistical method

Finally, the Ai-based block model exhibits blocks with values less than 0.02 kWh/t in blue, those between 0.02 kWh/t and 0.4 kWh/t in yellow, and those above 0.4 kWh/t in red (Figure 6.6). The minimum and maximum values of the abrasion index among the blocks are 0.02 kWh/t and 0.78 kWh/t, respectively.

Table 6.6. Abrasion index data generated from the geostatistical block model

Name	Abrasion Index (kWh/t)
Block Count	6 416
Volume	6 416 000 m ³
Minimum	0.02 kWh/t
Maximum	0.78 kWh/t

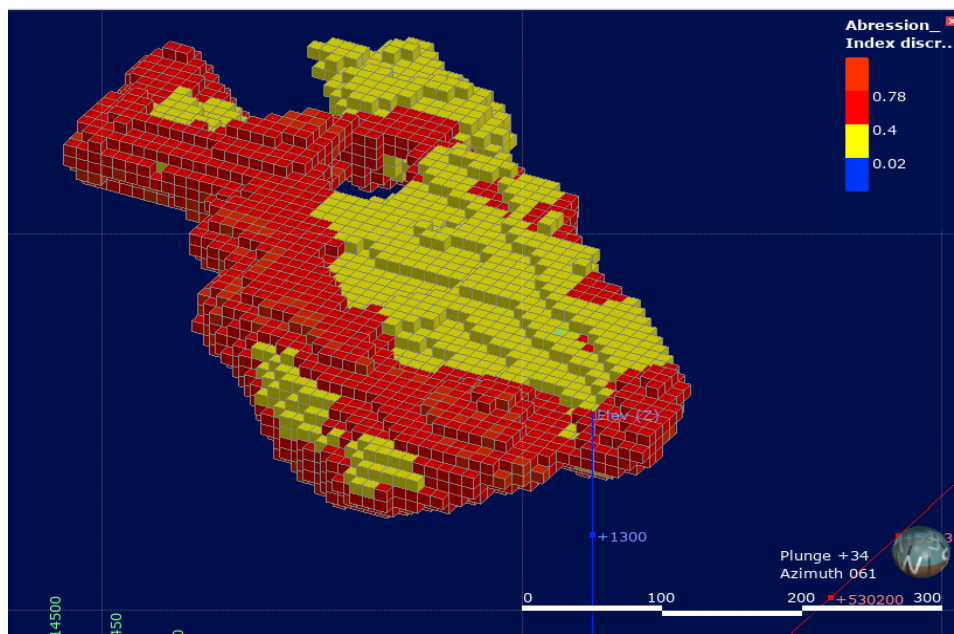


Figure 6.6: Block model of the abrasion index generated through the geostatistical method

6.3 Summary and conclusions

The main purpose of this chapter was to create a block model of geometallurgical data using the traditional geostatistical method. Ordinary Kriging was used as it is one of the widely used methods in estimation in mining. The block models were created using orebody domains as boundaries. The statistical data of the block model were used to present the results. The block model was also visualised. The block model results for

six geometallurgical parameters were presented in this chapter. The Bond Work Index block model was classified into three zones: red blocks with values less than 12 kWh/t, blue blocks between 12 kWh/t and 13.2 kWh/t, and yellow blocks above 13.2 kWh/t.

The rod mill Index, RQD Index, drop weight Index, Axb Index, and abrasion Index block models were also classified into three zones based on their respective values.

The minimum and maximum values for each parameter among the blocks were also reported. The BWI had a minimum value of 7 kWh/t and a maximum value of 19.43 kWh/t. The rod mill index had a minimum value of 7.0 kWh/t and a maximum value of 19.42 kWh/t. The RQD Index had a minimum value of 16.99% and a maximum value of 71.31%.

The drop weight Index had a minimum value of 0.06 kWh/t and a maximum value of 20.97 kWh/t. The Axb Index had a minimum value of 0.31 kWh/t and a maximum value of 41.10 kWh/t. The abrasion Index had a minimum value of 0.02 kWh/t and a maximum value of 0.78 kWh/t.

In conclusion, the geostatistical block modelling using Simple Kriging was successfully conducted for six geometallurgical parameters. The results of the block models were classified into three zones and the minimum and maximum values were reported. These block models will be useful for future resource estimation and mine planning.

As stated at the beginning of this chapter, the purpose of this chapter was to model the geometallurgical parameters for subsequent comparison with implicit geometallurgical modelling results (Section 5.5). Therefore, the following chapter will deal with the comparison between the two methods.

Chapter 7 Comparison of implicit modelling method with geostatistical method technique

7.1 Introduction

The objective of this chapter is to assess the efficacy of implicit geometallurgical modelling in comparison to geostatistical modelling. Specifically, the comparison is done by evaluating the performance of the implicit method in modelling geometallurgical data. The implicit geometallurgical results presented in Chapter 5 are compared with the geostatistical results presented in Chapter 6.

The comparison is conducted using three different methods: statistical comparison, swath plot comparison, and visual plot comparison. Tables and Figures generated using Leapfrog® Geo and Microsoft® Excel® software are utilized to present the data.

Tables 7.1 to 7.6 present the statistical comparison of geometallurgical parameter modelling between the two methods. Figures 7.1 to 7.6 present the swath plot comparison between the two methods. The swath plot is compared in the swath X direction, using the averages of the geometallurgical parameters. Figures 7.1 to 7.6 represent the visual comparison between the two methods. The circles in the Figures indicating differences between the block model were drawn using Microsoft® Paint®.

The geometallurgical parameters being studied in this chapter are the BWI, rod mill index, RQD, DWI, Axb and Ai. In addition, this chapter examines the results of the implicit geometallurgical block model in comparison to the geostatistical block model in mine planning applications. The evaluation is done through the use of a grade tonnage graph and resource estimation. Again, Leapfrog® Geo and Microsoft® Excel® are utilized to generate the data in the various tables and plot the figures.

7.2 Comparison of block models of Bond work index generated through implicit and geostatistical methods.

Based on the comparison of BWI between the implicit and geostatistical methods, it can be observed that the mean value for the implicit method is slightly lower (12.79 kWh/t) than the geostatistical method (12.82 kWh/t) (Table 7.1). This suggests that, on average, the implicit method tends to estimate slightly lower BWI values than the geostatistical method.

The standard deviation for the implicit method (2.02 kWh/t) is slightly higher than the geostatistical method (1.95 kWh/t), resulting in a higher coefficient of variation (0.16 kWh/t) for the implicit method compared to the geostatistical method (0.15 kWh/t).

This indicates that the data points in the BWI distribution are more spread out from the mean when using the implicit method, implying a slightly higher variability compared to the geostatistical method.

The variance for the implicit method (4.09 kWh/t) is higher than the geostatistical method (3.78 kWh/t). The higher variance for the implicit method further confirms that the BWI data points are more dispersed around the mean when using this method compared to the geostatistical method.

In terms of the distribution of the data, the minimum value for the implicit method (6.49 kWh/t) is lower than the geostatistical method (7 kWh/t). Finally, the maximum value for the implicit method (19.97 kWh/t) is higher than the geostatistical method (19.42 kWh/t).

In summary, the interpretation of the results suggests that while the implicit and geostatistical methods for estimating BWI show minor differences in their mean values, the geostatistical method appears to provide slightly more precise estimates with lower variability.

Table 7.1. Statistical comparison between implicit and geostatistical methods for the BWI-based block models

Name	Implicit BWI (kWh/t)	Geostatistical BWI (kWh/t)
Block Count	6 416	6 416
Volume	6 416 000 m ³	6 416 000 m ³
Mean	12.79 kWh/t	12.82 kWh/t
Standard deviation	2.02 kWh/t	1.95 kWh/t
Coefficient of variation	0.16 kWh/t	0.15 kWh/t
Variance	4.09 kWh/t	3.78 kWh/t
Minimum	6.49 kWh/t	7 kWh/t
Median	13.16 kWh/t	13.17 kWh/t
Maximum	19.97 kWh/t	19.42 kWh/t

The swath plot results show that both methods have very similar mean values for the BWI, with the geostatistical method having a slightly higher mean of 12.88 kWh/t compared to the average of implicit method of 12.81 kWh/t. However, the difference between the two means is relatively small, indicating that both methods perform similarly well in estimating the BWI.

It is further observed that geostatistical method has higher averages for almost all Swath numbers. However, it should be noted that there are Swath numbers where the implicit method has higher averages than the geostatistical method, particularly for Swath numbers 11 – 14 and 30 – 37.

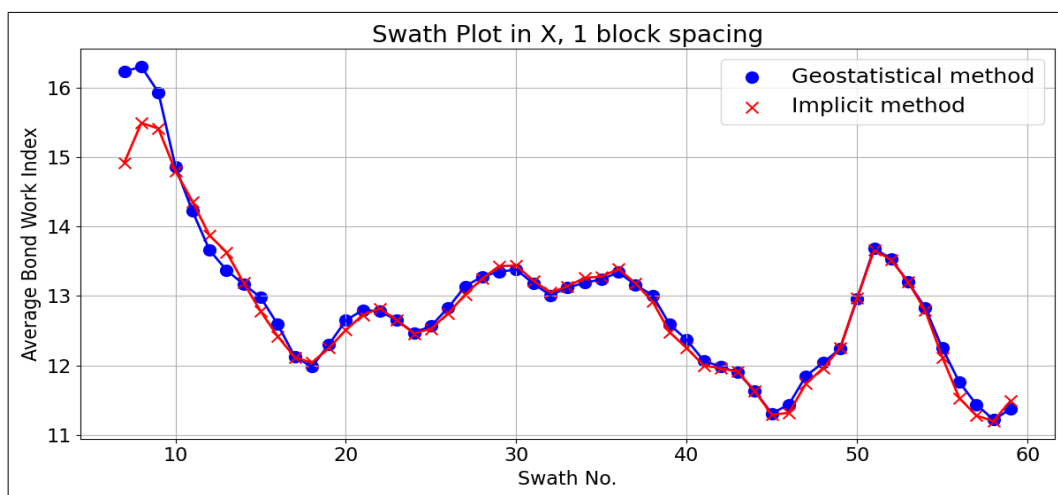


Figure 7.1: Comparison of swath plots between implicit and geostatistical methods for the BWI-based block models

The statistical and swath plot comparison indicated a minor difference, which can be observed more clearly when the two-block models are visualized (see Figure 7.2). As shown in the Figure, the green circle in the bottom left corner for the implicit method (Figure 7.2a) contains more blue blocks than the geostatistical method (Figure 7.2b) at the same circle. Similarly, these subtle distinctions can also be noticed in the black, white, brown, and grey circles.

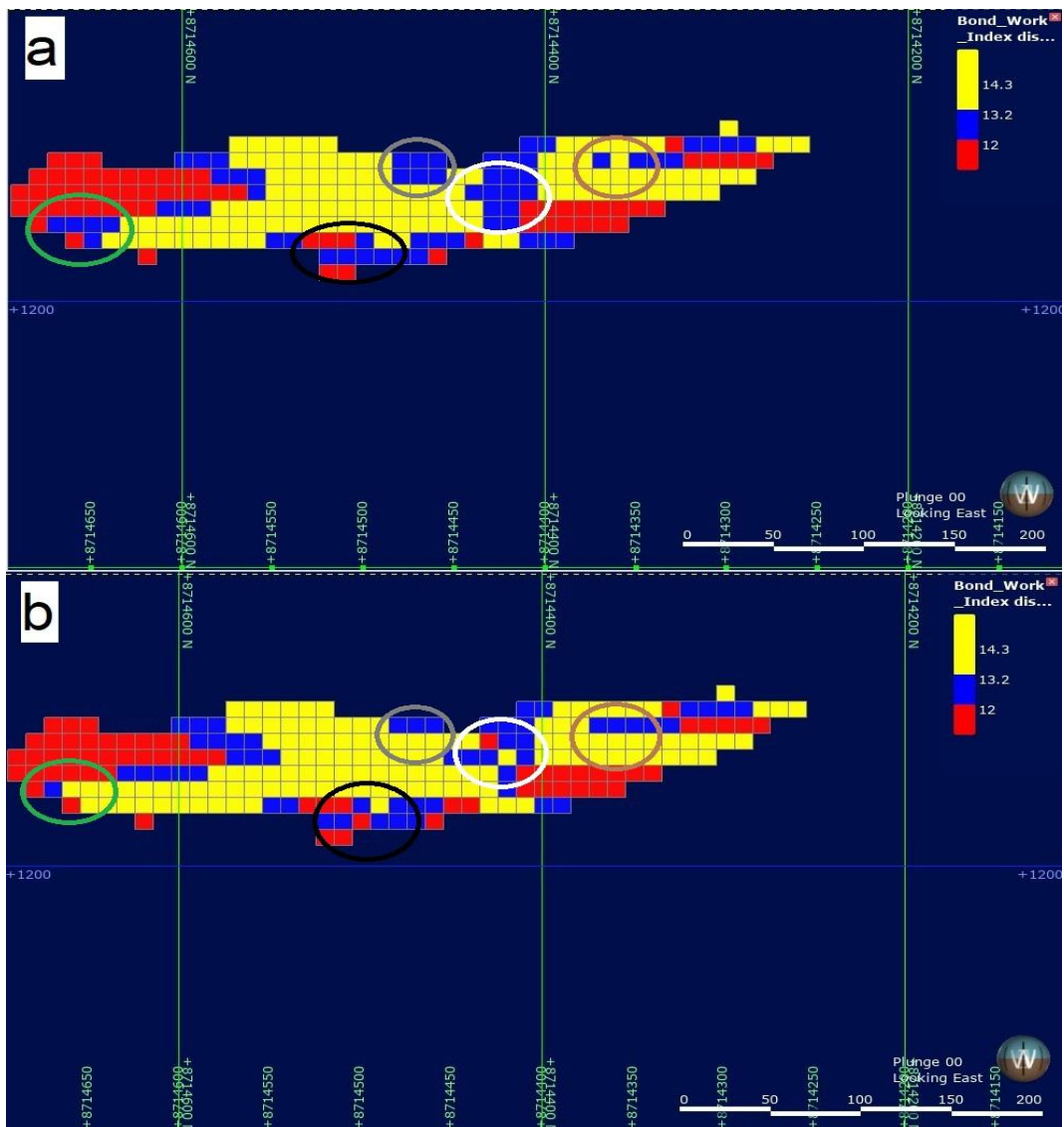


Figure 7.2: Visual comparison between a) implicit method and b) geostatistical method for the BWI-based block models

7.3 Comparison of block models of rod mill index generated through implicit and geostatistical methods.

The implicit method and geostatistical method both had the same block count and volume, indicating that they were analysed using the same spatial units.

In terms of the mean, the geostatistical method produced a slightly higher value of 15.19 kWh/t compared to the 15.15 kWh/t mean of the implicit method 15.15 kWh/t. This indicates that the geostatistical method provides slightly higher average rod mill index estimates compared to the implicit method.

The standard deviation for the geostatistical method was lower at 2.74 kWh/t compared to the 2.86 kWh/t standard deviation of the implicit method, indicating that the geostatistical method had less variability in its results. Lower standard deviation suggests that the rod mill index estimates from the geostatistical method have less variability around the mean, making it relatively more precise compared to the Implicit method.

The coefficient of variation, which is the ratio of the standard deviation to the mean, was slightly lower for the geostatistical method at 0.18 kWh/t compared to the 0.19 kWh/t CV implicit method. This suggests that the geostatistical method provides more consistent estimates relative to the mean rod mill index.

The variance, which is the square of the standard deviation, was lower for the geostatistical method at 7.5 kWh/t compared to the 8.18 kWh/t variance implicit method. A lower variance in the geostatistical method further confirms that its rod mill index estimates have less variability and are more tightly distributed around the mean compared to the Implicit method.

In terms of the minimum, the implicit method had a lower value of 3.73 kWh/t compared to the 4.25 kWh/t minimum geostatistical method. Finally, the maximum value for the implicit method was higher at 20.57 kWh/t compared to the 18.9 kWh/t maximum geostatistical method. Overall, the results

suggest that the geostatistical method tends to provide slightly higher mean estimates and is more precise in estimating the rod mill index compared to the implicit method. The lower standard deviation, variance, and coefficient of variation in the geostatistical method indicate that its estimates are more consistent and have less variability around the mean.

Table 7.2. Statistical comparison between implicit and geostatistical methods for the rod mill index block models

Name	Implicit rod mill index (kWh/t)	Geostatistical rod mill index (kWh/t)
Block Count	6 416	6 416
Volume	6 416 000 m ³	6 416 000 m ³
Mean	15.15 kWh/t	15.19 kWh/t
Standard deviation	2.86 kWh/t	2.74 kWh/t
Coefficient of variation	0.19 kWh/t	0.18 kWh/t
Variance	8.18 kWh/t	7.5 kWh/t
Minimum	3.73 kWh/t	4.25 kWh/t
Median	15.04 kWh/t	15.1 kWh/t
Maximum	20.57 kWh/t	18.9 kWh/t

In general, the implicit method seems to provide slightly lower average rod mill index values compared to the geostatistical method (Table 7.2). For instance, for swath number 10, the implicit method yielded an average rod mill index of 14.4032 kWh/t, while the geostatistical method yielded a value of 15.0712 kWh/t.

Figure 7.3 shows two different methods, geostatistical and implicit, used to estimate the rod mill index across multiple swath numbers. The averages for the Implicit method tend to be slightly lower than those for the geostatistical method. For implicit method, the mean of the rod mill index was 14.80 kWh/t while for geostatistical method being 14.83 kWh/t. This indicate that there is not much difference between the two estimates. The number of samples varies for different swath numbers, but both methods

generally have a similar trend as the swath numbers increase (Figure 7.3). It appears that the data is well-distributed with a considerable number of samples for most swath numbers. The average corresponding to the implicit method was higher than the geostatistical method in swath No. 8 – 9, 25 – 26 and 47. In these instances, the implicit method yielded higher average values compared to the geostatistical method.

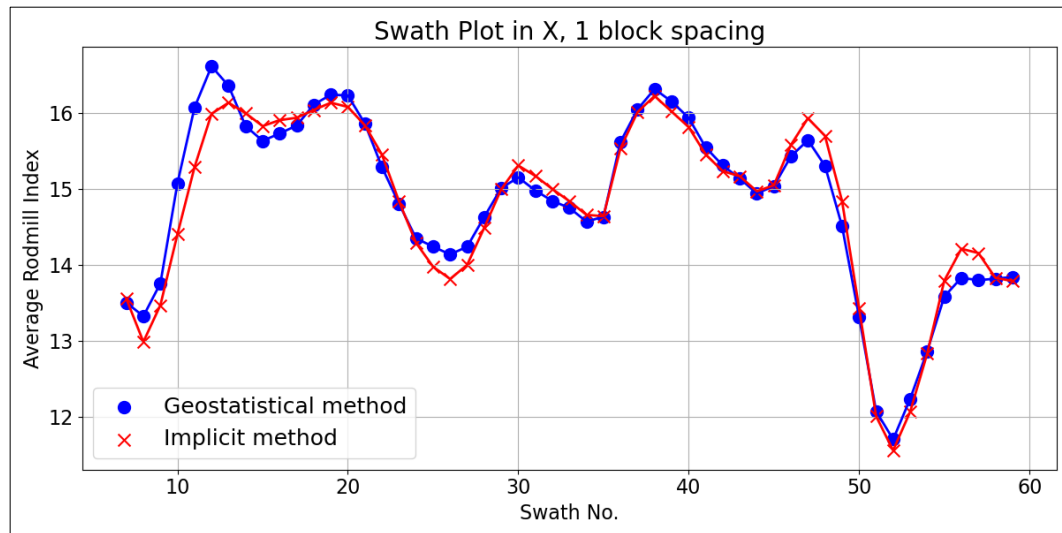


Figure 7.3: Comparison of swath plots between the implicit and geostatistical method for the block models of the rod mill index

Overall, while the geostatistical method tends to provide slightly higher average rod mill index values, the implicit method appears to be more consistent and reliable across swath numbers.

When the two-block models are visualized (Figure 7.4), the statistical and swath plot comparison's minor difference becomes apparent. The white circle for the implicit method (Figure 7.4a) contains more blue blocks than the geostatistical method (Figure 7.4b) at the same circle. Additionally, the black circle for the implicit method (Figure 7.4a) exhibits more green blocks than the geostatistical method, while the brown circle for the implicit method only has one green block, compared to the 2 green blocks of the geostatistical method. These visual observations reinforce the minor differences previously observed in the statistical and swath plot comparison.

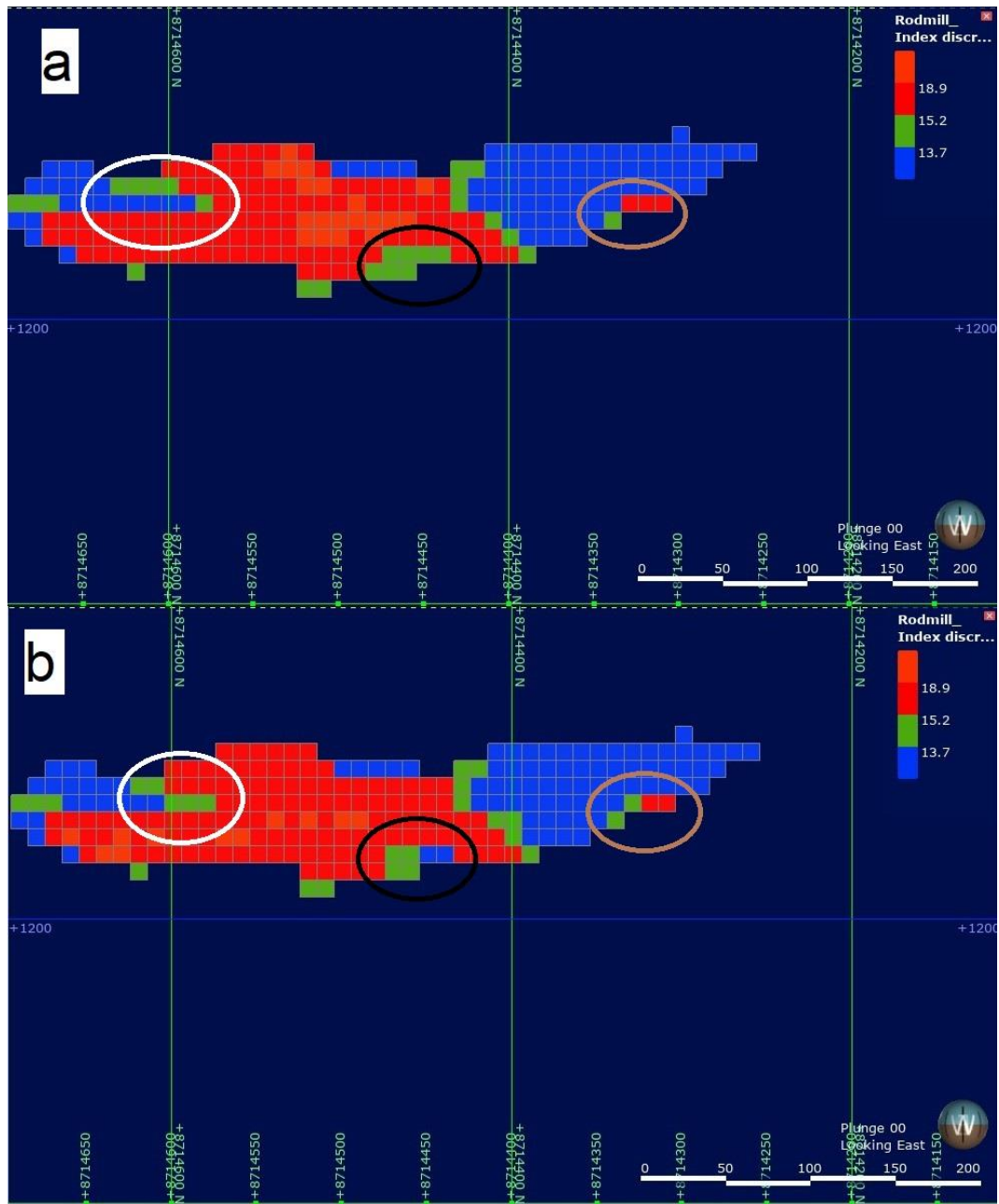


Figure 7.4: Visual comparison between a) implicit method and b) geostatistical method for the block models of the rod mill index

7.4 Comparison of block model for RQD index generated through implicit and geostatistical methods

The statistical comparison between implicit and geostatistical methods for the RQD-based block model is presented in Table 7.3. The block count and

volume are the same for both methods, indicating that they have used the same data and assumptions for the analysis. The mean is slightly higher for the geostatistical method compared to the implicit method (56.62% vs. 56.49%).

This indicates that the geostatistical method provides slightly higher average RQD estimates compared to the implicit method. The implicit method has a standard deviation of 10.41%, whereas the geostatistical method shows a slightly lower standard deviation of 10.04%. A lower standard deviation suggests that the RQD estimates from the geostatistical method have less variability around the mean, making it relatively more precise compared to the implicit method.

The Coefficient of Variation measures the relative variability of the RQD estimates between the two methods. Both methods have the same coefficient of variation, which is 0.18%. This indicates that the relative variability in RQD estimates is the same for both methods.

The implicit method has a variance of 108.43%, whereas the geostatistical method has a slightly lower variance of 100.81%. A lower variance in the geostatistical method confirms that its RQD estimates have less variability and are more tightly distributed around the mean compared to the implicit method.

The minimum RQD estimate obtained from the Implicit method is 15.03%, while the Geostatistical method yields a slightly higher minimum of 16.99%. The maximum RQD estimate from the Implicit method is 75.85%, whereas the Geostatistical method gives a lower maximum of 71.31%. The median, which represents the middle value, is the same (56.52%) for both methods.

The results suggest that the geostatistical method tends to provide slightly higher mean estimates of RQD and is slightly more precise in estimating RQD compared to the implicit method. The lower standard deviation, variance, and similar coefficient of variation in the geostatistical method indicate that its estimates are more consistent and have slightly less

variability around the mean. However, the differences between the two methods are relatively small, and both methods seem to provide reasonable estimates of RQD.

Table 7.3. Statistical comparison between implicit and geostatistical methods for the RQD-based block models

Name	Implicit RQD (%)	Geostatistical RQD (%)
Block Count	6 416	6 416
Volume	6 416 000 m ³	6 416 000 m ³
Mean	56.49 %	56.62 %
Standard deviation	10.41 %	10.04 %
Coefficient of variation	0.18 %	0.18 %
Variance	108.43 %	100.81 %
Minimum	15.03 %	16.99 %
Median	56.52 %	56.52 %
Maximum	75.85 %	71.31 %

From Figure 7.5, it can see that the average RQD values obtained by the geostatistical method range from 50.03% to 60.63%, while the implicit method gives average RQD values ranging from 48.53% to 58.56%. Both methods give similar RQD values for some swath numbers, while for others, the difference between the average RQD values obtained by the two methods is quite significant.

For example, in swath number 13, the geostatistical method gives an average RQD value of 59.29% while the implicit method gives an average RQD value of 58.54%. Similarly, in swath number 47, the geostatistical method gives an average RQD value of 55.91%, while the implicit method gives an average RQD value of 56.38%.

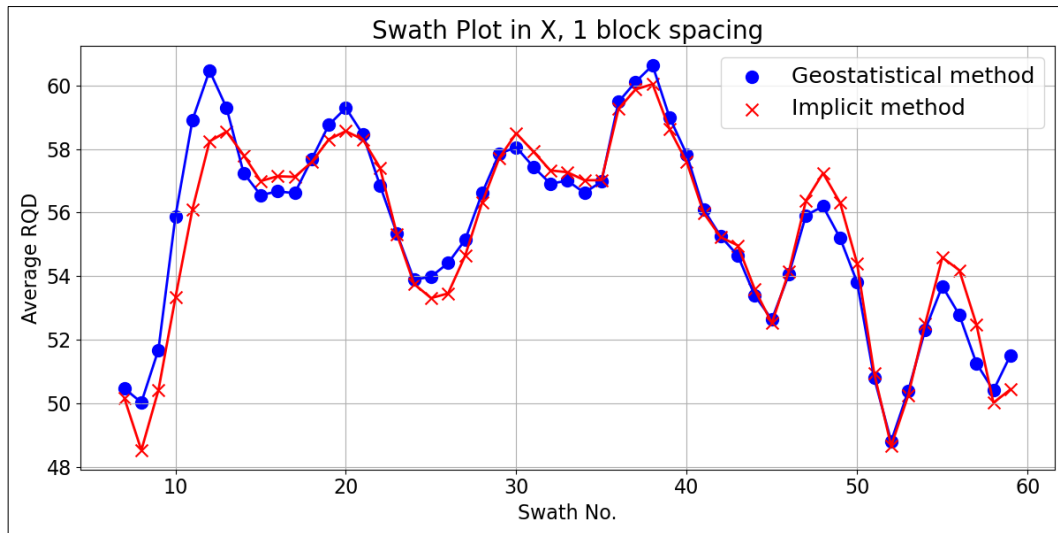


Figure 7.5: Comparison of swath plots between implicit and geostatistical methods for the RQD-based block models

Figures 7.6 offer visual representations that highlight the minor difference identified in the statistical and swath plot comparison. Upon observing the two block models, it becomes apparent that the white circle for the implicit method (Figure 7.6a) contains more red blocks than the geostatistical method (Figure 7.6b) at the same circle.

Additionally, the black circle for the implicit method (Figure 7.6a) displays more blue blocks than the geostatistical method, while the green circle for the implicit method exhibits two yellow blocks, in contrast to the single yellow block present in the geostatistical method. These visual cues reinforce the slight distinctions previously observed in the statistical and swath plot comparison.

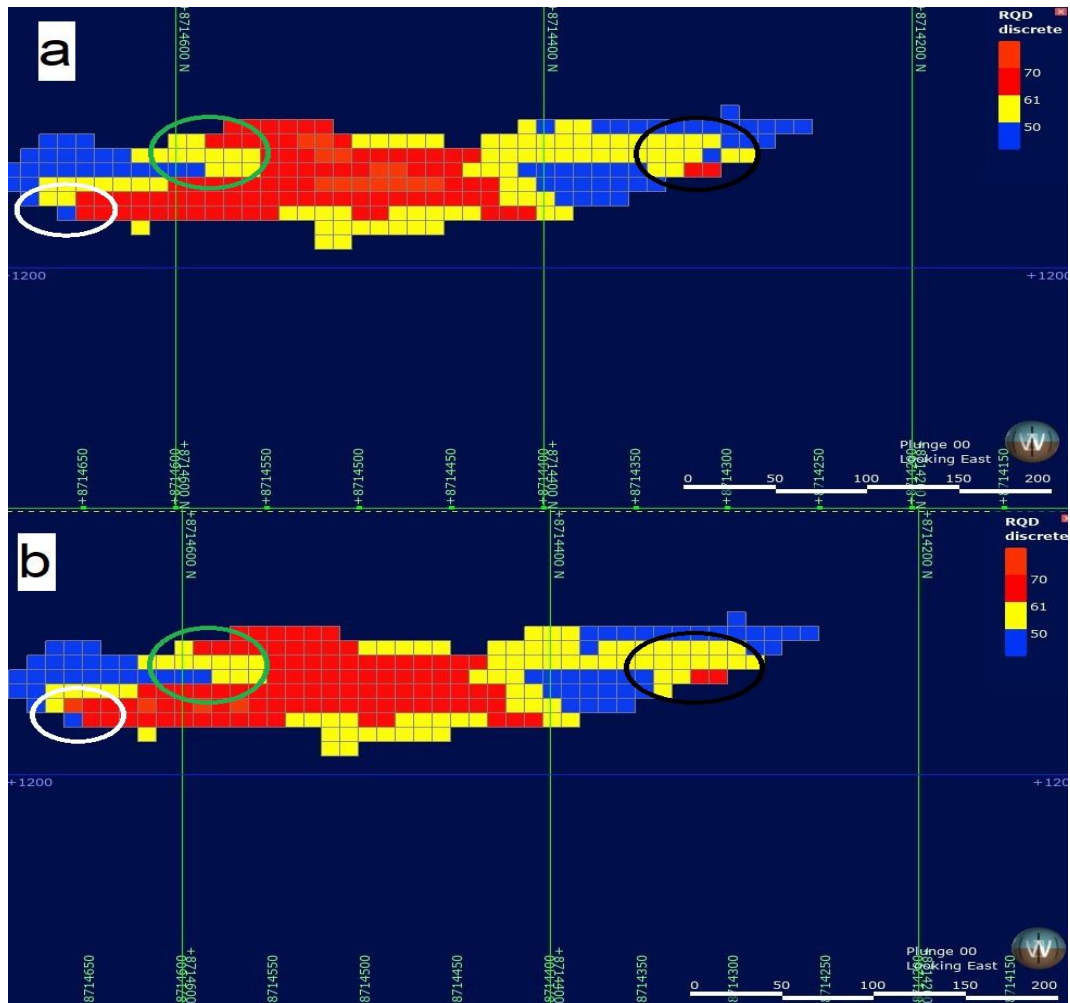


Figure 7.6: Visual comparison between a) implicit method and b) geostatistical method for the RQD-based block models

Overall, the results suggest that there are some differences between the implicit and geostatistical methods in terms of descriptive statistics, but the differences are relatively small. Further analysis and interpretation are needed to determine which method is more appropriate for the study.

7.5 Comparison of block model for drop weight index generated through implicit and geostatistical methods

Table 7.4 presents the results of modelling the drop weight index using the implicit method and geostatistical method. The block count and volume for

both methods are the same, indicating that the same number of blocks were used to create the model, and the volume of each block is also the same.

The mean value for the implicit method is slightly higher than the geostatistical method, at 10.75 kWh/t compared to 10.74 kWh/t, respectively. However, the difference is not significant. This indicates that the two methods provide nearly identical average DWI estimates.

The implicit method has a standard deviation of 3.79 kWh/t, whereas the geostatistical method shows a slightly lower standard deviation of 3.67 kWh/t. A lower standard deviation suggests that the DWI estimates from the geostatistical method have less variability around the mean, making it slightly more precise compared to the implicit method.

The CV for the implicit method is slightly higher at 0.35 kWh/t compared to 0.34 kWh/t for the geostatistical method. which suggests that the implicit method has slightly more variability than the geostatistical method. This means that the relative variability in DWI estimates is slightly lower for the geostatistical method.

The implicit method has a variance of 14.36 kWh/t, whereas the geostatistical method has a slightly lower variance of 13.48 kWh/t. A lower variance in the geostatistical method confirms that its DWI estimates have less variability and are more tightly distributed around the mean compared to the implicit method.

The minimum and maximum values for both methods are quite different, with the implicit method having a minimum value of 0.05 kWh/t and a maximum of 20.97 kWh/t, while the geostatistical method has a minimum value of 0 kWh/t and a maximum of 21.26 kWh/t. This indicates that the range of values for the implicit method is wider than for the geostatistical method. The differences between the minimum and maximum values are minimal and may not have significant practical implications.

The results suggest that both the implicit and geostatistical methods provide very similar estimates of DWI, as indicated by their almost identical mean

values. The geostatistical method appears to be slightly more precise, as evidenced by its lower standard deviation, variance, and coefficient of variation. However, the differences between the two methods are relatively small, and both methods seem to provide reasonable and comparable estimates of DWI.

Table 7.4. Statistical comparison between implicit and geostatistical methods for the DWI-based block models

	Implicit DWI (kWh/t)	Geostatistical DWI (kWh/t)
Block Count	6 416	6 416
Volume	6 416 000 m ³	6 416 000 m ³
Mean	10.75 kWh/t	10.74 kWh/t
SD	3.79 kWh/t	3.67 kWh/t
CV	0.35 kWh/t	0.34 kWh/t
Variance	14.36 kWh/t	13.48 kWh/t
Minimum	0.05 kWh/t	0.00 kWh/t
Maximum	20.97 kWh/t	21.26 kWh/t

Figure 7.7 shows the comparison between the geostatistical method and the implicit method for the DWI variable in different swath numbers. The average value and number of samples are provided for each method.

Looking at the results, it can be seen that the average values obtained by both methods are generally similar, but there are some differences in certain swath numbers. For example, in swath numbers 13, 14, and 15, the implicit method produces higher average values compared to the geostatistical method.

On the other hand, in swath numbers 51, 52, 53, 54, 55, 56, 57, and 58, the implicit method produces lower average values compared to the geostatistical method. The mean values for both implicit and geostatistical methods were 11.19 kWh/t and 11.26 kWh/t. It is clear that there is not many differences between the two methods in estimating the DWI.

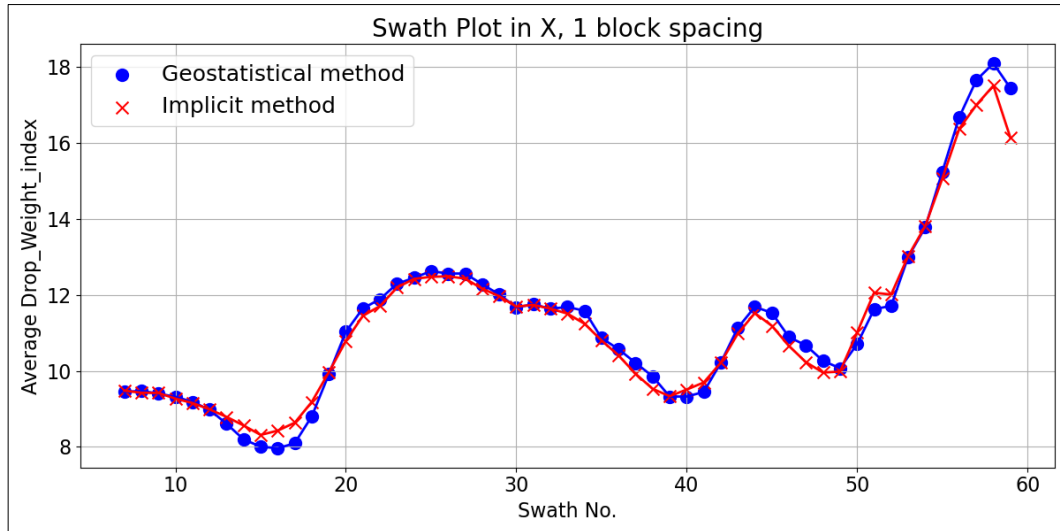


Figure 7.7: Comparison of swath plots between implicit and geostatistical methods for the DWI-based block model

It is also important to note the number of samples for each swath number. The number of samples is zero for some swath numbers in both methods, which could indicate a lack of data in those areas.

Visual comparisons between the implicit and geostatistical methods are illustrated in Figure 7.8, revealing slight disparities between the two approaches. Notably, in the white circle, the yellow blocks in the implicit method (Figure 7.8a) are clustered together, while they are dispersed in the same circle for the geostatistical method (Figure 7.8b).

Additionally, the white circle for the implicit method contains more yellow blocks than for the geostatistical method. Similarly, the black circle also displays visual differences between the two methods.

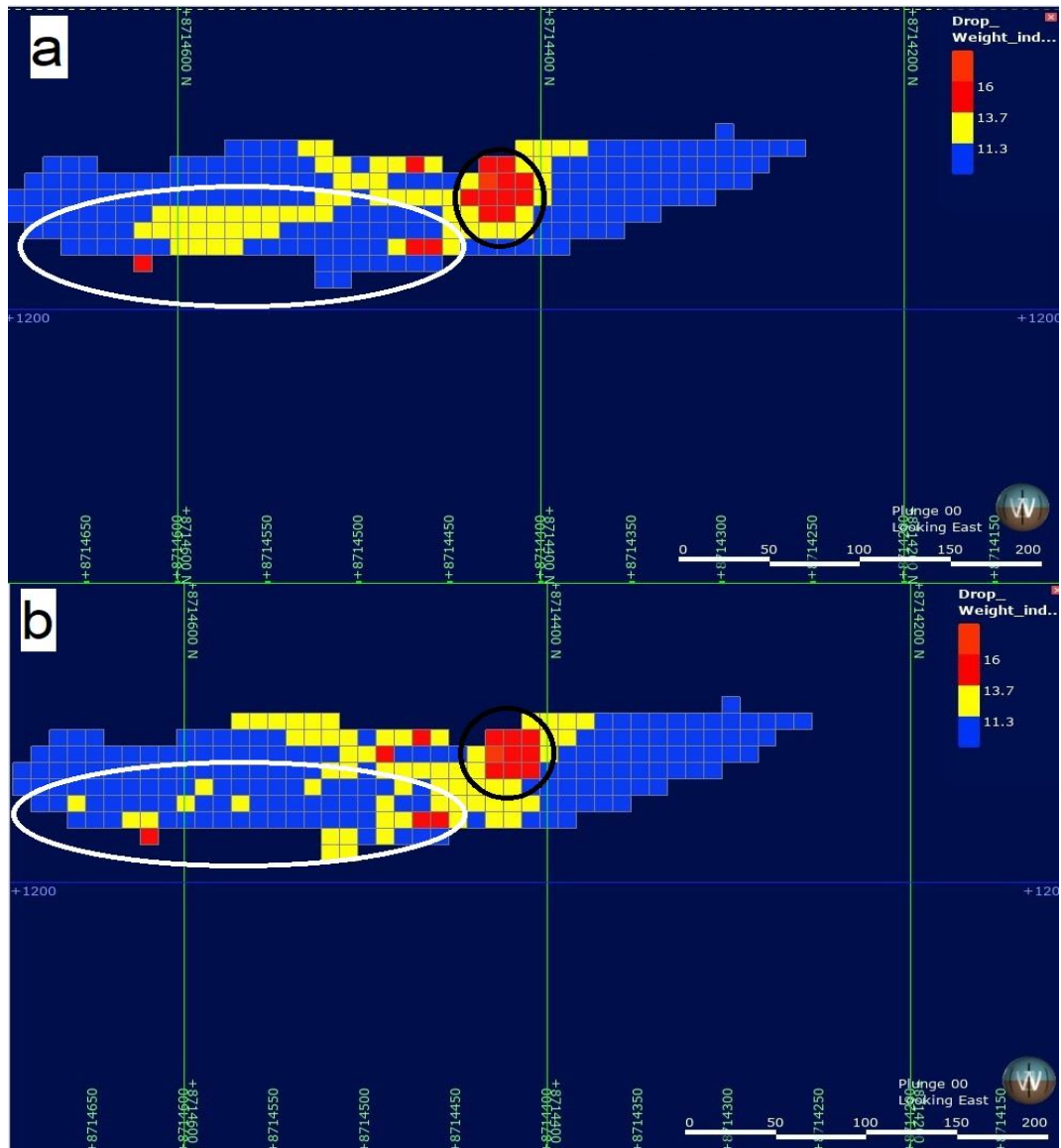


Figure 7.8: Visual comparison between a) implicit method and b) geostatistical method for the DWI-based block models

7.6 Comparison of block model for Axb index generated through an implicit and geostatistical method

The results show the comparison between the implicit method and geostatistical method for modelling Axb data. Both methods used the same block count and volume. The mean value obtained through the implicit method was 24.04 kWh/t and the geostatistical method was 24.15 kWh/t

(Table 7.5). This indicates that the geostatistical method provides slightly higher average A_{xb} estimates compared to the implicit method. The standard deviation obtained through the implicit method was 13.67 kWh/t and for the geostatistical method, it was 14.5 kWh/t. A higher standard deviation suggests that the A_{xb} estimates from the geostatistical method have more variability around the mean, making it less precise compared to the implicit method.

The CV was 0.57 kWh/t for the implicit method and 0.6 kWh/t for the geostatistical method. This means that the relative variability in A_{xb} estimates is slightly higher for the geostatistical method. The variance was 186.91 kWh/t for the implicit method and 210.33 kWh/t for the geostatistical method. A higher variance in the geostatistical method confirms that its A_{xb} estimates have more variability and are more dispersed around the mean compared to the implicit method.

The minimum value obtained through the implicit method was 0 kWh/t and for the geostatistical method, it was 0.31 kWh/t. The maximum value obtained through the implicit method was 44.67 kWh/t and for the geostatistical method, it was 41.1 kWh/t. These differences in minimum and maximum values may indicate that the two methods can provide different extreme estimates for A_{xb} .

Overall, the results suggest that the Geostatistical method tends to provide slightly higher mean estimates of A_{xb} compared to the Implicit method. However, the Implicit method seems to be slightly more precise, as indicated by its lower standard deviation, variance, and coefficient of variation.

It's worth noting that the differences in precision and variance are relatively small between the two methods. The minimum and maximum values also show some variation between the methods, indicating that extreme estimates can differ. Therefore, both methods can be used to model A_{xb} data, and the choice of method may depend on other factors such as computation time and ease of use.

Table 7.5. Statistical comparison between the implicit and geostatistical method for the block models of the Axb index

	Implicit Axb (kWh/t)	Geostatistical Axb (kWh/t)
Block Count	6 416	6 416
Volume	6 416 000 m ³	6 416 000 m ³
Mean	24.04 kWh/t	24.15 kWh/t
SD	13.67 kWh/t	14.5 kWh/t
CV	0.57 kWh/t	0.6 kWh/t
Variance	186.91 kWh/t	210.33 kWh/t
Minimum	0 kWh/t	0.31 kWh/t
Maximum	44.67 kWh/t	41.1 kWh/t

Looking at the results for the swath plot comparison (Figure 7.9), it can be seen that the average Axb values obtained by both methods are comparable across most swath numbers. In the range of swath numbers 7 to 35, the averages remain relatively close for both methods, indicating a reasonable agreement between them.

For swath numbers 51 to 59, the differences between the average Axb values of the two methods become more noticeable. The geostatistical method yields significantly lower average values for Swath Numbers 51 to 58 compared to the implicit method, indicating potential disparities in their estimations.

Furthermore, both methods show similar trends as the swath numbers increase. The Axb values tend to decrease gradually from swath numbers 12 to 25, and then there is a significant decrease at swath numbers 48 to 59.

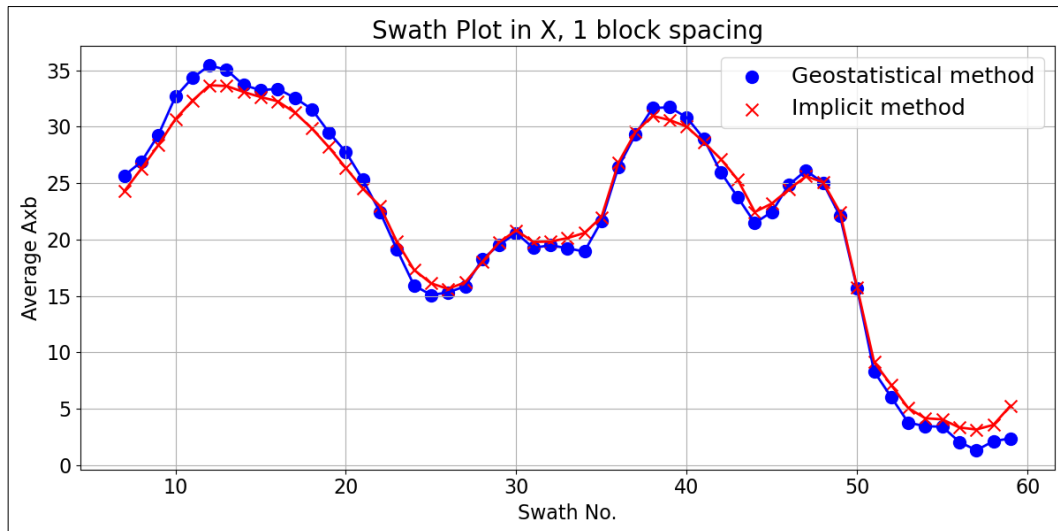


Figure 7.9: Comparison of swath plots between implicit and geostatistical methods for the block models of the Axb index

Figure 7.10 presents the results of a visual comparison between the two methods, revealing significant differences. Notably, the white circle for the implicit method (Figure 7.10a) contains no blue blocks, whereas the geostatistical method (Figure 7.10b) displays a blue block in the same circle. Equally, the black circle for the implicit method has a blue block, while the geostatistical method does not. Differences between the two methods are also observable in the blue, green, and brown circles.

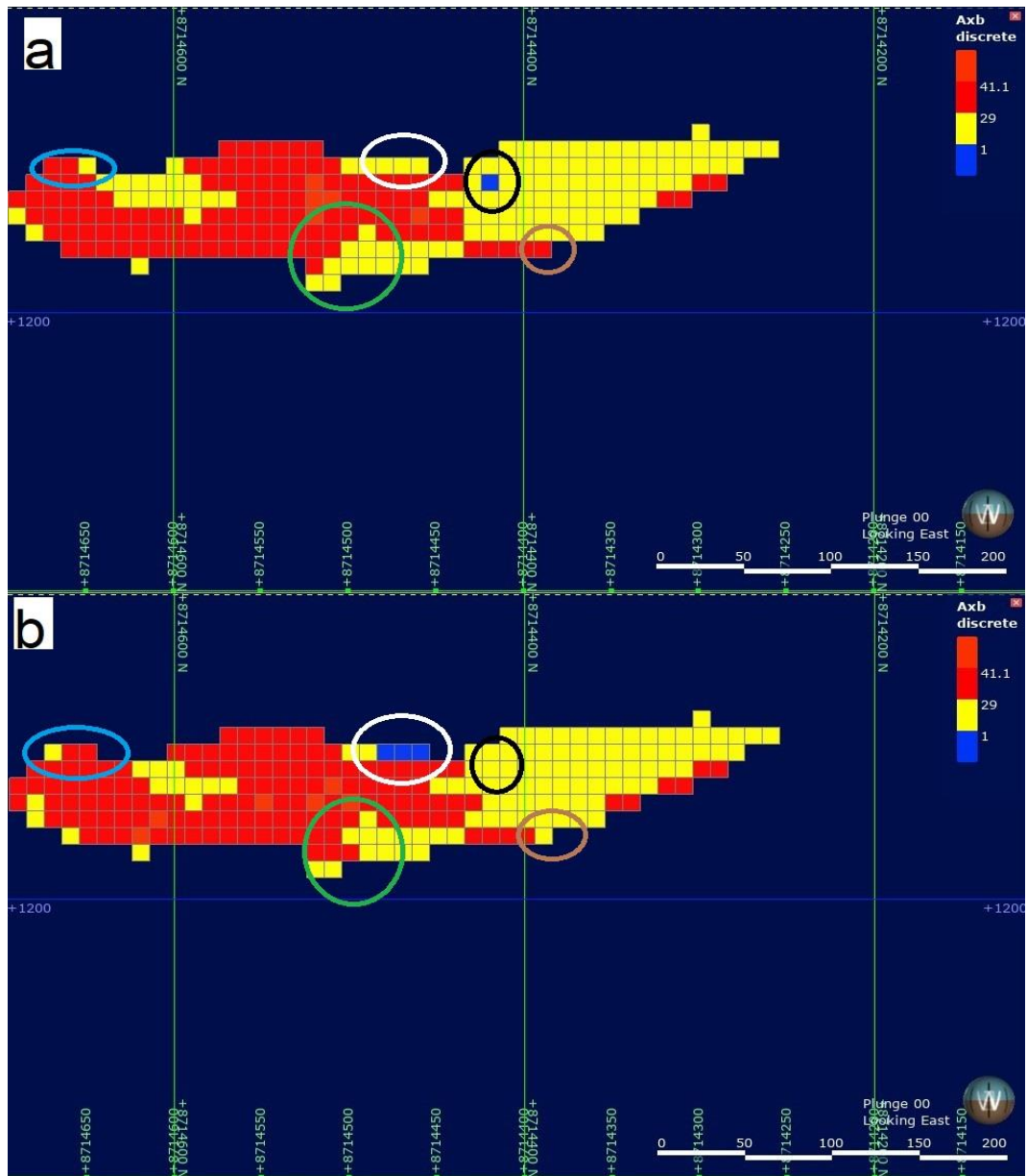


Figure 7.10: Visual comparison between a) implicit method and b) geostatistical method for the block models of the Axb index

Overall, these results suggest that the geostatistical method may be a slightly better option for predicting values of the variable of interest within the region, although the differences between the two methods are relatively small. It is also worth noting that these results only consider performance within the specific region studied and may not necessarily generalize to other regions or applications.

7.7 Comparison of block model for abrasion index generated through implicit and geostatistical methods

The two methods have very similar performance in terms of the mean, with both giving a mean abrasion index value of 0.49 kWh/t (Table 7.6). This indicates that both methods provide identical average Abrasion Index estimates. The geostatistical method has a slightly lower standard deviation (0.27 kWh/t compared to 0.28 kWh/t). A lower standard deviation suggests that the A_i estimates from the geostatistical method have slightly less variability around the mean, making it marginally more precise compared to the implicit method.

The Coefficient of Variation (CV) measures the relative variability of the A_i estimates between the two methods. The CV for the Implicit method is 0.58 kWh/t, while for the geostatistical method, it is slightly lower at 0.56 kWh/t. This means that the relative variability in A_i estimates is slightly lower for the geostatistical method.

The implicit method has a variance of 0.08 kWh/t, whereas the geostatistical method has a slightly lower variance of 0.07 kWh/t. A lower variance in the geostatistical method confirms that its A_i estimates have slightly less variability and are more concentrated around the mean compared to the implicit method.

Looking at the minimum and maximum values, it appears that the implicit method has a wider range of abrasion index values, with a minimum of 0 kWh/t and a maximum of 0.93 kWh/t. In contrast, the geostatistical method has a minimum value of 0.02 kWh/t and a maximum of 0.78 kWh/t. This suggests that the geostatistical method may be more reliable and consistent in estimating abrasion index values within a certain range.

The results suggest that both the Implicit and Geostatistical methods provide identical mean estimates of A_i . The Geostatistical method appears to be slightly more precise, as indicated by its lower standard deviation, variance, and coefficient of variation. However, the differences in precision

and variance between the two methods are relatively small. The minimum and maximum values show some variation between the methods, indicating that extreme estimates can differ.

Table 7.6. Statistical comparison between the implicit and geostatistical methods for the block models of the abrasion index

	Implicit Ai (kWh/t)	Geostatistical Ai (kWh/t)
Block Count	6 416	6 416
Volume	6 416 000 m ³	6 416 000 m ³
Mean	0.49 kWh/t	0.49 kWh/t
SD	0.28 kWh/t	0.27 kWh/t
CV	0.58 kWh/t	0.56 kWh/t
Variance	0.08 kWh/t	0.07 kWh/t
Minimum	0 kWh/t	0.02 kWh/t
Maximum	0.93 kWh/t	0.78 kWh/t

The results of the swath plot comparison between the implicit method and the geostatistical method are presented in Figure 7.11. The average Abrasion Index values obtained by both methods are relatively close to each other across most swath numbers.

This is further confirmed by the mean values for both methods being 0.45 kWh/t. From swath numbers 7 to 40, the averages remain similar for both methods, indicating a reasonable agreement between them. There is not much difference between the two methods, meaning that they performed the same.

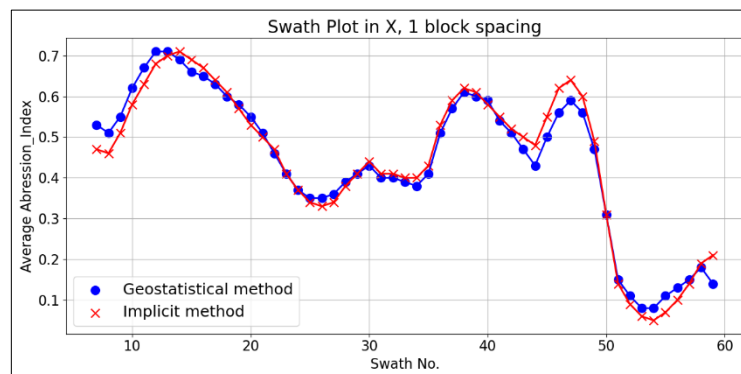


Figure 7.11: Comparison of swath plots between implicit and geostatistical methods for the block models of the abrasion index

Figure 7.12 displays the visual comparison results between the implicit and geostatistical methods, showcasing notable differences between the two approaches. In the white circle, the implicit method (Figure 7.12a) contains blue blocks, while the geostatistical method (Figure 7.12b) does not. The green circle exhibits the same pattern as the white circle, with the implicit method displaying blue blocks while the geostatistical method does not. Differences between the two methods are also observable in the black and brown circles.

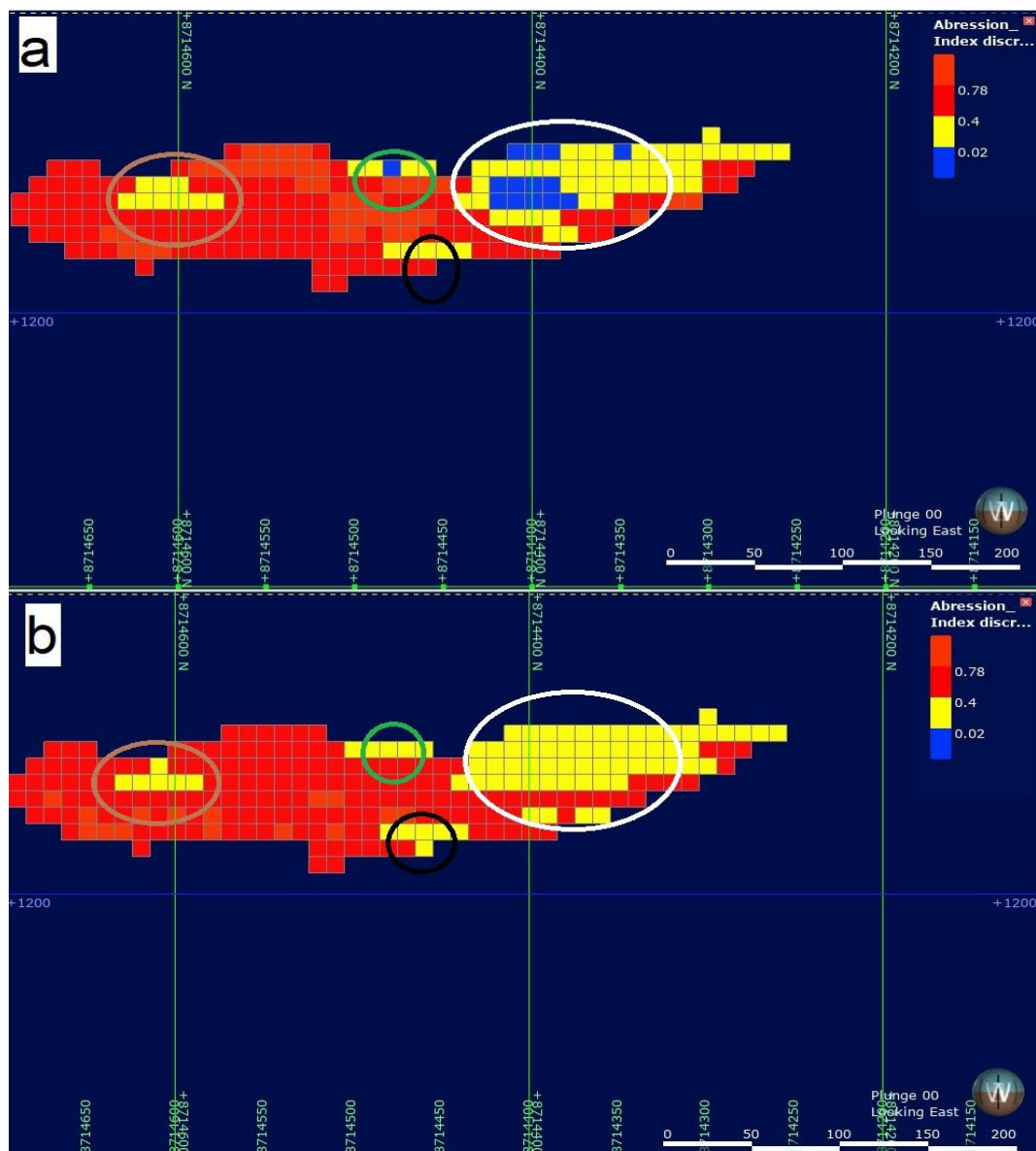


Figure 7.12: Visual comparison between a) implicit method and b) geostatistical method for the block model of the abrasion index

Overall, the swath plot suggests that the geostatistical method is a better option for estimating the abrasion index due to its higher average values and more consistent results. However, further analysis and comparison with other methods may be required to confirm this.

7.8 Application of geometallurgical block model on mine planning

In this section, the results of comparing the implicit method and geostatistical methods for mine planning applications were presented. As previously mentioned in this chapter, two methods were utilized: the grade-tonnage curve and resource estimation. The data used in this section was sourced from Section 5.2 and Chapter 6. The data, Figures, and tables in this section were generated using Leapfrog® Geo and Microsoft® Excel®.

7.8.1 Grade-tonnage curve: implicit vs geostatistical

The grade-tonnage curve is a graphical technique used to evaluate the performance of different estimation methods relative to each other. The curve provides a summary of the estimated tonnage and grade of materials at a given cut-off grade.

A comparison between the implicit and geostatistical methods for grade-tonnage estimation is shown in Figure 7.13. At the 0.5% cut-off grade, the implicit method estimates 11.29 million tonnes above the cut-off, with an average grade of 1.12% and containing metal of 90.83% of the ore. The Geostatistical method estimates 11.36 million tonnes above the cut-off grade, with an average grade of 1.34% and containing metal of 90.50%. The curves of the two methods are very similar, with only minor differences.

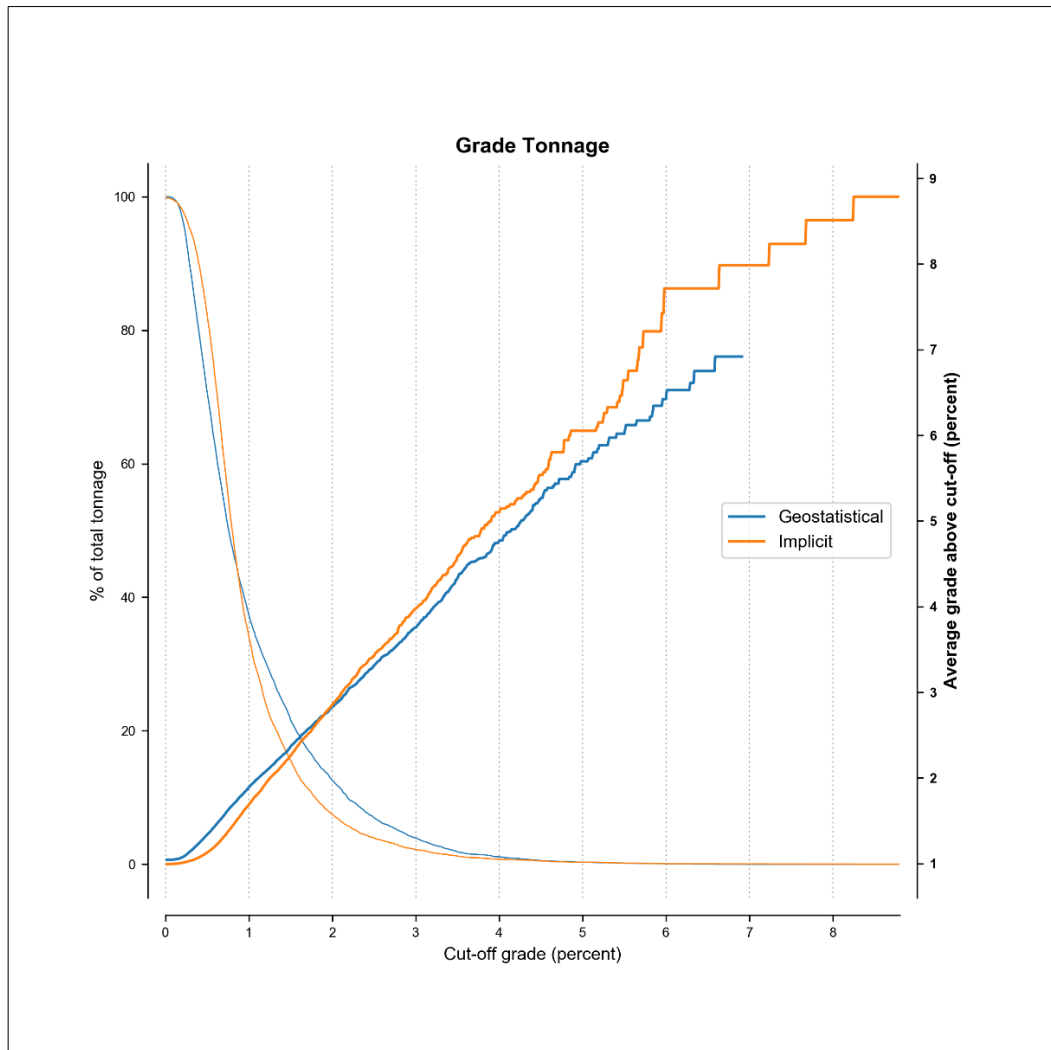


Figure 7.13: Comparison of grade tonnage curves generated using implicit and traditional methods.

7.8.2 Geometallurgical orebody models combined.

For this illustrative application, the cut-off grade of the deposit was set at 0.5% TCo based on the work by Mboyo (2018) in which a similar cut-off grade was used. The grade classification was divided into four classes as shown in Table 7.7.

Table 7.7. Grade classes of drillhole data

Intervals (%)	Class
0 % – 0.5 %	Waste
0.5 % – 1%	Low grade
1% – 3%	Medium grade
3 % – 99%	High grade

The classes that were created in Table 7.7 were used to construct a combined geometallurgical model for the orebody (Figure 7.14), which was divided into four classes: waste, low-grade ore, medium-grade ore, and high-grade ore.

Each block in the geometallurgical block contained values for the geometallurgical parameters, including TCo (%), BWI (kWh/t), rod mill index (kWh/t), RQD (%), DWI (kWh/t), Axb (kWh/t), and Ai (kWh/t). An example of the scene detail is provided in Figure 7.14. These parameters can then be directly utilized for mine planning or mine optimization from the geometallurgical block model.

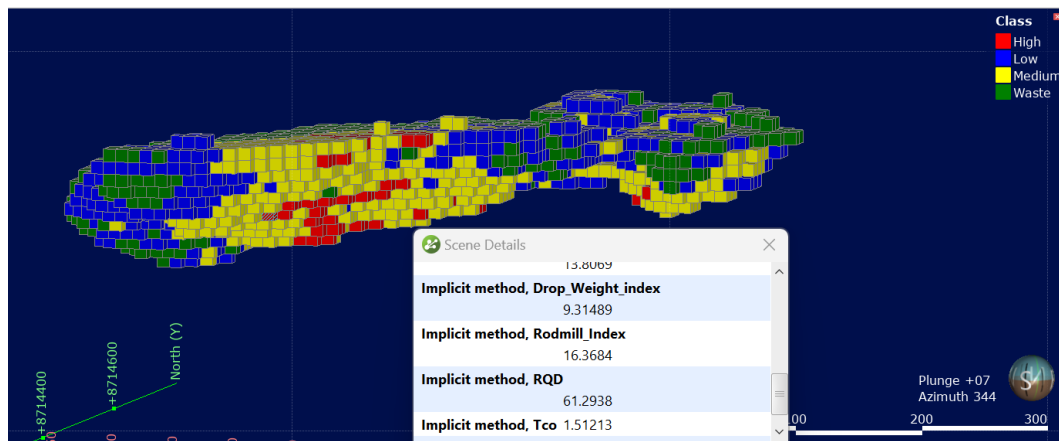


Figure 7.14: Combined geometallurgical block model generated using Implicit method

7.8.3 Resource estimation: implicit vs geostatistical

Tables 7.8 and 7.9 present the results of mine planning using the implicit and geostatistical methods. The data includes volume, density, mass, and several indices for each block within the mine, as well as the total values for each method.

Looking at the total values, the geostatistical method produced a higher TCo (%) value (1.05%) compared to the implicit method (0.99%), which indicates that the geostatistical method may result in a slightly higher recovery of ore from the mine.

The Axb (kWh/t) values were higher for the implicit method compared to the geostatistical method. The average Axb (kWh/t) value for the implicit method was 24.04 (kWh/t), while the average Axb (kWh/t) value for the geostatistical method was 24.15 (kWh/t). This suggests that the geostatistical method has a slightly higher average Axb (kWh/t) value compared to the implicit method.

The Ai (kWh/t) values were the same for the implicit method and the geostatistical method, indicating that both methods produced the same average.

The BWI (kWh/t), DWI (kWh/t), and rod mill index (kWh/t) values were all slightly higher for the geostatistical method compared to the implicit method.

The RQD (%) values for both methods were similar, with the geostatistical method producing slightly higher values.

For the class categories (High, Low, Medium and Waste), the implicit method produced a lower mass per ton for high-class (383 400.00 t) compared to the geostatistical method (683 100.00 t). However, the implicit method produced slightly high values for the other classes compared to geostatistical methods.

Table 7.8. Resource estimation using implicit method

Class	Volume	Density	Mass	Average Value						
				Tco	Abression_Index	Axb	Bond_Work_Index	Drop_Weight_index	Rodmill_Index	RQD
	m ³	g/cm ³	t	%	kWh/t	kWh/t	kWh/t	kWh/t	kWh/t	%
High	253 000.00	2.7	683 100.00	3.04	0.35	18.07	13.83	11.15	13.83	54.37
Low	2 145 000.00	2.7	5 791 500.00	0.77	0.53	25.83	12.7	10.65	15.55	57.71
Medium	2 147 000.00	2.7	5 796 900.00	1.39	0.45	22.69	13.02	11.08	14.97	56.75
Waste	1 871 000.00	2.7	5 051 700.00	0.51	0.51	24.35	12.5	10.39	15.08	55.07
Total	6 416 000.00	2.7	17 323 200.00	0.99	0.49	24.04	12.79	10.74	15.15	56.49

Table 7.9. Resource estimation using the geostatistical method

Class	Volume	Density	Mass	Average Value						
				TCo	Abression_Index	Axb	Bond_Work_Index	Drop_Weight_index	Rodmill_Index	RQD
	m ³	g/cm ³	t	%	kWh/t	kWh/t	kWh/t	kWh/t	kWh/t	%
High	142 000.00	2.7	383 400.00	3.78	0.33	16.54	14.04	11.13	13.45	52.35
Medium	2 049 000.00	2.7	5 532 300.00	1.72	0.42	21.27	13.12	11.41	14.93	56.89
Low	3 101 000.00	2.7	8 372 700.00	0.71	0.54	26.55	12.68	10.28	15.47	57.07
Waste	1 124 000.00	2.7	3 034 800.00	0.37	0.49	23.74	12.52	10.8	15.11	55.43
Total	6 416 000.00	2.7	17 323 200.00	1.05	0.49	24.15	12.82	10.75	15.19	56.62

7.9 Summary and conclusion

This chapter compares the efficacy of implicit geometallurgical modelling with geostatistical modelling in mine planning applications. The comparison is conducted using statistical comparison, swath plot comparison, and visual plot comparison. The results on the comparison between the implicit and geostatistical methods for modelling geometallurgical data reveals that both methods generally provide similar estimates for the studied factors. However, there are subtle differences in precision and variability between the two methods.

The geostatistical method tends to exhibit slightly better precision with lower standard deviations and variances for some factors (e.g., RQD and Axb) compared to the implicit method. However, these differences are relatively small, and both methods generally offer reasonable and comparable estimates for the geometallurgical parameters.

Looking at the results for the swath plot comparison, it can be seen that the geostatistical method generally performed better than the implicit method in terms of average values predicted in the swaths, although the differences are relatively small. The lower quartile and median values are slightly higher for the implicit method compared to the geostatistical method, while the upper quartile value is slightly higher for the geostatistical method compared to the implicit method.

For the block categories, a cut-off grade of 0.5% TCo for an ore deposit was set to classify the grades into four classes. The geometallurgical model was constructed based on these classes, and each block in the model contained values for geometallurgical parameters, which could be used for mine planning or optimization. The geostatistical method produced a high mass per ton of high-class (683 100.00 t) compared to the implicit method (383 400.00 t), indicating a potentially more profitable mine plan. However, the implicit method produced slightly high values for the other classes compared to geostatistical methods. The differences in the volume (m^3) of

materials within each class and the variation in TCo (%) grade have contributed to the distinct mass (t) observed between the two methods.

The geostatistical method produced slightly higher TCo (%) values, indicating a slightly higher recovery of ore, while the implicit method showed higher values for several indices such as A_{xb} (kWh/t) and A_i (kWh/t), indicating potentially more efficient mineral recovery and crushing of ore.

Overall, the results suggest that the choice of method may depend on the priority of the mine plan. If the priority is to recover the maximum volume of ore possible, the geostatistical method may be more suitable. However, if the priority is to maximize the profitability of the mine plan, the implicit method may be a better choice.

It is important to note that further analysis and considerations beyond these results may be necessary to make a final decision. This is because the differences between the implicit and geostatistical methods were minor, with both methods producing similar results for most parameters. However, the geostatistical method may have a slight advantage in terms of TCo and mass, while the implicit method may have a slight advantage in terms of A_{xb} and A_i .

Chapter 8 Conclusions and recommendations

8.1 Introduction

The main aim of this thesis was to investigate the potential of implicit modelling methods for modelling geometallurgical parameters for mine planning applications and to generate synthetic geometallurgical data using Generative Adversarial Networks (GAN) models. The Bond work index, rod mill index, rock quality designation index, drop weight index, Axb index and abrasion index were selected for modelling in this thesis.

For synthetic data generation, three types of GAN-based models were used to generate synthetic geometallurgical data (Chapter 4). These are CTGAN, CopulaGAN, and Gaussian Copula. An RBF-based implicit method was used to model the geometallurgical data using Leapfrog® Geo.

The results of the implicit geometallurgical modelling (Chapter 5) were also compared with the geostatistical method (Chapter 6) analysed in this study (Chapter 7). This chapter, therefore, presents the summarised findings of the thesis, the overall conclusion and recommendation for future research.

8.2 Summary of the thesis

In this thesis, three specific research objectives were set in alignment with the main objectives. These were to create simulated geometallurgical data using Generative Adversarial Networks (GAN) models, analyse the data using an implicit method and compare the results with geostatistical methods, and finally, develop an orebody model that incorporates geometallurgical data and test it in mine planning.

For synthetic data generation, the study evaluates the generated synthetic data using various metrics, including similarity scores, principal component analysis, and visual evaluation. The results indicate that GAN-based models can effectively generate synthetic geometallurgical data, with Gaussian

Copula performing the best in terms of preserving the correlation structure of the original data. The evaluation metrics suggest that the synthetic data is of high quality and closely resembles the real data.

Overall, the findings of this chapter demonstrate the potential of GAN-based methods in generating synthetic data for various applications, particularly in situations where data privacy and scarcity are a concern. The generated synthetic geometallurgical data can be used for modelling and analysis purposes, and the chapter highlights the importance of caution when interpreting the results.

The second objective of this thesis was to model geometallurgical parameters using implicit methods, compare them with geostatistical methods, and develop an orebody model for mine planning. An indicator RBF implicit method was used to delineate the orebody into two zones, and a cut-off grade of 0.5% TCo was used to delineate the ore.

The Leapfrog® Geo software was used to model the geometallurgical parameters using RBF-based methods. The results indicated that the RBF-based method can be used to model geometallurgical data, and the generated block models were compared with geostatistical block models. The comparison indicated that the two methods are similar, and the generated resources were compared with those estimated using the geostatistical method.

The results indicated no significant differences between the two methods, and an orebody model that includes geometallurgical parameters was generated for mine planning.

Lastly, a block model of the geometallurgical parameters was generated from the implicit 3D models. The block models are the final stage of modelling as they are used for mineral valuation and mine planning. The results of implicit modelling indicated that RBF based method can be used to model geometallurgical data.

To validate the results of the implicit modelling, geostatistical block models were compared with the generated implicit block model. The geostatistical block models were created using the Ordinary Kriging method. This was done through statistical, swath plot and visual comparison. The results of the comparison indicated that the two methods are closely similar with minor differences this closely similar relationship further validates the results of the implicit method.

The created implicit block models were used in mineral inventory application. This was done through the grade tonnage curve and resource estimation. The generated resources were compared with the resources estimated through the geostatistical method. The results indicated that there are not many differences between the two methods. This further validated the results from the implicit method. Finally, an orebody which included geometallurgical parameters was generated at the end of the study. This orebody model can be used for optimising and mine planning.

8.3 Overall conclusion

Based on the findings of this thesis, it was concluded that implicit modelling of geometallurgical data involves several steps. These steps include creating iso-surfaces, interpolating them using the radial basis function, and generating block models. Synthetic geometallurgical datasets can also be generated using GAN-based methods. This novel methodology offers the potential to generate realistic and related datasets while maintaining the privacy of the original data.

Furthermore, the thesis demonstrated that resources can be estimated using the implicit method, and these estimates were validated using traditional geostatistical methods. Comparing the two methods revealed a few differences. Additionally, the thesis proposed a methodology for incorporating geometallurgical data into a spatial block model, which can be useful in mine planning and resource optimization.

In conclusion, it can be inferred from this thesis that the implicit method has the potential to model geometallurgical parameters with high accuracy. Additionally, the GAN model was found to be capable of generating synthetic geometallurgical data of high quality that closely resembles the original data, but with a different data structure.

8.4 Recommendations for further research

Based on the scope of this thesis, there are several areas that could be explored in future studies. These include:

- Future research directions could include exploring other synthetic data generation methods beyond GAN-based approaches, such as investigating the performance of Tabular Generative Adversarial Network (TGAN) and Triplet-based Variable AutoEncoders (TVAE) models. Additionally, a comparative study could be conducted to compare the performance of GAN-based methods and RBF interpolation, as explored in the thesis, with alternative approaches like CTGAN and Gaussian simulation for generating synthetic geometallurgical data.
- Investigating different hyperparameter settings: The hyperparameters used in synthetic data generation can have a significant impact on the quality of the generated data. A further study could explore different hyperparameter settings to determine if the modules can perform better under different conditions.
- Incorporating additional constraints: This study did not consider all constraints when modelling geometallurgical data, such as financial constraints. A future study could investigate the impact of including these constraints in the modelling process.
- Exploring different implicit methods: This study used RBF-based methods for implicit modelling. Future studies could investigate other

implicit-based methods, such as potential field and HRBF, to determine their suitability for modelling geometallurgical data.

- A Study to compare different implicit modelling software packages for geometallurgical modelling should be undertaken.

REFERENCES

- Abdollahi Sharif, J., Jafarpour, A., Yousefi, S., 2020. A hybrid fuzzy MCDM approach to determine an optimal block size in open-pit mine modeling: A case study. *Journal of Mining and Environment (JME)*, vol. 11, no. 2, pp. 611-627.
- Abildin, Y., Madani, N., Topal, E., 2019. A hybrid approach for joint simulation of geometallurgical variables with inequality constraint. *Minerals*, vol. 9, no. 1, #29.
- Abuntori, C.A., Al-Hassan, S., Mireku-Gyimah, D., 2021. Assessment of ore grade estimation methods for structurally controlled vein deposits: A review. *Ghana Mining Journal*, vol. 21, no. 1, pp. 31-44.
- Abzalov, M.Z., 2006. Localised Uniform Conditioning (LUC): A new approach for direct modelling of small blocks. *Mathematical Geology*, vol. 38, no. 4, pp. 393-411.
- Addo Junior, E., 2019. Multivariate modelling of geological and geometallurgical variables. PhD Thesis, The University of Adelaide, Australia, 159 p.
- Adeli, A., Dowd, P., Emery, X., Xu, C., 2021. Using cokriging to predict metal recovery accounting for non-additivity and preferential sampling designs. *Minerals Engineering*, vol. 170, art. no. 106923, pp. 1-11.
- Ahmadi, R., Hashemzadehfini, M., Amini Parian, M., 2013. Rapid determination of bond rod-mill work index by modeling the grinding kinetics. *Advanced Powder Technology*, vol. 24, no. 1, pp. 441-445.
- Allasia, G., Cavoretto, R., De Rossi, A., 2018. Hermite–Birkhoff interpolation on scattered data on the sphere and other manifolds. *Applied Mathematics and Computation*, vol. 318, pp. 35-50.
- Assefa, S.A., Dervovic, D., Mahfouz, M., Tillman, R.E., Reddy, P., Veloso, M., 2020. Generating synthetic data in finance: Opportunities,

challenges and pitfalls. ICAIF 2020 - 1st ACM International Conference on AI in Finance, art. no. 44. pp. 1-8.

Aug, C., Chilès, J.-P., Courrioux, G., Lajaunie, C., 2005. 3D Geological modelling and uncertainty: The potential-field method. In: Leuangthong, O. and Deutsch, C.V (Eds.), *Geostatistics Banff 2004* Springer Netherlands, Dordrecht, pp. 145-154.

Basson, I.J., Anthonissen, C.J., McCall, M.J., Stoch, B., Britz, J., Deacon, J., Strydom, M., Cloete, E., Botha, J., Bester, M., Nel, D., 2017. Ore-structure relationships at Sishen Mine, Northern Cape, Republic of South Africa, based on fully-constrained implicit 3D modelling. *Ore Geology Reviews*, vol. 86, pp. 825-838.

Beatson, R.K., Light, W.A., Billings, S., 2001. Fast solution of the radial basis function interpolation equations: Domain decomposition methods. *SIAM Journal of Scientific Computing*, vol. 22, no. 5, pp. 1717-1740.

Benali, F., Bodénès, D., Labroche, N., de Runz, C., 2021. MTCopula: Synthetic complex data generation using copula. *CEUR Workshop Proceedings*, vol. 2840, pp. 51-60.

Biancolini, M.E., 2018. *Fast radial basis functions for engineering applications*. Springer International Publishing AG, 357 p.

Birch, C., 2014. New systems for geological modelling - black box or best practice? *Journal of the Southern African Institute of Mining and Metallurgy*, vol. 114, no. 12, pp. 993-1000.

Birch, C., 2019. Optimisation of mining block size for narrow tabular gold deposits. *Proceedings of the 27th International Symposium on Mine Planning and Equipment Selection - MPES 2018*. Springer International Publishing, pp. 121-141.

- Bloomenthal, J., Bajaj, C., Blin, J., Cani, M.P., Wyvill, B., Rockwood, A., Wyvill, G. (Eds.), 1997. Introduction to implicit surfaces. Morgan Kaufmann Publishers, Inc, San Francisco, California, 400 p.
- Bourou, S., El Saer, A., Velivassaki, T.H., Voulkidis, A., Zahariadis, T., 2021. A review of tabular data synthesis using GANs on an IDs dataset. Information, vol. 12, no. 9, p. 375.
- Brenninkmeijer, B., 2019. On the generation and evaluation of tabular data using GANs. PhD Thesis, Radboud University, 71 p.
- Buhmann, M.D., Levesley, J., 2004. Radial basis functions: Theory and implementations. Mathematics of Computation, vol. 73, no. 247, pp. 1578-1581.
- Bye, A.R., 2011. Case studies demonstrating value from geometallurgy initiatives. GeoMet 2011 - 1st AusIMM International Geometallurgy Conference 2011, pp. 9-30.
- Calcagno, P., Chilès, J.P., Courrioux, G., Guillen, A., 2008. Geological modelling from field data and geological knowledge: Part I. Modelling method coupling 3D potential-field interpolation and geological rules. Physics of the Earth and Planetary Interiors, vol. 171, no. 1, pp. 147-157.
- Caumon, G., Gray, G., Antoine, C., Titeux, M.O., 2013. Three-dimensional implicit stratigraphic model building from remote sensing data on tetrahedral meshes: Theory and application to a regional model of la Popa Basin, NE Mexico. IEEE Transactions on Geoscience and Remote Sensing, vol. 51, no. 3, pp. 1613-1621.
- Chakrabarti, D.M., 2000. Simple approach to estimation of the work index. Mineral Processing and Extractive Metallurgy, vol. 109, no. 2, pp. 83-89.

- Chanderman, L., 2017. 3D geological modelling and resource estimation for a gold deposit in Mali. *Journal of the Southern African Institute of Mining and Metallurgy*, vol. 117, no. 2, pp. 189-197.
- Chiles, J.P., Aug, C., Guillen, A., Lees, T., 2004. Modelling the geometry of geological units and its uncertainty in 3D from structural data: The potential-field method. *Orebody Modelling and Strategic Mine Planning*, vol. 22, pp. 313-320.
- Chiles, J.P., Aug, C., Guillen, A., Lees, T., 2007. Modelling the geometry of geological units and its uncertainty in 3D from structural data: The potential-field method. *Australasian Institute of Mining and Metallurgy Publication Series*, vol. 14, pp. 355-362.
- Chilès, J.P., Delfiner, P., 1999. *Geostatistics: Modeling spatial uncertainty*. John Wiley & Sons, New York, NY, USA, 702 p.
- Chilès, J.P., Desassis, N., 2018. Fifty years of kriging. *Handbook of Mathematical Geosciences: Fifty Years of IAMG*, pp. 589-612.
- Choudhury, S., 2017. Radial basis function supported implicit geological modelling tool for mining industry. *Journal of Mines, Metals and Fuels*, vol. 65, no. 1, pp. 13-18.
- Chung, S.Y., Venkatramanan, S., Elzain, H.E., Selvam, S., Prasanna, M.V., 2019. Supplement of missing data in groundwater-level variations of peak type using geostatistical methods (Chapter 4). *GIS and Geostatistical Techniques for Groundwater Science*, Elsevier, pp. 33-41.
- Clout, J.M.F., Manuel, J.R., 2022. Mineralogical, chemical, and physical metallurgical characteristics of iron ore (Chapter 2). *Iron Ore, Second Edition*, Elsevier, pp. 59-108.
- Cowan, E.J., Beatson, R.K., Fright, W.R., McLennan, T.J., Mitchell, T.J., 2002. Rapid geological modelling. *Applied Structural Geology for Mineral Exploration and Mining, International Symposium*, pp. 1-8.

- Cowan, E.J., Spragg, K.J., Everitt, M.R., 2011. Wireframe-free geological modelling - An oxymoron or a value proposition? Proceedings of the 8th International Mining Geology Conference 2011, pp. 247-259.
- Cowan, M.W., Beatson, R.K., Ross, H.J., Fright, W.R., McLennan, T.J., Evans, T.R., Carr, J.C., Lane, R.G., Bright, D.V., Gillman, A.J., Oshust, P.A., Titley, M., 2003. Practical implicit geological modelling. Fifth International Mining Geology Conference. pp. 17-19.
- Coward, S., Dowd, P., 2015. Geometallurgical models for the quantification of uncertainty in mining project value chains. Application of Computers and Operations Research in the Mineral Industry - Proceedings of the 37th International Symposium, APCOM 2015, pp. 360-369.
- Cressie, N., 1990. The origins of kriging. *Mathematical Geology*, vol. 22, no. 3, pp. 239-252.
- Creus, P.K., Basson, I.J., Koegelenberg, C.K., Ekkerd, J., de Graaf, P.J.H., Bester, M., Mokele, T., 2019. 3D Fabric analysis of Venetia Mine, South Africa: Using structural measurements and implicitly-modelled surfaces for improved pit slope design and risk management. *Journal of African Earth Sciences*, vol. 155, pp. 137-150.
- Cullen, D., Halladay, J., Briner, N., Basnet, R., Bergen, J., Doleck, T., 2022. Evaluation of synthetic data generation techniques in the domain of anonymous traffic classification. *IEEE Access*, vol. 10, pp. 129612-129625.
- Danish, B., 2017. Geometallurgical estimation of comminution indices for porphyry copper deposit applying mineralogical approach. PhD Thesis, Luleå University of Technology, 91 p.
- David, D., 2007. The importance of geometallurgical analysis in plant study, design and operational phases. Australasian Institute of Mining and Metallurgy Publication Series. pp. 241-247.

- Dehaine, Q., Tijsseling, L.T., Glass, H.J., Törmänen, T., Butcher, A.R., 2021. Geometallurgy of cobalt ores: A review. *Minerals Engineering*, vol. 160, art. no. 106656, pp. 1-28.
- Deutsch, C.V., Journel, A.G., 1998. *GSLIB: Geostatistical Software Library and User's Guide, Second Edition*. Oxford University Press, New York, NY, USA, 125 p.
- Deutsch, C.V., Wilde, B.J., 2013. Modeling multiple coal seams using signed distance functions and global kriging. *International Journal of Coal Geology*, vol. 112, pp. 87-93.
- Deutsch, J.L., 2015. *Multivariate spatial modeling of metallurgical rock properties*. PhD Thesis, University of Alberta, 182 p.
- Deutsch, J.L., Palmer, K., Deutsch, C. V., Szymanski, J., Etsell, T.H., 2016. Spatial modeling of geometallurgical properties: Techniques and a case study. *Natural Resources Research*, vol. 25, no. 2, pp. 161-181.
- Dominy, S.C., O'connor, L., Parbhakar-Fox, A., Glass, H.J., Purevgerel, S., 2018. Geometallurgy – A route to more resilient mine operations. *Minerals*, vol. 8, no. 12, pp. 1-33.
- Dunham, S., Vann, J., 2007. Geometallurgy, geostatistics and project value – Does your block model tell you what you need to know? *Australasian Institute of Mining and Metallurgy Publication Series*, pp. 189-196
- Ehrig, K., 2013. Geometallurgy – what do you really need to know from exploration through to production? *Metallurgical Plant Design and Operating Strategies, MetPlant 2013*, pp. 28-33.
- Fallara, F., Legault, M., Rabeau, O., 2006. 3-D integrated geological modeling in the Abitibi subprovince (Québec, Canada): Techniques and applications. *Exploration and Mining Geology*, vol. 15, no. 1-2, pp. 27-42.
- Feng, C., Yang, P., Xu, B., 2010. Rapid geological modeling by using implicit 3D potential field interpolation method. *2010 International*

- Conference on Computer Design and Applications, ICCDA 2010, vol. 5, pp. 0-3.
- Ganguly, K., 2017. Learning generative adversarial networks: Next-generation deep learning simplified. Packt Publishing, 203 p.
- Garrido, M., Sepulveda, E., Ortiz, J., Navarro, F., Townley, B., 2018. A methodology for the simulation of synthetic geometallurgical block models of porphyry ore bodies. Procemin 14th International Mineral Processing Conference (PROCEMIN), 5th International Seminar on Geometallurgy (GEOMET), December 2018, pp. 1-10.
- Garrido, M., Sepúlveda, E., Ortiz, J., Townley, B., 2020. Simulation of synthetic exploration and geometallurgical database of porphyry copper deposits for educational purposes. Natural Resources Research, vol. 29, no. 6, pp. 3527-3545.
- Gonçalves, Í.G., Kumaira, S., Guadagnin, F., 2017. A machine learning approach to the potential-field method for implicit modeling of geological structures. Computers and Geosciences, vol. 103, pp. 173-182.
- Goodfellow, I., Pouget-Abadie, J., Mirza, M., Xu, B., Warde-Farley, D., Ozair, S., Courville, A., Bengio, Y., 2014. Generative adversarial nets. In: Ghahramani, Z., Welling, M., Cortes, C., Lawrence, N. and Weinberger, K.Q. (Eds.), Advances in Neural Information Processing Systems, Curran Associates, Inc., vol. 27, pp. 2672-2680.
- Goodfellow, I., Pouget-Abadie, J., Mirza, M., Xu, B., Warde-Farley, D., Ozair, S., Courville, A., Bengio, Y., 2020. Generative adversarial networks. Communications of the ACM. Association for Computing Machinery, New York, NY, USA, vol. 63, no. 11, pp. 139-144.
- Grose, L., Ailleres, L., Laurent, G., Jessell, M., 2021. LoopStructural 1.0: time-aware geological modelling. Geoscientific Model Development, vol. 14, pp. 3915-3937.

- Grose, L., Laurent, G., Aillères, L., Armit, R., Jessell, M., Caumon, G., 2017. Structural data constraints for implicit modeling of folds. *Journal of Structural Geology*, vol. 104, pp. 80-92.
- Guo, J., Wang, J., Wu, L., Liu, C., Li, C., Li, F., Lin, M., Jessell, M.W., Li, P., Dai, X., Tang, J., 2020. Explicit-implicit-integrated 3-D geological modelling approach: A case study of the Xianyan Demolition Volcano (Fujian, China). *Tectonophysics*, vol. 795, no. 228648, pp. 1-16.
- Guo, J., Wang, Z., Li, C., Li, F., Jessell, M.W., Wu, L., Wang, J., 2022. Multiple-point geostatistics-based three-dimensional automatic geological modeling and uncertainty analysis for borehole data. *Natural Resources Research*, vol. 31, no. 5, pp. 2347-2367.
- Guo, J., Wu, L., Zhou, W., Li, C., Li, F., 2018. Section-constrained local geological interface dynamic updating method based on the HRBF surface. *Journal of Structural Geology*, vol. 107, pp. 64-72.
- Hardy, R.L., 1971. Multiquadric equations of topography and other irregular surfaces. *Journal of Geophysical Research*, vol. 76, no. 8, pp. 1905-1915.
- Hernandez, M., Epelde, G., Alberdi, A., Cilla, R., Rankin, D., 2022. Synthetic data generation for tabular health records: A systematic review. *Neurocomputing*, vol. 493, pp. 28-45.
- Hillier, M., 2020. Radial basis functions. In: Daya Sagar, B.S., Cheng, Q., McKinley, J. and Agterberg, F. (Eds.), *Encyclopedia of Mathematical Geosciences*. Springer International Publishing, Cham, pp. 1-8.
- Hillier, M.J., de Kemp, E.A., Schetselaar, E.M., 2017. Implicit 3-d modelling of geological surfaces with the Generalized Radial Basis Functions (GRBF) algorithm: Geological Survey of Canada Open File. No. 7814, p. 15.
- Hillier, M.J., Schetselaar, E.M., de Kemp, E.A., Perron, G., 2014. Three-dimensional modelling of geological surfaces using generalized

interpolation with radial basis functions. *Mathematical Geosciences*, vol. 46, no. 8, pp. 931-953.

Hines, T., 2022. Interpolate – RBF. Available at:

<https://Rbf.Readthedocs.io/En/Latest/Interpolate.Html#rbf-Interpolation> [Accessed March 2022].

Hittmeir, M., Ekelhart, A., Mayer, R., 2019. On the utility of synthetic data. *Proceedings of the 14th International Conference on Availability, Reliability and Security*, ACM, New York, NY, USA, pp. 1-6.

Hunt, J., Kojovic, T., Berry, R., 2013. Estimating comminution indices from ore mineralogy, chemistry and drill core logging. *The Second AusIMM International Geometallurgy Conference*, pp. 173-176.

Jakobsson, S., Andersson, B., Edelvik, F., 2009. Rational radial basis function interpolation with applications to antenna design. *Journal of Computational and Applied Mathematics*, vol. 233, no. 4, pp. 889-904.

Jessell, M., Aillères, L., Kemp, E. de, Lindsay, M., Wellmann, F., Hillier, M., Laurent, G., Carmichael, T., Martin, R., 2014. Next generation three-dimensional geologic modeling and inversion. *Building Exploration Capability for the 21st Century*, Society of Economic Geologists, pp. 261-271.

Jordon, J., Szpruch, L., Houssiau F., Bottarelli, M., Cherubin, G., Maple, C., Cohen, S.N., Weller, A., 2022. Synthetic data – what, why and how ?. Report, The Alan Turing Institute, The Royal Society, UK, 58 p.

Journel, A.G., 1989. Imaging of spatial uncertainty: a non-Gaussian approach. *Geostatistical, Sensitivity, and Uncertainty Methods for Ground-Water Flow and Radionuclide Transport Modeling*. Proceedings of the DOE/AECL Conference, San Francisco, CA (USA), pp. 585-599.

- Kashpur, O.F., 2021. Hermite–Brinkhoff interpolation polynomial of minimum norm in Hilbert space. *Cybernetics and Systems Analysis*, vol. 57, no. 5, pp. 803-808.
- Kentwell, D.J., 2019. Destroying the distinction between explicit and implicit geological modelling. 11th International Proceedings Mining Geology Conference, The Australasian Institute of Mining and Metallurgy, Melbourne, pp. 154160.
- Keylock, C.J., 2019. Hypothesis testing for nonlinear phenomena in the geosciences using synthetic, surrogate data. *Earth and Space Science*, vol. 6, no. 1, pp. 41-58.
- de la Varga, M., Schaaf, A., Wellmann, F., 2019. GemPy 1.0: open-source stochastic geological modeling and inversion. *Geoscientific Model Development*, vol. 12, no. 1, pp. 1-32.
- Lajaunie, C., Courrioux, G., Manuel, L., 1997. Foliation fields and 3D cartography in geology: Principles of a method based on potential interpolation. *Mathematical Geology*, vol. 29, no. 4, pp. 571-584.
- Laurent, G., Ailleres, L., Grose, L., Caumon, G., Jessell, M., Armit, R., 2016. Implicit modeling of folds and overprinting deformation. *Earth and Planetary Science Letters*, vol. 456, pp. 26-38.
- Li, T., Li, P., Zhang, T., Liu, J., Duan, X., 2021. An optimized potential field geological modeling method for a high-level radioactive-waste geological disposal repository. *IOP Conference Series: Earth and Environmental Science*, vol. 861, no. 4, pp. 1-9.
- Li, Z., Zhong, D., Wang, L., Tang, Q., Wu, Z., 2022. Mesh processing for snapping feature points and polylines in orebody modeling. *Mathematics*, vol. 10, no. 15, pp. 1-23.
- Lishchuk, V., 2018. Bringing predictability into a geometallurgical program: An iron ore case study. Doctoral Thesis, Luleå University of Technology, 106 p.

- Little, C., Elliot, M., Allmendinger, R., Samani, S.S., 2021. Generative adversarial networks for synthetic data generation: A Comparative Study. Available at: <https://arxiv.org/abs/2112.01925>.
- Liu, S., Wang, C.C.L., Brunnett, G., Wang, J., 2016. A closed-form formulation of HRBF-based surface reconstruction by approximate solution. *Computer-Aided Design*, vol. 78, pp. 147-157.
- Lotfolah Hamedani, M., Plimer, I.R., Xu, C., 2012. Orebody modelling for exploration: the western mineralisation, Broken Hill, NSW. *Natural Resources Research*, vol. 21, no. 3, pp. 325-345.
- Macêdo, I., Gois, J.P., Velho, L., 2009. Hermite interpolation of implicit surfaces with radial basis functions. *Proceedings of SIBGRAPI 2009, 22nd Brazilian Symposium on Computer Graphics and Image Processing*, pp. 1-8.
- Macêdo, I., Gois, J.P., Velho, L., 2011. Hermite radial basis functions implicits. *Computer Graphics Forum*, vol. 30, no. 1, pp. 27-42.
- Mallet, J.L., 2003. *Geomodeling (Book review)*. *Computers & Geosciences*, vol. 29, pp. 811-812.
- Mambwe, P., Shengo, M., Kidyanama, T., Mucchez, P., Chabu, M., 2022. Geometallurgy of cobalt black ores in the Katanga Copperbelt (Ruashi Cu-Co deposit): A new proposal for enhancing cobalt recovery. *Minerals*, vol. 12, no. 3, pp. 1-22.
- Martin, R., Boisvert, J.B., 2017. Iterative refinement of implicit boundary models for improved geological feature reproduction. *Computers & Geosciences*, vol. 109, pp. 1-15.
- Matheron, G., 1981. Splines and Kriging: Their formal equivalence. In: Merriam, D.F. (Eds.). *Down-to-earth statistics: Solutions looking for geological problems*, Syracuse University Geological Contributions, pp. 77-95.

- Mboyo, L.H., 2018. Optimisation et planification de l'exploitation du gisement de Karu-est. Bachelor's Project, Faculté Polytechnique, University of Lubumbashi, 97 p.
- McInerney, P., Goldberg, A., Calcagno, P., Courrioux, G., Guillen, R., Seikel, R., 2007. Improved 3D geology modelling using an implicit function interpolator and forward modelling of potential field data. Proceedings of Exploration 07, Fifth Decennial International Conference on Mineral Exploration, Toronto, Canada, pp. 919-922.
- McLennan, J., Deutsch, C.V., 2006. Implicit Boundary Modeling (BOUNDSIM). Centre for Computational Geostatistics, Edmonton.
- McLennan, J.A., 2007. The decision of stationarity. PhD Thesis, University of Alberta, Canada, 191 p.
- Meyer, D., Nagler, T., Hogan, R., 2020. Copula-based synthetic data generation for machine learning emulators in weather and climate: application to a simple radiation model. Geoscientific Model Development Discussions. DOI: [10.5194/gmd-2020-427](https://doi.org/10.5194/gmd-2020-427).
- Musafer, G.N., Thompson, M.H., 2017. Non-linear optimal multivariate spatial design using spatial vine copulas. Stochastic Environmental Research and Risk Assessment, vol. 31, no. 2, pp. 551-570.
- Myers, D.E., 1982. Matrix formulation of co-kriging. Journal of the International Association for Mathematical Geology, vol. 14, no. 3, pp. 249-257.
- Myers, D.E., 1992. Kriging, cokriging, radial basis functions and the role of positive definiteness. Computers and Mathematics with Applications, vol. 24, no. 12, pp. 139-148.
- Myers, D.E., Armstrong, M., 2000. Basic linear geostatistics. Technometrics, vol. 42, no. 4, p. 437.

- Napier-Munn, T.J., Morrell, S., Morrison, R.D., Kojovic, T., 1999. Mineral comminution circuits, their operation and optimisation. Julius Kruttschnitt Mineral Research Centre, Indooroopilly, Australia, 413 p.
- Navarra, A., Grammatikopoulos, T., Waters, K., 2018. Incorporation of geometallurgical modelling into long-term production planning. *Minerals Engineering*, vol. 120, pp. 118-126.
- Newell, A.J., 2018. Implicit geological modelling: A new approach to 3D volumetric national-scale geological models. Report OR/19/004, British Geological Survey, Nottingham, UK, 37 p.
- Norgaard, S., Saeedi, R., Sasani, K., Gebremedhin, A.H., 2018. Synthetic sensor data generation for health applications: a supervised deep learning approach. *Proceedings of the Annual International Conference of the IEEE Engineering in Medicine and Biology Society, EMBS*, pp. 1164-1167.
- Öfner, W., Zaurith, G., 2016. The drop weight test revisited: characterization of the crushability of hot sinter and validation of the approach with natural rocks. *BHM Berg- Und Hüttenmännische Monatshefte*, vol. 161, no. 6, pp. 277-282.
- Ortiz, J.M., Kracht, W., Townley, B., Lois, P., Cardenas, E., Miranda, R., Alvarez, M., 2015. Workflows in geometallurgical prediction: Challenges and outlook. *Proceedings of IAMG 2015, 17th Annual Conference of the International Association for Mathematical Geosciences*, pp. 228-233.
- Osher, S., Fedkiw, R., 2002. The level set methods and dynamic implicit surfaces. *Applied Mechanics Reviews*, vol. 57, no. 3, pp. B15.
- Pandey, N., Patnaik, P.K., Gupta, S., 2020. Data pre-processing for machine learning models using python libraries. *International Journal of Engineering and Advanced Technology*, vol. 9, no. 4, pp. 1995-1999.

- Park, N., Mohammadi, M., Gorde, K., Jajodia, S., Park, H., Kim, Y., 2018. Data synthesis based on generative adversarial networks. Proceedings of the VLDB Endowment, vol. 11, no. 10.
- Patki, N., Wedge, R., Veeramachaneni, K., 2016a. GaussianCopula – The synthetic data vault SDV. Proceedings of the 3rd IEEE International Conference on Data Science and Advanced Analytics, DSAA 2016, pp. 399-410.
- Patki, N., Wedge, R., Veeramachaneni, K., 2016b. The synthetic data vault. Proceedings of the 3rd IEEE International Conference on Data Science and Advanced Analytics, DSAA 2016, pp. 399-410.
- Philander, C., Rozendaal, A., 2013. The application of a novel geometallurgical template model to characterise the Namakwa Sands heavy mineral deposit, West Coast of South Africa. Minerals Engineering, vol. 52, pp. 82-94.
- Piret, C., Dissanayake, N., Gierke, J.S., Fornberg, B., 2020. The radial basis functions method for improved numerical approximations of geological processes in heterogeneous systems. Mathematical Geosciences, vol. 52, no. 4, pp. 477-497.
- Poniewierski, J., 2019. Block model knowledge for mining engineers: An introduction. White paper, Deswik®, 33 p.
- Powell, M., 2013. Utilising orebody knowledge to improve comminution circuit design and energy utilisation improve comminution circuit design. Second AusIMM International Geometallurgy Conference, pp. 27-35.
- Renard, D., Wagner, L., Chilès, J.-P., Vann, J., Deraisme, J., 2013. Modeling the geometry of a mineral deposit domain with a potential field. 36th APCOM, 3 – 8 November 2013, Porto Allegre, Brazil, pp. 21-39.

- Rojimol J., 2013. Development of optimal geostatistical model for geotechnical applications. Master's Dissertation, Indian Institute of Technology Hyderabad, 68 p.
- Rolo, R.M., Radtke, R., Costa, J.F.C.L., 2017. Signed distance function implicit geologic modeling. *Revista Escola de Minas*, vol. 70, no. 2, pp. 221-229.
- Roy, I., Chandra Sarkar, B., Sarkar, B.C., 2000. Orebody modelling: An integrated geological-geostatistical approach. In: *Geology and Mineral Resources of Bihar and Jharkhand*. IGE, Patna (Eds.), pp. 170-179.
- Salehi, P., Chalechale, A., Taghizadeh, M., 2020. Generative adversarial networks (GANs): An overview of theoretical model, evaluation metrics, and recent developments. <https://doi.org/10.48550/arXiv.2005.13178>.
- Sanchidrián, J.A., Ouchterlony, F., Moser, P., Segarra, P., López, L.M., 2012. Performance of some distributions to describe rock fragmentation data. *International Journal of Rock Mechanics and Mining Sciences*, vol. 53, pp. 18-31.
- Savchenko, V.V., Pasko, A.A., Okunev, O.G., Kunii, T.L., 1995. Function representation of solids reconstructed from scattered surface points and contours. *Computer Graphics Forum*, vol. 14, no. 4, pp. 181-188.
- Seequent®, 2022. Welcome to Seequent support. Available at: <https://www.seequent.com/help-support/> [Accessed 1 October 2022].
- Sharkawy, A.-N., 2020. Principle of neural network and its main types: Review. *Journal of Advances in Applied & Computational Mathematics*, vol. 7, pp. 8-19.
- Silva, D., 2015. Signed distance function modeling with multiple categories. University of Alberta. PhD Thesis, 247 p.
- Sivakumar, J., Ramamurthy, K., Radhakrishnan, M., Won, D., 2022. Synthetic sampling from small datasets: A modified mega-trend

diffusion approach using k-nearest neighbors. Knowledge-Based Systems, vol. 236, p. 12.

Steward, M., 2014. Sources of geological modelling uncertainty investigated. Unearthing 3D implicit modelling. Available at: <http://www.leapfrog3d.com/online-resources/ebooks>. Accessed February 2022.

Stoch, B., Anthonissen, C.J., McCall, M.J., Basson, I.J., Deacon, J., Cloete, E., Botha, J., Britz, J., Strydom, M., Nel, D., Bester, M., 2018. 3D implicit modeling of the Sishen Mine: New resolution of the geometry and origin of Fe mineralization. Mineralium Deposita, vol. 53, no. 6, pp. 835-853.

Vieira, M., Costa, J.F.C.L., 2018. Geometallurgical modelling to help in predicting zinc metallurgical recovery. 24th World Mining Congress Proceedings, Rio de Janeiro, pp. 51-61.

Vollgger, S.A., Cruden, A.R., Ailleres, L., Cowan, E.J., 2015. Regional dome evolution and its control on ore-grade distribution: Insights from 3D implicit modelling of the Navachab gold deposit, Namibia. Ore Geology Reviews, vol. 69, pp. 268-284.

Wambeke, T., Benndorf, J., 2014. Integrated geometallurgical modelling of heavy mineral sands accounting for profitability, extractability and processability under uncertainty. Freiburger Forschungsforum, Geokinematischer Tag, Freiberg, Germany. pp. 1-9.

Wang, G., Li, R., Carranza, E.J.M., Zhang, S., Yan, C., Zhu, Y., Qu, J., Hong, D., Song, Y., Han, J., Ma, Z., Zhang, H., Yang, F., 2015. 3D geological modeling for prediction of subsurface Mo targets in the Luanchuan district, China. Ore Geology Reviews, vol. 71, pp. 592-610.

Wang, J., Zhao, H., Bi, L., Wang, L., 2018. Implicit 3D modeling of ore body from geological boreholes data using Hermite radial basis functions. Minerals, vol. 8, no. 10, p. 443.

- Wang, S., Li, X., Wang, S., Li, Q., Chen, C., Feng, F., Chen, Y., 2016. Three-dimensional orebody modelling and intellectualized longwall mining for stratiform bauxite deposits. *Transactions of Nonferrous Metals Society of China*, vol. 26, no. 10, pp. 2724-2730.
- Webster, R. and Oliver, M.A., 2008. *Geostatistics for environmental scientists*. Second Edition, 315 p.
- Wellmann, F., Caumon, G., 2018. 3-D Structural geological models: Concepts, methods, and uncertainties. *Advances in Geophysics*, vol. 59, pp. 1-121.
- Wu, X., Liang, L., Shi, Y., Fomel, S., 2019. FaultSeg3D: Using synthetic data sets to train an end-to-end convolutional neural network for 3D seismic fault segmentation. *Geophysics*, vol. 84, no. 3, pp. IM35-IM45.
- Xu, L., Skoularidou, M., Cuesta-Infante, A., Veeramachaneni, K., 2019. Modeling tabular data using conditional GAN. *Advances in Neural Information Processing Systems*, vol. 32, p. 11.
- Xu, L., Veeramachaneni, K., 2018. Synthesizing tabular data using generative adversarial networks. *arXiv preprint arXiv:1811.11264*.
- Yang, L., Achtziger-Zupančič, P., Caers, J., 2021. 3D modeling of large-scale geological structures by linear combinations of implicit functions: application to a large, banded iron formation. *Natural Resources Research*, vol. 30, no. 5, pp. 3139-3163.
- Yu, H., Xie, T., Paszczyński, S., Wilamowski, B.M., 2011. Advantages of radial basis function networks for dynamic system design. *IEEE Transactions on Industrial Electronics*, vol. 58, no. 12, pp. 5438-5450.
- Zhang, Z., Yan, C., Lasko, T.A., Sun, J., Malin, B.A., 2021. SynTEG: A framework for temporal structured electronic health data simulation. *Journal of the American Medical Informatics Association*, vol. 28, no. 3, pp. 596-604.

- Zhong, D., Wang, L., 2020. Solution optimization of RBF interpolation for implicit modeling of orebody. *IEEE Access*, vol. 8, pp. 13781-13791.
- Zhong, D., Wang, L., Bi, L., Jia, M., 2019. Implicit modeling of complex orebody with constraints of geological rules. *Transactions of Nonferrous Metals Society of China*, vol. 29, no. 11, pp. 2392-2399.
- Zhong, D., Zhang, J., Wang, L., 2019. Fast implicit surface reconstruction for the radial basis functions interpolant. *Applied Sciences*, vol. 9, no. 24, p. 5335.
- Zhong, D., Zhang, J., Wang, L., Bi, L., 2022. Implicit modeling of narrow vein type ore bodies based on Boolean combination constraints. *Scientific Reports*, vol. 12, no. 1, p. 6086.
- Zhong, D.Y., Wang, L.G., Bi, L., 2019. Implicit surface reconstruction based on generalized radial basis functions interpolant with distinct constraints. *Applied Mathematical Modelling*, vol. 71, pp. 408-420.
- Zhong, D.-Y., Wang, L.-G., Wang, J.-M., 2021. Combination constraints of multiple fields for implicit modeling of ore bodies. *Applied Sciences*, vol. 11, no. 3, pp. 1-15.
- Zůvala, R., Fišerová, E., Marek, L., 2016. Mathematical aspects of the kriging applied on landslide in Halenkovice (Czech Republic). *Open Geosciences*, vol. 8, no. 1, pp. 275-288.

APPENDICES

Appendix A: Python® code for collar synthetic data generation

Jupyter® notebooks and files used to create synthetic data can be obtained on my GitHub channel.

<https://github.com/ChaukeT/Sythetic-data>

Appendix B: Economic composite of drillhole datasets

id	holeid	from	to	Tco	status	true_lengt	linear_gra	dilution_tr	dilution_li	pct_missing
1	KRED207	0.0	60.5	0.09468...	Waste	60.5	5.7284	2.8	3.2622	58
2	KRED207	60.5	76.5	2.8101375	Ore	16.0	44.9622	1.9	0.0	12
3	KRED207	76.5	104.5	0.04351...	Waste	28.0	1.2185	0.0	0.0	68
4	KRED209	0.0	83.0	0.02396...	Waste	83.0	1.9895	0.6	0.4128	79
5	KRED209	83.0	94.5	1.17926...	Ore	11.5	13.5616	2.8	0.0	24
6	KRED209	94.5	113.0	0.08789...	Waste	18.5	1.6261	1.6	1.4588	67
7	KRED211	0.0	84.5	0.02139...	Waste	84.5	1.8079	1.2	1.0339	93
8	KRED211	84.5	89.8	1.34128...	Ore	5.3	7.1088	1.6	0.0	30
9	KRED211	89.8	104.8	0.32178	Waste	15.0	4.8267	2.9	2.0025	0
10	KRED211	104.8	139.2	1.46124...	Ore	34.4	50.2668	14.2	1.2867	20
11	KRED211	139.2	155.0	0.00584...	Waste	15.8	0.0923	0.0	0.0	60
12	KRED212	0.0	29.8	0.04465...	Waste	29.8	1.3307	0.0	0.0	49
13	KRED212	29.8	65.0	0.91014...	Ore	35.2	32.0372	12.6	2.8416	14
14	KRED212	65.0	87.5	0.08569...	Waste	22.5	1.9282	0.7	0.6776	49
15	KRED212	87.5	109.1	0.91475...	Ore	21.6	19.7588	6.5	0.0	30
16	KRED212	109.1	131.0	0.18254...	Waste	21.9	3.9977	1.6	1.131	21
17	KRED212	131.0	148.5	3.03795...	Ore	17.5	53.1642	2.3	0.0	13
18	KRED212	148.5	161.0	0.036192	Waste	12.5	0.4524	0.0	0.0	10
19	KRED218	0.0	107.0	0.02774...	Waste	107.0	2.9688	0.0	0.0	84
20	KRED218	107.0	117.5	2.44634...	Ore	10.5	25.6866	2.5	0.2064	16
21	KRED218	117.5	120.5	0.26763...	Waste	3.0	0.8029	0.0	0.0	0
22	KRED218	120.5	130.4	8.79151...	Ore	9.9	87.036	1.0	0.0	10
23	KRED218	130.4	170.0	0.00178...	Waste	39.6	0.0706	0.0	0.0	89
24	KRED219	0.0	80.0	0.07667...	Waste	80.0	6.1337	1.7	4.102	75
25	KRED219	80.0	92.0	2.74908...	Ore	12.0	32.989	4.1	0.0	34
26	KRED219	92.0	125.0	0.00351...	Waste	33.0	0.1161	0.0	0.0	88
27	KRED220	0.0	58.5	0.09708...	Waste	58.5	5.6794	1.5	1.2103	51
28	KRED220	58.5	65.5	0.759	Ore	7.0	5.313	2.2	0.0	31
29	KRED220	65.5	90.0	0.08569...	Waste	24.5	2.0996	1.5	1.5738	49
30	KRED220	90.0	102.6	1.27826...	Ore	12.6	16.1061	7.4	0.2841	36
31	KRED220	102.6	189.0	0.00329...	Waste	86.4	0.2844	0.0	0.0	94

33	KRED221	90.5	96.0	0.78890...	Ore	5.5	4.339	0.7	0.2352	0
34	KRED221	96.0	96.5	0.0	Waste	0.5	0.0	0.0	0.0	100
35	KRED221	96.5	103.5	0.66661...	Ore	7.0	4.6663	2.1	0.6744	9
36	KRED221	103.5	126.5	0.19403...	Waste	23.0	4.4627	3.2	2.7672	54
37	KRED221	126.5	131.0	1.36253...	Ore	4.5	6.1314	0.0	0.0	0
38	KRED221	131.0	155.0	0.17843...	Waste	24.0	4.2824	0.8	0.56	4
39	KRED221	155.0	171.5	1.73840...	Ore	16.5	28.6837	3.5	0.7898	4
40	KRED221	171.5	189.0	0.00879...	Waste	17.5	0.1539	0.0	0.0	40
41	KRED222	0.0	83.1	0.05405...	Waste	83.1	4.4918	0.0	0.0	43
42	KRED222	83.1	89.5	2.0884375	Ore	6.4	13.366	0.0	0.0	0
43	KRED222	89.5	132.0	0.14678...	Waste	42.5	6.2384	3.1	3.3672	19
44	KRED223	0.0	53.0	0.03914...	Waste	53.0	2.0746	0.6	0.396	66
45	KRED223	53.0	74.0	1.69008...	Ore	21.0	35.4917	0.7	0.3213	0
46	KRED223	74.0	119.0	0.01915...	Waste	45.0	0.862	0.0	0.0	80
47	KRED22...	0.0	44.7	0.02324...	Waste	44.7	1.0391	0.0	0.0	84
48	KRED22...	44.7	117.5	1.39546...	Ore	72.8	101.5902	15.3	0.0	21
49	KRED22...	117.5	140.5	0.01739...	Waste	23.0	0.4	0.0	0.0	80
50	KRED22...	0.0	75.8	0.08059...	Waste	75.8	6.1093	1.7	1.1325	45
51	KRED22...	75.8	125.1	2.00586...	Ore	49.3	98.889	14.1	1.3989	21
52	KRED22...	125.1	146.5	0.02732...	Waste	21.4	0.5848	0.0	0.0	65
53	KRED227	0.0	59.0	0.02659...	Waste	59.0	1.5692	0.0	0.0	87
54	KRED227	59.0	65.0	0.6108	Ore	6.0	3.6648	0.5	0.0	8
55	KRED227	65.0	87.5	0.20508	Waste	22.5	4.6143	2.4	1.5039	12
56	KRED227	87.5	100.3	0.55871...	Ore	12.8	7.1516	4.4	0.6357	18
57	KRED227	100.3	108.5	0.28346...	Waste	8.2	2.3244	1.3	0.7245	17
58	KRED227	108.5	128.7	1.45456...	Ore	20.2	29.3823	2.3	0.0	11
59	KRED227	128.7	161.0	0.15033...	Waste	32.3	4.85567	3.7	3.9243	62
60	KRED228	0.0	88.3	0.02867...	Waste	88.3	2.5316	0.8	0.4064	90
61	KRED228	88.3	124.3	0.655075	Ore	36.0	23.5827	12.4	3.7727	6
62	KRED228	124.3	135.5	0.34463...	Waste	11.2	3.8599	1.5	1.1746	9

63	KRED228	135.5	144.0	0.69071...	Ore	8.5	5.8711	2.6	0.2586	13
64	KRED228	144.0	155.0	0.00369...	Waste	11.0	0.0406	0.0	0.0	59
65	KRED229	0.0	108.5	0.00978...	Waste	108.5	1.0614	0.0	0.0	86
66	KRED230	0.0	72.8	0.02812...	Waste	72.8	2.0472	1.5	0.9379	91
67	KRED230	72.8	76.0	0.60678...	Ore	3.2	1.9417	0.8	0.3704	0
68	KRED230	76.0	272.0	0.01812...	Waste	196.0	3.5516	3.5	2.6396	96
69	KRED231	0.0	52.0	0.11153...	Waste	52.0	5.7999	2.7	2.6585	52
70	KRED231	52.0	70.5	1.1866	Ore	18.5	21.9521	9.8	0.913	35
71	KRED231	70.5	120.5	0.164294	Waste	50.0	8.2147	1.8	5.6977	41
72	KRED232	0.0	181.5	0.02832...	Waste	181.5	5.1404	1.4	0.8981	79
73	KRED233	0.0	80.2	0.05612...	Waste	80.2	4.5009	0.0	0.0	47
74	KRED233	80.2	89.3	2.34621...	Ore	9.1	21.3506	0.9	0.4023	0
75	KRED233	89.3	99.0	0.08914...	Waste	9.7	0.8647	0.0	0.0	46
76	KRED233	99.0	122.2	3.07331...	Ore	23.2	71.3008	2.4	0.0	10
77	KRED233	122.2	132.0	0.07997...	Waste	9.8	0.78375	0.0	0.0	31
78	KRED234	0.0	92.0	0.12924...	Waste	92.0	11.8908	6.4	4.3633	25
79	KRED234	92.0	95.0	1.1698	Ore	3.0	3.5094	0.0	0.0	0
80	KRED234	95.0	114.5	0.02505...	Waste	19.5	0.4886	0.0	0.0	77
81	KRED235	0.0	155.0	0.01990...	Waste	155.0	3.0857	1.5	0.807	93
82	KRED235	155.0	165.6	1.077	Ore	10.6	11.4162	3.1	0.142	20
83	KRED235	165.6	255.0	0.00578...	Waste	89.4	0.5168	0.0	0.0	87
84	KRED237	0.0	70.5	0.01070...	Waste	70.5	0.7548	0.0	0.0	90
85	KRED237	70.5	76.5	0.73978...	Ore	6.0	4.4387	0.7	0.0	12
86	KRED237	76.5	88.5	0.0945	Waste	12.0	1.134	0.0	0.0	23
87	KRED237	88.5	95.3	1.03976...	Ore	6.8	7.0704	3.2	0.0504	43
88	KRED237	95.3	99.0	0.24	Waste	3.7	0.888	0.7	0.518	54
89	KRED237	99.0	116.1	0.97166...	Ore	17.1	16.6154	4.1	1.0411	11
90	KRED237	116.1	117.8	0.23435...	Waste	1.7	0.3984	0.0	0.0	53
91	KRED237	117.8	121.5	0.54994...	Ore	3.7	2.0348	1.6	0.7048	0
92	KRED237	121.5	150.0	0.01149...	Waste	28.5	0.3275	0.0	0.0	84

93	KRED238	0.0	178.0	0.01899...	Waste	178.0	3.3804	0.8	0.5096	90
94	KRED239	0.0	116.0	0.01533...	Waste	116.0	1.7794	1.4	1.2894	95
95	KRED239	116.0	121.0	0.7754	Ore	5.0	3.877	1.0	0.0	20
96	KRED239	121.0	224.0	0.00581...	Waste	103.0	0.5988	0.0	0.0	95
97	KRED240	0.0	224.0	0.04732...	Waste	224.0	10.6	8.8	5.6623	84
98	KRED241	0.0	54.8	0.03196...	Waste	54.8	1.7518	0.0	0.0	84
99	KRED241	54.8	62.4	1.03744...	Ore	7.6	7.8846	1.5	0.6718	0
100	KRED241	62.4	103.5	0.01417...	Waste	41.1	0.5826	0.0	0.0	94
101	KRED249	0.0	68.2	0.03940...	Waste	68.2	2.6874	0.0	0.0	69
102	KRED249	68.2	72.0	1.30794...	Ore	3.8	4.9702	0.0	0.0	0
103	KRED249	72.0	118.5	0.04479...	Waste	46.5	2.083	0.0	0.0	69
104	KRED250	0.0	92.0	0.00162...	Waste	92.0	0.1493	0.0	0.0	98
105	KRED250	92.0	95.8	1.53478...	Ore	3.8	5.8322	0.7	0.2604	0
106	KRED250	95.8	97.3	0.2436	Waste	1.5	0.3654	0.0	0.0	0
107	KRED250	97.3	131.8	3.03651...	Ore	34.5	104.7596	10.4	2.3655	3
108	KRED250	131.8	159.5	0.01204...	Waste	27.7	0.3337	0.0	0.0	87
109	KRED25...	0.0	155.0	0.02869...	Waste	155.0	4.4476	1.7	4.342	96
110	KRED252	0.0	287.5	0.00051...	Waste	287.5	0.1468	0.0	0.0	99
111	KRED30...	0.0	76.5	0.02114...	Waste	76.5	1.6178	0.5	0.3545	93
112	KRED30...	76.5	80.3	0.56094...	Ore	3.8	2.1316	0.8	0.0	21
113	KRED30...	80.3	115.5	0.10949...	Waste	35.2	3.8541	2.6	1.8006	62
114	KRED30...	115.5	122.3	1.58777...	Ore	6.8	10.7969	0.7	0.2653	0
115	KRED30...	122.3	144.0	0.05189...	Waste	21.7	1.1262	0.0	0.0	74
116	KRED30...	144.0	164.4	2.18123...	Ore	20.4	44.4971	6.3	1.1004	15
117	KRED30...	164.4	181.5	0.05292...	Waste	17.1	0.905	0.6	0.528	53
118	KRED302	0.0	74.1	0.01690...	Waste	74.1	1.2524	0.0	0.0	93
119	KRED302	74.1	77.7	0.92405...	Ore	3.6	3.3266	0.8	0.0	22
120	KRED302	77.7	99.8	0.16868...	Waste	22.1	3.728	0.8	0.5392	10
121	KRED302	99.8	102.8	0.95336...	Ore	3.0	2.8601	0.2	0.0	7
122	KRED302	102.8	114.2	0.31464...	Waste	11.4	3.5869	2.1	1.853	13
123	KRED302	114.2	121.7	1.70684	Ore	7.5	12.8013	2.1	0.0	28

124	KRED302	121.7	128.2	0.20146...	Waste	6.5	1.3095	0.3	0.1908	37
125	KRED302	128.2	141.5	3.25	Ore	13.3	43.225	4.4	0.0	33
126	KRED302	141.5	157.0	0.03065...	Waste	15.5	0.4751	0.6	0.4044	30
127	KRED303	0.0	64.5	0.02362...	Waste	64.5	1.5238	0.0	0.0	81
128	KRED303	64.5	68.3	1.54605...	Ore	3.8	5.875	1.3	0.0	34
129	KRED303	68.3	70.5	0.17113...	Waste	2.2	0.3765	0.0	0.0	14
130	KRED303	70.5	95.3	2.61254...	Ore	24.8	64.791	13.6	1.029	27
131	KRED303	95.3	114.0	0.00180...	Waste	18.7	0.0337	0.0	0.0	70
132	KRED304	0.0	93.3	0.06004...	Waste	93.3	5.6019	2.1	1.9983	74
133	KRED304	93.3	116.3	4.01889...	Ore	23.0	92.4346	3.8	0.6864	10
134	KRED304	116.3	194.0	0.00077...	Waste	77.7	0.0604	0.0	0.0	94
135	KRED30...	0.0	56.8	0.06967...	Waste	56.8	3.9578	0.0	0.0	26
136	KRED30...	56.8	60.3	2.56514...	Ore	3.5	8.978	0.2	0.0	6
137	KRED30...	60.3	72.5	0.23080...	Waste	12.2	2.8158	1.5	0.7995	24
138	KRED30...	72.5	89.0	3.1198	Ore	16.5	51.4767	2.9	0.0	18
139	KRED30...	89.0	96.5	0.15708	Waste	7.5	1.1781	0.0	0.0	13
140	KRED30...	96.5	104.7	1.19023...	Ore	8.2	9.7599	3.1	0.2802	30
141	KRED30...	104.7	120.5	0.00494...	Waste	15.8	0.0782	0.0	0.0	87
142	KRED306	0.0	122.8	0.02551...	Waste	122.8	3.1334	2.5	1.4036	92
143	KRED306	122.8	140.8	1.88603...	Ore	18.0	33.9486	3.7	0.5438	14
144	KRED306	140.8	221.0	0.00166...	Waste	80.2	0.1336	0.0	0.0	97
145	KRED307	0.0	75.5	0.08297...	Waste	75.5	6.2649	5.1	3.885	74
146	KRED307	75.5	104.8	3.04231...	Ore	29.3	89.13995	3.1	0.0	11
147	KRED307	104.8	123.5	0.03018...	Waste	18.7	0.5644	0.0	0.0	78
148	KRED308	0.0	93.0	0.10092...	Waste	93.0	9.3856	5.4	3.5514	57
149	KRED308	93.0	99.0	0.9717	Ore	6.0	5.8302	0.8	0.0	13
150	KRED308	99.0	105.0	0.28005	Waste	6.0	1.6803	1.6	0.9086	42
151	KRED308	105.0	133.2	1.43214...	Ore	28.2	40.3865	9.1	0.0	32
152	KRED308	133.2	163.5	0.00122...	Waste	30.3	0.0372	0.0	0.0	90
153	KRED309	0.0	127.0	0.08827...	Waste	127.0	11.2114	1.0	0.5825	46
154	KRED310	0.0	63.5	0.07022...	Waste	63.5	4.4595	0.7	0.938	31

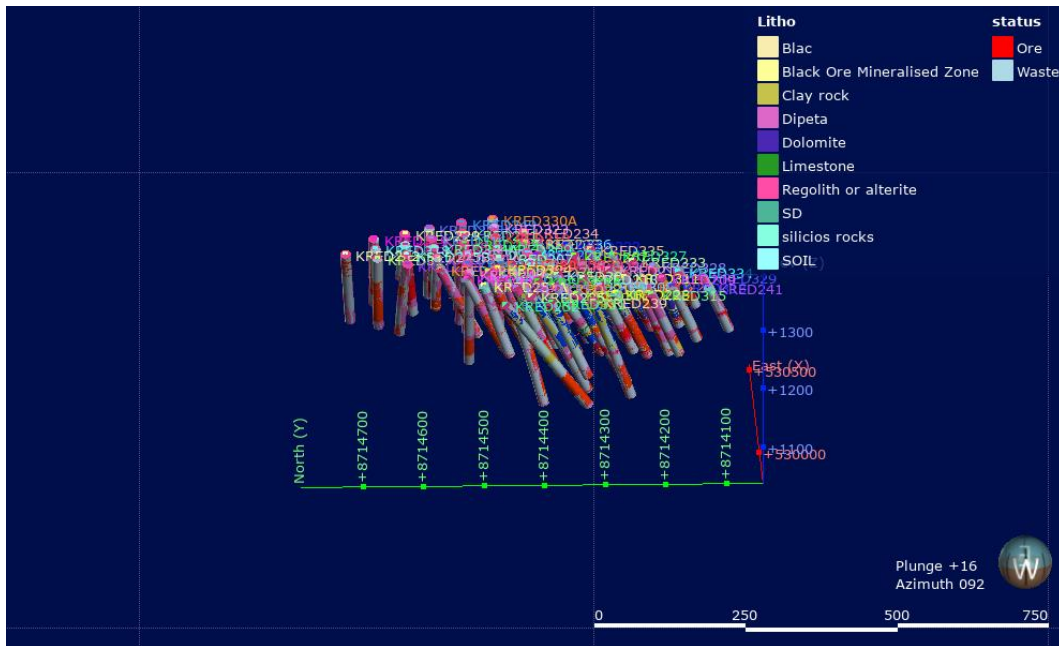
155	KRED310	63.5	69.0	2.17290...	Ore	5.5	11.951	0.8	0.0	15
156	KRED310	69.0	83.0	0.02956...	Waste	14.0	0.4139	0.0	0.0	6
157	KRED310	83.0	126.7	2.06704...	Ore	43.7	90.3297	16.4	1.2369	23
158	KRED310	126.7	180.0	0.00406...	Waste	53.3	0.2165	0.0	0.0	93
159	KRED311	0.0	79.0	0.03057...	Waste	79.0	2.4157	0.0	0.0	72
160	KRED311	79.0	110.4	1.69978...	Ore	31.4	53.3732	15.7	0.4552	23
161	KRED311	110.4	128.5	0.00341...	Waste	18.1	0.0619	0.0	0.0	90
162	KRED31...	0.0	106.5	0.09482...	Waste	106.5	10.09835	6.7	4.4317	58
163	KRED31...	106.5	116.8	1.19328...	Ore	10.3	12.2908	4.9	0.1155	19
164	KRED31...	116.8	126.0	0.10704...	Waste	9.2	0.9848	0.6	0.915	70
165	KRED313	0.0	101.0	0.15914...	Waste	101.0	16.0739	7.6	5.4584	47
166	KRED313	101.0	106.3	1.24030...	Ore	5.3	6.5736	0.6	0.0	11
167	KRED313	106.3	128.0	0.00539...	Waste	21.7	0.117	0.0	0.0	84
168	KRED31...	0.0	36.5	0.05976...	Waste	36.5	2.1814	0.5	0.271	67
169	KRED31...	36.5	52.2	0.90328...	Ore	15.7	14.1815	3.7	0.302	17
170	KRED31...	52.2	74.0	0.06752...	Waste	21.8	1.4721	0.8	0.5127	58
171	KRED31...	74.0	106.9	2.41148...	Ore	32.9	79.3377	5.9	1.1393	9
172	KRED31...	106.9	116.0	0.05381...	Waste	9.1	0.4897	0.0	0.0	4
173	KRED315	0.0	86.5	0.08089...	Waste	86.5	6.9972	2.1	1.3144	54
174	KRED315	86.5	90.3	1.01831...	Ore	3.8	3.8696	0.5	0.0	13
175	KRED315	90.3	97.8	0.29134...	Waste	7.5	2.1851	1.2	0.744	21
176	KRED315	97.8	102.6	0.828125	Ore	4.8	3.975	1.0	0.252	6
177	KRED315	102.6	145.0	0.12168...	Waste	42.4	5.1596	2.7	2.5155	67
178	KRED316	0.0	142.0	0.07056...	Waste	142.0	10.0201	4.7	4.8565	54
179	KRED317	0.0	85.2	0.03057...	Waste	85.2	2.6052	2.0	1.268	88
180	KRED317	85.2	88.3	0.76374...	Ore	3.1	2.3676	0.2	0.0	6
181	KRED317	88.3	171.5	0.00201...	Waste	83.2	0.1679	0.0	0.0	96
182	KRED318	0.0	59.0	0.03331...	Waste	59.0	1.9655	1.0	0.7944	76
183	KRED318	59.0	67.5	1.02727...	Ore	8.5	8.7318	1.7	0.0	20
184	KRED318	67.5	78.5	0.23602...	Waste	11.0	2.5963	1.8	1.5987	38
185	KRED318	78.5	110.8	0.65822...	Ore	32.3	21.2606	13.2	1.8545	8

186	KRED318	110.8	144.5	0.00892...	Waste	33.7	0.3009	0.0	0.0	94
187	KRED319	0.0	68.3	0.00999...	Waste	68.3	0.6828	0.0	0.0	72
188	KRED319	68.3	75.9	1.57609...	Ore	7.6	11.9783	1.4	0.0	18
189	KRED319	75.9	170.0	0.00130...	Waste	94.1	0.1225	0.0	0.0	99
190	KRED320	0.0	93.0	0.0044	Waste	93.0	0.4092	0.0	0.0	97
191	KRED320	93.0	103.4	0.66533...	Ore	10.4	6.9195	1.3	0.1074	7
192	KRED320	103.4	165.5	0.04680...	Waste	62.1	2.9068	2.8	1.6965	86
193	KRED321	0.0	74.5	0.03146...	Waste	74.5	2.3445	1.2	0.6637	90
194	KRED321	74.5	119.2	1.42660...	Ore	44.7	63.7691	8.0	0.0	18
195	KRED321	119.2	182.5	0.00098...	Waste	63.3	0.0624	0.0	0.0	97
196	KRED322	0.0	45.5	0.06496...	Waste	45.5	2.9558	0.6	0.3702	41
197	KRED322	45.5	59.8	1.04803...	Ore	14.3	14.9869	2.3	0.0	16
198	KRED322	59.8	103.0	0.01173...	Waste	43.2	0.5069	0.0	0.0	94
199	KRED323	0.0	64.2	0.06039...	Waste	64.2	3.8772	0.0	0.0	40
200	KRED323	64.2	70.7	1.22396...	Ore	6.5	7.9558	3.3	0.4545	31
201	KRED323	70.7	83.0	0.40728...	Waste	12.3	5.0096	1.6	2.541	34
202	KRED323	83.0	103.0	1.73323	Ore	20.0	34.6646	13.8	1.8676	21
203	KRED323	103.0	154.5	0.25738...	Waste	51.5	13.2551	8.5	6.4306	17
204	KRED324	0.0	74.7	0.00432...	Waste	74.7	0.3229	0.0	0.0	97
205	KRED324	74.7	117.3	1.13430...	Ore	42.6	48.3216	10.4	0.3292	14
206	KRED324	117.3	119.0	0.08411...	Waste	1.7	0.143	0.1	0.143	94
207	KRED324	119.0	125.0	0.88535	Ore	6.0	5.3121	1.1	0.0	18
208	KRED324	125.0	161.0	0.28792...	Waste	36.0	10.3652	5.8	8.2439	28
209	KRED325	0.0	122.6	0.05438...	Waste	122.6	6.6672	2.3	1.4965	66
210	KRED325	122.6	129.2	1.05477...	Ore	6.6	6.9615	1.7	0.0	26
211	KRED325	129.2	210.5	0.00016...	Waste	81.3	0.0137	0.0	0.0	97
212	KRED326	0.0	56.8	0.07863...	Waste	56.8	4.4662	0.0	0.0	40
213	KRED326	56.8	67.8	0.69957...	Ore	11.0	7.6953	2.9	0.797	6
214	KRED326	67.8	86.6	0.00926...	Waste	18.8	0.1741	0.0	0.0	94
215	KRED327	0.0	37.1	0.04585...	Waste	37.1	1.7014	0.0	0.0	47
216	KRED327	37.1	47.6	5.60509...	Ore	10.5	58.8535	1.4	0.0	13

216	KRED327	37.1	47.6	5.60509...	Ore	10.5	58.8535	1.4	0.0	13
217	KRED327	47.6	77.0	0.05033...	Waste	29.4	1.47975	0.8	0.9	65
218	KRED328	0.0	44.0	0.04904...	Waste	44.0	2.1578	1.0	1.49	53
219	KRED328	44.0	74.8	2.72473...	Ore	30.8	83.9218	5.3	0.0	17
220	KRED328	74.8	101.0	0.00290...	Waste	26.2	0.076	0.0	0.0	82
221	KRED329	0.0	30.5	0.03002...	Waste	30.5	0.9159	0.6	0.396	76
222	KRED329	30.5	48.0	0.88194...	Ore	17.5	15.434	5.2	0.5018	19
223	KRED329	48.0	50.0	0.2267	Waste	2.0	0.4534	0.0	0.0	45
224	KRED329	50.0	54.1	0.63190...	Ore	4.1	2.5908	0.8	0.0	20
225	KRED329	54.1	89.0	0.10349...	Waste	34.9	3.6121	1.3	1.5481	60
226	KRED33...	0.0	105.5	0.10006...	Waste	105.5	10.557	1.3	0.7256	33
227	KRED331	0.0	170.0	0.00766...	Waste	170.0	1.30285	0.0	0.0	90
228	KRED332	0.0	107.7	0.00366...	Waste	107.7	0.3942	0.0	0.0	89
229	KRED332	107.7	112.6	1.11779...	Ore	4.9	5.4772	0.3	0.0	6
230	KRED332	112.6	168.5	0.07767...	Waste	55.9	4.3418	3.6	2.9522	62
231	KRED333	0.0	35.0	0.02048...	Waste	35.0	0.7171	0.9	0.45	90
232	KRED333	35.0	56.0	3.68547...	Ore	21.0	77.395	2.2	0.0	10
233	KRED333	56.0	69.5	0.148	Waste	13.5	1.998	1.6	1.1217	24
234	KRED333	69.5	73.3	0.77168...	Ore	3.8	2.9324	0.3	0.0	8
235	KRED333	73.3	78.5	0.27753...	Waste	5.2	1.4432	1.5	1.0083	37
236	KRED334	0.0	37.8	0.03720...	Waste	37.8	1.4062	0.9	0.4581	59
237	KRED334	37.8	65.7	1.80487...	Ore	27.9	50.3561	2.7	0.0	10
238	KRED334	65.7	84.5	0.04770...	Waste	18.8	0.8969	0.0	0.0	14
239	KRED335	0.0	27.5	0.02247...	Waste	27.5	0.618	0.5	0.403	81
240	KRED335	27.5	33.2	2.56087...	Ore	5.7	14.597	0.2	0.0	4
241	KRED335	33.2	42.5	0.36674...	Waste	9.3	3.4107	1.4	1.4578	16
242	KRED335	42.5	45.5	0.85703...	Ore	3.0	2.5711	0.3	0.0	10
243	KRED335	45.5	52.5	0.2477	Waste	7.0	1.7339	1.5	0.9022	14
244	KRED335	52.5	61.3	0.71794...	Ore	8.8	6.3179	3.3	0.3975	22
245	KRED335	61.3	79.5	0.02975...	Waste	18.2	0.5415	0.0	0.0	69
246	KRED336	0.0	50.0	0.01612	Waste	50.0	0.806	0.0	0.0	94

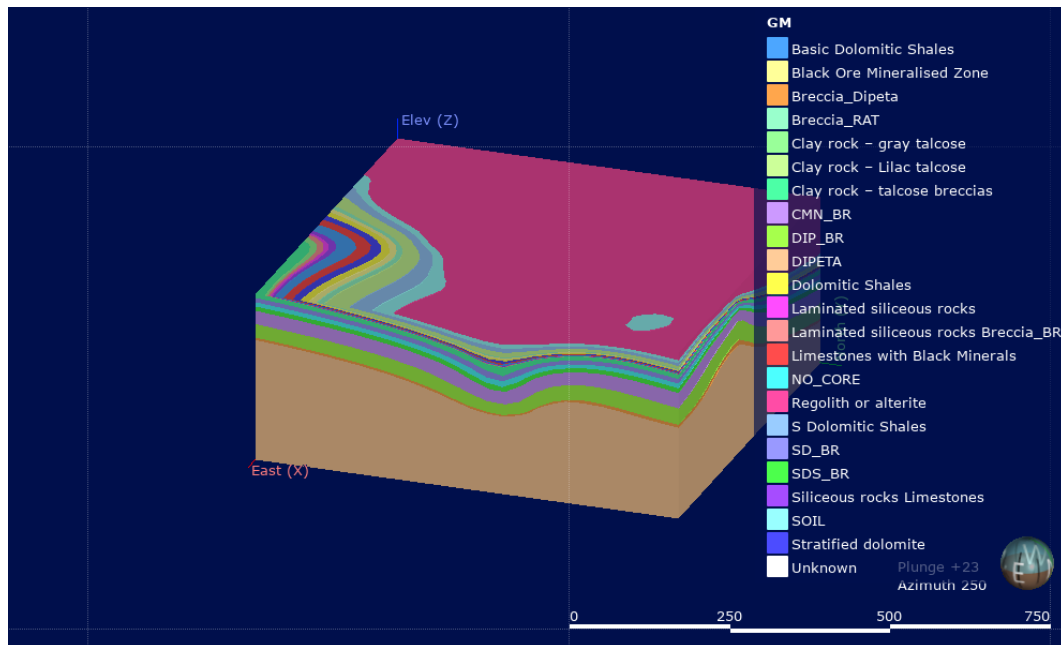
247	KRED336	50.0	62.0	0.99163...	Ore	12.0	11.8996	1.3	0.0	11
248	KRED336	62.0	92.0	0.10152	Waste	30.0	3.0456	1.4	0.7728	59

Appendix C: Drillhole datasets combination





Appendix D: Geological modelling created through implicit modelling

A geological model of Sediment-Hosted Stratiform Copper-Cobalt deposit classified according to the geology of the area.



Appendix E: Ethical clearance certificate

	
UNISA SCHOOL OF ENGINEERING (SOE) RESEARCH ETHICS REVIEW COMMITTEE	
31 March 2022	ERC Reference # : 2022/CSET/SOE/012 Name : Mr Tiyani Chauke Student #: 66377056 Staff #: N/A
Dear Mr Tiyani Chauke	
Decision: Ethics Approval from 31/03/2022 to 31/03/2027 [No humans involved]	
<hr/>	
Researcher(s): Name: Mr Tiyani Chauke E-mail address: 66377056@mylife.unisa.ac.za Telephone #: 079 146 9726	
Supervisor (s): Name: Prof Francois Mulenga E-mail address: mulenf@unisa.ac.za Telephone #: 011 471 2692	
Working title of research: Development of an implicit orebody modelling algorithm for use in geometallurgical and mine planning applications	
Qualification: PhD in Science, Engineering, and Technology	
<hr/>	
Thank you for the application for research ethics clearance by the Unisa School of Engineering Research Ethics Review Committee for the above mentioned research. Ethics approval is granted for 5 years.	
<i>The negligible risk application was reviewed by the School of Engineering Research Ethics Review Committee on 25 March 2022 in compliance with the Unisa Policy on Research Ethics and the Standard Operating Procedure on Research Ethics Risk Assessment. The decision will be tabled at the next Committee meeting on 25 April 2022 for ratification.</i>	
	<small>University of South Africa Pretorius Street, Muckleneuk Ridge, City of Tshwane PO Box 392 UNISA 0003 South Africa Telephone: +27 12 429 3111 Facsimile: +27 12 429 4150 www.unisa.ac.za</small>

The proposed research may now commence with the provisions that:

1. The researcher(s) will ensure that the research project adheres to the values and principles expressed in the UNISA Policy on Research Ethics.
2. Any adverse circumstance arising in the undertaking of the research project that is relevant to the ethicality of the study should be communicated in writing to the School of Engineering Research Ethics Committee.
3. The researcher(s) will conduct the study according to the methods and procedures set out in the approved application.
4. Any changes that can affect the study-related risks for the research participants, particularly in terms of assurances made with regards to the protection of participants' privacy and the confidentiality of the data, should be reported to the Committee in writing, accompanied by a progress report.
5. The researcher will ensure that the research project adheres to any applicable national legislation, professional codes of conduct, institutional guidelines and scientific standards relevant to the specific field of study. Adherence to the following South African legislation is important, if applicable: Protection of Personal Information Act, no 4 of 2013; Children's act no 38 of 2005 and the National Health Act, no 61 of 2003.
6. Only de-identified research data may be used for secondary research purposes in future on condition that the research objectives are similar to those of the original research. Secondary use of identifiable human research data requires additional ethics clearance.
7. The researcher will ensure that the research project adheres to the relevant guidelines set out in the Unisa COVID-19 position statement on research ethics attached.
8. No field work activities may continue after the expiry date 31 March 2027. Submission of a completed research ethics progress report will constitute an application for renewal of Ethics Research Committee approval.

Note:

The reference number 2022/CSET/SOE/012 should be clearly indicated on all forms of communication with the intended research participants, as well as with the Committee.

Yours sincerely,



Dr TY Leswifi
Chair of School of Engineering Research Ethics Review Committee
College of Science, Engineering and Technology (CSET)
E-mail: leswity@unisa.ac.za
Tel: (011) 670 9288



PP

Prof. F Nemavhola
Director: School of Engineering
College of Science Engineering and
Technology (CSET)
E-mail: masitfj@unisa.ac.za
Tel: (011) 471 2354



Prof. B Mamba
Executive Dean
College of Science Engineering and
Technology (CSET)
E-mail: mambabb@unisa.ac.za
Tel: (011) 670 9230